EXHALED BREATH ANALYSIS FOR NON-INVASIVE DIAGNOSIS OF TROPICAL DISEASES

Tesfalem Geremariam Welearegay

UNIVERSITAT ROVIRA i VIRGILI

Exhaled Breath Analysis for Non-Invasive Diagnosis of Tropical Diseases

Tesfalem Geremariam Welearegay

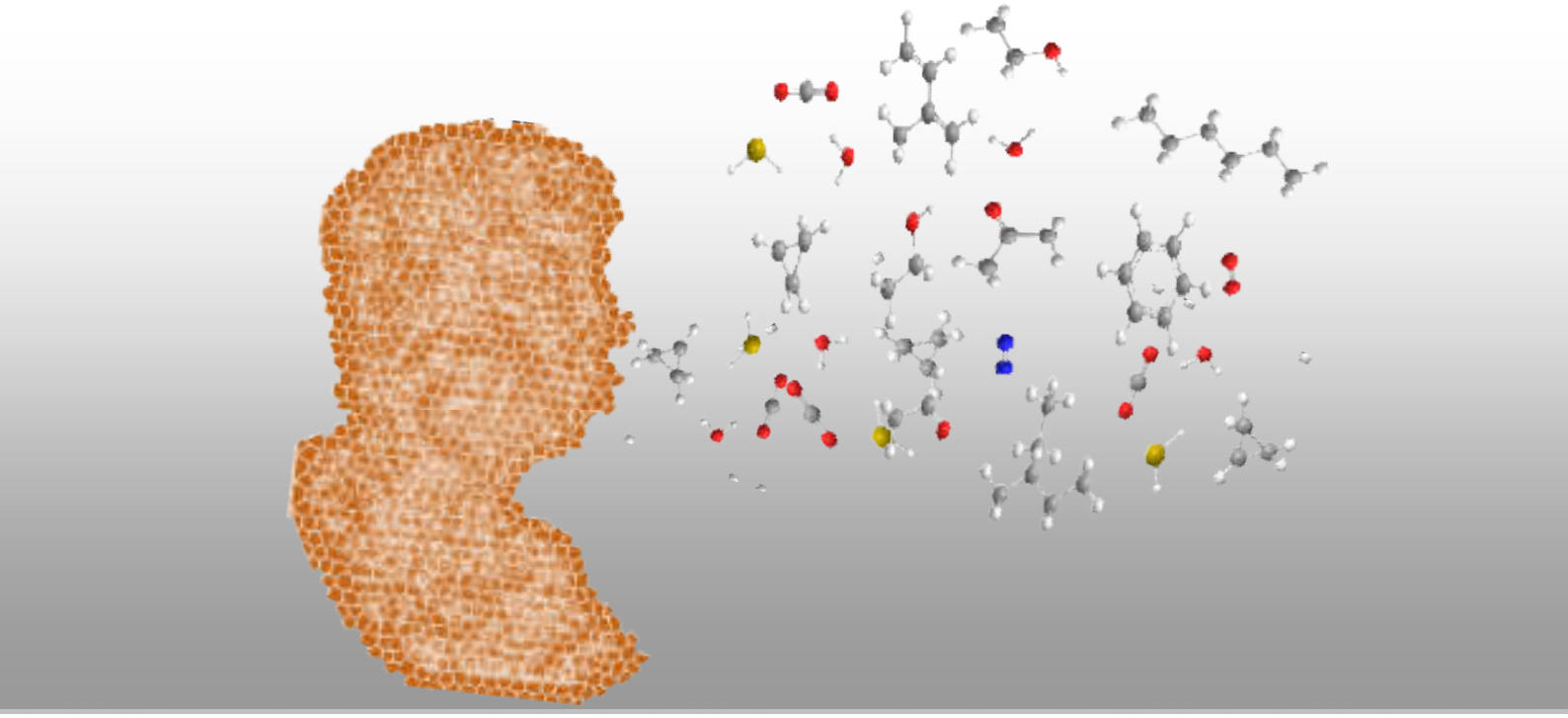

Doctoral Thesis
2018

UNIVERSITAT ROVIRA I VIRGILI
EXHALED BREATH ANALYSIS FOR NON-INVASIVE DIAGNOSIS OF TROPICAL DISEASES
Tesfalem Geremariam Welearegay

Exhaled Breath Analysis for Non-Invasive Diagnosis of Tropical Diseases

Ph.D Thesis

Tesfalem Geremariam Welearegay

UNIVERSITAT ROVIRA i VIRGILI

Department of Electronic, Electrical and Automatic Control Engineering

UNIVERSITAT ROVIRA I VIRGILI
EXHALED BREATH ANALYSIS FOR NON-INVASIVE DIAGNOSIS OF TROPICAL DISEASES
Tesfalem Geremariam Welearegay

UNIVERSITAT ROVIRA I VIRGILI
EXHALED BREATH ANALYSIS FOR NON-INVASIVE DIAGNOSIS OF TROPICAL DISEASES
Tesfalem Geremariam Welearegay

UNIVERSITAT ROVIRA I VIRGILI
EXHALED BREATH ANALYSIS FOR NON-INVASIVE DIAGNOSIS OF TROPICAL DISEASES
Tesfalem Geremariam Welearegay

Tesfalem Geremariam Welearegay

Exhaled Breath Analysis for Non-Invasive Diagnosis of Tropical Diseases

Ph.D Thesis

Supervised by:

Dr. Septimiu Radu Ionescu

Prof. Eduard Llobet Valero

Department of

Electronic, Electrical, and Automatic Control Engineering

UNIVERSITAT ROVIRA i VIRGILI

Tarragona

2018

UNIVERSITAT ROVIRA I VIRGILI
EXHALED BREATH ANALYSIS FOR NON-INVASIVE DIAGNOSIS OF TROPICAL DISEASES
Tesfalem Geremariam Welearegay

UNIVERSITAT ROVIRA i VIRGILI
Department d'Enginyeria Electrònica, Elèctrica i Automàtica
Escola Tècnica Superior D'Enginyria
Campus Sescelades
Avinguda dels Països Catalans, 26
43007 Tarragona
Espanya
Tel: +34 977559 610/559 728
Fax: +34 977 559 605

FAIG CONSTAR que aquest treball, titulat "Exhaled Breath Analysis for Non-Invasive Diagnosis of Tropical Diseases", que presenta Tesfalem Geremariam Welearegay per a l'obtenció del títol de Doctor, ha estat realitzat sota la meva direcció al Department d'Enginyeria Electrònica, Elèctrica i Automàtica d'aquesta universitat.

HAGO CONSTAR que el presente trabajo, titulado "Exhaled Breath Analysis for Non-Invasive Diagnosis of Tropical Diseases", que presenta Tesfalem Geremariam Welearegay, ha sido realizado bajo mi dirección en el Departmento de Ingeniería Electrónica, Eléctrica y Automática de esta universidad.

I STATE that the present study, entitled "Exhaled Breath Analysis for Non-invasive Diagnosis of Tropical Diseases", presented by Tesfalem Geremariam Welearegay for the award of the degree of Doctor of Philosophy, has been carried out under our supervision at the Department of Electronic, Electrical and Automatic Control Engineering, of this University. Rovira i Virgili Univeristy.

November 2018, Tarragona, Spain

El/s director/s de tesi doctoral

El/los director/es de la tesis doctoral

Doctoral thesis supervisor/s

Septimiu Radu Ionescu

Eduard Llobet Valero

UNIVERSITAT ROVIRA I VIRGILI
EXHALED BREATH ANALYSIS FOR NON-INVASIVE DIAGNOSIS OF TROPICAL DISEASES
Tesfalem Geremariam Welearegay

Acknowledgement

First and foremost, I would like to extend my sincere gratitude to my supervisor, Dr. Radu Ionescu, and co-supervisor Prof. Eduard Llobet, for their invaluable guidance, abiding interest, and unreserved support most generously given through out my thesis work. Thank you for your trust and opportunity you have given to me to pursue my PhD study under such multidisciplinary and interesting research topic. This thesis would have not been possible without your respective guidance and continuous encouragement during those years.

I am also grateful to the group of Prof. Lars Österlund, Division of Solid State Physics, Uppsala University, for hosting me in his research lab to carry out the most fundamental work of my thesis work. I would like to thank Dr. Umut Cindemir, Prof. Lars Lab, who had been there for every technical assistance on Advancd Gas Deposition technique, and the times we spent in clean room for nanomaterial characterization. Thank you all for the technical assistance, fruitful discussions and above all providing me an open lab to dig out all experimental and instrumental facilities in your lab. I would also like to acknoweldge to all members of the FTF; Prof. Claes-Göran Granquvist, Prof. Gunnar Niklasson, Dr. Andreas Mattsson, for the discussions and morning fika time during my research stay in Uppsala University.

I would like to thank Prof. Dr. Boris Mizaikoff from the Institute of Analytical and Bioanalytical Chemistry (IABC), Ulm University, for allowing me to spend my research stay in his well equiped laboratory and helped me acquire alternative methods for the synthesis of metal nanoparticles (nanostars). Moreover, I would like to acknowledge to the members of the group, Mrs. Marie Bowman, and other for their generous hospitality and coffee time.

Additionally, I would like to extend my gratitude to Dr. Mohamed Fethi Diouani, from Laboratory of Epidemiology and Veterinary Microbiology, Pasteur Institute of Tunis, for hosting me in his lab to perform online breath testing with my sensing devices. I greatly appreciate your cooperation and committement in handling and recruiting volunteers for online breath sampling and analysis. I wish to thank to all your team members for the great collaboration in collecting breath samples at different Hospital centers and sending them to URV for offline breath analysis.

Furthermore, I also would like to express my deep appreciation to many collaborating partners for providing us a cohort of breath samples collected by, Dr. Sebastian Borys, Medical University of Gdansk (Poland), Prof. Cristhian Manuel Durán-Acevedo, Universidad de Pamplona (Colombia) and members of the team (Aylen Lisset, Omar, Oscar…), and Tarik Saidi, Moulay Ismail University (Moroco) for the collaborative work here in our lab.

Many individuals provided me their due support in GCMS analysis (Rosa, Giovani, Irati) at Center for Omics Sciences (Reus), and Servicio de Recursos Científicos y Técnicos from URV (Lukasz, Marianna,Mercé, Rita), mechanical workshops from URV (Badi, Jose, Ernest..) and you all are appreciated for your help. Special thanks also goes to Florina Ionescu for your help in the chrmotagraphic data, as well as for your generous support in all administrative issues during my frequent travel.

Finally, I owe a deep gratitude to the current and former members of MINOS group for creating such a friendly and pleasant working environment: Juan, Raul, Oriol, Sergio, Fatima, Pierrick Eric, Miriam, Ernest, Angel, Xavier, Serena. Moreover, I also sincerely thanks to my Habesha friends here in Tarragona, especially Pash community for the wonderful time we had spent and sharing all day today interesting discussions.

I especially thank Universitat Rovira i Virgili, MINECO (Spain) for financially supporting my PhD work, and the EU-TROPSENSE project for financing my conference travels, short course training and summer school courses.

Finally, my contributions to scientific knowledge would be absolutely nothing without the support from my family, which definietly deserves my most sincere gratitude. Thank you all!

Dedicated to my family, especially to my Mom…

UNIVERSITAT ROVIRA I VIRGILI
EXHALED BREATH ANALYSIS FOR NON-INVASIVE DIAGNOSIS OF TROPICAL DISEASES
Tesfalem Geremariam Welearegay

Abstract

Neglected Tropical Diseases (NTDs) belong to the group of infectious diseases. They are endemic in most parts of the world, affecting more than one billion people worldwide, especially low income populations from developing regions. The infection to humans is characterized by a chronic and prolonged asymptomatic incubation period without noticeable symptoms of the disease, which delays the prescription of a suitable and timely medical treatment. The prevention, diagnosis and control of these diseases still remain an unsolved medical challenge.

This thesis is aimed to develop a non-invasive, safe and patient-friendly methodology for rapid diagnosis of NTDs. The thesis work was founded on disease diagnosis via exhaled breath samples analyses, which are easy to obtain and present no discomfort or risk for patients' health. The thesis work was focused on three different types of neglected tropical diseases (Dengue, Echinococcosis and Leishmaniasis) caused by three different pathogens (viral, helminthic and protozoan infections, respectively). One of the challenges was to introduce and implement a simple and user friendly procedure for breath sampling, which was optimized in this study. For analyzing the breath samples, at first standard analytical techniques were employed for the identification of breath volatile biomarkers of these diseases. In the second part of the thesis work, an array of cross reactive chemical gas sensors based on ultrapure metal nanoparticles – ligand nanoassemblies comprising diverse functional organic ligands was designed, fabricated and employed for the analysis of the breath print profiles of the diseases under study. The responses of the chemical gas sensors to the breath samples were used to build predictive pattern recognition models for the diagnoses of these diseases. The results obtained revealed that exhaled breath analysis with cross reactive gas sensors

arrays based on ultrapure metal nanoparticles-ligand nanoassemblies holds significant potential as a cost-effective, simple and non-invasive diagnostic test for NTDs.

The thesis is organized as follows:

Chapter 1 presents a brief introduction to the neglected tropical diseases, with focus on the three diseases that I studied in my PhD thesis: Dengue, Leishmaniasis and Echinococcosis.

Chapter 2 presents the state of the art in breath analysis, with emphasis on analytical methods and chemical gas sensors.

Chapter 3 explains the experimental methods that I employed for the fabrication, deposition and characterization of chemical gas sensors based on ligand capped ultrapure metal nanoparticles.

Chapter 4 presents the methods for breath sampling and study population statistics that employed in the breath analysis of volunteers.

Chapter 5 presents the analytical studies and breath biomarkers identification. A discussion on their possible origin is also provided.

Chapter 6 presents the sensing measurements and the results of the sensing tests.

Chapter 7 summarizes the conclusions of my study and presents future perspective.

Resumen

Las enfermedades tropicales desatendidas (ETD) pertenecen al grupo de enfermedades infecciosas. Son endémicas en la mayor parte del mundo y afectan a más de mil millones de personas, especialmente a las poblaciones de bajos ingresos de las regiones en desarrollo. La infección en humanos se caracteriza por un período de incubación asintomática crónica y prolongada sin síntomas notables de la enfermedad, lo que retrasa la prescripción de un tratamiento médico adecuado y oportuno. La prevención, el diagnóstico y el control de estas enfermedades siguen siendo un desafío médico no resuelto.

Esta tesis ha tenido como objetivo desarrollar una metodología no invasiva, segura y amigable para el paciente para un diagnóstico rápido de las ETD. El enfoque de mi tesis se basó en el diagnóstico de la enfermedad a través del análisis de muestras de aliento exhalado, que son fáciles de obtener y no presentan molestias ni riesgos para la salud de los pacientes. El trabajo de mi tesis se centró en tres tipos diferentes de enfermedades tropicales desatendidas (dengue, equinococosis y leishmaniasis) causadas por tres patógenos diferentes (infecciones virales, helmínticas y protozoarias, respectivamente). Uno de los desafíos fue introducir e implementar un procedimiento de muestreo de muestras de aliento simple y fácil de usar, que se optimizó durante mi tesis. Para analizar las muestras de aliento, primero se emplearon técnicas analíticas estándar para la identificación de los biomarcadores volátiles de estas enfermedades. En la segunda parte del trabajo de mi tesis se diseñó y fabricó una matriz de sensores de gases químicos con sensibilidades cruzadas basados en nanopartículas de metal ultrapuro funcionalizadas con diversos compuestos orgánicos, que se empleó para el análisis de los patrones de las enfermedades estudiadas en las muestras de aliento. Las respuestas

de los sensores químicos de gases expuestos a las muestras de aliento se usaron para construir modelos de reconocimiento de patrones para el diagnóstico de estas enfermedades. Los resultados obtenidos han revelado que el análisis del aliento exhalado con una matriz de sensores de gases basados en nanoensamblajes de nanopartículas de metal ultrapuro tiene un gran potencial como prueba de diagnóstico fiable, simple y no invasiva para las ETD.

Resum

Les malalties tropicals desateses (ETD) pertanyen al grup de malalties infeccioses. Són endèmiques en la major part del món i afecten més de mil milions de persones, especialment a les poblacions de baixos ingressos de les regions en desenvolupament. La infecció en humans es caracteritza per un període d'incubació asimptomàtica crònica i perllongada sense símptomes notables de la malaltia, el que retarda la prescripció d'un tractament mèdic adequat i oportú. La prevenció, el diagnòstic i el control d'aquestes malalties segueixen sent un desafiament mèdic no resolt.

Aquesta tesi ha tingut com a objectiu desenvolupar una metodologia no invasiva, segura i amigable per al pacient per a un diagnòstic ràpid de les ETD. L'enfocament de la meva tesi es va basar en el diagnòstic de la malaltia a través de l'anàlisi de mostres d'alè exhalat, que són fàcils d'obtenir i no presenten molèsties ni riscos per a la salut dels pacients. El treball de la meva tesi es va centrar en tres tipus diferents de malalties tropicals desateses (dengue, equinococcosi i leishmaniosi) causades per tres patògens diferents (infeccions virals, helmíntiques i protozoàries, respectivament). Un dels reptes va ser introduir i implementar un procediment de mostreig d'alè simple i fàcil d'usar, que es va optimitzar durant la meva tesi. Per analitzar les mostres d'alè, primer es van emprar tècniques analítiques estàndard per a la identificació dels biomarcadors volàtils d'aquestes malalties. A la segona part del treball de la meva tesi es va dissenyar i va fabricar una matriu de sensors de gasos químics amb sensibilitats creuades basats en nanopartícules de metall ultrapur funcionalitzades amb diversos compostos orgànics, que es va emprar per a l'anàlisi dels patrons de les malalties estudiades en les mostres d'alè. Les respostes dels sensors químics de gasos exposats a les mostres d'alè es van usar per a construir models de reconeixement de patrons per al diagnòstic d'aquestes

malalties. Els resultats obtinguts han revelat que l'anàlisi de l'alè exhalat amb una matriu de sensors de gasos basats en nanoensamblajes de nanopartícules de metall ultrapur té un gran potencial com a prova de diagnòstic fiable, simple i no invasiva per les ETD.

UNIVERSITAT ROVIRA I VIRGILI
EXHALED BREATH ANALYSIS FOR NON-INVASIVE DIAGNOSIS OF TROPICAL DISEASES
Tesfalem Geremariam Welearegay

Table of Contents

CHAPTER 1

1. NEGLECTED TROPICAL DISEASES

Included in this chapter are brief introduction to Neglected Tropical Diseases (NTDs), and the infection, diagnosis and global distribution of the pathogenic diseases studied in my thesis.

1.1. Background

Nowadays, the world contends with tremendous global challenges in many parts of the globe, associated to global warming, frequent human and natural disasters, global immigration, population growth, wars and violence. Such diverse and enormous challenges are provoking huge environmental and economic distortions, which affect the life and well-being of the humans, and increase the mortality.

The World Health Organization (WHO) classifies the causes of death in three major groups [1]:

- *Group I* – related to communicable diseases, maternal, perinatal and nutritional causes. They are very common in poorer populations;
- *Group II* – associated to non-communicable diseases. Account for about 60% of deaths, and are highly dominant in high-income countries;
- *Group III* – injuries, accidents and others, which contribute to a large amount of deaths and disabilities.

Notably, as the world is in continuous swing, the global health problem is alarmingly increasing, and affects millions of people in every corner of the world [2]. Based on the data retrieved from the global diseases burden index reported in 2016, about 740 deaths per 100,000 people are caused by 21 categorical diseases (**Figure 1.1**) [3].

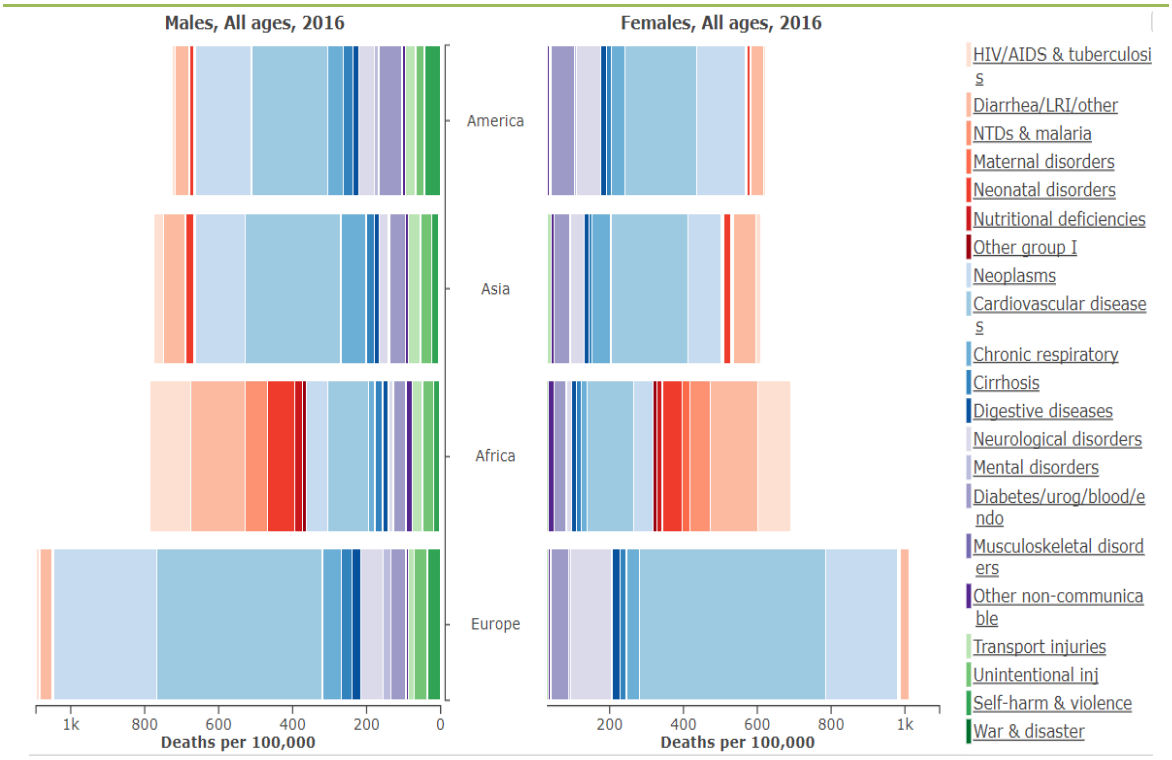

Figure 1.1: Global death caused by 21 categorical diseases, adapted from [3].

Out of 56.4 million deaths in 2015, more than 54% were caused by top 10 diseases, among which Ischemic heart disease and stroke are the world's biggest killers of non-communicable diseases [1].

In low income countries, more than 50% of deaths are due to communicable diseases [1], among which infectious diseases are the main cause of death as a result of infectious pathogens and outbreaks. The Disability Adjusted Life Years (DALYs) indicator, which represents the number of years loss from early deaths and years lost from disability due to illness per 1000 people, revealed that more than 31% of total DALYs were caused by communicable diseases in 2015 [1]. Even though HIV/AIDS, Malaria and Tuberculosis are among the major global killers among communicable diseases, infectious diseases (including NTDs) have also a major contribution to chronic disability, and thwart the economic development in the poorest countries.

1.2. Neglected Tropical Diseases

Tropical diseases encompass all diseases that occur solely, or principally, in the tropics, and the term is often taken to infectious diseases that thrive in hot, humid conditions. Within the tropical diseases, WHO defined a group of 20 neglected tropical diseases: *Buruli ulcer; Chagas disease; Dengue and Chikungunya; Dracunculiasis (guinea-worm disease); Echinococcosis; Foodborne trematodiases; Human African trypanosomiasis (sleeping sickness); Leishmaniasis; Leprosy; Lymphatic filariasis; Mycetoma, chromoblastomycosis and other deep mycoses; Onchocerciasis (river blindness); Rabies; Scabies and other ectoparasites; Schistosomiasis; Soil-transmitted helminthiases; Snakebite envenoming; Taeniasis/Cysticercosis; Trachoma; and Yaws (Endemic treponematoses)* [4,5]. These diseases are categorized in function of the pathogen: bacteria, virus, helminths, and protozoa (**Figure 1.2**).

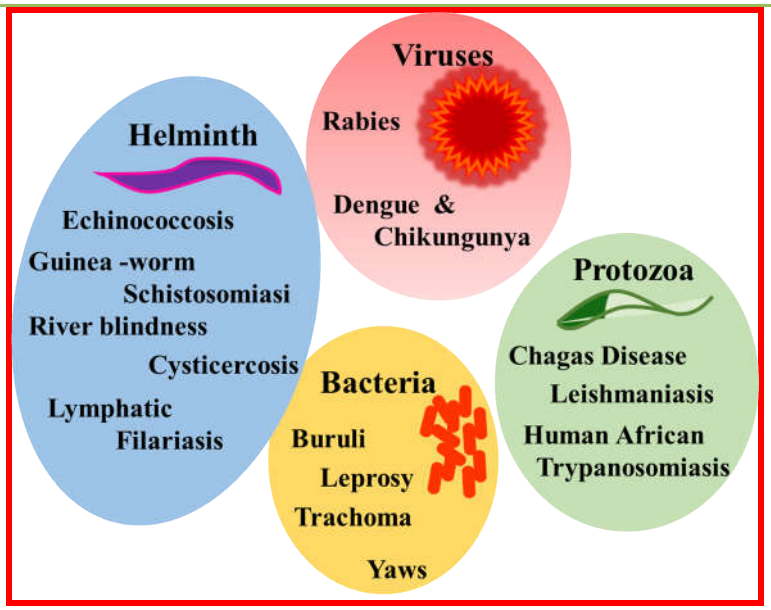

Figure: 1.2: Neglected Tropical Diseases caused by a variety of infectious pathogens including bacteria, virus, helminths, and protozoa.

In terms of geographical distribution, the NTDs are most prevalent in Africa, South America, and most parts of Asia (**Figure 1.3**), where vector transmission and distribution match with high population density and marginalized societies.

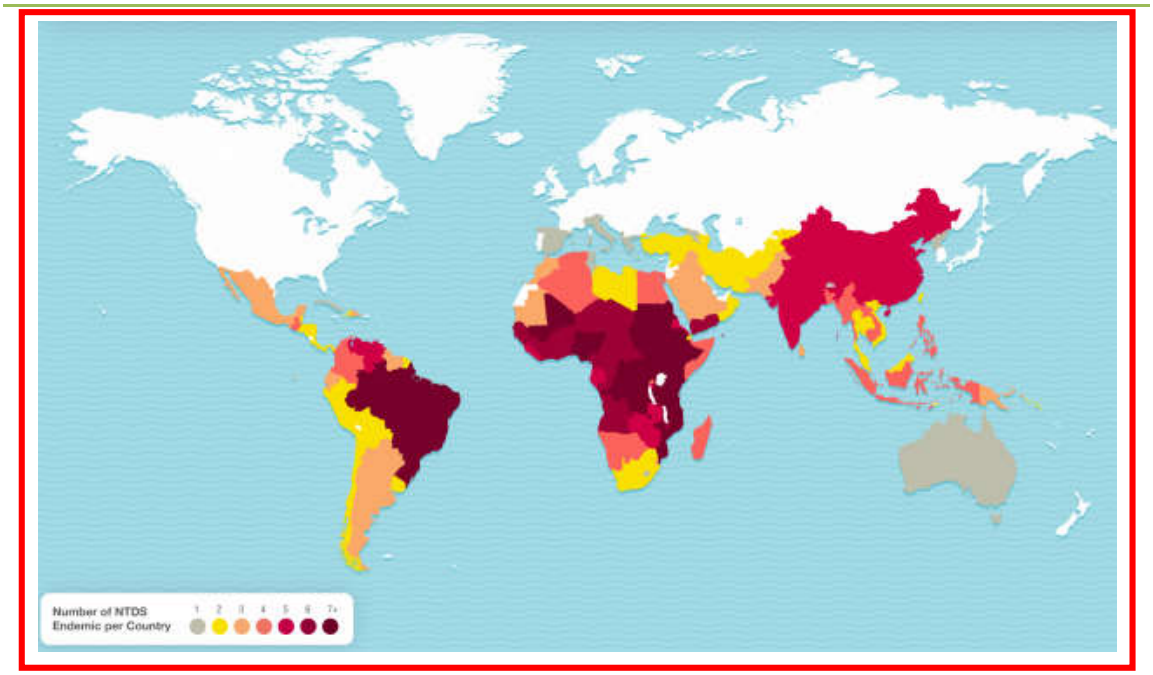

Figure 1.3: The global prevalence and distribution of Neglected Tropical Diseases by country. The burden of NTDs in different countries is expressed as the number of NTDs prevalent in the country. Reproduced from [4].

NTDs are characterized by high morbidity and low mortality. One billion people are currently infected by one or several NTDs, and more than half of world's population is at risk [4]. Annually, NTDs cause more than half a million deaths. Transmission to humans may be either direct, or indirect through vectors such as mosquitos, animal reservoirs, or other zoonotic agents found in water, food, and soil. Some vectors are likely to better reproduce and transmit the disease under certain environmental conditions, for example at high temperature and humidity, or near water reservoirs.

The NTDs cause massive suffering, life-long disability and death, stigma, mental distress and discrimination, as well as severe impairment and years of silent infection. They are mainly concentrated in remote rural areas and shantytowns, and their distribution is subject to socioeconomic factors such as inaccessibility to health facilities, consume of unpurified water, malnutrition, poor housing, poor sanitation, and high exposure to the vectors. Therefore, these diseases share common features related to impoverished population with low visibility and little political voice, and they cause stigma and discrimination, especially in girls and women.

Importantly, NTDs can be controlled, prevented, and eliminated using effective and feasible solutions [5]. In this regard, WHO introduced global health initiatives and control polices to eradicate and eliminate NTDs through intensive public health interventions and vector controls. However, currently the control and eradication of NTDs remain a top global health challenge. They require a strategy based on interventions centered on reaching poor and marginalized communities.

The implementation of alternative diagnostic approaches that could be easily deployed in areas lacking suitable healthcare resources for identifying the disease at an early stage, or that could be employed for mass screening, would be highly desirable in interventional and control programs.

In my PhD studies, I assessed a new non-invasive, fast, easy-to-use and cost-effective diagnostic method for NTDs diagnosis based on exhaled breath analysis, which I tested on representative categories of NTDs (Dengue, Echinococcosis and Leishmaniasis) caused by different pathogens (viral, helminthic and protozoan infections, respectively). These diseases are briefly discussed in the following subchapters.

1.2.1. Dengue fever

Dengue is the most important viral vector-borne disease in the world [6]. It is an acute systemic viral disease transmitted through the bite of infected female mosquito *Aedes aegypti* (as primary vector) or *Aedes albopictu*. Dengue virus (DENV) belongs to the genus *Flavivirus* of the family *Flaviviridae*, which consists of more than 70 species that include other important viruses such as Zika and Chikungunya [7].

Dengue disease is characterized by fever, arthralgia, myalgia, abdominal pain, rash and viremia that begin 3-4 days following the infection by the bite of the DENV-transmitting mosquito. The disease is caused by four distinct but closely related DENV serotypes: Dengue virus non-structured proteins (NS) types 1 to 4 (DENV-NS1, DENV-NS2, DENV-NS3 and DENV-NS4) [7,8]. The infection to humans with any of these serotypes leads to mild fever, known as Dengue fever (DF), which can be characterized by clinical responses of the body, but also by no clinical manifestation at all. Infections by two different DENV serotypes can lead to severe syndromes, commonly known as Dengue haemorrhagic fever/Dengue shock syndrome (DHF/DSS), which are characterized by rapid onset of capillary leakage and a potential damage of the liver [9]. Although primary infection with a particular serotype induces lifelong protective immunity to that serotype, the protection against the other DENV serotypes is generally weak. After a short period of cross protection, typically between 2-3 months, individuals infected with one serotype are again susceptible to infection with the other serotypes, in which case the severity of the disease increases, and sometimes progresses even into fatal outcomes [10].

Owing to the uncontrolled urbanization, global immigration, and increased spread of DENV-transmitting mosquitoes, Dengue epidemics has increased both in frequency and

magnitudes in many parts of the world, and is ubiquitous throughout the tropics [7,10-12]. As a result, Dengue infection is a major public health threat with a global estimation of about 400 million new infections every year. Moreover, over two million DHF/DSS cases and 20,000 deaths are estimated to occur each year [13]. Reported WHO estimations refer to 50-100 million Dengue infections every year, and over 2.5 billion people are currently at risk from Dengue. Informal online data sources that were collected by the web-based system HealthMap, which estimates infectious diseases outbreak, revealed dengue outbreak of more than 1000 cases between January and April of 2018 [14].

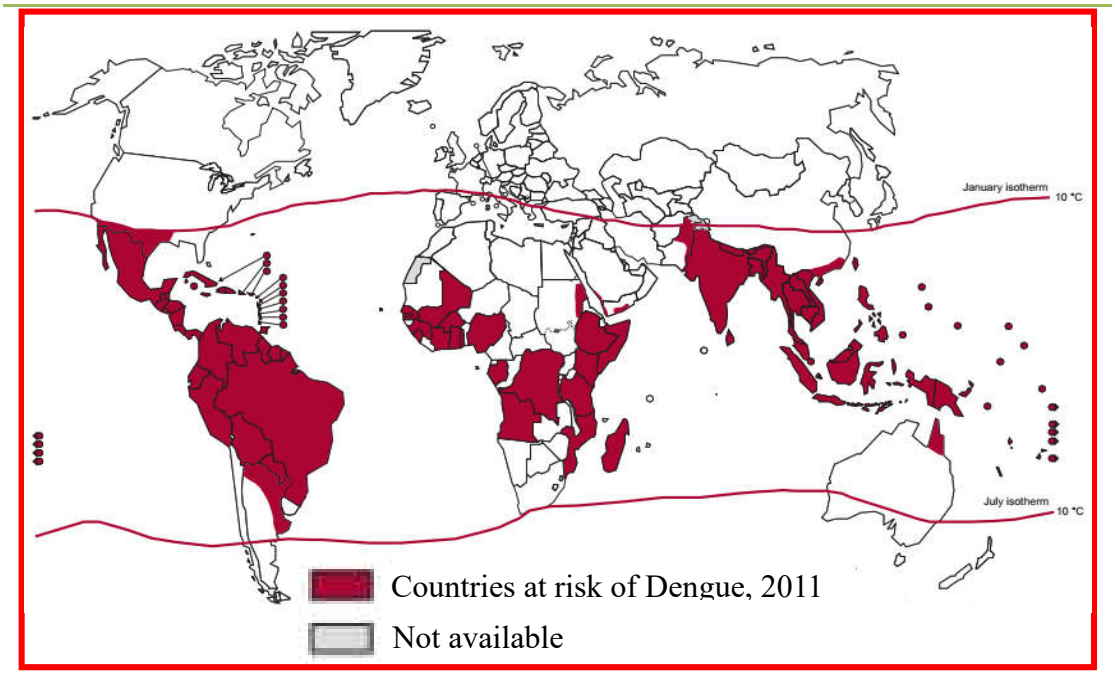

Figure 1.4: Countries at risk of Dengue transmission; the two contour lines indicate the potential geographical limits of the northern and southern hemispheres for year round survival of *Aedes Aegypti* mosquito vector of DEN, from [15].

More than 100 countries are seriously affected by Dengue infection (**Figure 1.4**) [16]. South America and Asia has larger contributions to the global burden of Dengue

disease, which might be related to the high suitability of the disease transmission because of proper environmental conditions and high population density in these regions [13]. However, the number of cases varies substantially from year to year, and underreporting and misdiagnoses are possible obstacles in understanding of the full burden of Dengue.

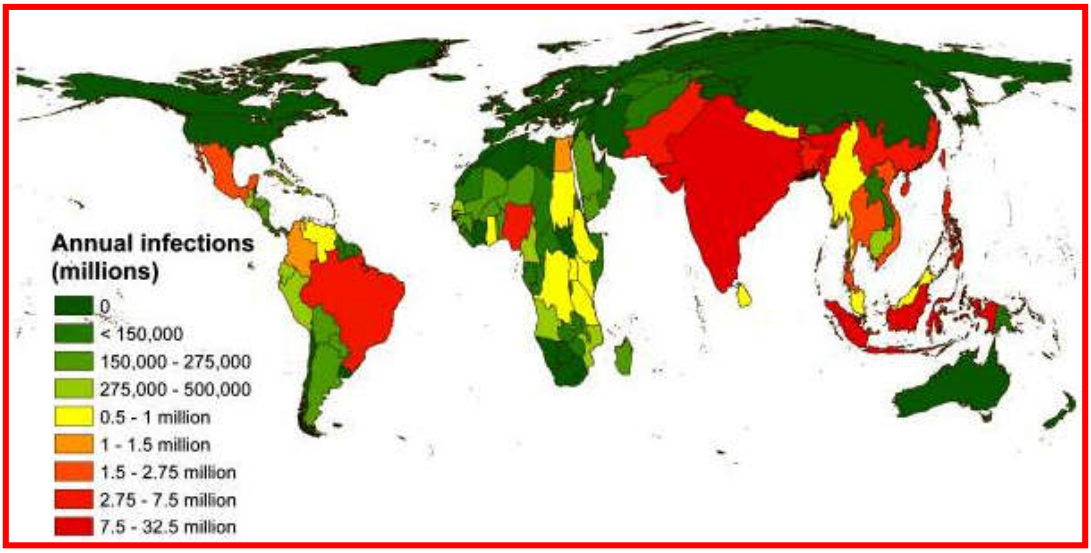

Figure 1.5: Global risk and burden of Dengue (2010). Reproduced from [13].

Notably, in tropical areas where the spread and epidemics of DENV-transmitting mosquitoes is favourable, the outbreak of Dengue infection is a huge health and economic problem [13,17]. As mosquito-borne disease, Dengue transmission is climate sensitive for several reasons: mosquitoes require standing water to breed and warm ambient temperature, while if the climate is too cold, viral development is slow and mosquitoes are unlikely to survive long enough to transmit the infection [11].

Nevertheless, the symptoms of Dengue are generally difficult to recognise from a normal flu or other viral infections, and in most cases the disease is asymptomatic or mild, and can even pass unobserved [18]. Due to its asymptomatic symptoms, the

control and diagnosis of Dengue infection remain a top global health challenge. Current laboratory diagnosis methods for confirming DENV infection relies either on direct viral detection in serum (i.e., isolation of virus in cell culture, and identification of nucleic acid or antigens), or on indirect methods that involve serological tests for the detection of virus specific antibodies [19] (**Figure 1.6**). Direct virus detection could be also used for serotype specific identification of dengue infection in the acute phase of the disease [19-21]. For this, DENV is isolated by inoculation of diagnostic samples into mosquitoes for cell culturing, detection of viral nucleic acid in serum by polymerase chain reaction (PCR) assays, or detection of non-structured protein type 1 (NS1) by enzyme linked immunosorbent assay (ELISA), providing better sensitivity and accuracy during the acute stage of the disease [19]. Nevertheless, the sensitivity and accuracy of the direct methods are influenced by the duration of the patient's illness. Moreover, diagnosis of Dengue infection by direct detection of viral components in serum is not routinely performed, as these methods require expertise and expensive laboratory equipment [19], which are of limited access in the endemic areas.

By contrast, serologic diagnosis of Dengue (i.e., through indirect methods) relies on the detection of high levels of serum immunoglobulin M or G (IgM, IgG) that bind Dengue virus antigens in an ELISA based assays. However, the specificity of these assays varies depending on whether the individual has a primary or secondary Dengue infection. As these antibodies are immune responses to foreign antigens, the presence of IgM in the diagnostic assay might not be associated only to Dengue infection, but could be also related to other similar flavivirus infections [8,19]. Hence, serological tests based on IgM based assay could provide false results. Although there is no specific treatment for Dengue fever or for haemorrhagic Dengue, its diagnosis at an early stage can decrease

mortality rates below 1% [21]. However, all these diagnostic tests may be negative in the early stage of the disease.

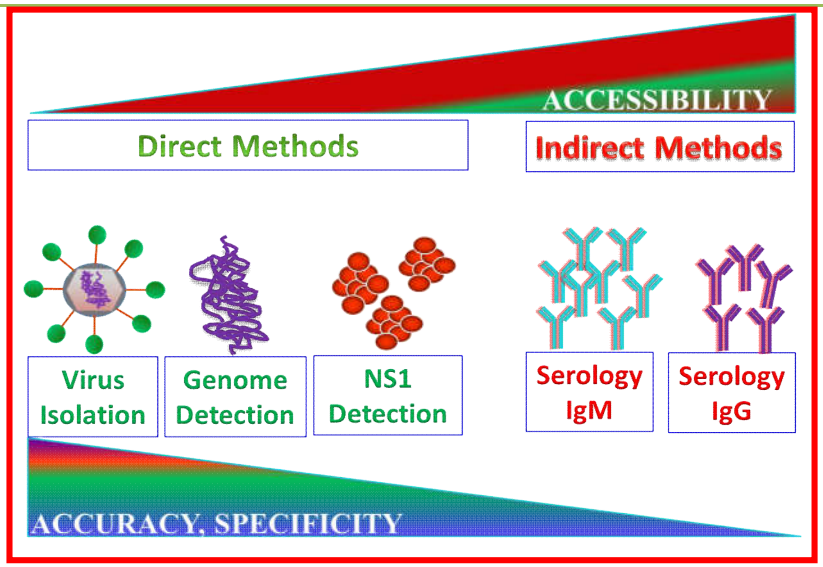

Figure 1.6: Comparisons of different laboratory methods for the diagnosis of Dengue infection and their accessibility and/or diagnostic reliability [19,21].

Moreover, with the exception of serology, these laboratory tests are only of diagnostic value during the acute phase of the illness, whereas the tests for Dengue virus-specific antibodies (IgG and IgM) can be useful to confirm the diagnosis in the later stages of the infection, as both IgG and IgM are produced after 5-7 days from the onset of the disease.

1.2.2. Leishmaniasis

Leishmaniasis is caused by several protozoal parasites of the genus *Leishmania*, and is transmitted by the bite of infected female phlebotomine sandflies. There are over 20 *Leishmania* species, and over 90 sandfly species are known to be *Leishmania*-transmitting vectors. The various species of *Leishmania* parasites relevant to humans are divided into two broad categories: New World species such as *L. chagasis*, *L.*

Mexicana, L. braziliensis, *L. shawi*, *L. amazonensis*, *L. naïffi,* and *L. guyanensis* – which are endemic in Middle and South America; and Old World species including *L. lnfantum*, *L. major*, *L. tropica* – which are highly prevalent in the Mediterranean basins, the Middle East, the horn of Africa and India [22].

Depending on the infecting species, three major forms of the *Leishmania* diseases are developed: Visceral Leishmaniasis (VL), also known as kala-azar, which is the most severe form of the disease, and in some cases it is lethal if left untreated; Cutaneous Leishmaniasis (CL); and Mucocutaneous Leishmaniasis (ML). CL is the most prevalent clinical form of Leishmaniasis [23], caused by a variety of *Leishmania* species: *L. major*, *L. tropica*, *L. Mexicana* and *L. Braziliensis*. Therefore, the clinical manifestation of CL tends to vary between and within these regions [22].

Unlike other infectious tropical diseases, the incidence of Leishmaniasis is continuously increasing [24,25]. Leishmaniasis disease is endemic in about 98 countries. More than 350 million people are susceptible to *Leishmania* parasite, and 2 million new cases occur every year. About 95% cases of Leishmaniasis disease belong to Cutaneous Leishmaniasis, and they mostly occur in the Americas, the Mediterranean basins, Middle East and Central Asia (**Figure 1.8**). In most cases, infections by *Leishmania* remain asymptomatic. In the case of CL, the skin lesions usually develop within several weeks or months after exposure [27]. They eventually develop to ulcers and skin lesions, leaving life-long scars, serious disability as well as substantial psychological burden [28].

The diagnosis and identification of *Leishmania* parasite is often laborious, and depends on the variety of the *Leishmania* parasite. In some cases, routine identification might be necessary, as the *Leishmania* species strongly determines how the diseases evolve. For this reason, a number of diagnostic methods have been described [23]. However, none

of these methods showed adequate sensitivity and accuracy for the diagnosis and detection of Leishmaniasis disease.

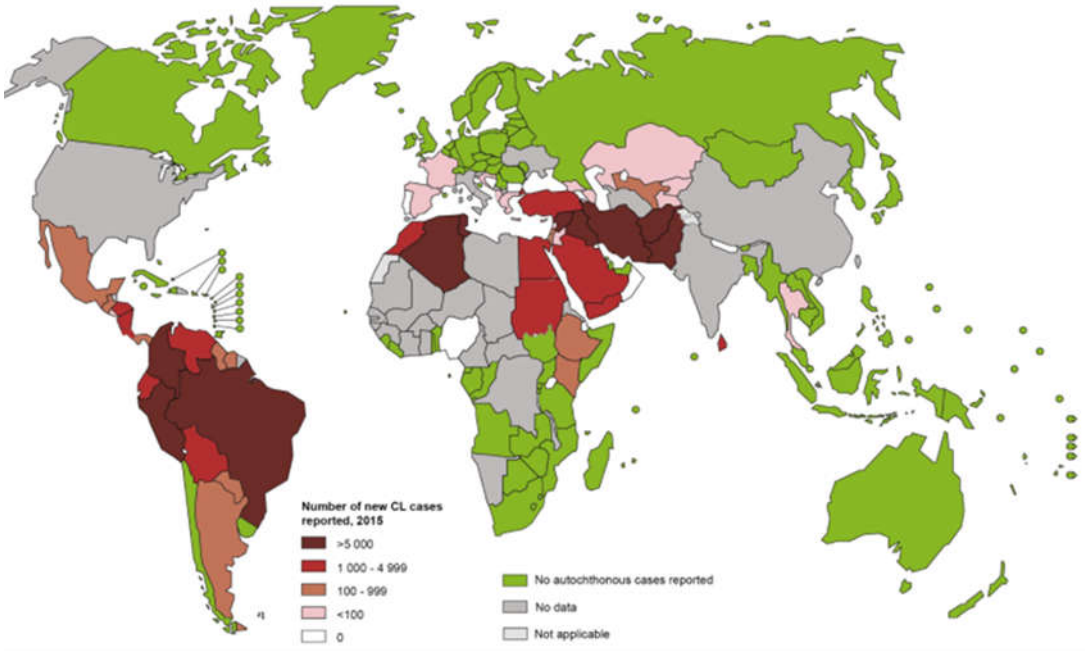

Figure 1.8: Global status of Cutaneous Leishmaniasis, 2015, WHO report. Reproduced from [26].

And the absence of microscopy capabilities in many endemic regions makes diagnosis even more difficult. The current existing diagnosis and treatment practice are expensive and complicated, and thus the detection and control of the disease becomes challenging. Indirect parasitological examinations including microscopy, histopathology, and parasite culture, and/or indirect testing with serology and molecular diagnosis, often provide a huge variation in diagnostic accuracy [29].

1.2.3. Echinococcosis

Human Echinococcosis (HE) is a zoonotic infection caused by the larval stage (metacestode) of the tapeworm that belongs to the genus *Echinococcus* of the family *Taeniidae*. It is characterized by a long-term growth of metacestode-larval stages (i.e.,

hydatid cysts) in internal organs (mainly in the lungs and liver) of intermediate host animals. Although there are different species of Echinococcosis, only four of them (*Echinococcus granulosus*, *Echinococcus multilocularis*, *Echinococcus oligarithms*, *Echinococcus Vogeli*) are recognized as taxonomically relevant. The most frequent clinical and epidemiological forms of Echinococcosis that are pathogenic to humans are Cystic Echinococcosis (CE) and Alveolar Echinococcosis (AE), caused by the species *Echinococcus granulosus* and *Echinococcus multilocularis*, respectively.

The lifecycle of *Echinococcus* species involves two hosts: a definitive carnivore host such as dog and fox, and an intermediate herbivore host including sheep, cattle, and goat. The intermediate hosts become infected by ingesting parasite's eggs, which are then released in the feces of definitive hosts. The eggs hatch in the gastrointestinal tract and become activated larvae, which penetrate the intestinal wall and enter the bloodstream, eventually locating in internal organs where they develop into hydatid cysts. Thus, the parasite lifecycle alternates between an adult segmented egg-producing tapeworm in the small intestine of a canid definitive host, and a larval cystic stage of the tissues of ungulates and rodents.

Infection to humans occurs through the ingestion of parasite eggs in contaminated water, food or soil, or through direct contact with animal hosts. The two main forms of Echinococcosis disease, CE and AE, are distinguished by the development of unilocular fluid filled bladders (i.e., hydatid cysts), and a multilocular root-like network of interconnecting vesicotubular structures, respectively. The larval growth of the parasites separates the malignant AE from the benign CE [30]. CE is the most common type of echinococcosis and the cyst growth usually occur in the liver (rarely in the lungs), upon infection by the species *E. granulosus*. AE affects the liver (>98% of cases), which is characterized by tissue fibrosis and necrosis, and commonly with a poor prognosis [31].

Infections with Echinococcosis are a major public health concern that is globally spread, particularly in developing regions with limited economic resources, whereas in some areas it has become an emerging or reemerging disease [32-36]. The CE form of the disease is globally distributed in every continent (**Figure 1.7**). AE, which is life threatening and severe (90% of AE patients die if left untreated), is endemic in most regions of China and remerging in many European countries [36,37]. In the endemic areas, CE incidence ranges from less than 1 to 200 per 100,000 person-years, and that of AE from 0.03 to 1.2 per 100, 000 persons-years [38,39].

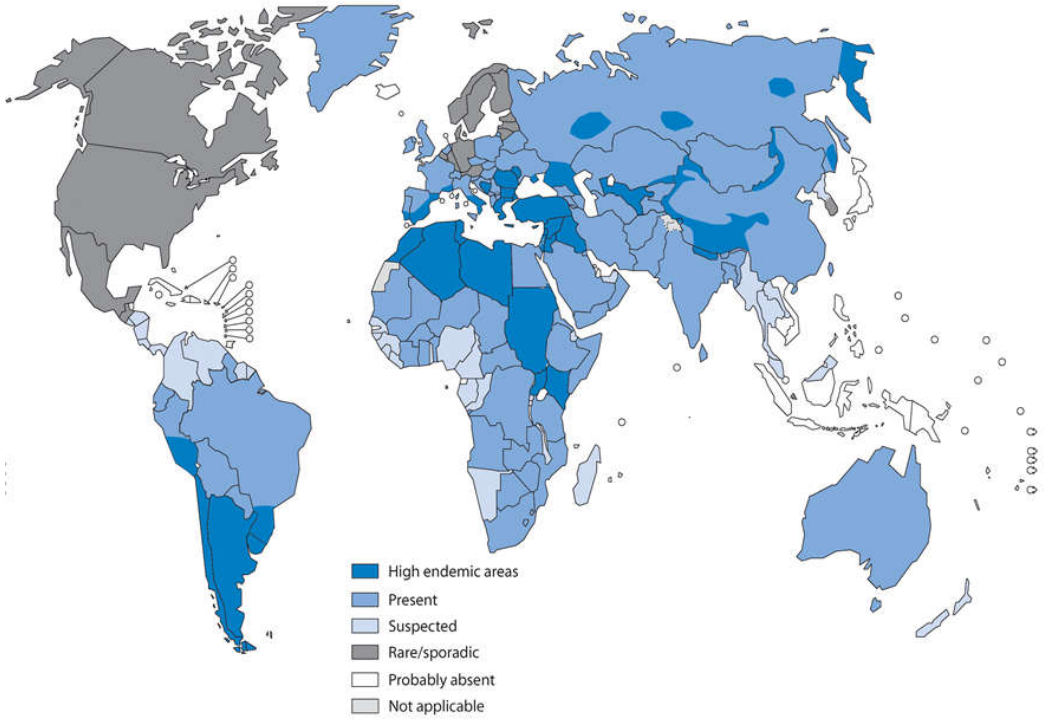

Figure 1.7: Global distribution of *Echinococcus granulosus* and Cystic echinococcosis, WHO report, 2009. Reproduced from [40].

Despite its wide spread in most of the tropical zones, the mortality rate of CE is lower than for AE, but it might increase considerably if medical treatment and care are inadequate [38]. This zoonotic disease causes chronic infections in humans characterized by an initial asymptomatic period, which could last several years prior to

the onset of clinical signs associated with pressure effect exerted by the cyst or tissue necrosis in the affected area (in the case of CE), or the development of a tumor-like lesion, normally in the liver (in the case of AE). Diagnosis of Echinococcosis is generally done by physical imaging techniques that include ultrasonography, computed axial tomography (CT scanning), Magnetic Resonance Imaging (MRI) and radiology, which are generally accompanied by serological tests [33,41]. In most cases, image based and stage-specific diagnosis of CE disease are useful to choose the best treatment options from percutaneous treatment, surgery, anti-infective drug treatment or watch and wait approaches, even though there is no best treatment options [42]. Nevertheless, imaging techniques are constrained by the small size of lesions that are visualized, and moreover they are expensive and inaccessible in most remote areas. Thus, the diagnoses of echinococcal infections by imaging techniques are usually performed in the late stages of the disease, which makes difficult the control and treatment of the infection, especially in the case of AE.

Immunological tests have been considered as useful methods for confirming clinical findings in the early stage of infection, as well as whenever imaging techniques had failed to visualize the parasite, or when imaging techniques are not readily available [43]. The immunological tests of CE are related to the evaluation of specific antibodies and native antigens including *E. granulosus* hydatid cyst fluid (HCF) and purified components from HCF, as well as *E. granulosus* adult-worm antigens; in this regard, crude HCF has shown higher sensitivity than purified components of HCF [43,44]. However, not all patients with hydatic cysts may produce detectable serum (IgG) antibodies, and ELISA test might exhibit false negative results. The AE specific antigen, Em18, derived from *E. multilocularis*, is considered the potential species-specific antigen for the immunodiagnosis of AE; it is capable of differentiation between

AE and CE, and it can distinguish active and inactive AE. In general, immunodiagnostic tests for the confirmation of AE or CE are relatively easy to use and are suitable for large-scale screening of population at risk in the early stage of the infection [44]. However, all the diagnostic tools developed so far are generally applicable at laboratory scale. In addition, both the diagnosis and treatment of HE are relatively expensive. The disease is complicated to treat, and in some cases it requires extensive surgery and/or prolonged drug therapy, as well as socio-economical and psychological burden [34].

1.3. Conclusions

The neglected tropical diseases affect many regions across the world and represent a huge global health threat. The control, prevention and treatment of these infections require extensive interventions, global coalition and strong policies centered on reaching poor and marginalized communities, where most cases occur. Early detection and prompt treatment in endemic areas would help to reduce transmission and to monitor the spread and burden of these diseases. The current lack of suitable resources and equipment in these areas make their diagnosis extremely challenging. Therefore, the development of a simple, rapid, fast and non-invasive diagnostic method that is user friendly and accessible in low economic and low resource settings is of paramount importance to combat the neglected tropical diseases globally.

1.4. References

1. WHO. Mortality and global health estimates, global health observatory (gho) data, (http://www.Who.Int/gho/mortality_burden_disease/en/ : Accessed: May 01, 2018).

2. Organization, W.H. *The world health report 2003: Shaping the future*. World Health Organization: 2003.
3. Global burden of disease, institute of health metrics and evaluation, (http://www.Healthdata.Org/, accessed: May 01, 2018)
4. WHO. Neglected tropical diseases, world health organization, (http://www.Who.Int/neglected_diseases/diseases/en/, accessed: May 01, 2018).
5. Organization, W.H. Working to overcome the global impact of neglected tropical diseases: First who report on neglected tropical diseases. **2010**.
6. Organization, W.H. Who report on global surveillance of epidemic-prone infectious diseases, who, geneva. **2000**.
7. Ngono, A.E.; Shresta, S. Immune response to dengue and zika. *Annual Review of Immunology* **2018**, *36*, 279-308.
8. Simmons, C.P.; Farrar, J.J.; van Vinh Chau, N.; Wills, B. Dengue. *New England Journal of Medicine* **2012**, *366*, 1423-1432.
9. Halstead, S.B. Dengue. *The Lancet* **2007**, *370*, 1644-1652.
10. Halstead, S. Pathogenesis of dengue: Challenges to molecular biology. *Science* **1988**, *239*, 476-481.
11. Hales, S.; De Wet, N.; Maindonald, J.; Woodward, A. Potential effect of population and climate changes on global distribution of dengue fever: An empirical model. *The Lancet* **2002**, *360*, 830-834.
12. Messina, J.P.; Brady, O.J.; Scott, T.W.; Zou, C.; Pigott, D.M.; Duda, K.A.; Bhatt, S.; Katzelnick, L.; Howes, R.E.; Battle, K.E. Global spread of dengue virus types: Mapping the 70 year history. *Trends in microbiology* **2014**, *22*, 138-146.

13. Bhatt, S.; Gething, P.W.; Brady, O.J.; Messina, J.P.; Farlow, A.W.; Moyes, C.L.; Drake, J.M.; Brownstein, J.S.; Hoen, A.G.; Sankoh, O., *et al.* The global distribution and burden of dengue. *Nature* **2013**, *496*, 504.

14. Messina, J.P.; Brady, O.J.; Pigott, D.M.; Brownstein, J.S.; Hoen, A.G.; Hay, S.I. A global compendium of human dengue virus occurrence. *Scientific Data* **2014**, *1*, 140004.

15. United to combat. Burden map—neglected tropical diseases. . (Accessed, May 01,2018),

16. http://www.wpro.who.int/mvp/Dengue_Strategic_Plan.pdf?ua=1. The dengue strategic plan, for the asia pacific region, 2008-2015, **Accessed May 04, 2018**.

17. *Dengue guidelines for diagnosis, treatment, prevention and control*. 2009.

18. Chastel, C. Eventual role of asymptomatic cases of dengue for the introduction and spread of dengue viruses in non-endemic regions. *Frontiers in physiology* **2012**, *3*.

19. Peeling, R.W.; Artsob, H.; Pelegrino, J.L.; Buchy, P.; Cardosa, M.J.; Devi, S.; Enria, D.A.; Farrar, J.; Gubler, D.J.; Guzman, M.G., *et al.* Evaluation of diagnostic tests: Dengue. *Nature reviews. Microbiology* **2010**, *8*, S30-38.

20. Guzman, M.G.; Halstead, S.B.; Artsob, H.; Buchy, P.; Farrar, J.; Gubler, D.J.; Hunsperger, E.; Kroeger, A.; Margolis, H.S.; Martínez, E. Dengue: A continuing global threat. *Nature Reviews Microbiology* **2010**, *8*, S7-S16.

21. TDR/WHO. Dengue guidelines for diagnosis, treatment, prevention and control. *TDR/WHO, Geneva, Switzerland* **2009**.

22. Organization, W.H. In *Control of the leishmaniases: Report of a meeting of the who expert committee on the control of leishmaniases*, Control of the

leishmaniases: report of a meeting of the WHO expert committee on the control of leishmaniases., 2010; World Health Organization.

23. de Vries, H.J.C.; Reedijk, S.H.; Schallig, H.D.F.H. Cutaneous leishmaniasis: Recent developments in diagnosis and management. *American Journal of Clinical Dermatology* **2015**, *16*, 99-109.
24. Alvar, J.; Velez, I.D.; Bern, C.; Herrero, M.; Desjeux, P.; Cano, J.; Jannin, J.; den Boer, M. Leishmaniasis worldwide and global estimates of its incidence. *PLoS One* **2012**, *7*, e35671.
25. Brandao-Filho, S.P.; Campbell-Lendrum, D.; Brito, M.E.; Shaw, J.J.; Davies, C.R. Epidemiological surveys confirm an increasing burden of cutaneous leishmaniasis in north-east brazil. *Transactions of the Royal Society of Tropical Medicine and Hygiene* **1999**, *93*, 488-494.
26. WHO. Endemicity of cutaneous leishmaniasis, 2015 *WHO Leishmaniasis Control Programme, Annual Country Reports* **2017**.
27. Andrade-Narvaez, F.J.; Loria-Cervera, E.N.; Sosa-Bibiano, E.I.; Van Wynsberghe, N.R. Asymptomatic infection with american cutaneous leishmaniasis: Epidemiological and immunological studies. *Mem Inst Oswaldo Cruz* **2016**, *111*, 599-604.
28. Yanik, M.; Gurel, M.S.; Simsek, Z.; Kati, M. The psychological impact of cutaneous leishmaniasis. *Clinical and experimental dermatology* **2004**, *29*, 464-467.
29. Goto, H.; Lindoso, J.A. Current diagnosis and treatment of cutaneous and mucocutaneous leishmaniasis. *Expert review of anti-infective therapy* **2010**, *8*, 419-433.

30. Organization, W.H. Report of the who informal working group on cystic and alveolar echninococcosis surveillance, prevention and control, with the participation of the food and agriculture organization of the united nations and the world organisation for animal health, 22-23 june 2011, department of control of neglected tropical diseases, who, geneva, switzerland. **2011**.

31. Craig, P.S.; Budke, C.M.; Schantz, P.M.; Li, T.; Qiu, J.; Yang, Y.; Zeyhle, E.; Rogan, M.T.; Ito, A. Human echinococcosis: A neglected disease? *Tropical Medicine and Health* **2007**, *35*, 283-292.

32. Davidson, R.K.; Romig, T.; Jenkins, E.; Tryland, M.; Robertson, L.J. The impact of globalisation on the distribution of echinococcus multilocularis. *Trends in parasitology* **2012**, *28*, 239-247.

33. Kern, P.; Menezes da Silva, A.; Akhan, O.; Mullhaupt, B.; Vizcaychipi, K.A.; Budke, C.; Vuitton, D.A. The echinococcoses: Diagnosis, clinical management and burden of disease. *Advances in parasitology* **2017**, *96*, 259-369.

34. Eckert, J.; Deplazes, P. Biological, epidemiological, and clinical aspects of echinococcosis, a zoonosis of increasing concern. *Clinical microbiology reviews* **2004**, *17*, 107-135.

35. Sarkar, S.; Roy, H.; Saha, P.; Sengupta, M.; Sarder, K.; Sengupta, M. Cystic echinococcosis: A neglected disease at usual and unusual locations. *Tropical Parasitology* **2017**, *7*, 51-55.

36. Torgerson, P.R.; Keller, K.; Magnotta, M.; Ragland, N. The global burden of alveolar echinococcosis. *PLOS Neglected Tropical Diseases* **2010**, *4*, e722.

37. Romig, T.; Dinkel, A.; Mackenstedt, U. The present situation of echinococcosis in europe. *Parasitology international* **2006**, *55 Suppl*, S187-191.

38. PAWLOWSKI ZS, E.J.; Vuitton, D.; Amman, R.; Kern, P.; Craig, P.; Dar, K.; De Rosa, F.; Filice, C.; Gottstein, B.; Grimm, F. Echinococcosis in humans: Clinical aspects, diagnpsis and treatment. *WHO/OIE Manual on Echinococcosis in Humans: a public health problem of global concern* **2001**, 20-66.

39. Alexander, S.; Rudolf, W.A.; Daniel, C.; Pierre-Alain, C.; Johannes, E.; Bruno, G.; Nerman, H.; Beat, M.; Bettina Mareike, P.; Juerg, R.*, et al.* Human alveolar echinococcosis after fox population increase, switzerland. *Emerging Infectious Disease journal* **2007**, *13*, 878.

40. WHO. Distribution of echinococcus granulosus and cystic echinococcosis (hydatidosis), 2009. *Working to overcome the global impact of Neglected Tropical Diseases first WHO report on neglected tropical dieseases* **2010**.

41. Junghanss, T.; da Silva, A.M.; Horton, J.; Chiodini, P.L.; Brunetti, E. Clinical management of cystic echinococcosis: State of the art, problems, and perspectives. *The American journal of tropical medicine and hygiene* **2008**, *79*, 301-311.

42. Brunetti, E.; Kern, P.; Vuitton, D.A. Expert consensus for the diagnosis and treatment of cystic and alveolar echinococcosis in humans. *Acta Tropica* **2010**, *114*, 1-16.

43. Wang, J.-y.; Gao, C.-h.; Steverding, D.; Wang, X.; Shi, F.; Yang, Y.-t. Differential diagnosis of cystic and alveolar echinococcosis using an immunochromatographic test based on the detection of specific antibodies. *Parasitology Research* **2013**, *112*, 3627-3633.

44. Zhang, W.; Li, J.; McManus, D.P. Concepts in immunology and diagnosis of hydatid disease. *Clinical Microbiology Reviews* **2003**, *16*, 18-36.

CHAPTER 2

2. EXHALED BREATH ANALYSIS

Included in this chapter are brief introduction to exhaled breath, possible origin of exhaled air components in abnormal body's conditions, analytical techniques commonly used for breath analysis and biomarkers identification, and a short review on exhaled breath analysis with electronic devices based on chemical gas sensors.

2.1. Introduction

Breath testing dates back to the early history of medicine in Ancient Greece, when physicians started to consider that human breath contains a clue to the body's health and physiological status. They observed that the aroma of patient's breath could be associated to a certain disease, and breath testing might provide an insight into the pathophysiological processes in the body during illness [1]. For example, a sweet smell of exhaled breath indicates uncontrolled diabetes mellitus, while a urine-like odor smell is considered a result of kidney failure, and a musty or fishy reek smell of breath is related to liver disease [2,3]. Therefore, they tried to diagnose illnesses by the distinctive breath odors that were perceived as indicators of the disease.

Later in the 18th century, Antoine Lavoisier reported the first quantitative analysis of carbon dioxide (CO_2) in Guinea pig breath, whereas CO_2 was also found in human breath as a product of slow burning of oxygen and food in the body [1,4,5]. Starting from these findings, specific breath test applications have begun to be implemented, and the first breath test called Capnography was developed [6]. Capnometry measurements are used to monitor the level of carbon dioxide in exhaled breath and to gather information from the systemic metabolism of the patient, as well as data from both circulatory and respiratory systems [7]. Subsequently, many other breath testing

applications were developed, and some of them are currently in use, including the alcohol Breathalyzer that is used to determine the amount of alcohol in blood through indirect ethanol measurements in breath [8], as well as the urea breath test for the detection of Helicobacter pylori bacteria [9].

On the other hand, acetone was found in urine of diabetic patients, and the strange apple-like odor breath of diabetics was presumed to be due to the presence of acetone in exhaled air [5]. Additionally, the presence of water vapor in exhaled breath has been used as a non-invasive approach for mortality monitoring for many years.

Based on all these findings, the idea of using information in breath to determine the physiological state of humans has been followed aiming the development of non-invasive diagnostic devices for breath testing.

2.2. Exhaled Breath

For many beings, it is essential to inhale oxygen and in turn to exhale carbon dioxide as a result of the respiration process. Such gas exchange occurs at the alveolar–blood capillary membrane of the respiratory tract, where the diffusion of gases with significant vapor pressure is governed by their concentration differences across the alveoli–blood capillary junction [10]. The compounds from the inhaled air tend to pass into the blood, and the molecules from the blood tend to pass into the breath, respectively.

During the exhalation process, thousands of molecules are expired into the air. The composition of the exhaled breath is constituted by nitrogen (74%), oxygen (21%), small inorganic gases such as NO, H_2, NO_2 CO, H_2S, NH_3, CO_2 (totally accounting for almost 5%), water vapor and trace amounts of several thousands of volatile organic compounds (VOCs) and non-volatile organic compounds [3,11]. Most of the VOCs in

the breath are present in very low concentrations that range from parts per trillion (ppt) to parts per million (ppm), which makes them far complex to detect as compared to the dominant molecules such as nitrogen, oxygen, water vapor and carbon dioxide [10]. Notably, the total amount of these VOCs account for not more than 100 ppm of the total breath volume, being acetone, isoprene and alcohols the most abundant, whereas aldehydes, ketones and pentane are found at very low concentrations [12].

The VOCs reach the exhaled breath from the deeper parts of the lungs called alveoli, as a result of the exchange process with the blood, therefore they are found in the so-called "alveolar breath". Although the specific biochemical pathways of their generation, distribution and origins is not well understood, some of them can be associated with normal metabolism (e.g., ethanol, isoprene, propanone, and methanol), others are products of oxidative stress (e.g., ethane and pentane), while others result from environmental and occupational exposures (e.g., trichloromethane and benzene derivatives) [5,13].

The terms *exogenous* and *endogenous* are used to describe the origins of the VOCs that come from external sources (during inhalation of environmental air, ingestion of food and beverages, smoking, or entered the body through other routes such as dermal absorption) or are produced inside the body (during the metabolism, or originated from bacteria in the gut or the airways), respectively.

The concentration of exogenous VOCs in the breath is generally higher than that of the endogenous compounds [14]. The exogenous volatiles are possibly metabolized in the body, mainly by the liver enzymes. They can be modified or stored, and excreted by expiration or through other body fluids [15]. In many cases, these VOCs are considered highly reactive and typically cause physiological damage to different cell structures

such as lipids, DNA and proteins, and/or are stored in different body organs or tissues causing later different diseases and body complications [16]. Typical examples of exogenous VOCs are aromatic hydrocarbons, such as benzene, ethylbenzene, p-xylene, para-dichlorobezene and other hydrocarbons, which derive from environmental contaminants and other exposure sources [17], and alkanes derived from different air pollutants.

Endogenous VOCs are biologically generated compounds during the physiological processes occurring in the body. Mainly they are hydrocarbons such as isoprene, acetone, methanol, ethanol, pentane and acetaldehyde, and nitrogen and sulfur containing compounds. Table 2.1 shows some of the common breath endogenous VOCs and their physiological origins. Acetaldehyde is derived from ethanol metabolism, methyilamine is derived from proteins metabolism, ethane and pentane are a result of lipid peroxidation of the polyunsaturated fatty acids (PUFAs), isoprene is generated by cholesterol biosynthesis, etc [18]. The endogenous VOCs are continuously excreted from the body via the skin, feces, urine, breath, saliva, etc [19].

Volatile organic compounds	**Physiological basis**
Hydrocarbons	Lipid peroxidation
Acetone	Decarboxylation of acetoacetate
Acetaldehyde	Ethanol metabolism
Ammonia	Protein metabolism
Ethane, pentane	Lipid peroxidation
Carbon disulfide, ethanol, hydrogen	Gut bacteria
Isoprene	Cholesterol biosynthesis
Methylamine	Protein metabolism

Table 2.1: Physiological origins of some endogenous breath VOCs [20]

2.3. Volatile organic compounds generated by abnormal body conditions

Some of the physiological phenomena that generate VOCs in abnormal body conditions are explained below.

Oxidative damage

Molecular oxygen is an essential molecule for cellular metabolism, and the body has developed a protective mechanism to sustain oxygen homeostasis in order the normal physiological functioning of the body to be maintained. During the process of aerobic energy metabolism, oxygen is reduced by cytochrome c oxidase (four electron reduction) to water and energy required by the body, which makes the mitochondrial oxidative phosphorylation the major source of energy [6]. Oxygen uptake in neutrophils and macrophages is due to the action of NADPH-oxidase complex associated with the plasma membrane. The electrons released by NADPH oxidation reduce oxygen to superoxide radicals. In some cases, the four electron transfer process undergoes a stepwise reduction producing highly unstable intermediate radicals containing unpaired electrons or ions called reactive oxygen species (ROS), such as the superoxide oxygen ion (O_2^-), hydrogen peroxide (H_2O_2), hydroxyl radical ($^{\bullet}OH$), as well as nitric oxide (NO) and others, which are highly toxic for biological systems [21]. These superactive molecules with unpaired electrons are easily carried and can bind to different components of the cell.

In the process of phagocytic killing of foreign molecules, the body relies on the toxicity of ROS produced molecules through the NADPH-dependent oxidase activity present in monocytes [6]. For example, the recruitment, differentiation and activation of

monocytes are mostly signaled by ROS molecules. On the other hand, the biological systems develop a multiple antioxidant defense mechanism such as specific enzymes (superoxide dismutase) and non-enzymatic species such as Vitamins A, C and glutathione as a defense to protect against foreign toxins. All these antioxidants tend to control the formation of ROS molecules by reducing them into less reactive molecules such as water or non-oxygen centered reactive molecules. **Figure 2.2** shows the successive production of ROS molecules, where the red ones are the most toxic to cell components.

In abnormal body conditions, the production of ROS molecules overwhelm the normal antioxidant capacity, and uncontrolled formation of ROS molecules inflicts adverse modifications to the cell components, such as lipids, proteins, carbohydrates and DNA [18]. Hence, the cells suffer a cellular condition known as *oxidative stress*, which occurs when the balance between oxidants and ROS is disrupted because of either depletion of antioxidants or accumulation of ROS molecules in the cell periphery. During oxidative stress, the cells attempt to counteract the oxidant effects and restore the redox balance by activation or silencing of genes encoding transcription factors, defensive enzymes and structural proteins [22].

Lipid peroxidation

Lipids are molecular components of cellular and subcellular membranes. They have hydrophobic and hydrophilic layers of long chain fatty acids, and are the most exposed parts of the cellular membrane. These fatty acids, which are either saturated, monounsaturated and polyunsaturated, are highly susceptible to ROS molecules due to the presence of less energetic *bis*-allylic hydrogen in the carbon chain between the double bonds [23].

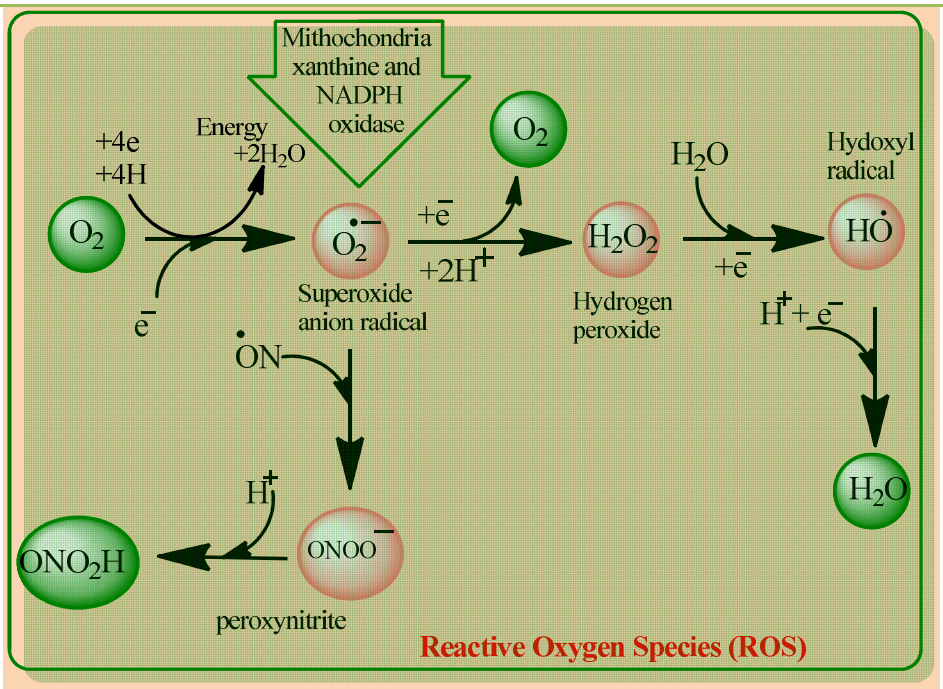

Figure 2.2: Formation and elimination of Reactive Oxygen Species (ROS)

Lipid peroxidation is an oxidative chain reaction initiated by any primary free radicals with sufficient reactivity to subtract an allylic hydrogen atom from a reactive methylene group (-CH_2-) of polyunsaturated fatty acid side chains [24]. The oxidation process follows the self-initiated chain reactions. It begins with the formation of initiating species upon the attack produced by a radical molecule, and is accompanied by bond rearrangement that is stabilized by diene-conjugates formation. The lipid radicals take up oxygen to form highly unstable peroxy radicals (ROO*). Shortly after this initiation process, the peroxy radicals are able to synthesize H from an adjacent fatty acid, causing an autocatalytic chain reaction that leads to the formation of lipid hydroperoxides. This reaction can be repeated many times during the propagation phase [23,24]. An initial event triggering lipid peroxidation by active radicals such as ROS molecules can be multiplied as long as oxygen supplies and unoxidized polyunsaturated fatty acids chains are available. The chain reaction terminates when either two radicals with unpaired

electrons (i.e., peroxy radicals) react, forming stable non-radical products, or when an antioxidant species reduces the peroxyl to a hydroperoxide whereas it is transformed into another stable radical. The lipid peroxyl radicals initiate or enhance other cellular processes such as cholesterol oxidation, reaction with proteins, and impairment of critical enzymatic functions and receptors, thereby disrupting the normal physiological processes of the body [24]. The accumulation of hydroperoxides and their subsequent decomposition into different subcomponents including alkoxyl and peroxyl radicals can accelerate the chain reaction of polyunsaturated fatty acid peroxidation, leading to oxidative damage of the cells.

Lipid peroxidation can also be initiated by different enzymatic activities such as cyclooxygenase and lipoxygenase, which are associated with normal cellular physiology. Under normal physiological conditions, these enzymes catalyze the addition of molecular oxygen to various polyunsaturated fatty acids, and they are converted into biologically active molecules including prostaglandins along with other fatty acid hydroperoxides [24,25]. However, in abnormal conditions, the physiological balance can be disrupted and excessive enzymatic lipid peroxidation will prevail, inducing oxidative damage to the cells and tissue membranes.

Figure 2.3 shows the schematic representation of lipid peroxidation and the biochemical pathways of hydrocarbon formation. Primary lipid peroxidation yields a variety of secondary reactions with evolvement of hydrocarbons (both saturated and unsaturated), aldehydes, ketones, and other low molecular weight volatile substances [14]. Examples of compounds produced by lipid peroxidation are ethane and pentane, which derive from the oxidation of n-3 and n-6 polyunsaturated fatty acids, respectively [26,27].

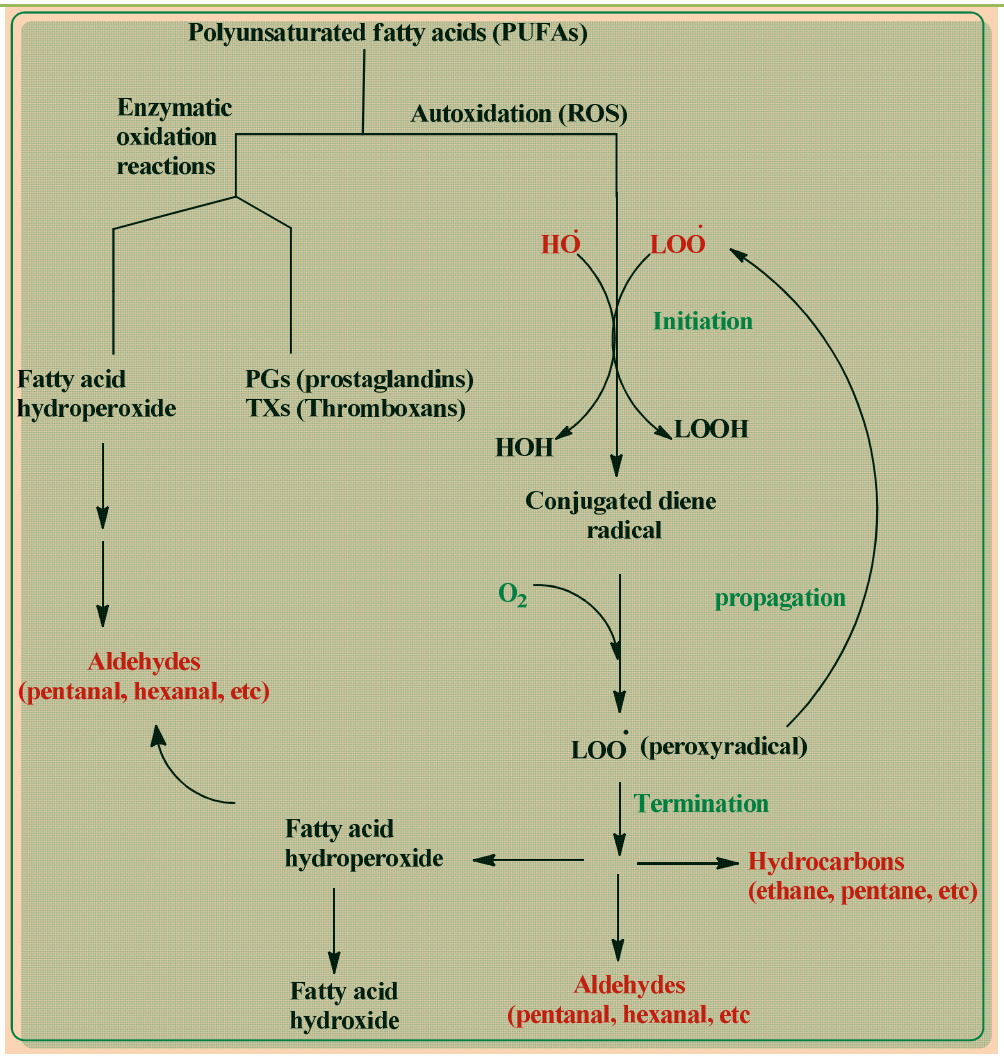

Figure 2.3: Polyunsaturated fatty acid oxidation and the biochemical pathway of hydrocarbons adapted from [23].

Hence, exhaled concentration of pentane and ethane can be used to monitor the degree of oxidative damage in the body [28]. In addition, in vivo studies of lipid peroxidation of n-4 and n-7 polyunsaturated fatty acids demonstrated an increased emission of propane and hexane in rats, respectively [26]. Therefore, the classification of VOCs produced during lipid peroxidation also depends on the type of PUFAs implied in the free radicals oxidation process. Furthermore, secondary products of lipid peroxidation can be accumulated in human fats depots and released slowly over a period of several

days, and during this time they might be further metabolized by different body enzymes. For example, pentane is partially metabolized by the hepatic cytochrome – P450 systems, whereas ethane is highly volatile and relatively insoluble in tissues and exhaled as produced [18,29]. On the other hand, alkanes are metabolized to alkyl alcohols by cytochrome –P450-mixed oxidase enzymes [30].

Apart from saturated hydrocarbons, unsaturated hydrocarbons such as isoprene are endogenously produced by cholesterol biosynthesis during cholesterol related disorders and oxidative damage [14,18]. Isoprene is always present in human breath and thought to be produced along the mevalonic pathway of cholesterol synthesis [14,31].

Oxygen containing breath VOCs, such as acetone and acetaldehyde, are originated either as products of lipolysis during lipid peroxidation or as a result of endogenous carbon metabolism in the liver [18]. For example, when the body lacks of primary energy, energy sources such as fatty acids become a secondary source of fuel for the cell, which leads to the endogenous formation of ketone bodies including acetoacetate, acetone, and 3-hydroxybutyrate [14]. This is apparently common in individuals with diabetic mellitus complications, in whose case the presence of these ketone bodies are clearly manifested in body fluids [21]. **Figure 2.4** illustrates the general biochemical formation of ketone bodies including isoprene and acetone generated via the decarboxylation of excess acetyl-CoA as a result of fatty acid β-oxidation. Ketone bodies (e.g., acetone), are oxidized via Krebs cycle in the peripheral tissue. Acetone, which is abundant in humans, is ultimately produced by the liver via decarboxylation of acetoacetate [15,32].

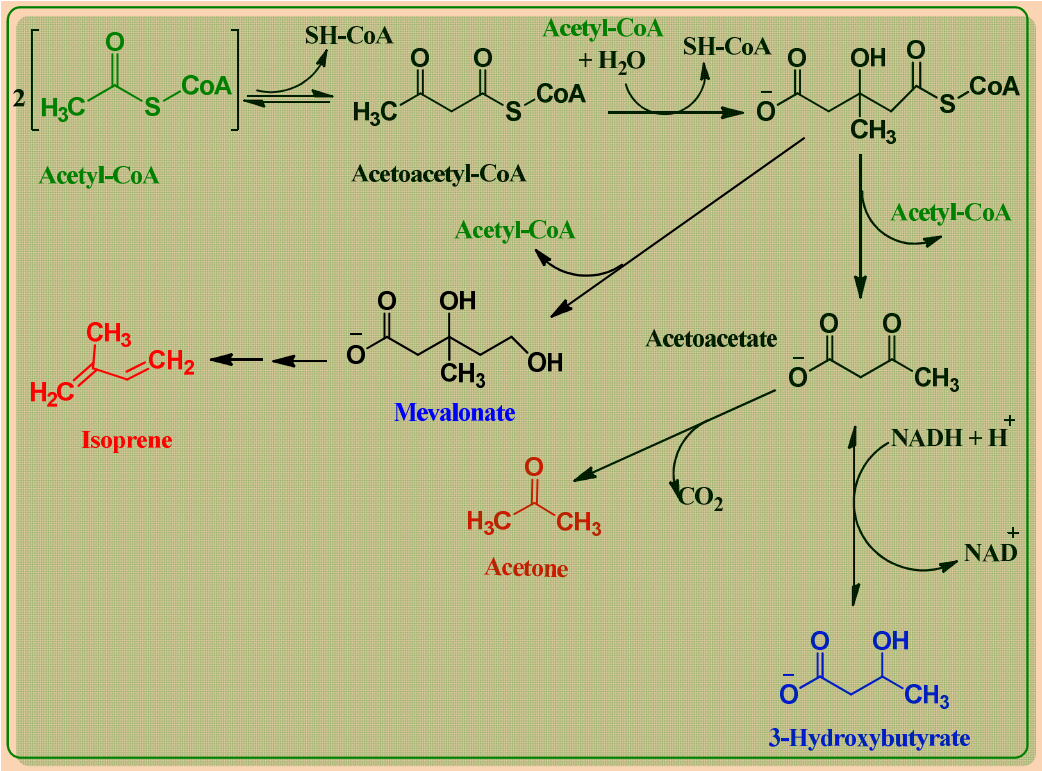

Figure 2.4: Decarboxylation of excess acetyl-CoA for ketone bodies generation and biochemical pathway of acetone generation.

Other Nitrogen and/or Sulfur containing VOCs

Endogenous breath VOCs also includes sulfur or nitrogen containing compounds. Sulfur containing compounds are endogenously generated through both normal and abnormal metabolic processes occurring in the body [19]. For example, volatile sulfur containing compounds such as ethyl mercaptane and dimethylsulfide, are generated by incomplete metabolism of methionine in the transamination pathways [33,34]. These sulfur containing compounds are dominant in patients with liver impairment of liver function and they are associated with hepatic diseases and malodor [14,32]. It is thought that the ROS molecules deplete intracellular thiols, which lead to the inducement and stimulation of the redox sensitive transcription factors AP1 and NF KB that cause the production of inflammatory cytokines IL1 and TNF beta [35].

Finally, nitrogen containing compounds such as dimethylamine and trimethylamine are associated with the impairment of liver function in converting ammonia into urea and other compounds [14,18,36]. Ammonia is endogenously produced from protein and nucleic acid metabolism, and significant level of ammonia appears in the blood of uremic patients [35]. Thus, the presence of nitrogen containing compounds in breath is associated with the imbalance of urea metabolism due to kidney disorders or ulcers caused by bacterial stomach infections [18].

2.4. Breath Biomarkers

The presence of a physiological malfunction in the course of infection or metabolic disorder (i.e., an abnormality) leads to changes in the breath VOCs concentrations, or to the generation of new VOCs characteristic to the physiological changes occurring in the body. As a result, the composition of the exhaled breath air is altered. The detection and measurement of the changes in the exhaled VOCs pattern can give an insight about the disease and can provide a mean for diseases diagnosis and monitoring [18].

A ***breath biomarker*** is a chemical compound endogenously produced within the body or exogenously introduced into the organism, which can be detected and measured in the exhaled breath, and serves as an indicator to differentiate between the normal and abnormal state of the body [37]. Generally, the concentration of disease-related VOCs is higher in the disease state as compared to the normal condition, with the exception of the cases when certain compounds are retained by malfunctioning organs that cannot adequately treat them [18]. Nevertheless, the concentration of VOCs in breath is always higher when their origin is exogenous.

A specific disorder is characterized by a volatile biomarkers pattern rather than a specific biomarker, while some breath VOCs are related to more than one disease [38]. For example, specific sets of volatile biomarkers (e.g., styrene and toluene) are indicators of very different diseases or disease states, such as oxidative stress [39], lung cancer [40], cystic fibrosis [41,42] and liver diseases [43]. The association of some volatile biomarkers to different types of diseases suggests that it should be some commonality in the effects of pathogenesis associated with various diseases, which may result in similar alterations in the biochemical pathways produced within the body that generate the same abnormal VOC metabolites in unrelated diseases [37]. Hence, the presence of these specific VOC biomarkers may be a good general indication of abnormal conditions in the body, and prompt to other diagnostic investigations to identify the specific disease among those that are mostly associated with the particular biomarkers detected.

Many studies have focused so far on the identification of VOCs that differ qualitatively and/or quantitatively between groups of diseased and healthy subjects. However, the origin and the pathophysiological significance of the putative biomarkers identified in these studies have been frequently neglected. Thus, regardless of their origin, any volatiles whose concentrations significantly differed between healthy subjects and patients have been claimed as potential disease biomarkers of the disease under investigation [44]. For example, environmental contaminants including hydrocarbons such as octane, decane, and benzene derivatives commonly known as BTEX (benzene, toluene, ethylbenzene, xylene) have been also considered as disease biomarkers [44,45]. Obviously, these patterns of exogenous VOCs in exhaled breath are mostly likely to derive from body exposure to pollutant VOCs absorbed into the body, which were

exhaled back either in the same form as inhaled or modified by the organism. Therefore, they should be rather used for human exposure assessment to pollutant environments, cigarette smoke, or other external conditions.

Thus, despite many (exogenous and endogenous) VOCs have been claimed as potential biomarkers, only a few of them have been consistently demonstrated for clinical conditions. **Table 2.2** presents some examples of breath VOC biomarkers and their clinical significance. These VOCs are believed to be generated by endogenous body processes, and the biochemical pathways of their generation have been well studied.

VOCs	Family	Clinical significance	Metabolic pathway
Ethane, pentane	Saturated hydrocarbons	Oxidative damage	Lipid peroxidation **[14,18,35]**
Methylated hydrocarbons	¿?	Lung or breast cancer	Oxidative stress/Lipid peroxidation [46]
Isoprene	Unsaturated hydrocarbon	Oxidative damage	Cholesterol biosynthesis [14,18]
Acetone	Oxygen containing compounds	Diabetes mellitus, Ketonemia	Decarboxylation of acetoacetate and Acetyl-CoA [14,18],
Acetaldehyde	¿?	Lung cancer	Ethanol metabolism [40,47]
Ethanol	¿?	Gut bacteria	Intestinal bacterial flora [18,47]
Dimethylamine, Trimethylamine	Nitrogen containing compounds	Kidney & liver impairment, Uremia	Urea conversion [14,18]
Dimethyl sulfide Dimethyldisulfide Ethylmercaptane	Sulfur containing compounds	Liver impairment	Metabolism of methionine and transamination pathways [14,18]

Table 2.2: Examples of breath VOC biomarkers and their clinical relevance

On the other hand, small inorganic volatiles such as hydrogen sulfide (H_2S), nitric oxide (NO) and carbon monoxide (CO) have been identified as important breath biomarkers for respiratory–specific diseases such as asthma [48-50]. H_2S, which originates from the lower respiratory tract, is also used as biomarker of airway inflammations [51,52], while high concentration of NO in breath manifests higher risk of inflammatory diseases [53].

In contrast, exhaled NO remains normal in patients with chronic obstructive pulmonary disease (COPD), which is one of the most common airway inflammatory diseases. However, CO showed an increase in both asthma and COPD patients, and hence exhaled CO and NO are complementarily used as breath biomarkers for pulmonary diseases [50,53].

Nevertheless, most of the breath biomarkers of a disease appear in much lower concentrations and are far dominated by other irrelevant VOCs during breath analysis. Moreover, it is important to take into account the level and presence of the biomarkers in the exhaled breath of healthy people, referred to as normal or nonexistent levels. The abnormal levels of these breath volatiles indicative of adverse clinical conditions can only be recognized after the ranges of their normal levels have been identified or established. On the other hand, the inter-individual physiological differences give rise to inconsistencies in the level of the breath biomarkers within the study population and hold considerable challenges that require serious debates.

Although with a few breath VOCs it is already possible to asses a relevant span of diseases, the capability to analyze the entire volume of exhaled breath composition would possess countless advantages in the diagnosis of specific diseases. Hence, breath samples can be analyzed not only for the search of biomarkers, but as a whole complex matrix with thousands of volatile organic compounds that can offer a general profile or pattern to distinguish and identify the disease. Instead of seeking for the evidence of already determined compounds, the attempt to extract relevant information from the "big picture" and link it with a particular health condition provides a panel of possible volatiles pattern with an explicit advantage over single biomarkers analysis.

Studies that analyzed the whole breath volume and linked it to different groups of diseases were already reported. For example, breath tests were employed to diagnose lung diseases (e.g., lung cancer, asthma, COPD, cystic fibrosis, bronchiectasis and pneumonia), gastrointestinal diseases (e.g., starch metabolism, lactase deficiency, bacterial overgrowth, *Helicobacter pylori* infection and liver impairment), as well as to understand the state of oxidative stress in the body [3].

2.5. Analytical Methods

The analytical methods are useful for the identification and quantification of individual compounds in gaseous mixtures. Since 1970s, analytical techniques have been widely employed for the analysis of VOCs in exhaled breath samples as a promising disease diagnostic approach. During that distant period, Teranishi *et al*. reported the use of gas chromatographic analysis of volatiles from breath, and demonstrated the presence of many volatile organic compounds in exhaled breath that can indicate the presence of body malfunctions in human beings [54]. Pauling *et al*. used a cold trap to freeze the breath VOCs, followed by heating the sample and injecting it into a gas chromatograph, and concluded that the chromatographic analysis of normal human breath samples reveals many different VOCs in very low concentrations [55]. However, exhaled breath analysis remains very difficult to perform because most of the breath VOCs that are clinically relevant are present in very low concentrations, the relative humidity of exhaled breath is very high (generally around 80%), and it is a lack of sufficiently sensitive and capable measurement techniques. The scientific and technical advances of different analytical techniques over the years has progressively improved their performance for the quantitative and qualitative determination of VOCs in exhaled

breath [1]. For the purpose of this thesis, some of the most common techniques that have been employed so far for the measurement of breath samples are next presented.

2.5.1. Gas Chromatography Techniques

Pauling *et al.* pioneered the comprehensive breath analysis using Gas Chromatography (GC) [55]. Since then, GC became one of the most widely used analytical technique to detect and quantify compounds in exhaled breath [54,56]. The GC technique allows for separating the multicomponent matrix of exhaled breath in individual constituent compounds, and provides information about the molecular composition and the molecular identity of the compounds. For being analyzed, the sample is injected into an inert carrier gas (usually helium), which transports it into the chromatographic column. Compounds separation occurs due to their different partitioning rates when coming in contact with the stationary phase of the column. According to the affinity and relative interaction of the different compounds with the stationary phase, each compound elutes at a different time, i.e., each compound has a specific retention time and reaches the detector at a different time. The retention time of each compound depends on different parameters such as temperature, molecular identity and column's length. The column is typically coiled, thin (usually having 0.25 mm internal diameter) and very long (tens of meters in length), and is placed in a relatively small temperature controlled oven [57].

However, given the low concentration and the complex nature of the compounds from the exhaled breath, the analysis of breath using GC has important limitations for accurately identifying the breath volatiles at low concentrations. For this reason, GC combined with other analytical techniques such as flame ionization detection (FID), mass spectrometry (MS) or ion-mobility spectrometry (IMS), is commonly employed in the analysis of trace components in exhaled breath.

GC-FID is a widely used technique in breath analysis, where FID is mostly used for the detection of organic compounds [3,26]. This method is based on the combustion of organic compounds in the FID, which produces ions and electrons that can conduct electric potential that is used for the qualitative and quantitative detection of the breath components. In general, GC based on FID detectors provides fairly high sensitivity and large linear response ranges, however it tends to be mass sensitive and its response is independent of the flow rate of the mobile phase. Employing GC-FID, Phillips *et al.* reported the accurate quantification of isoprene and several other compounds in the breath [58]. On the other hand, gas chromatography coupled with ion mobility spectroscopy (GC-IMS), was also introduced for the use of field monitoring technique or detecting vapor phase organic compounds, widely used for the detection of chemical warfare agents [59]. IMS detection methods involve the ionization of molecules into constituents ions by an electric field against a drift gas, and ions are detected based on mobility which depends on mass, charge, size and shape of ions [60]. IMS enables the identification of and quantification of of gas phase molecules and its important characteristics and is extremely sensitive while the results are obtained rapidly and the simple experimental setup enables the construction of handy instruments [61].

Later in the 1990's, the further advancement of analytical techniques has emboldened gas chromatography coupled with mass spectrometry (GC-MS) as one of the gold standard techniques for the qualitative and quantitative analysis of trace components in exhaled breath. Phillips *et al.* systematically assayed VOCs and their variations in the breath of 50 healthy humans using GC-MS, reporting more than 3400 VOCs that were totally found in the breath samples of this study population, whereas only 27 VOCs were common for all 50 subjects [29]. Gordon *et al.* developed a special breath

collection method and computer assisted GC-MS to analyze breath samples of lung cancer patients and healthy controls, and the breath VOCs profiles obtained completely distinguished lung cancer patients (12 samples) from healthy controls (17 samples) [62].

2.5.2. Proton Transfer Reaction –Mass Spectroscopy (PTR-MS)

Proton Transfer Reaction-Mass Spectroscopy is a modern analytical technique that is mostly employed to detect VOCs in air [63]. For breath analysis, it is an alternative to the GC that enables direct sample measurement and real time identification and quantification of VOCs [63-65].

PTR-MS technique is based on the soft chemical ionization through proton transfer of a gaseous sample in a reaction chamber (drift tube), which is a conducting enclosure connected at a constant potential. The charged particles suffer no change in velocity inside the drift tube, enabling a stable reaction time for the ions as they flow through the tube [64]. PTR-MS generally uses the hydronium ions (H_3O^+) as precursors. Basically, pure water vapor enters in the ion source hollow cathode, where it is protonized to H_3O^+ and transported to the drift tube where encounters with the gaseous VOCs sample. As a result, the VOCs from the sample experience the non-dissociative proton transfer and are analyzed by a mass spectrometer, whose results are easily interpretable and trustable [64]. PTR-MS devices commonly perform the separation of protonized compounds by a quadrupole mass filter, and this technique is limited by low mass resolving power, hence different compounds with the same normal mass may not be accurately discriminated, and moreover the sensitivity is poor. As an alternative to the quadruple filter analyzer, the time-of-flight (TOF) mass analyzer has been more recently introduced as detector. This mass analyzer produces continuous highly resolved mass

spectra, enabling the possibility to discriminate nominally isobaric compounds on the basis of accurate masses [63,66,67].

The first application of PTR-MS in breath analysis dates from 1994, when it was used to measure methanol, ethanol and acetone in human breath [68]. Since then, the use of PTR-MS to measure and monitor the composition of breath as an indicator of a disease has been increasingly explored [63,69,70]. Example of studied diseases are lung cancer [71], breast cancer [72], *H. Pylori* infection [73,74], Coeliac diseases [75], kidney malfunction [76], as well as risk environment monitoring through exhaled breath analysis [77].

2.6. Chemical gas sensors

In contrast with the analytical techniques, which are employed for individual compounds identification but are not able to identify complex breath sample signatures as a whole, the chemical gas sensors can analyze the overall complex composition of the sample. They present various advantages, such as small size, simple operation and low cost. Therefore, they can be easily miniaturized and are suitable for developing portable breath analysis devices. Compounds detection with these devices is realized indirectly, by analyzing the change in one of more of the sensors properties when exposed to the sample. They are not compound selective, but depending on the sensing material employed, they are prone to react with certain families of chemical compounds.

Electronic noses or *e-noses* are gas sensing systems that contain an array of cross reactive chemical gas sensors, where every sensor has a different sensing material and responds differently to the complex VOCs mixture from the sample. Their responses are

analyzed by specific data analysis tools and pattern recognition algorithms for building classification models [78,79]. A major advantage of using e-noses for diseases diagnoses is that they provide quick results and cause less stress or anxiety to the patients.

A wide range of chemical gas sensors based on different operating technologies have been used in clinical disease diagnostic applications [78]. The most common types include surface acoustic wave, quartz crystal microbalance and chemiresistive sensors based on different sensing materials such as metal oxides and metal oxide nanowires, carbon nanotubes, organically capped metal nanoparticles, and conducting polymers. In particular, the chemical gas sensors of chemiresistive type based on different broadly cross-sensitive sensing elements arose as one of the most promising approaches in the breath analysis field [37].

A simple schematic representation of a chemiresistive gas sensor is shown in **Figure 2.5**, together with the ideal characteristic response signal showing the changes in sensor's resistance upon the interaction with an analyte. The chemical and/or physical adsorption/desorption processes of the analyte on the sensing material is usually reversible, leading to the recuperation of the initial baseline conditions of the measured sensor's characteristic (resistance in Figure 2.5) after analyte evacuation.

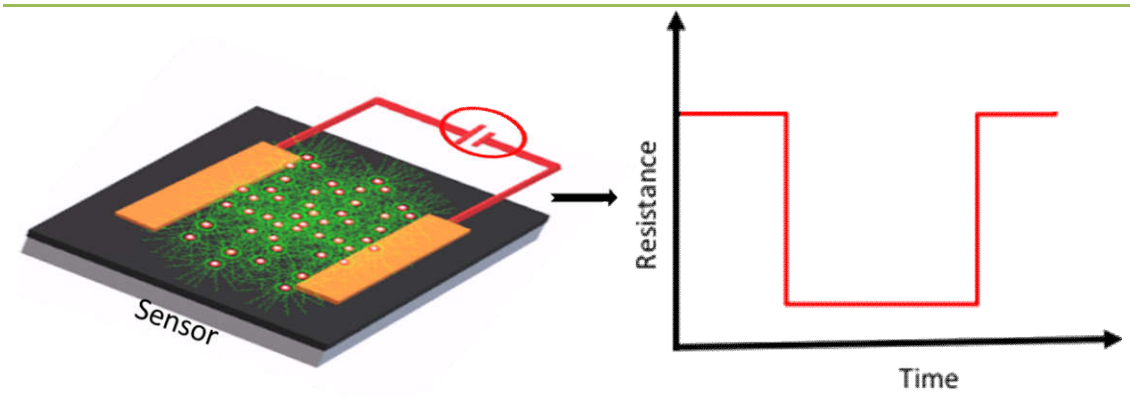

Figure 2.5: Typical schematic representation of a chemiresistive gas sensor with a sensing film deposited between two parallel electrodes (left); Measured resistance changes over time in the absence/presence of the analyte (right).

2.6.1. Nanomaterial Based Chemical Gas Sensors for Breath Analysis

The nanomaterials are preferred as sensing films for the chemical gas sensors because of their high surface-to-volume ratio, which provides an increased number of interaction sites for the exposing volatiles [80,81]. A broad range of functional nanomaterials have been used as transduction elements for breath VOCs detection, including metal oxides [82], silicon nanowires [83-85], metal nanoparticles [86-91], carbon nanotubes (CNTs) [92-94], and polymers [95] are among others [81,86,93,96-99]. The use of selectively permeable, hydrophobic materials simultaneously serving as water passivators and VOCs preconcentrators can further enhance breath VOCs detection [81,93].

2.6.1.1. Chemical Sensors Based on Ligand-capped Metal Nanoparticles

Metal nanoparticles functionalized or capped with different organic ligands, also known as ligand-capped metal nanoparticles, emerged as a new frontier of gas sensing nanomaterials since twenty years ago [100]. They are hybrid materials that combine the advantage of the organic ligand's affinity to targeted breath VOCs, with the robustness of inorganic metal nanoparticles (Au, Ag, Pt, Cu, Ni, and others), offering better selectivity and specificity to the sensed VOCs, as well as lower power consumption because of room temperature operation features [101]. Gold is the most preferred choice for the metal, whereas the capping ligands are usually selected from the thiol group because that can easily bind to the metal nanoparticles [102]. Sensors based on ligand-nanoparticles nanoassemblies are also of special interest due to their high sensitivity, low detection limit, fast response, low output impedance and easy integration with standard microelectronics [88,103]. These hybrid nanomaterials have been integrated in a variety of sensors types, including resistors [104,105], capacitors [106,107], quartz crystal microbalances [108,109], colorimetric sensors [110], and Schottky diode sensors [111].

For example, Han *et al*. reported nanostructured sensing arrays that consisted of thin film assemblies of different alkanethiols-monolayer capped gold nanoparticles for the detection of VOCs and nitro-aromatic compounds [112]. The sensing elements of these sensing devices displayed linear responses to the concentrations of the VOCs tested (hexane, benzene, toluene, p-xylene, o-xylene, m-xylene, nitrobenzene, 2-nitrotoluene,

and 3-nitotoluene). Whereas the response profiles of the different sensing films for the same VOC were similar, the sensitivities varied dramatically.

Dovgolevsky *et al*. fabricated chemiresistors based on cubic platinum nanoparticles (PtNPs) functionalized with four representative organic ligands (11-mercaptoundecanoic acid, 11-mercaptoundecanol, benzylmercaptan, and oleylamine) for VOCs sensing in highly humid atmosphere simulating the relative humidity in breath [87], and revealed that the sensing of nonpolar VOCs (mostly reported as disease biomarkers) was much higher than that of polar VOCs, including water vapor [87].

Chemiresistive sensors based on molecularly modified metal nanoparticles have been actively engaged in breath analysis for the diagnosis and monitoring of several diseases. Promising results have been obtained in the diagnosis of different type of cancers such as gastric cancer lung cancer, prostate cancer, as well as colorectal cancer [104,113-116], kidney injury [116], chronic kidney disease [115,117,118], diabetes mellitus [118,119], Alzheimer's and Parkinson's diseases [115,120], renal disease [92], gastric cancer asthma and obstructive pulmonary disease [85,121], and multiple sclerosis, among others diseases [115].

2.6.1.2. Sensing Mechanism of Ligand-capped Metal Nanoparticles Sensors

In VOCs sensing with ligand-capped metal nanoparticles films, the metallic nanoparticles provide the electric conductivity through the film, while the organic ligand provides sorption sites for the analytes. The physical properties of the sensing film are mainly controlled by features such as nanoparticles size, type of capping ligand,

and distance between adjacent MNPs. Although it is still under debate, the conductivity of ligand-capped metal nanoparticles films has been qualitatively discussed from the view of an activated tunneling model [101,122]. In the context of this theory, VOCs response mechanism of the ligand-MNPs nanoassemblies in electrical sensors involves electrons tunneling between the metal cores, and charge hopping through the atoms of the organic ligand. The electronic conduction, σ_{el} in a ligand-capped metal nanoparticles film is described by [101,107]:

$$\sigma_{el} = \sigma_o \exp(-\beta\delta) \exp\left(-\frac{E_a}{k_B T}\right) \quad \text{..... (1)}$$

and $$E_a = \frac{e^2}{4\pi\varepsilon_r\varepsilon_0 r} \quad \text{..... (2)}$$

where σ_o is a constant pre-exponential tunneling factor, β is the electron tunneling coefficient, δ is the edge-to-edge separation of the metal cores, E_a is the tunneling activation energy associated with the charging of adjacent metal cores, k_B is the Boltzmann constant, and T is the absolute temperature.

The two exponential factors in Eq. (1) describe two types of contributions to the electronic conductivity of the film. The first exponential factor takes into account the charge tunneling between neighboring particles through the organic ligand, which also describes the exponential dependence of σ_{el} on δ [123]. The second exponential factor includes the activation energy, E_a, which is required to generate one positively and one negatively charged metal cores from two initially neutral cores, for charge transport to occur between them. Eq. (1) contains moreover the electric field induced activated tunneling, whereby adjacent metal cores become charged/discharged as electrons pass

through the intercore dielectric medium. Hence, the activation energy E_a also accounts the electronic charge, e, the dielectric constant of the surrounding medium, ε_r, and the permittivity of the free space, ε_0, as well as nanoparticles radius, r as described by Eq. (2). Therefore, during VOCs sorption into the ligand capped-MNPs films, the molecules contact and react with tailored organic functional groups attached (or linked) to the MNPs, leading to changes in the measured electrical properties of the film, which can induce ligand-MNPs films swelling and/or change the permittivity of the medium between the MNPs metal cores [87]. These two competitive mechanisms induce electrical changes according to either of the following mechanism: i) reduction/increment in the number of electrically conductive percolation pathways between the MNPs (i.e., changes in the core-edge-to edge distance (δ), and/or ii) changes in the dielectric constant (ε_r), which can be a crucial factor during the absorption of small dielectrically different molecules into the sensing film [89]. For example, analyte molecules with high dielectric constant (e.g., ethanol, water, methanol, and ethanol) tend to provoke a decrease in the resistance of the film, while those with low dielectric constants (e.g., toluene and n-hexane) produce an increase in the resistance [124].

The conductivity changes in ligand-capped MNPs nanoassemblies upon analytes exposure are also predominantly affected by the size and morphology of the metal cores as well as by the functional organic ligand attached to the MNPs [88]. **Figure 2.6** illustrates the response model for ligand-capped MNPs films to an analyte exposure as a function of film morphology and thickness. It is noted that two metal nanoparticles separated from each other can be electrically treated as a capacitor in parallel with a

resistor, where the organic matrix separates the two metal particles in a similar manner as a dielectric medium separates a plate capacitor [125]. In isolated ligand-MNPs films, where the distance between the metal cores becomes small enough, the charge can tunnel between the MNPs promoting a capacitive or resistive behavior of the junction when applying a bias. On the contrary, Joseph *et al*. showed that for ligand capped MNPs where the metal cores are separated by a large distance, the film remains non-conductive and the ligand-MNPs nanoassemblies exhibit no response upon exposure to the analyte [101], as it is shown in **Figure 2.6a** [91]**.** On the other hand, as the core-to-core MNPs are close enough, providing an island dominated morphology, charge transport occurs after a 1-dimensioanl percolation pathway is formed. Therefore, this percolation pathway contains large island-to-island gaps, which are bottlenecks for charge transport due to their high resistance, and result in Coulomb blockade behavior. Notably, changes in permittivity and a swelling-induced decrease of the distance of the island to island gaps are thought to be responsible for the observed decrease in resistance shown in **Figure 2.6b**. The origin of the non-linearity in the I-V curves can be related to the fact that the bottleneck junctions are single electron-charging carriers in the percolation pathways [91]. In a 3-dimensional network-like film, as the one shown in **Figure 2.7c**, where many percolation pathways are possibly formed, the ligand-MNPs films usually respond with an increase in resistance when dosed with an analyte, assuming that film swelling increases the tunneling distance between the neighboring particles [91]. However, the films may swell only along the normal pathways, thereby only the percolation pathways that contribute to analyte sorption are influenced by the swelling [101]. On the contrary, swelling in the direction of the substrate might lead a decrease (shrinking) in the interparticles separation within the continuous 3D network-like structure of the film, and hence the resistance of the film decreases.

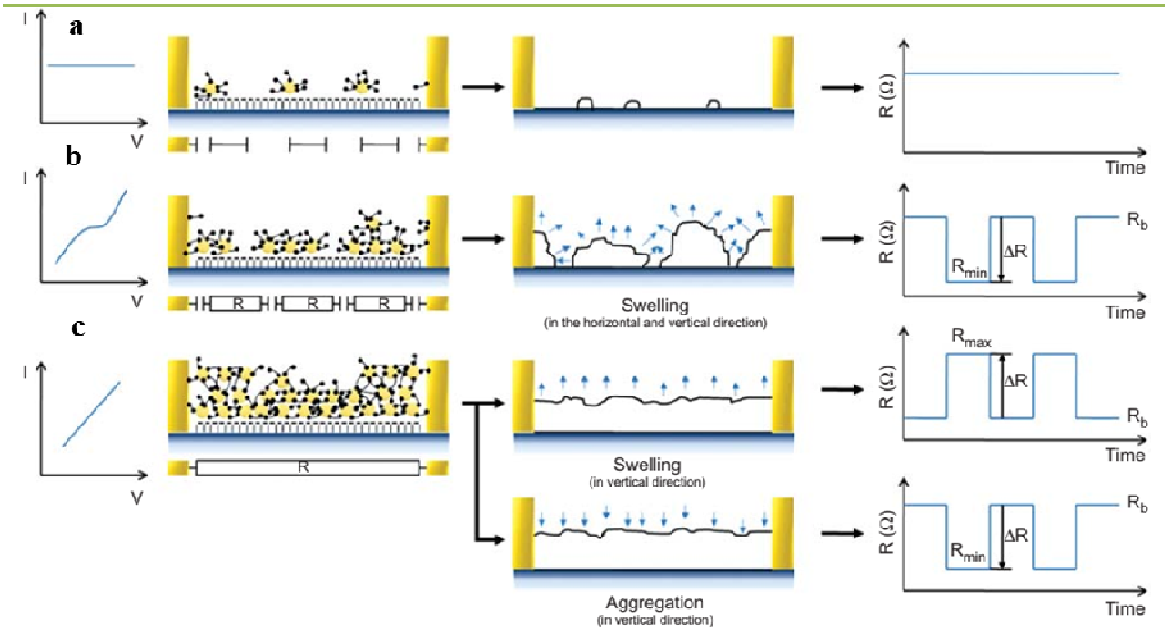

Figure 2.6: Model for the ligand capped metal nanoparticles nanoassemblies film growth upon exposure to an analyte: a) during island nuclei formation and island growth; b) film at the percolation threshold; c) in three dimensional film after the percolation threshold, and their characteristic I-V curves measured during film exposure to the analyte ($R(\Omega)$ – film resistance, R_{min} & R_b – minimum and initial resistance, and ΔR –resistance change). Adapted from [91].

2.7. Conclusion

Due to its broad scope and applicability, breath analysis holds a great potential for diseases diagnosis because the VOCs profile in exhaled breath can provide both non-invasive and continuous information on the metabolic and physiological state of an individual. Analytical techniques allow for the identification of the specific biomarkers of a disease, and can provide new insight into understanding the pathobiology of the disease. Electronic systems based on cross-reactive chemical gas sensors are suitable for the analysis of the overall complex mixture of volatiles from the exhaled breath, and due to their miniaturization features hold great potential for building small, easy-to-use, portable breath analysis diagnostic tools.

2.8. References

1. Phillips, M. Breath tests in medicine. *Scientific American* **1992**, *267*, 74-79.
2. Bogusław, B.; Martyna, K.; Tomasz, L.; Anton, A. Human exhaled air analytics: Biomarkers of diseases. *Biomedical Chromatography* **2007**, *21*, 553-566.
3. Kim, K.H.; Jahan, S.A.; Kabir, E. A review of breath analysis for diagnosis of human health. *TrAC Trends in Analytical Chemistry* **2012**, *33*, 1-8.
4. Donovan, A. *Antoine lavoisier: Science, administration and revolution*. Cambridge University Press: 1996; Vol. 5.
5. Anton, A.; Ben de Lacy, C.; Wolfram, M.; Jochen, S.; Bogusław, B.; Joachim, P.; Norman, R.; Terence, R. The human volatilome: Volatile organic compounds (vocs) in exhaled breath, skin emanations, urine, feces and saliva. *Journal of Breath Research* **2014**, *8*, 034001.
6. Amann, A.; Miekisch, W.; Schubert, J.; Buszewski, B.; Ligor, T.; Jezierski, T.; Pleil, J.; Risby, T. Analysis of exhaled breath for disease detection. In *Annual Review of Analytical Chemistry*, 2014; Vol. 7, pp 455-482.
7. Cheng, E.Y.; Woehlck, H.; Mazzeo, A.J. Capnography in critical care medicine. *Journal of Intensive Care Medicine* **1997**, *12*, 18-32.
8. Borkenstein, R.F.; Smith, H. The breathalyzer and its applications. *Medicine, Science and the Law* **1961**, *2*, 13-22.
9. Ferwana, M.; Abdulmajeed, I.; Alhajiahmed, A.; Madani, W.; Firwana, B.; Hasan, R.; Altayar, O.; Limburg, P.J.; Murad, M.H.; Knawy, B. Accuracy of urea breath test in helicobacter pylori infection: Meta-analysis. *World journal of gastroenterology: WJG* **2015**, *21*, 1305.
10. Risby, T.H.; Solga, S.F. Current status of clinical breath analysis. *Applied Physics B* **2006**, *85*, 421-426.

11. Cao, W.; Duan, Y. Current status of methods and techniques for breath analysis. *Critical Reviews in Analytical Chemistry* **2007**, *37*, 3-13.

12. Fenske, J.D.; Paulson, S.E. Human breath emissions of vocs. *Journal of the Air & Waste Management Association* **1999**, *49*, 594-598.

13. Pavagadhi, S.; Balasubramanian, R. Quantitative analysis of vocs in exhaled breath from asian volunteers: A pilot study. *Journal of Molecular Biomarkers & Diagnosis* **2014**, *5*, 1.

14. Miekisch, W.; Schubert, J.K.; Noeldge-Schomburg, G.F.E. Diagnostic potential of breath analysis—focus on volatile organic compounds. *Clinica Chimica Acta* **2004**, *347*, 25-39.

15. Ma, W.; Liu, X.; Pawliszyn, J. Analysis of human breath with micro extraction techniques and continuous monitoring of carbon dioxide concentration. *Analytical and Bioanalytical Chemistry* **2006**, *385*, 1398-1408.

16. Haick, H.; Broza, Y.Y.; Mochalski, P.; Ruzsanyi, V.; Amann, A. Assessment, origin, and implementation of breath volatile cancer markers. *Chemical Society Reviews* **2014**, *43*, 1423-1449.

17. Cao, W.; Duan, Y. Breath analysis: Potential for clinical diagnosis and exposure assessment. *Clinical chemistry* **2006**, *52*, 800-811.

18. Buszewski, B.; Kesy, M.; Ligor, T.; Amann, A. Human exhaled air analytics: Biomarkers of diseases. *Biomedical chromatography : BMC* **2007**, *21*, 553-566.

19. de Lacy Costello, B.; Amann, A.; Al-Kateb, H.; Flynn, C.; Filipiak, W.; Khalid, T.; Osborne, D.; Ratcliffe, N.M. A review of the volatiles from the healthy human body. *J Breath Res* **2014**, *8*, 014001.

20. Risby, T.H. Current status of clinical breath analysis. In *Breath analysis for clinical diagnosis and therapeutic monitoring: (with cd-rom)*, World Scientific: 2005; pp 251-265.

21. Buljubasic, F.; Buchbauer, G. The scent of human diseases: A review on specific volatile organic compounds as diagnostic biomarkers. *Flavour and fragrance journal* **2015**, *30*, 5-25.

22. Timothy P. Dalton; Howard G. Shertzer, a.; Puga, A. Regulation of gene expression by reactive oxygen. *Annual Review of Pharmacology and Toxicology* **1999**, *39*, 67-101.

23. Kinter, M. Analytical technologies for lipid oxidation products analysis. *Journal of Chromatography B: Biomedical Sciences and Applications* **1995**, *671*, 223-236.

24. Rice-Evans, C. Formation of free radicals and mechanisms of action in normal biochemical prcesses and pathological states. *Free Radical Damage and Its Control* **1994**, 129-151.

25. Porter, N.A.; Caldwell, S.E.; Mills, K.A. Mechanisms of free radical oxidation of unsaturated lipids. *Lipids* **1995**, *30*, 277-290.

26. Kneepkens, C.M.; Lepage, G.; Roy, C.C. The potential of the hydrocarbon breath test as a measure of lipid peroxidation. *Free radical biology & medicine* **1994**, *17*, 127-160.

27. Aghdassi, E.; Allard, J.P. Breath alkanes as a marker of oxidative stress in different clinical conditions. *Free Radical Biology and Medicine* **2000**, *28*, 880-886.

28. Risby, T.H.; Sehnert, S.S. Clinical application of breath biomarkers of oxidative stress status. *Free Radical Biology and Medicine* **1999**, *27*, 1182-1192.

29. Phillips, M.; Herrera, J.; Krishnan, S.; Zain, M.; Greenberg, J.; Cataneo, R.N. Variation in volatile organic compounds in the breath of normal humans. *Journal of Chromatography B: Biomedical Sciences and Applications* **1999**, *729*, 75-88.

30. Watanabe, M. Polymorphic cyp genes and disease predisposition--what have the studies shown so far? *Toxicology letters* **1998**, *102-103*, 167-171.

31. Stone, B.G.; Besse, T.J.; Duane, W.C.; Dean Evans, C.; DeMaster, E.G. Effect of regulating cholesterol biosynthesis on breath isoprene excretion in men. *Lipids* **1993**, *28*, 705-708.

32. Libardoni, M.; Stevens, P.T.; Waite, J.H.; Sacks, R. Analysis of human breath samples with a multi-bed sorption trap and comprehensive two-dimensional gas chromatography (gc×gc). *Journal of Chromatography B* **2006**, *842*, 13-21.

33. Scislowski, P.W.D.; Pickard, K. The regulation of transaminative flux of methionine in rat liver mitochondria. *Archives of Biochemistry and Biophysics* **1994**, *314*, 412-416.

34. Kaji, H.; Hisamura, M.; Saito, N.; Murao, M. Evaluation of volatile sulfur compounds in the expired alveolar gas in patients with liver cirrhosis. *Clinica chimica acta; international journal of clinical chemistry* **1978**, *85*, 279-284.

35. Schubert, J.K.; Miekisch, W.; Geiger, K.; Nöldge–Schomburg, G.F.E. Breath analysis in critically ill patients: Potential and limitations. *Expert Review of Molecular Diagnostics* **2004**, *4*, 619-629.

36. Simenhoff, M.L.; Burke, J.F.; Saukkonen, J.J.; Ordinario, A.T.; Doty, R.; Dunn, S. Biochemical profile of uremic breath. *New England Journal of Medicine* **1977**, *297*, 132-135.

37. Wilson, A. Advances in electronic-nose technologies for the detection of volatile biomarker metabolites in the human breath. *Metabolites* **2015**, *5*, 140.

38. Righettoni, M.; Amann, A.; Pratsinis, S.E. Breath analysis by nanostructured metal oxides as chemo-resistive gas sensors. *Materials Today* **2015**, *18*, 163-171.

39. Phillips, M.; Cataneo, R.N.; Cummin, A.R.C.; Gagliardi, A.J.; Gleeson, K.; Greenberg, J.; Maxfield, R.A.; Rom, W.N. Detection of lung cancer with volatile markers in the breath. *Chest* **2003**, *123*, 2115-2123.

40. Phillips, M.; Gleeson, K.; Hughes, J.M.B.; Greenberg, J.; Cataneo, R.N.; Baker, L.; McVay, W.P. Volatile organic compounds in breath as markers of lung cancer: A cross-sectional study. *Lancet* **1999**, *353*, 1930-1933.

41. McGrath, L.T.; Patrick, R.; Mallon, P.; Dowey, L.; Silke, B.; Norwood, W.; Elborn, S. Breath isoprene during acute respiratory exacerbation in cystic fibrosis. *European Respiratory Journal* **2000**, *16*, 1065-1069.

42. Paredi, P.; Kharitonov, S.A.; Leak, D.; Shah, P.L.; Cramer, D.; Hodson, M.E.; Barnes, P.J. Exhaled ethane is elevated in cystic fibrosis and correlates with carbon monoxide levels and airway obstruction. *American Journal of Respiratory and Critical Care Medicine* **2000**, *161*, 1247-1251.

43. Sehnert, S.S.; Jiang, L.; Burdick, J.F.; Risby, T.H. Breath biomarkers for detection of human liver diseases: Preliminary study. *Biomarkers* **2002**, *7*, 174-187.

44. Kwak, J.; Preti, G. Volatile disease biomarkers in breath: A critique. *Current pharmaceutical biotechnology* **2011**, *12*, 1067-1074.

45. Caro, J.; Gallego, M. Environmental and biological monitoring of volatile organic compounds in the workplace. *Chemosphere* **2009**, *77*, 426-433.

46. Hakim, M.; Broza, Y.Y.; Barash, O.; Peled, N.; Phillips, M.; Amann, A.; Haick, H. Volatile organic compounds of lung cancer and possible biochemical pathways. *Chemical Reviews* **2012**, *112*, 5949-5966.

47. Turner, C.; Španěl, P.; Smith, D. A longitudinal study of ethanol and acetaldehyde in the exhaled breath of healthy volunteers using selected-ion flow-tube mass spectrometry. *Rapid Communications in Mass Spectrometry: An International Journal Devoted to the Rapid Dissemination of Up-to-the-Minute Research in Mass Spectrometry* **2006**, *20*, 61-68.

48. Gustafsson, L.E.; Leone, A.; Persson, M.; Wiklund, N.; Moncada, S. Endogenous nitric oxide is present in the exhaled air of rabbits, guinea pigs and humans. *Biochemical and biophysical research communications* **1991**, *181*, 852-857.

49. Lundberg, J.; Weitzberg, E.; Lundberg, J.; Alving, K. Nitric oxide in exhaled air. *European Respiratory Journal* **1996**, *9*, 2671-2680.

50. Kharitonov, S.A.; Barnes, P.J. Biomarkers of some pulmonary diseases in exhaled breath. *Biomarkers* **2002**, *7*, 1-32.

51. Suarez, F.; Furne, J.; Springfield, J.; Levitt, M. Morning breath odor: Influence of treatments on sulfur gases. *Journal of dental research* **2000**, *79*, 1773-1777.

52. Mathew, T.; Pownraj, P.; Abdulla, S.; Pullithadathil, B. Technologies for clinical diagnosis using expired human breath analysis. *Diagnostics* **2015**, *5*, 27.

53. Kharitonov, S.A.; Gonio, F.; Kelly, C.; Meah, S.; Barnes, P.J. Reproducibility of exhaled nitric oxide measurements in healthy and asthmatic adults and children. *European Respiratory Journal* **2003**, *21*, 433-438.

54. Teranishi, R.; Mon, T.R.; Robinson, A.B.; Cary, P.; Pauling, L. Gas chromatography of volatiles from breath and urine. *Analytical Chemistry* **1972**, *44*, 18-20.

55. Pauling, L.; Robinson, A.B.; Teranishi, R.; Cary, P. Quantitative analysis of urine vapor and breath by gas-liquid partition chromatography. *Proceedings of the National Academy of Sciences of the United States of America* **1971**, *68*, 2374-2376.

56. Poole, C. *Gas chromatography*. 2012.

57. Littlewood, A.B. *Gas chromatography: Principles, techniques, and applications*. Elsevier: 2013.

58. Phillips, M.; Greenberg, J. Method for the collection and analysis of volatile compounds in the breath. *Journal of Chromatography B: Biomedical Sciences and Applications* **1991**, *564*, 242-249.

59. Borsdorf, H.; Eiceman, G.A. Ion mobility spectrometry: Principles and applications. *Applied Spectroscopy Reviews* **2006**, *41*, 323-375.

60. Simpson, G.; Klasmeier, M.; Hill, H.; Atkinson, D.; Radolovich, G.; Lopez-Avila, V.; Jones, T.L. Evaluation of gas chromatography coupled with ion mobility spectrometry for monitoring vinyl chloride and other chlorinated and aromatic compounds in air samples. *Journal of High Resolution Chromatography* **1996**, *19*, 301-312.

61. Vautz, W.; Franzke, J.; Zampolli, S.; Elmi, I.; Liedtke, S. On the potential of ion mobility spectrometry coupled to gc pre-separation – a tutorial. *Analytica Chimica Acta* **2018**, *1024*, 52-64.

62. Gordon, S.M.; Szidon, J.P.; Krotoszynski, B.K.; Gibbons, R.D.; O'Neill, H.J. Volatile organic compounds in exhaled air from patients with lung cancer. *Clinical chemistry* **1985**, *31*, 1278-1282.

63. Blake, R.S.; Monks, P.S.; Ellis, A.M. Proton-transfer reaction mass spectrometry. *Chemical Reviews* **2009**, *109*, 861-896.

64. Lindinger, W.; Jordan, A. Proton-transfer-reaction mass spectrometry (ptr–ms): On-line monitoring of volatile organic compounds at pptv levels. *Chemical Society Reviews* **1998**, *27*, 347-375.

65. Hansel, A.; Jordan, A.; Warneke, C.; Holzinger, R.; Wisthaler, A.; Lindinger, W. Proton-transfer-reaction mass spectrometry (ptr-ms): On-line monitoring of volatile organic compounds at volume mixing ratios of a few pptv. *Plasma Sources Science and Technology* **1999**, *8*, 332.

66. Graus, M.; Müller, M.; Hansel, A. High resolution ptr-tof: Quantification and formula confirmation of voc in real time. *Journal of the American Society for Mass Spectrometry* **2010**, *21*, 1037-1044.

67. Blake, R.S.; Whyte, C.; Hughes, C.O.; Ellis, A.M.; Monks, P.S. Demonstration of proton-transfer reaction time-of-flight mass spectrometry for real-time analysis of trace volatile organic compounds. *Analytical Chemistry* **2004**, *76*, 3841-3845.

68. Lagg, A.; Taucher, J.; Hansel, A.; Lindinger, W. Applications of proton transfer reactions to gas analysis. *International Journal of Mass Spectrometry and Ion Processes* **1994**, *134*, 55-66.

69. Zhan, X.; Duan, J.; Duan, Y. Recent developments of proton-transfer reaction mass spectrometry (ptr-ms) and its applications in medical research. *Mass Spectrometry Reviews* **2013**, *32*, 143-165.

70. Hansel, A.; Jordan, A.; Holzinger, R.; Prazeller, P.; Vogel, W.; Lindinger, W. Proton transfer reaction mass spectrometry: On-line trace gas analysis at the ppb level. *International Journal of Mass Spectrometry and Ion Processes* **1995**, *149-150*, 609-619.

71. Wehinger, A.; Schmid, A.; Mechtcheriakov, S.; Ledochowski, M.; Grabmer, C.; Gastl, G.A.; Amann, A. Lung cancer detection by proton transfer reaction mass-spectrometric analysis of human breath gas. *International Journal of Mass Spectrometry* **2007**, *265*, 49-59.

72. Li, J.; Peng, Y.; Liu, Y.; Li, W.; Jin, Y.; Tang, Z.; Duan, Y. Investigation of potential breath biomarkers for the early diagnosis of breast cancer using gas chromatography–mass spectrometry. *Clinica Chimica Acta* **2014**, *436*, 59-67.

73. Amann, A.; Poupart, G.; Telser, S.; Ledochowski, M.; Schmid, A.; Mechtcheriakov, S. Applications of breath gas analysis in medicine. *International Journal of Mass Spectrometry* **2004**, *239*, 227-233.

74. Iain, R.W.; Kerry, A.W.; Chris, W.; Rebecca, C.; Robert, S.B.; Andrew, J.W.; Satish, R.; Jonathan, G.; Andrew, M.E.; Paul, S.M. Real-time multi-marker measurement of organic compounds in human breath: Towards fingerprinting breath. *Journal of Breath Research* **2013**, *7*, 017112.

75. Aprea, E.; Cappellin, L.; Gasperi, F.; Morisco, F.; Lembo, V.; Rispo, A.; Tortora, R.; Vitaglione, P.; Caporaso, N.; Biasioli, F. Application of ptr-tof-ms to investigate metabolites in exhaled breath of patients affected by coeliac disease under gluten free diet. *Journal of Chromatography B* **2014**, *966*, 208-213.

76. Ingrid, K.; Jonathan, B.; Ferguel, C.-B.; Jens, H.; Dunkl, J.; Olaf, T.; Martin, T.; Claudia, B.; Armin, W.; Martin, B.*, et al.* First observation of a potential non-

invasive breath gas biomarker for kidney function. *Journal of Breath Research* **2013**, *7*, 017110.

77. Lirk, P.; Bodrogi, F.; Rieder, J. Medical applications of proton transfer reaction-mass spectrometry: Ambient air monitoring and breath analysis. *International Journal of Mass Spectrometry* **2004**, *239*, 221-226.

78. Wilson, A.D. Application of electronic-nose technologies and voc-biomarkers for the noninvasive early diagnosis of gastrointestinal diseases (†). *Sensors (Basel, Switzerland)* **2018**, *18*, 2613.

79. Krisher, S.; Riley, A.; Mehta, K. Designing breathalyser technology for the developing world: How a single breath can fight the double disease burden. *Journal of medical engineering & technology* **2014**, *38*, 156-163.

80. Tisch, U.; Haick, H. Nanomaterials for cross-reactive sensor arrays. *MRS Bulletin* **2010**, *35*, 797-803.

81. Tisch, U.; Haick, H. Chemical sensors for breath gas analysis: The latest developments at the breath analysis summit 2013. *J Breath Res* **2014**, *8*, 027103.

82. Fruhberger, B.; Stirling, N.; Grillo, F.G.; Ma, S.; Ruthven, D.; Lad, R.J.; Frederick, B.G. Detection and quantification of nitric oxide in human breath using a semiconducting oxide based chemiresistive microsensor. *Sensors and Actuators, B: Chemical* **2001**, *76*, 226-234.

83. Paska, Y.; Stelzner, T.; Assad, O.; Tisch, U.; Christiansen, S.; Haick, H. Molecular gating of silicon nanowire field-effect transistors with nonpolar analytes. *ACS Nano* **2012**, *6*, 335-345.

84. Shehada, N.; Brönstrup, G.; Funka, K.; Christiansen, S.; Leja, M.; Haick, H. Ultrasensitive silicon nanowire for real-world gas sensing: Noninvasive diagnosis of cancer from breath volatolome. *Nano Letters* **2015**, *15*, 1288-1295.

85. Shehada, N.; Cancilla, J.C.; Torrecilla, J.S.; Pariente, E.S.; Brönstrup, G.; Christiansen, S.; Johnson, D.W.; Leja, M.; Davies, M.P.A.; Liran, O.*, et al.* Silicon nanowire sensors enable diagnosis of patients via exhaled breath. *ACS Nano* **2016**, *10*, 7047-7057.

86. Broza, Y.Y.; Haick, H. Nanomaterial-based sensors for detection of disease by volatile organic compounds. *Nanomedicine* **2013**, *8*, 785-806.

87. Dovgolevsky, E.; Konvalina, G.; Tisch, U.; Haick, H. Monolayer-capped cubic platinum nanoparticles for sensing nonpolar analytes in highly humid atmospheres. *The Journal of Physical Chemistry C* **2010**, *114*, 14042-14049.

88. Dovgolevsky, E.; Tisch, U.; Haick, H. Chemically sensitive resistors based on monolayer-capped cubic nanoparticles: Towards configurable nanoporous sensors. *Small* **2009**, *5*, 1158-1161.

89. Hossam, H. Chemical sensors based on molecularly modified metallic nanoparticles. *Journal of Physics D: Applied Physics* **2007**, *40*, 7173.

90. Nakhleh, M.K.; Broza, Y.Y.; Haick, H. Monolayer-capped gold nanoparticles for disease detection from breath. *Nanomedicine* **2014**, *9*, 1991-2002.

91. Tisch, U.; Haick, H. Arrays of chemisensitive monolayer-capped metallic nanoparticles for diagnostic breath testing. In *Reviews in Chemical Engineering*, 2010; Vol. 26, p 171.

92. Haick, H.; Hakim, M.; Patrascu, M.; Levenberg, C.; Shehada, N.; Nakhoul, F.; Abassi, Z. Sniffing chronic renal failure in rat model by an array of random networks of single-walled carbon nanotubes. *ACS Nano* **2009**, *3*, 1258-1266.

93. Tisch, U.; Haick, H. Nanomaterials for cross-reactive sensor arrays. *MRS Bulletin* **2011**, *35*, 797-803.

94. Zilberman, Y.; Ionescu, R.; Feng, X.; Mullen, K.; Haick, H. Nanoarray of polycyclic aromatic hydrocarbons and carbon nanotubes for accurate and predictive detection in real-world environmental humidity. *ACS Nano* **2011**, *5*, 6743-6753.

95. Vishinkin, R.; Haick, H. Nanoscale sensor technologies for disease detection via volatolomics. *Small* **2015**, *11*, 6142-6164.

96. Hoel, A.; Reyes, L.F.; Heszler, P.; Lantto, V.; Granqvist, C.G. Nanomaterials for environmental applications: Novel wo3-based gas sensors made by advanced gas deposition. *Current Applied Physics* **2004**, *4*, 547-553.

97. Konvalina, G.; Haick, H. Sensors for breath testing: From nanomaterials to comprehensive disease detection. *Accounts of Chemical Research* **2014**, *47*, 66-76.

98. Xu, Z.q.; Broza, Y.Y.; Ionsecu, R.; Tisch, U.; Ding, L.; Liu, H.; Song, Q.; Pan, Y.y.; Xiong, F.x.; Gu, K.s.*, et al.* A nanomaterial-based breath test for distinguishing gastric cancer from benign gastric conditions. *Br J Cancer* **2013**, *108*, 941-950.

99. Potyrailo, R.A. Toward high value sensing: Monolayer-protected metal nanoparticles in multivariable gas and vapor sensors. *Chemical Society Reviews* **2017**, *46*, 5311-5346.

100. Zhang, H.L.; Evans, S.D.; Henderson, J.R.; Miles, R.E.; Shen, T.H. Vapour sensing using surface functionalized gold nanoparticles. *Nanotechnology* **2002**, *13*, 439.

101. Joseph, Y.; Guse, B.; Vossmeyer, T.; Yasuda, A. Gold nanoparticle/organic networks as chemiresistor coatings: The effect of film morphology on vapor sensitivity. *The Journal of Physical Chemistry C* **2008**, *112*, 12507-12514.

102. Wang, L.; Luo, J.; Schadt, M.J.; Zhong, C.-J. Thin film assemblies of molecularly-linked metal nanoparticles and multifunctional properties. *Langmuir* **2010**, *26*, 618-632.

103. Peng, G.; Tisch, U.; Adams, O.; Hakim, M.; Shehada, N.; Broza, Y.Y.; Billan, S.; Abdah-Bortnyak, R.; Kuten, A.; Haick, H. Diagnosing lung cancer in exhaled breath using gold nanoparticles. *Nature Nanotechnology* **2009**, *4*, 669.

104. Zhao, W.; Al-Nasser, L.F.; Shan, S.; Li, J.; Skeete, Z.; Kang, N.; Luo, J.; Lu, S.; Zhong, C.-J.; Grausgruber, C.J.*, et al.* Detection of mixed volatile organic compounds and lung cancer breaths using chemiresistor arrays with crosslinked nanoparticle thin films. *Sensors and Actuators B: Chemical* **2016**, *232*, 292-299.

105. Guo, J.; Pang, P.; Cai, Q. Effect of trace residual ionic impurities on the response of chemiresistor sensors with dithiol-linked monolayer-protected gold (nano)clusters as sensing interfaces. *Sensors and Actuators B: Chemical* **2007**, *120*, 521-528.

106. Mlsna, T.E.; Cemalovic, S.; Warburton, M.; Hobson, S.T.; Mlsna, D.A.; Patel, S.V. Chemicapacitive microsensors for chemical warfare agent and toxic industrial chemical detection. *Sensors and Actuators B: Chemical* **2006**, *116*, 192-201.

107. Steinecker, W.H.; Rowe, M.P.; Zellers, E.T. Model of vapor-induced resistivity changes in gold−thiolate monolayer-protected nanoparticle sensor films. *Analytical Chemistry* **2007**, *79*, 4977-4986.

108. Scholten, K.; Wright, L.K.; Zellers, E.T. Vapor discrimination with single- and multitransducer arrays of nanoparticle-coated chemiresistors and resonators. *IEEE Sensors Journal* **2013**, *13*, 2146-2154.

109. Dalfovo, M.C.; Salvarezza, R.C.; Ibañez, F.J. Improved vapor selectivity and stability of localized surface plasmon resonance with a surfactant-coated au nanoparticles film. *Analytical Chemistry* **2012**, *84*, 4886-4892.

110. Ionescu, R.; Cindemir, U.; Welearegay, T.G.; Calavia, R.; Haddi, Z.; Topalian, Z.; Granqvist, C.-G.; Llobet, E. Fabrication of ultra-pure gold nanoparticles capped with dodecanethiol for schottky-diode chemical gas sensing devices. *Sensors and Actuators B: Chemical* **2017**, *239*, 455-461.

111. Han, L.; Shi, X.; Wu, W.; Kirk, F.L.; Luo, J.; Wang, L.; Mott, D.; Cousineau, L.; Lim, S.I.I.; Lu, S.*, et al.* Nanoparticle-structured sensing array materials and pattern recognition for voc detection. *Sensors and Actuators B: Chemical* **2005**, *106*, 431-441.

112. Peng, G.; Hakim, M.; Broza, Y.Y.; Billan, S.; Abdah-Bortnyak, R.; Kuten, A.; Tisch, U.; Haick, H. Detection of lung, breast, colorectal, and prostate cancers from exhaled breath using a single array of nanosensors. *British Journal Of Cancer* **2010**, *103*, 542.

113. Chang, J.E.; Lee, D.S.; Ban, S.W.; Oh, J.; Jung, M.Y.; Kim, S.H.; Park, S.; Persaud, K.; Jheon, S. Analysis of volatile organic compounds in exhaled breath for lung cancer diagnosis using a sensor system. *Sensors and Actuators, B: Chemical* **2018**, *255*, 800-807.

114. Di Natale, C.; Macagnano, A.; Martinelli, E.; Paolesse, R.; D'Arcangelo, G.; Roscioni, C.; Finazzi-Agrò, A.; D'Amico, A. Lung cancer identification by the analysis of breath by means of an array of non-selective gas sensors. *Biosensors and Bioelectronics* **2003**, *18*, 1209-1218.

115. Nakhleh, M.K.; Amal, H.; Jeries, R.; Broza, Y.Y.; Aboud, M.; Gharra, A.; Ivgi, H.; Khatib, S.; Badarneh, S.; Har-Shai, L.*, et al.* Diagnosis and classification of

17 diseases from 1404 subjects via pattern analysis of exhaled molecules. *ACS Nano* **2017**, *11*, 112-125.

116. Nakhleh, M.K.; Amal, H.; Awad, H.; Gharra, A.l.; Abu-Saleh, N.; Jeries, R.; Haick, H.; Abassi, Z. Sensor arrays based on nanoparticles for early detection of kidney injury by breath samples. *Nanomedicine: Nanotechnology, Biology and Medicine* **2014**, *10*, 1767-1776.

117. Marom, O.; Nakhoul, F.; Tisch, U.; Shiban, A.; Abassi, Z.; Haick, H. Gold nanoparticle sensors for detecting chronic kidney disease and disease progression. *Nanomedicine* **2012**, *7*, 639-650.

118. Saidi, T.; Zaim, O.; Moufid, M.; El Bari, N.; Ionescu, R.; Bouchikhi, B. Exhaled breath analysis using electronic nose and gas chromatography–mass spectrometry for non-invasive diagnosis of chronic kidney disease, diabetes mellitus and healthy subjects. *Sensors and Actuators, B: Chemical* **2018**, *257*, 178-188.

119. Ping, W.; Yi, T.; Haibao, X.; Farong, S. A novel method for diabetes diagnosis based on electronic nose. *Biosensors and Bioelectronics* **1997**, *12*, 1031-1036.

120. Tisch, U.; Schlesinger, I.; Ionescu, R.; Nassar, M.; Axelrod, N.; Robertman, D.; Tessler, Y.; Azar, F.; Marmur, A.; Aharon-Peretz, J.*, et al.* Detection of alzheimer's and parkinson's disease from exhaled breath using nanomaterial-based sensors. *Nanomedicine* **2013**, *8*, 43-56.

121. Fens, N.; Zwinderman, A.H.; Schee, M.P.v.d.; Nijs, S.B.d.; Dijkers, E.; Roldaan, A.C.; Cheung, D.; Bel, E.H.; Sterk, P.J. Exhaled breath profiling enables discrimination of chronic obstructive pulmonary disease and asthma. *American Journal of Respiratory and Critical Care Medicine* **2009**, *180*, 1076-1082.

122. Ahn, H.; Chandekar, A.; Kang, B.; Sung, C.; Whitten, J.E. Electrical conductivity and vapor-sensing properties of ω-(3-thienyl)alkanethiol-protected gold nanoparticle films. *Chemistry of Materials* **2004**, *16*, 3274-3278.

123. Terrill, R.H.; Postlethwaite, T.A.; Chen, C.-h.; Poon, C.-D.; Terzis, A.; Chen, A.; Hutchison, J.E.; Clark, M.R.; Wignall, G. Monolayers in three dimensions: Nmr, saxs, thermal, and electron hopping studies of alkanethiol stabilized gold clusters. *Journal of the American Chemical Society* **1995**, *117*, 12537-12548.

124. Joseph, Y.; Peić, A.; Chen, X.; Michl, J.; Vossmeyer, T.; Yasuda, A. Vapor sensitivity of networked gold nanoparticle chemiresistors: Importance of flexibility and resistivity of the interlinkage. *The Journal of Physical Chemistry C* **2007**, *111*, 12855-12859.

125. Shuster, G.; Baltianski, S.; Tsur, Y.; Haick, H. Utility of resistance and capacitance response in sensors based on monolayer-capped metal nanoparticles. *The Journal of Physical Chemistry Letters* **2011**, *2*, 1912-1916.

CHAPTER 3

3. FABRICATION AND CHARACTERIZATION OF ULTRAPURE LIGAND-CAPPED METAL NANOPARTICLES CHEMICAL GAS SENSORS

This chapter presents the .fabrication and characterization of the ultrapure ligand-capped metal nanoparticles chemical gas sensors, and prelimary VOCs sensing measurements.

3.1. State-of-the-art

A large number of metal nanoparticles- MNPs (Au, Cu, Pt, Pd, Ag, Fe, Zn, Cd) can be nowadays synthesized through different preparation routes, including chemical methods (*e.g.,* chemical reduction of metal salts [1,2], sonochemical reduction [3], chemical vapor deposition [4], microemulsions [5], supercritical fluids [6,7], electrochemical synthesis [8]), and physical methods (physical vapor deposition [4,9], microwave irradiation [10], pulsed laser deposition [11], thermal evaporation [9], gamma radiation [12,13]). Generally, nanoparticles fabrication can be roughly divided into two categories: bottom-up approaches that comprise nanoparticles synthesis from their atomic and molecular precursors through chemical reactions while controlling their nucleation and growth to obtain the desired size and morphology, and top-down approaches that comprise nanoparticles synthesis from macroscopic precursors through subsequent subdivision into smaller particles through physical processes such as lithography, sputtering, laser ablation, and vapour phase deposition.

The chemical methods are based on the use of microheterogenous systems such as colloids, liquids, crystals, gels or micellar solutions. The particles formed are suspended-like colloids, usually with particles size below 100 nm [14]. Through this method, the metal nanoparticles are produced in a liquid phase by reduction of their metallic salt precursors upon addition of reducing agents [14]. For example, gold

nanoparticles are synthesized using a two phase reduction approach as reported by Brust et al [14] (**Figure 3.1**).

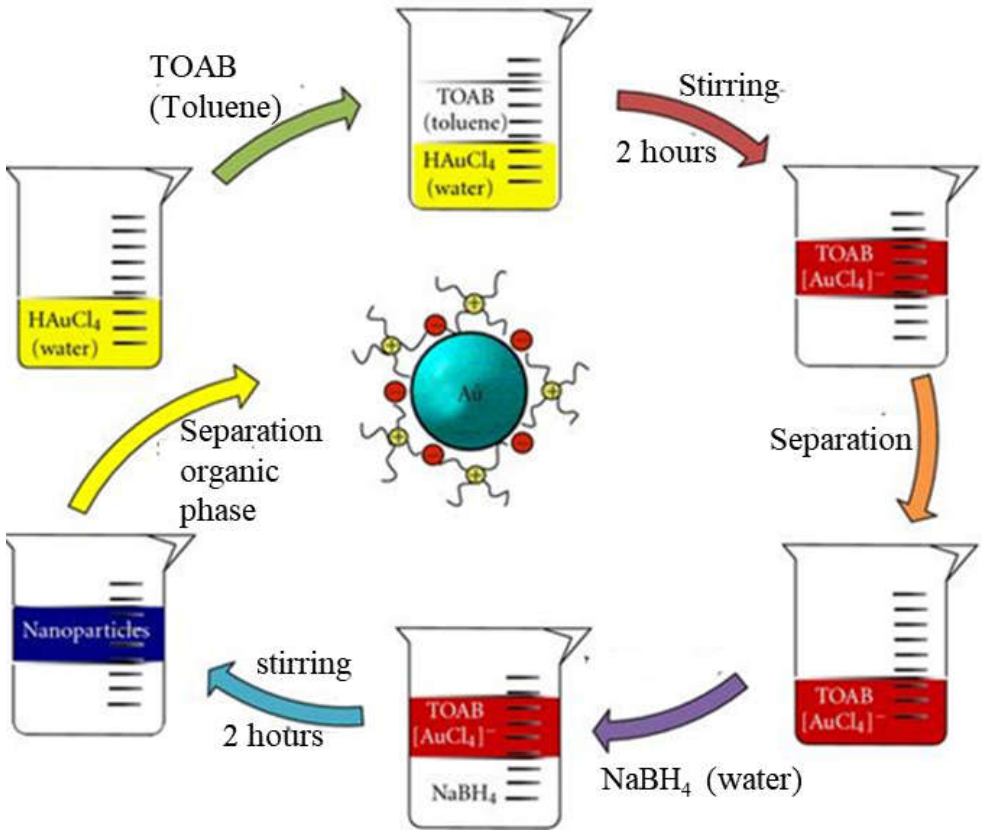

Figure 3.1: Brust's method for the synthesis of gold nanoparticles by two phase chemical reduction process. Reproduced from [15].

The method involves the transfer of gold hydrocholorate solution ($HAuCl_4.2H_2O$) into an organic phase (usually toluene) through tetraoctylammonium bromide (TOAB), which is used as a stabilizing phase transfer agent, followed by the addition of aqueous sodium brorhydride (NaBH4) to reduce Au(III) to Au(0). This simple procedure allows the formation of 5-6 nm size AuNPs. However, the as produced nanoparticles have a natural tendency to form agglomerations or coalescence, and hence an efficient surface modification and stabilization are required. Strong nanoparticles stabilization can be

obtained by the use of alkylic thiols (usually from C_6-C_{18} groups), resulting in a self-assembled monolayer of nanoparticles. Nevertheless, the solvent based chemical synthesis of metal nanoparticles presents the drawback of using contaminants such as polymers that leave traces in the synthesized film, and requires a two phase process during nanoparticles surface modification with the desired functional organic ligand. Metallic nanoparticles can also be prepared by physical methods from their bulk metals through application of mechanical pressure, high energy radiation, evaporation or condensation as well as thermal energy to cause abrasion. These methods that mainly operate on the top-down approach are advantageous as they are free of solvent contamination and produce uniform nanoparticles.

In view of these considerations, in my thesis I introduced an innovative physical route based on the Advanced Gas Deposition (AGD) technique, aiming at the fabrication of ultrapure monodispersed metal nanoparticles. The AGD process allows for log-normal size distribution of the nanoparticles, and crystalline ultrapure nanoparticles can be produced. The nanoparticles are less prone to agglomeration and coalescence, which are the major problems in the case of the MNPs prepared by other physical methods [16,17].

3.2. Fabrication of Ultrapure MNPs by Advanced Gas Deposition Technique

Three different MNPs (AuNPs, PtNPs and CuNPs) were directly generated from their pure metal precursors and deposited on different substrates by the advanced non-reactive gas deposition technique (Ultra Fine Particle Equipment, ULVAC Ltd, Japan [17]). The AGD technique consists two separating chambers, a lower chamber

evaporation occurs at (P1), and an upper depositing chamber- which is kept under good vaccuum (P2). A pellet of a precursor to be converted into particles is placed on top of a pedestal in the evaporation chamber and is heated by an inducton copper coil to the required temperature. Hense, the intense heating cuases the precursor to be evaporated. In addition, a a high purity cooling gas, usually inert gases (He or Ar), is introduced at the bootom of the lower chamber, and allows the vapor to transport from the vapor zone, thereby collides with the gas atoms or molecules and hence cooled, leading to the formation of clusters of atoms, which ends up formation of ultrafine particles. Finally, the single nanopartiles are quickly transported to the deposition chmaber owing to the pressure gradient [17]. Hence, in our fabrication process, high purity metal pieces of gold (99.999 % purity), platinum wire (99.99 % purity), and copper pellets (99.99 % purity), were used as precursors for nanoparticles fabrication.

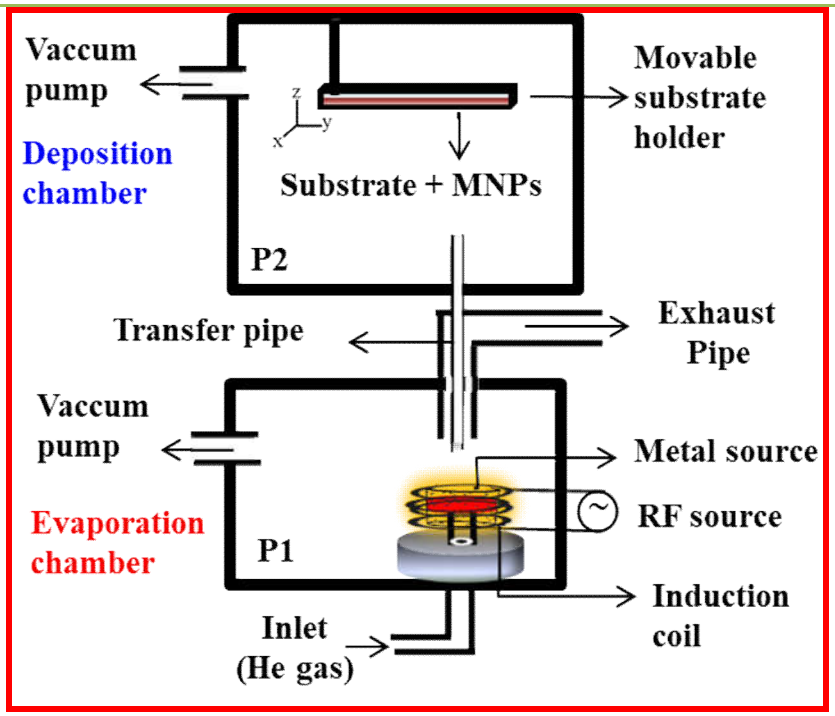

Figure 3.2: Schematic representation of the AGD equipment adopted in this study for ultrapure monodispersed metal nanoparticles fabrication

The AGD setup adopted in this study for the fabrication of ultrapure monodispersed metal nanoparticles is shown in **Figure 3.2**. Before starting nanoparticles synthesis process, the two AGD chambers (lower evaporation chamber and upper deposition chamber) were evacuated by means of several oil pumps until their pressure reached ~0.02 mbar, in order to eliminate all the impurities from the equipment. After that their pressures were set to the adequate values that were determined for each metal in part (see Table 3.1), being the lower chamber kept at higher pressure (adjusted for each MPNs formation – see Table 3.1) and the upper chamber at lower pressure (~ 0.09 mbar) during metal nanoparticles synthesis.

By applying a suitable power to the induction coil surrounding the metal source (4 kW for Au, 12 kW for Pt, and 3 kW for Cu), the metal precursor started to melt. The vapour zone formed above the molten metal consisted of metal atoms that gradually cooled down while they diffused through the He carrier gas introduced underneath the heated metal piece at a flow rate of 20 L/min, which carried them upwards. As the metal atoms experienced several collisions with each other, they started to agglomerate in such a way that nanoparticles were formed, leading to the nucleation and growth of ultrafine metal nanoparticles in the lower chamber. The stream of ultrafine nanoparticles generated in the lower chamber was then propelled to the upper chamber through the thin transfer pipe (3 mm diameter) that linked the two AGD chambers, which was heated by applying 40 kW power for avoiding condensations on its walls. Due to the pressure difference between the two chambers, the metal nanoparticles impinged at high speed onto the deposition substrate placed on the movable support in the upper chamber, and got sticky deposited on it. The speed of the movable support and the number of deposition cycles (*i.e.*, number of times that the stream of nanoparticles

impinged onto the substrate during its movement inside the upper AGD chamber) were optimized to obtain a monolayer of dispersed metal nanoparticles.

MNPs	Precursor Purity (%)	Metal Melting Point (°C)	Power (kW)	p_{dep} (mbar)	p_{ev} (mbar)	He flow (L/min)
AuNPs	99.999	1064	4	0.09	90.8	20
PtNPs	99.99	1768	12	0.09	90.8	20
CuNPs	99.99	1085	3	0.09	94	20

Table 3.1: Optimal conditions for the synthesis of monodispersed MNPs, where P_{dep} and P_{ev} correspond to P_2 and P_1 of the deposition and evaporation chambers.

3.2.1. AuNPs Fabrication

For AuNPs synthesis, by optimizing the pressure in the evaporation chamber of the AGD equipment at 90.8 mbar, the formation of monodispersed AuNPs was achieved during one deposition cycle for the speed of the movable support set to 1 mm/sec (**Figure 3.3a**). The increase of the pressure in the evaporation chamber to 100 mbar favored the formation of small clusters of AuNPs because of the tendency of the nanoparticles to agglomerate due to Van der Waals interactions occurring between them at this higher pressure, which led to the deposition of small aggregates of AuNPs even at the highest speed of the movable support (2.5 mm/sec), set in order to minimize the deposition time of the AuNPs onto the substrate (**Figure 3.3b**). Importantly, nanoparticles size and shape did not change by modifying the pressure in the evaporation chamber, as it can be seen by the closer examination of the AuNPs clusters in **Figure 3.3b**. Further increase of the number of deposition cycles led to the formation of continuous networks of linked AuNPs (**Figure 3.3c**). A continuous thin film of AuNPs that fully covered the substrate (~30 nm thicknesses) was achieved by increasing the deposition time through lowering the speed of the movable support to 1.25 mm/sec (**Figure 3.3d**).

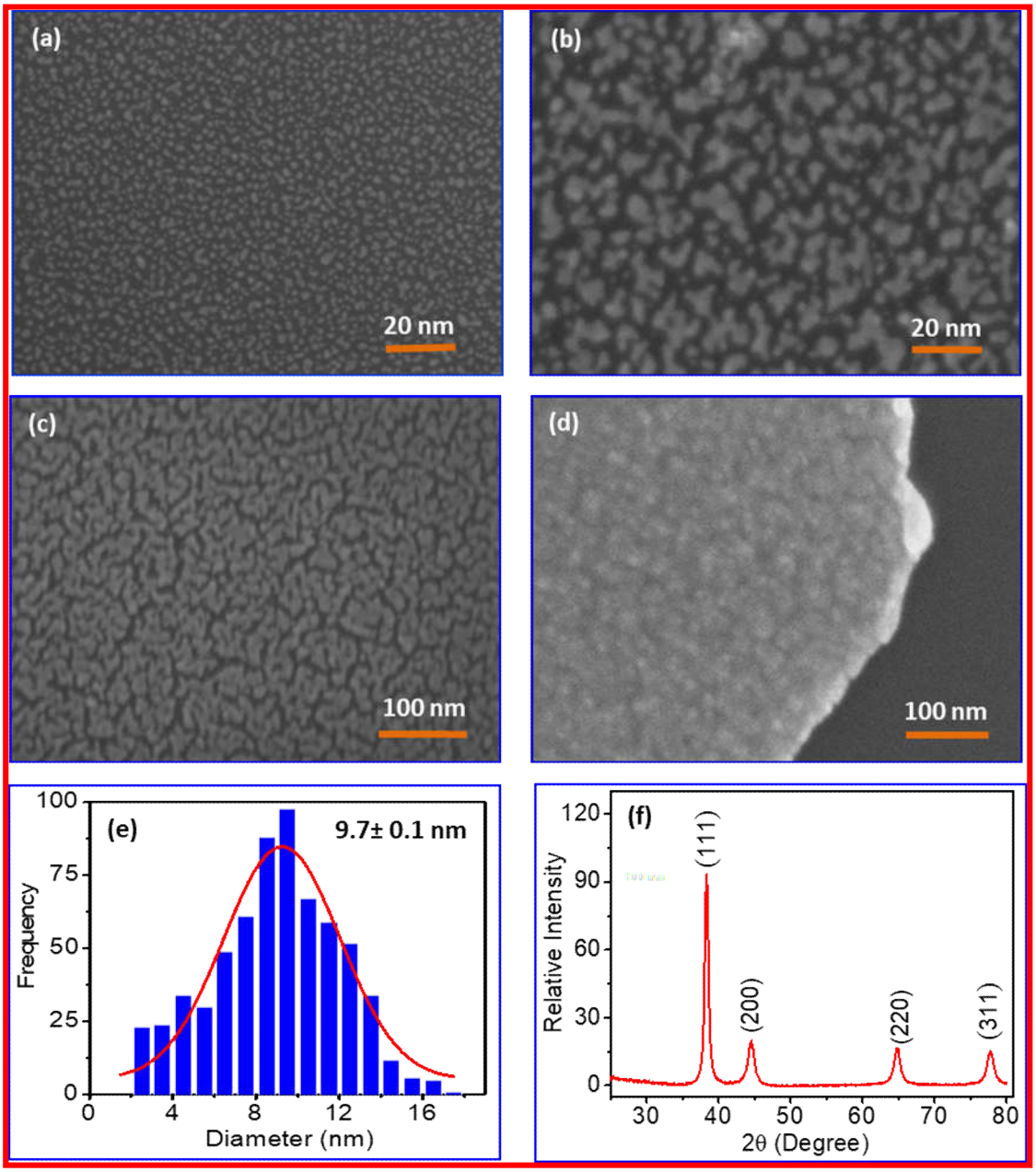

Figure 3.3: SEM images of the AuNPs synthesised using the following experimental parameters of AGD (pressure in the evaporation chamber, speed of the movable support, and number of deposition cycles): (a) 90.8 mbar, 1 mm/sec, 1 cycle; (b) 100 mbar, 2.5 mm/sec, 1 cycle; (c) 100 mbar, 2.5 mm/sec, 3 cycles; (d) 100 mbar, 1.25 mm/sec, 3 cycles. (e) Histogram of particles size distribution for the SEM image shown in **Figure 3.3a**. (f) X-ray diffractogram of the AuNPs thin film shown in **Figure 3.3d**.

Particles size distribution displayed in **Figure 3.3e** showed that the monodispersed AuNPs had a normal distribution, with a mean diameter of 9.7 ± 0.1 nm. The XRD

spectra acquired on the thin AuNPs film, depicted in **Figure 3.3f,** exhibited diffraction peaks at 2θ diffraction angles of ~ 38.3^0, 44.4^0, 64.8^0 and 77.8^0, which were indexed to the (1 1 1), (2 0 0), (2 2 0) and (3 1 1) planes corresponding to face-centred cubic (fcc) Au (ICCD: 04-003.5615). A very strong intensity peak for Au (1 1 1) plane was observed at 2θ ~ 38.3^0, while weak intensity peaks were observed for Au (2 0 0) and Au (2 2 0) planes, which corresponds to the formation of pure crystalline AuNPs in agreement with that elemental Au. The mean crystallites size of the AuNPs calculated using Scherrer's equation applied to the Au (1 1 1) peak at 38.3^0 was found to be ~10.7 nm, which is in good agreement with the particles size distribution obtained from the SEM image of monodispersed AuNPs. This finding further confirmed that the size of the nanoparticles deposited by AGD does not change as a function of coverage, and even in the limit of a dense film the MNPs size is maintained.

3.2.2. PtNPs Fabrication

The deposition conditions determined for the synthesis of dispersed AuNPs were next applied for the generation and deposition of platinum nanoparticles (PtNPs) from their pure metal precursor. However, a higher induction heating power was needed for the generation of PtNPs because of the considerable higher melting point of Pt (1768 ºC) as compared with Au (1064 ^{0}C). Because of the different chemical and physical characteristics of the two metals, including saturated vapour pressure and melting temperature, a quasi-continuous thin film of PtNPs was formed (**Figure 3.4a**). The shape and particles size depend on the heating temperature, molecular weight, total pressure and flow rate of the inert gas [17]. Therefore, the size and distribution of the PtNPs deposited by AGD were different from those of the AuNPs employing the same experimental conditions, with the exception of the higher heating induction power. The

mean PtNPs size calculated from the histogram of the PtNPs shown in **Figure 3.4a** was found to be 3.0 ± 0.1 nm, while the narrow size distribution of the nanoparticles exhibited a statistical log-normal distribution (see **Figure 3.4b**), as it is commonly observed in the case of nanoparticles evaporated in an inert gas [17]. Because of the low diffusion rate of the Pt atoms into the He career gas, Pt particles nucleation and growth was rather limited, leading to the synthesis of ultrafine PtNPs of extremely small size. The X-ray diffractogram of the PtNPs thin film shown in **Figure 3.4a**, depicted in **Figure 3.4c,** indicated four peaks attributed to four different crystalline phases of Pt at 2θ ~ 39.8º, 46.2º, 67.4º and 81.2º, indexed as (1 1 1), (2 0 0), (2 2 0) and (3 1 1) planes, respectively (ICCD: 04-001-0112). The spectra exhibiting a strong diffraction peak at ~ 39.8º depicted the deposition of pure crystalline PtNPs with a preferred growth orientation of Pt (1 1 1). The broadening and weak intensities of the other three diffraction peaks suggested relatively small surface density and particles size. Applying Scherrer's formula to the (1 1 1) peak, the mean crystallites size was calculated as ~3 nm, which is in excellent agreement with the mean Pt particles size estimated from the SEM analysis.

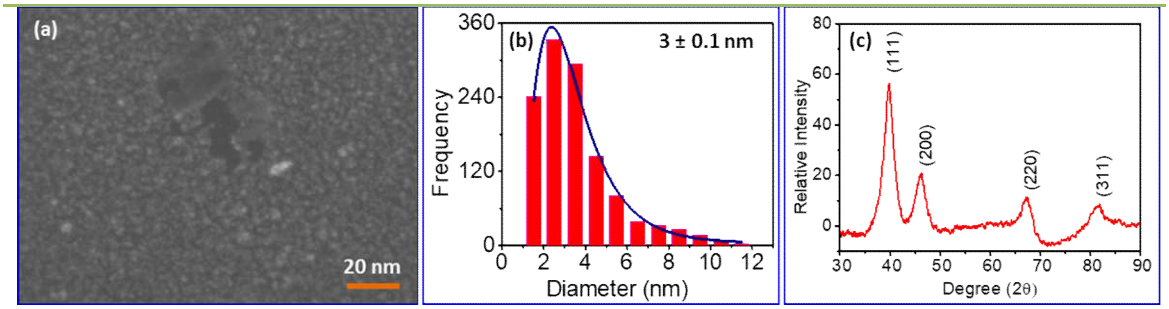

Figure 3.4. (a) SEM image of the PtNPs deposited by AGD using the following processing parameters: 90.8 mbar pressure in the evaporation chamber; 1 mm/sec speed of the movable support; 1 deposition cycle. (b) Histogram of PtNPs size distribution calculated from **Figure 3.4a**. (c) XRD spectra acquired on the PtNPs thin film shown in **Figure 3.4a**.

3.2.3. CuNPs Fabrication

Finally, the same experimental conditions were employed for the generation and deposition of CuNPs. As copper has a melting point (1085 ^{0}C) close to the gold (1064 ^{0}C), similar characteristics were expected for the CuNPs, comparable with those of the AuNPs. However, the vapor region formed above the melted Cu precursor contained a very low concentration of Cu atoms in the He carrier gas where particles nucleation and growth took place. For this reason, barely few nanoparticles were deposited on the substrate. In order to enhance particles nucleation, the pressure in the evaporation chamber was increased to 94 mbar. **Figure 3.5a** shows the SEM image of the thin film formed on the substrate when the pressure in the evaporation chamber was set to 94 mbar. This figure revealed the deposition of a continuous layer of ultrafine particles of extremely small grain size. The CuNPs, moreover, showed to be partly oxidized under the low vacuum conditions employed in AGD, and a thin oxide protective layer was inferred from XRD and FTIR studies. This is not surprising considering that Cu is known to be highly susceptible to oxidation [18]. The histogram of particles size distribution indicated a mean particles size of 2 ± 0.05 nm, with narrow size and statistical log-normal distribution (**Figure 3.5b**), similar to the case of PtNPs. The structure and surface analysis of the thin film shown in **Figure 3.5a** was next characterised by XRD. The diffraction peaks acquired, shown in **Figure 3.5c**, confirmed the formation of both metallic CuNPs and cuprous oxide (Cu_2O). The diffractogram of the film analyzed inferred six diffraction patterns, with 2θ diffraction angles at ~ 29.9º, 36.9º, 43.3º, 50.4º, 62.2º and 74.1º, indexed with the Cu_2O (1 1 0), Cu_2O (1 1 1), Cu (1 1 1), Cu (2 0 0), Cu_2O (2 0 0) and Cu_2O (3 1 1) planes characteristic for metal copper and its Cu_2O oxide, respectively (ICDD:04-006-5764; ICCD:04-004-7864) [19,20]. The strong diffraction peaks observed at 2θ ~ 36.9º and 43.3º exhibited characteristic peaks

corresponding to cuprous oxide and metallic Cu in their (1 1 1) preferred crystallite phase orientation. The weak intensity peak at 74.1° where Cu (2 2 0) and Cu_2O (3 1 1) crystal planes overlapped, confirming the coexistence of both metallic CuNPs and cuprous oxide.

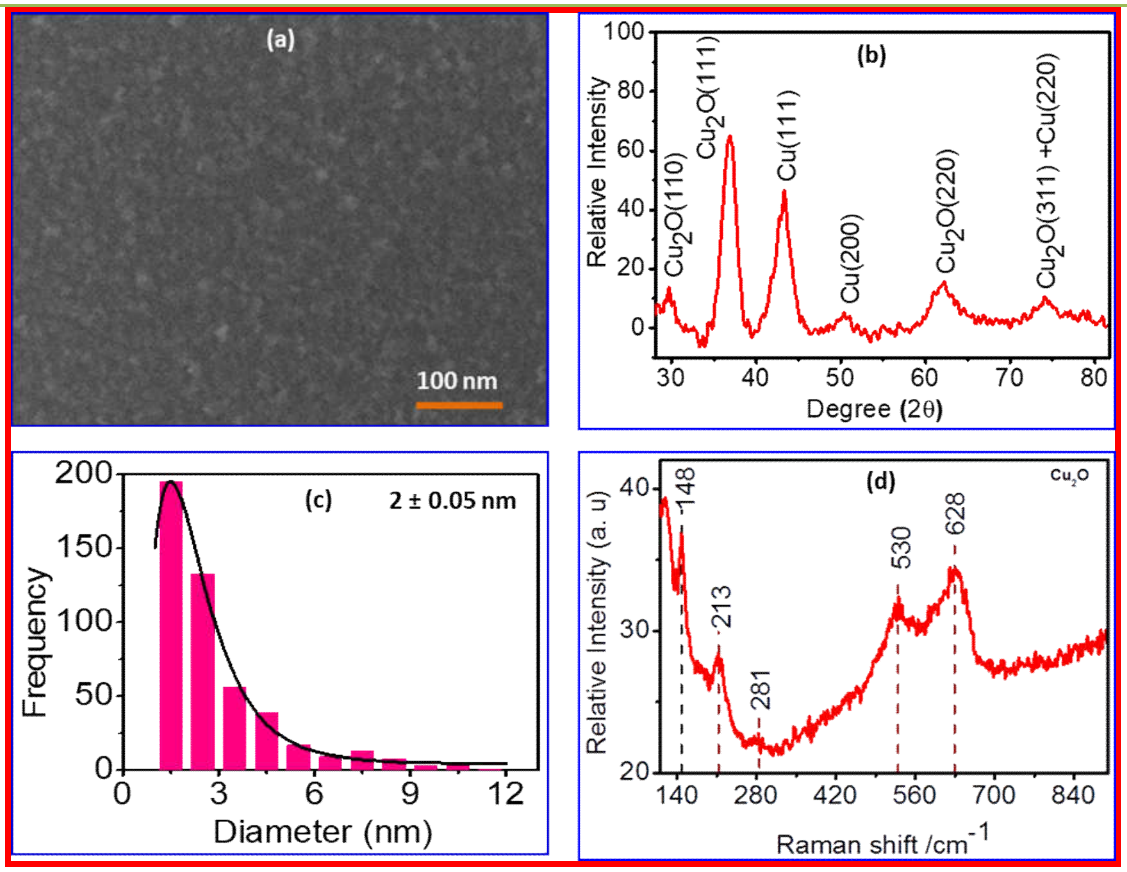

Figure 3.5: (a) SEM image of CuNPs deposited by AGD using the following processing parameters: 94 mbar pressure of the evaporation chamber, 1 mm/sec speed of the movable support, 1 deposition cycle. (b) Histogram of Cu nanoparticles size distribution calculated from Figure 3.5a. (c) XRD spectra acquired on CuNPs thin film shown in Figure 3.5d. Raman spectra of the CuNPs film showing traces of Cu_2O layer.

In general, the XRD analysis revealed the generation and deposition of ultrafine single crystalline metallic CuNPs and Cu_2O nanoparticles. No characteristic peaks of cupric oxide (CuO) were observed in the XRD pattern, indicating the formation of an ultrapure nanocrystalline thin film. The mean crystallites size of the nanoparticles, calculated

using Scherrer's formula applied to the (2θ) peaks at ~ 36.9º and 43.3º, were found to be ~4 nm and ~4.5 nm for CuNPs and Cu_2O, respectively. The difference between crystallites size calculated by applying Scherrer's formula and the mean particles size estimated from the SEM histogram presented in **Figure 3.5b** came from the level of SEM resolution.

Raman spectroscopy studies ascertained the formation of cuprous oxide layer at the surface of the metallic copper nanoparticles.

The corresponding Raman spectra shown in **Figure 3.5d** revealed a composite Cu_2O/CuNPs film exhibiting characteristic Cu Raman peaks at 148 cm^{-1} and 213 cm^{-1}, and peaks at 530 cm^{-1} and 628 cm^{-1} that were assigned to the Cu_2O phase [21]. No Raman bands were recorded above 800 cm^{-1}, which further indicates that no other oxides were formed.

3.3. Surface Functionalization of the as-Deposited MNPs

In the next experimental step, the metal nanoparticles as-deposited by AGD were functionalized with a broad range of organic ligands with different carbon chains (C3 to C18), tail structures and head groups (either thiol or amine), for promoting the formation of MNPs-organic nanoassemblies through the nanoparticles-ligand interaction [22]. The selected molecular ligands comprized either a long hydrocarbon chain or an aromatic ring in their tail, which enables the interaction between neighbouring tails, while the thiol or amine head groups provide binding affinity with the MNPs surface [23]. The ligands were selected such as to cover a wide range of possible tail functional groups, head groups and chain lengths, for assessing the ability of the MNPs fabricated by AGD to build strong and stable self-assembled MNPs-

organic ligand nanoassemblies. The following four groups of organic ligand were totally employed:

I. Ligands with non-polar hydrocarbon chain in their tail and a thiol head group: **(A)** 2-butanethiol (2-BUT), **(B)** 1-decanethiol (1-DT), **(C)** 1-dodecanethiol (1-DDT);
II. Ligands with non-polar aromatic ring in their tail and a thiol head group: **(D)** 4-methoxy-α-toluenethiol (4-MTT), **(E)** 2-mercaptobenzoxazole (2-MBZO);
III. Ligands with hydrocarbon chain and polar functionality in their tail and a thiol head group: **(F)** 11-mercaptoundecanol (11-MUD), **(G)** 11-mercaptoundecanoic acid (11-MUDA), **(H)** methyl-3-mercaptopropionate (MMPP);
IV. Ligand with long hydrophobic chain with non-polar tail and amine head group: **(I)** oleylamine (ODA).

The structures of the selected organic ligands are shown in **Figure 3.6**.

For MNPs functionalization, solutions were prepared as follows: 100 µL of 2-butanethiol, 1-deanethiol, 1-dodecanethiol, oleylamine, 4-methoxy-α-toluenethiol and methyl-3-mercaptopropionate (liquid in their normal sate) were dissolved in 20 mL ethanol; 10 mg of 11-mercaptoundecanoic acid and 75 mg of 2-mercaptobenzoxazole (solid in their normal state) were dissolved in 20 mL of ethanol; and 5 mg of 11 mercapto-1-undecanol (solid in its normal state) was dissolved in 5 mL of chloroform. The solutions were stirred with a magnetic stirrer for 30 min at room temperature to ensure homogeneity.

The dip coating method was then employed for the functionalization of the as-deposited metal nanoparticles with the organic ligands.

The substrates with the metal nanoparticles deposited by AGD were dipped into the solution of each ligand for one hour, and then the substrates were dried in an oven for

one hour at 50 ^{0}C with a ramp of 10 ^{0}C/min to ensure solvent evaporation. This process was repeated in some cases several times until a self-assembled MNPs-organic ligand monolayer was formed. In the case of AuNPs, the functionalization was performed on the monodispersed AuNPs structure shown in **Figure 3.3a**, while in the case of PtNPs and CuNPs, ligand bonding was done on the structures shown in **Figure 3.4a** and **Figure 3.5a**, respectively.

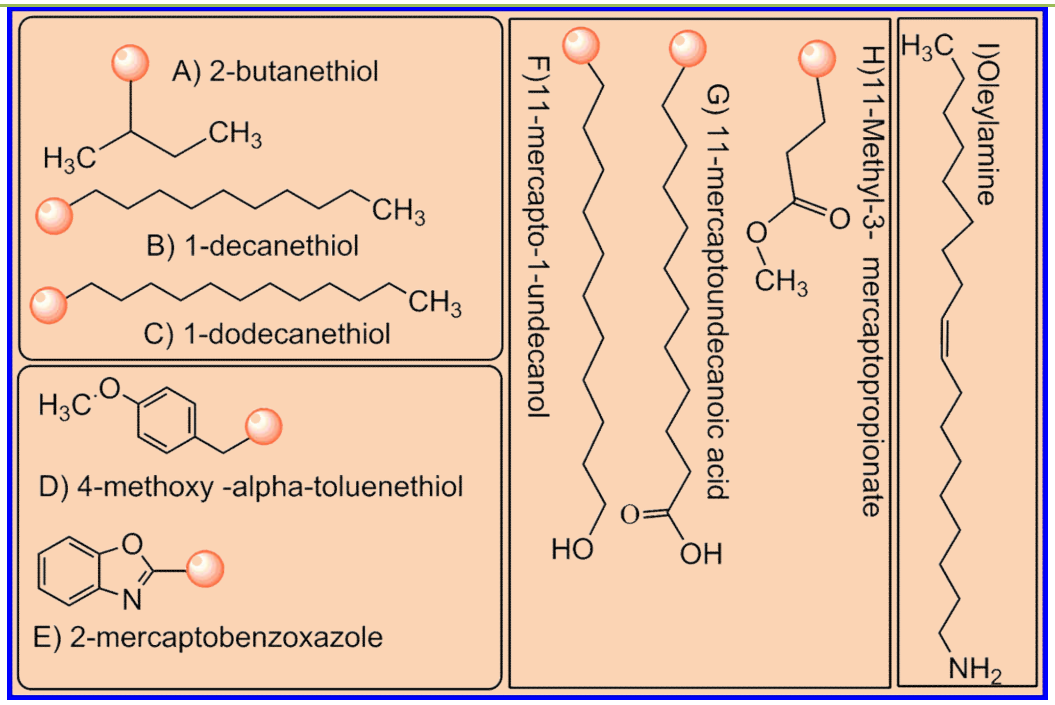

Figure 3.6: Molecular structure of the organic ligands used for MNPs functionalization.

The ligands bounded through the thiol or amine head groups to the free regions of the MNPs not attached to the substrate, available for molecules attachment. The capping ligands under study had distinct characteristics, which produced different nanoassemblies structures and different surface coverage for each ligand, which are summarized in **Table 3.2**.

The morphology of the nanoassemblies characterised by SEM is presented in **Figure 3.7** for some of the organic ligands.

In the case of AuNPs functionalization, all ligands were able to bind the surface of the AuNPs, producing self-assembled monolayer nanoassemblies after a single or several dipping processes into the ligand solution. It is assumed that the monodispersed AuNPs provided surface interactions for the ligands through their head group, while the tail-tail interactions of neighbouring ligands completed the network.

Organic ligand	AuNPs	PtNPs	CuNPs
2-BUT	Clusters network, low coverage (24%)	No ligand capping	No ligand capping
1-DT	Linked nanoparticles network, low coverage (26%)	No ligand capping	Well ordered, medium coverage (60%)
1-DDT	Well ordered, low coverage (34%)	Medium coverage (56%)	Clusters network, low coverage (37%)
4-MTT	High coverage (86%)	Medium coverage (58%)	Medium coverage (55%)
2-MBZO	Short-linked clusters network, high coverage (84%)	Isolated clusters, low coverage (29%)	Well ordered, medium coverage (51%)
11-MUD	Low coverage (18%)	No ligand capping	Low coverage (16%)
11-MUDA	Low coverage (24%)	High coverage (71%)	Medium coverage (66%)
MMPP	Low coverage (20%)	Medium coverage (53%)	No ligand capping
ODA	Low coverage (25%)	Isolated clusters, low coverage (42%)	Low coverage (26%)

Table 3.2. MNPs-ligand nanoassemblies characteristics. Low coverage refers to surface coverage below 50%; medium coverage to surface coverage between 50% and 70%; and high coverage to surface coverage over 70%.

The self-assembly of the alkanethiols was driven by the strong affinity between the sulphur and the gold, with Van der Waals interactions between the alkyl (aromatic) chains, and dipole interactions between the polar end groups.

Figure 3.7a displays a well-ordered self-assembled monolayer of 1-dodecanethiol linking the AuNPs, which fairly covered the surface of the base substrate, while figure **Figure 3.7b** depicts a denser monolayer of 4-methoxy-α-toluenethiol chemisorbed onto AuNPs surfaces. These two ligands most likely exhibited strong attachment on AuNPs surfaces and achieved tail to tail hydrogen bonding with the neighbouring attached

ligands. **Figure 3.7c** also demonstrates a high density self-assembled monolayer for 2-mercaptobenzoxazole bonded on AuNPs surfaces. The ligands 4-MTT and 2-MBZO consisted of polar aromatic ring structures in their tail, and multiple H-bonding might have been developed between neighboring molecules leading to well-ordered self-assembled monolayer nanoassemblies (**Figure 3.7**(**b-c**)).

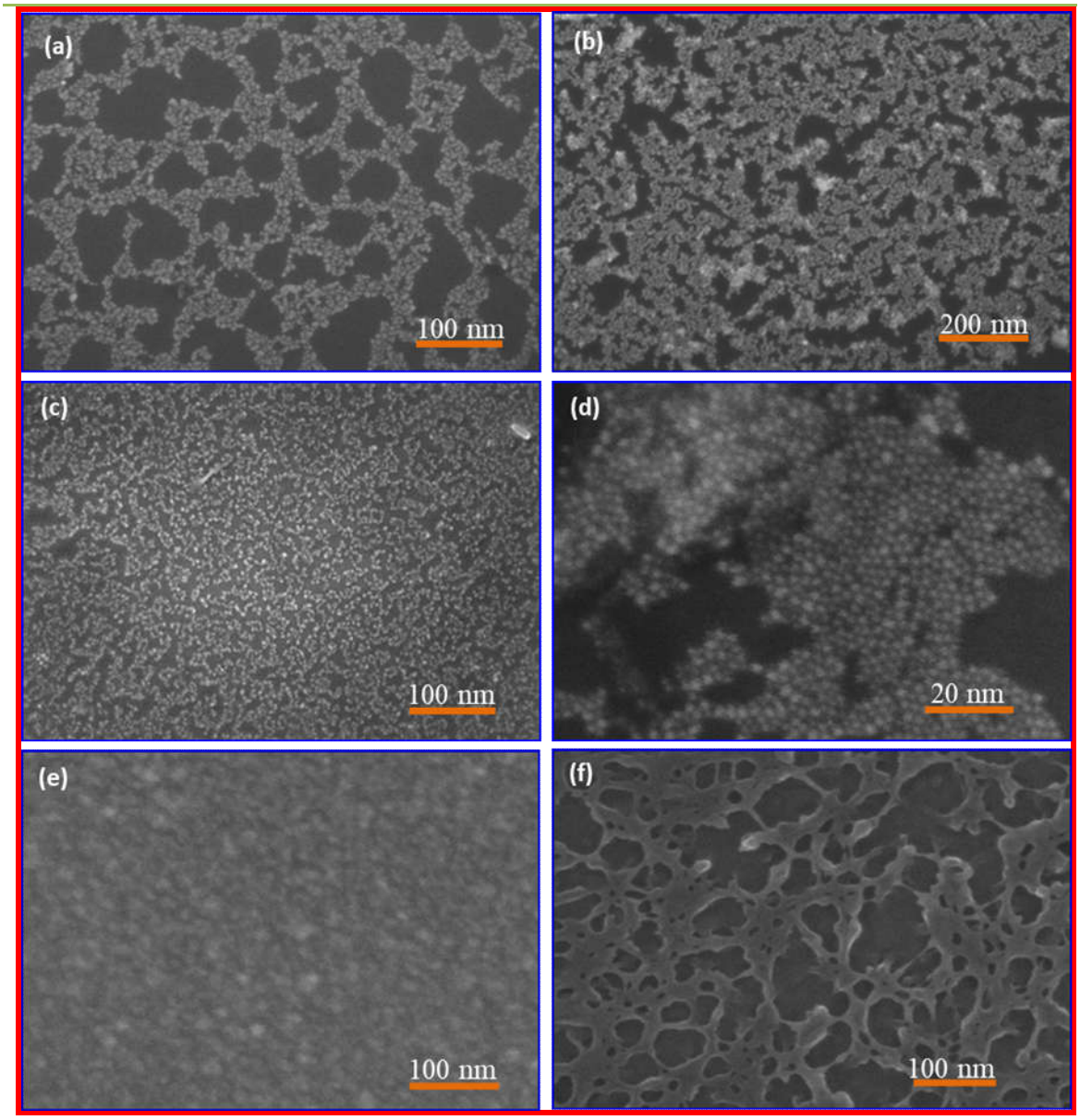

Figure 3.7: SEM images of self-assembled: (a) AuNPs capped with 1-DDT; (b) AuNPs capped with 4-MTT; (c) AuNPs capped with 2-MBZO; (d) AuNPs capped with 1-DT; (e) PtNPs capped with 1-BUT; (f) CuNPs capped with 2-MBZO.

Figure 3.7d shows the formation of a less-ordered monolayer with low surface coverage when the AuNPs were capped with 1-decanethiol, probably due to the steric stability of the AuNPs that drastically reduced the surface charge interactions towards the thiol, avoiding strong covalent bonding. In the case of PtNPs functionalization, some organic ligands (MMPP, 11-MUDA, 4-MTT, and 1-DDT) could form quite dense and rather homogenous monolayers of PtNPs-organic nanoassemblies, probably due to the extremely small crystallites size of PtNPs (3 nm mean diameter, in comparison with 10.7 nm for AuNPs), which influenced their interaction with the organic ligands. For the first three ligands, this might be explained as these molecular organic ligands contain either polar or aromatic tail and a thiol head group that was chemisorbed on the surface of the PtNPs, promoting stable NPs-ligand nanoassemblies with strong tail-tail electrostatic interactions and hydrogen-bonding. The adsorption of the non-polar 1-DDT on the surface of ultrafine PtNPs might be due to the compromize between the hydrocarbon chain length, suitable for the formation of a self-assembled monolayer, and the strong Pt-S interactions, leading to substantially stable NPs-ligand nanoassemblies. The organic ligands with hydrophobic and non-polar tail that did not form stable NPs-ligand nanoassemblies had shorter carbon chains that might have accommodated head-tail steric effects on the surface of the NPs (see **Figure 3.7e** as a representative example for this case). Although presenting a similar structure with 11-MUDA, the less polar 11-MUD organic ligand has neither achieved suitable PtNPs linking.

For CuNPs functionalization, all molecular ligands except 2-BUT led to the formation of NPs-organic nanoassemblies. The morphology of the CuNPs-organic nanoassemblies revealed the formation of a flatted ligand-nanoparticles layer (**Figure 3.7f**). It is likely that the presence of the protective thin oxide layer on the nanoparticles surface enhanced the surface attachment of the ligands

through Cu_2O-S, Cu-O=C and COO-Cu bonding in addition to the expected Cu-S attachment. In this case, the ligands might have multiple interactions through a strong H-bonding with the surface coating oxide and the NPs. In the case of 2-BUT, the failure of adequate ligand capping could be explained as the smaller C-C chain length of this ligand was not suitable to maintain tail-to-tail networking able to form ligand-NPs nanoassemblies.

Notably, the CuNPs and PtNPs exhibited very different assembly patterns although their particle sizes were quite similar each other, which is attributed to the susceptibility to oxidation of the CuNPs surface expozed to environmental air, leading to composite Cu_2O/CuNPs films (see **Figure 3.5**).

The surface coverage of each nanoassembly was calculated considering the area covered by the MNPs and by the ligands networking the nanoparticles. For this end it was applied image analysis in Matlab, and the percentage of surface coverage was calculated as the fraction of the pixels covered by the nanoassmbly from the total number of pixels of the image. As a representative example, **Figure 3.8** shows the AuNPs-1-DDT nanoassembly and the corresponding image mapping in Matlab that was used to calculate the surface coverage. For this nanoassembly the calculated surface coverage was 34%.

XPS studies were also performed to further investigate the elemental composition of the nanoassemblies surfaces. The elemental surface composition of the MNPs before and after functionalization with different organic ligands is presented in **Figure 3.9**.

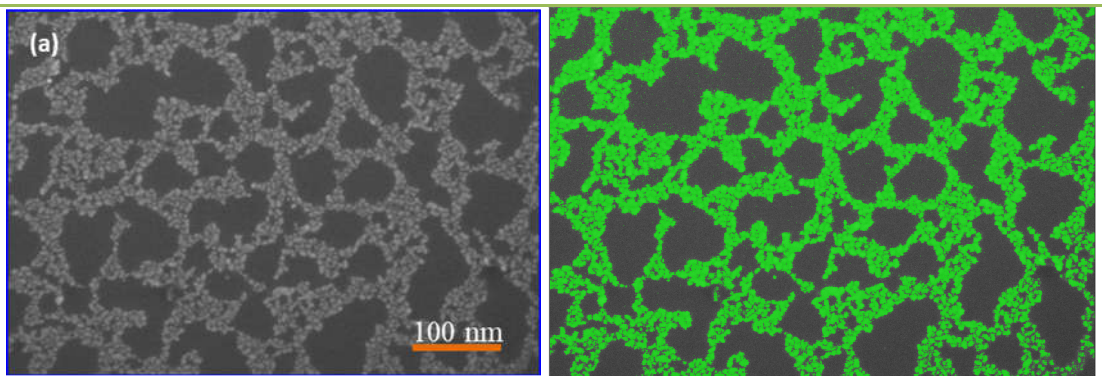

Figure 3.8: (a) SEM image of the AuNPs-1-DDT nanoassembly; (b) Image mapping of the SEM image from **Figure 3.7a**, used for image analysis in Matlab.

PtNPs samples composition is not shown in **Figure 3.9** because the PtNPs were too small and the XPS elemental composition was mostly dominated by photoelectrons coming from the substrate atoms corresponding to Si and O.

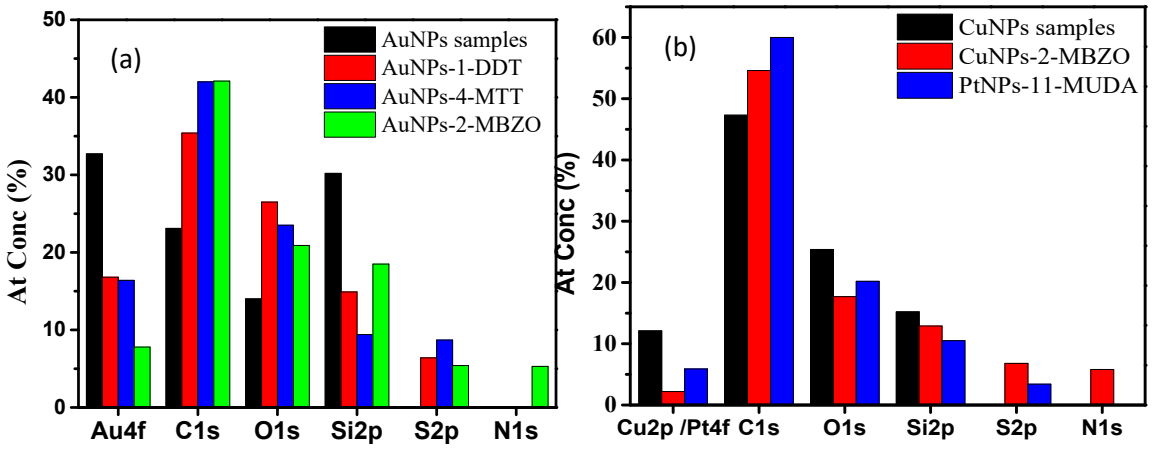

Figure 3.9: Surface elemental composition calculated from the XPS spectra for: (a) AuNPs and various AuNPs-ligand nanoassemblies; (b) CuNPs, and both CuNPs-ligand and PtNPs-ligand nanoassemblies.

As representative examples of AuNPs-ligand nanoassemblies, **Figure 3.10a** shows the XPS spectra of the AuNPs capped with three organic ligands (1-DDT, 4-MTT and 2-MBZO). The XPS spectra of these films are consistent with the successful functionalization of the AuNPs with the organic ligands, as manifested

by the signal intensity of each core level region in each sample. Due to samples exposure to air, the XPS spectra revealed detectable oxygen in all MNPs-ligand nanoassemblies in addition to oxygen coming from the SiO_2/Si base substrate.

The elemental surface characterization of the nanoassembly formed by the PtNPs capped with 11-MUDA is shown in **Figure 3.10b** as a representative example of the self-assembled PtNPs-organic monolayers. The XPS spectra of this nanoassembly exhibited the presence of core-level spectra of Pt4f, C1s, S2p and O1s, which originated from the PtNPs and the corresponding adsorbed ligand, respectively. The XPS signal for Si2p is associated with the uncovered SiO_2/Si substrate where the nanoparticles were deposited and functionalized.

The elemental surface analysis of the CuNPs-organic nanoassemblies revealed that, in general, the sulphur S2p signal was very weak due to inelastic scattering of S2p electrons by the molecules in the monolayer, and in some cases the metal-S covalent bonding resulted in partial oxidation at the metal-S interfaces mediated by the metal nanoparticles. The ultrafine CuNPs, however, exhibited high surface density atoms that enhanced the surface attachment of the organic ligands. XPS spectra of different CuNPs-organic nanoassemblies are presented in **Figure 3.10c**, for 11-MUDA, ODA and 2-MBZO capping. The acquired spectra illustrated that the surface density of the CuNPs-2-MBZO nanoassembly was much higher as compared with the CuNPs functionalized with 11-MUDA and ODA. This might be related to the surface charge density of the aromatic ring that electrostatically stabilized the small size CuNPs. Besides, the XPS surface analysis of the CuNPs-ODA and CuNPs-11-MUDA nanoassemblies presented very low percentages of CuNPs, which was beyond the sensitivity of the device that was unable to recognize the surface electrons originated from the CuNPs.

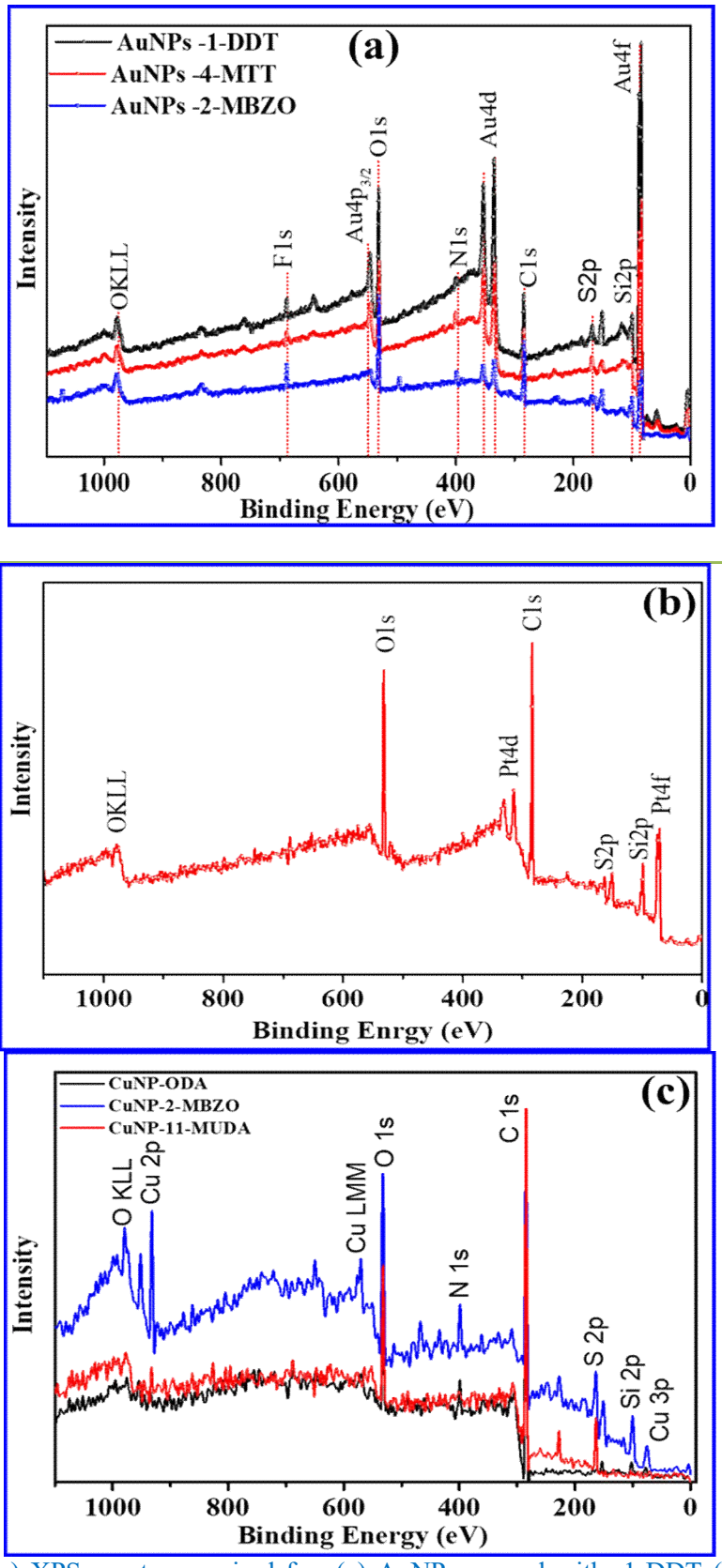

Figure 3.10: (a) XPS spectra acquired for: (a) AuNPs capped with: 1-DDT (black); 4-MTT (red); 2-MBZO (blue); (b) PtNPs capped with 11-MUDA; (c) CuNPs capped with: oleylamine (ODA) (black), 2-mercaptobenzoxazole (2-MBZO) (blue), and 11-mercaptoundecanoic acid (11-MUDA) (red).

Deeper XPS investigations focussed on the elemental scans of the nanoassemblies surfaces are shown in **Annex I**.

3.4. Fabrication and Characterization of Ligand-Capped MNPs Chemical Gas Sensors

3.4.1. Sensors Design and Fabrication

Gas sensing devices were fabricated on a 2-inch, *p*-type, 10-20 Ω, <100> oriented, 275 µm thick, single-side polished silicon wafer. A 200 nm thick SiO_2 layer was first grown on top of the silicon wafer by dry thermal oxidation at 1100 ºC. Two parallel 15-µm gapped gold electrodes were then patterned using thin positive photoresist and laser lithography. A 200 nm thick gold film and 15 nm thick titanium (Ti) was sputtered on the SiO_2 surface, and a lift-off process with acetone was finally employed for removing the Au/Ti outside the electrodes area. **Figure 3.11** illustrates the standard microfabrication process and the sensing substrates and the sensing devices.

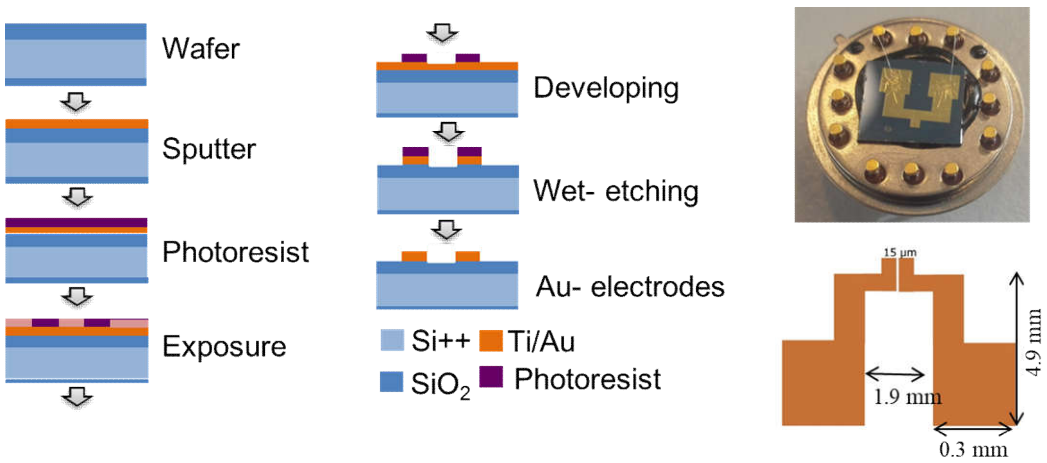

Figure 3.11: Sensors substrates microprocessing (left and middle), sensing devices (right)

3.4.2. Electrical Characterzation

The electrical resistance of the MNPs films deposited between the two 15 μm gapped sensors parallel gold electrodes was characterized after MNPs deposition, and after MNPs functionalization with the different organic ligands.

No electrical current could be measured between the electrodes after the deposition of monodispersed MPNs by AGD, which confirmed that the MNPs were not linked with each other. After MNPs functionalization, the self-assembled nanostructures generally formed uninterrupted core-shell nanoparticle-ligand networks that promoted an electric path between the electrodes. **Figure 3.12** shows the electrical resistance measured for all the nanoassemblies produced in this study; however, it is important to point out that the electrical properties of these nanoassemblies can be tuned by adjusting the fabrication parameters.

As depicted in **Figure 3.12**, all capping ligands produced a continuous network of the self-assembled monolayer with the AuNPs (~10.7 nm mean diameter). Despite the smaller crystallites size of CuNPs (~4 nm mean diameter), most CuNPs-organic nanoassemblies exhibited an electrical resistances between the electrodes, while the nanoassemblies of monolayer-capped PtNPs (~3 nm mean diameter) were able to promote electronic conduction only for few organic ligands: MMPP, 11-MUDA, 4-MTT and 1-DDT. The electrical resistance of these films was lower, confirming the medium-high surface coverage presented in **Table 3.2**. The robustness of the developed nanoassemblies was evidenced by the small drift produced in the electrical resistance during one year period (below 12% for all nanomaterials).

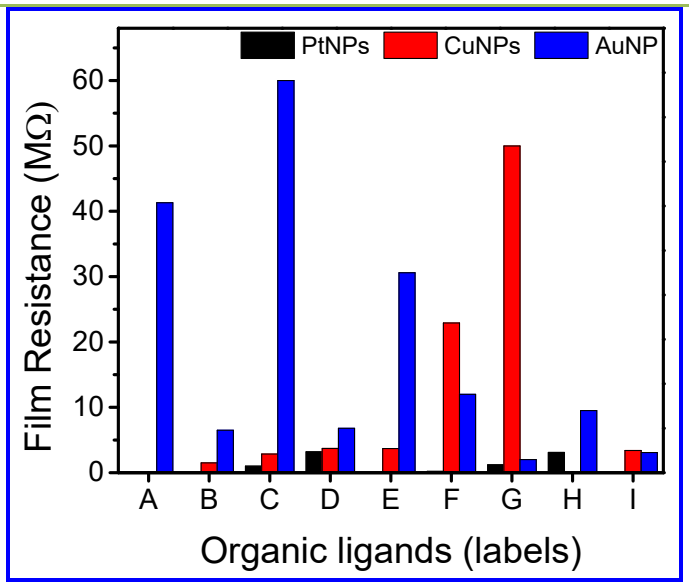

Figure 3.12: Electrical resistance of all the MNPs-ligand nanoassemblies produced.

In these MNPs-ligand nanoassemblies, the MNPs are assembled via organic molecules that act as interparticles mediators, and the conduction through these nanostructures is provided by the electron tunnelling mechanism throughout the nanoparticles-ligand network. The MNPs provide the electronic charge, and electrons transport occurs by electrons jumping between neighboring nanoparticles through the organic matrix [24,25]. Even in the case of the long organic ligand that has no conjugation (*i.e.*, 11-MUDA), the carboxylic group from its tail could induce a chemical interaction with the tail of the neighboring organic molecule, which linked the MNPs and as a result an active percolation path was developed through the nanoassembly [26].

The further electrical characterization of the MNPs-ligand nanoassemblies revealed that the monolayer-capped AuNPs and the monolayer-capped PtNPs showed a Schottky diode behavior, where the electron transport through the sensing film is determined by the nano-assembly's distribution of conducting paths, and the electrical conductivity depends on the actual current injection site that determines the positive and negative electrode, as indicated by the asymmetry of the *I–V* characteristic (**Figure 3.13(a-b)**).

On the other hand, the monolayer-capped CuNPs showed a resistor behaviour that is attributed to the formation of the thin Cu_2O passivation layer on the nanoparticles surface (**Figure 3.13c**).

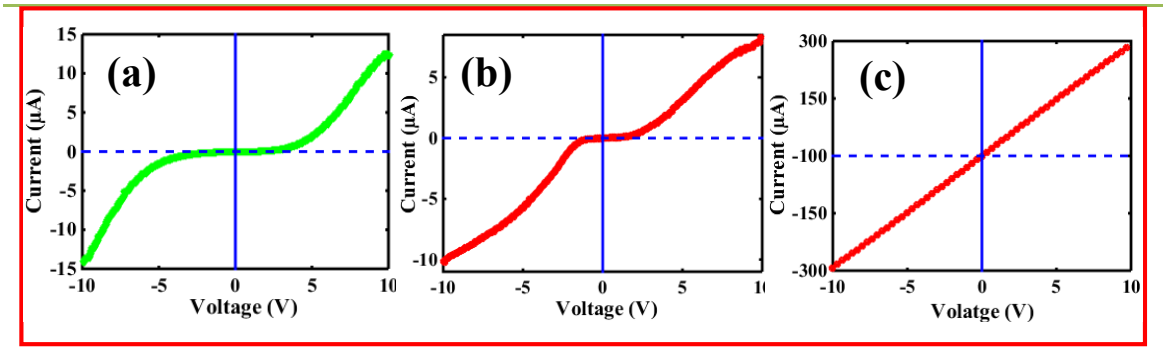

Figure 3.13: *I-V* characteristic curves of: (a) AuNPs capped with 2-MBZO; (b) PtNPs capped with 4-MTT; (c) CuNPs capped with 2-MBZO.

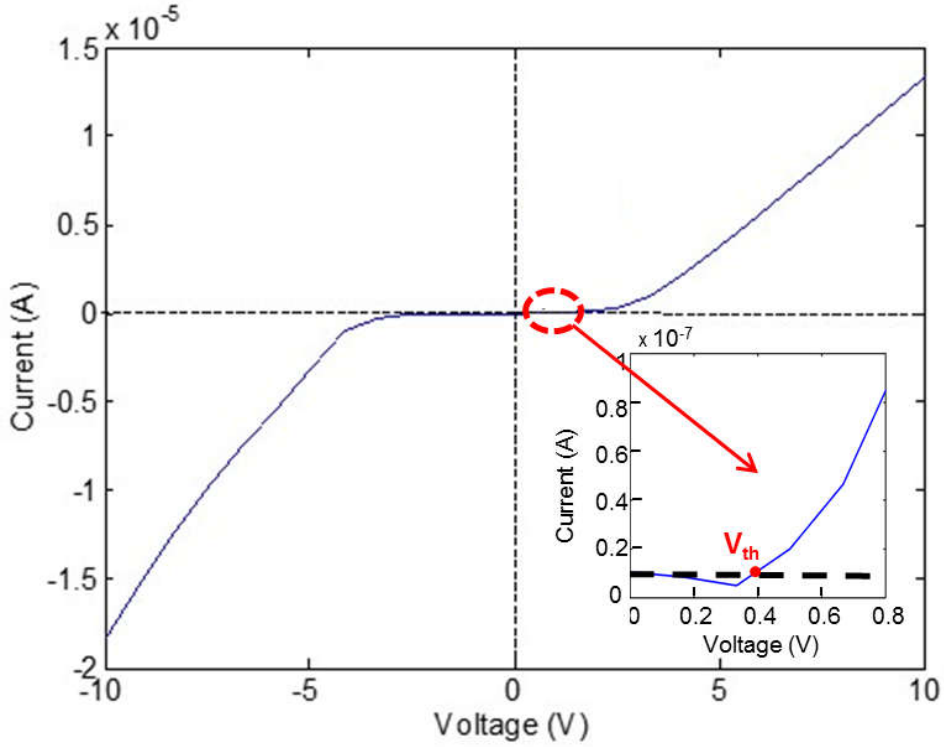

Figure 3.14: *I-V* characteristic of the dodecanethiol-capped AuNPs device. The zoom shows the value of the threshold voltage.

Deeper characterization was performed on the dodecanethiol-capped AuNPs diode, which revealed a conduction threshold voltage of ~0.4 V, which is in line with data for

typical metal-weakly doped semiconductor Schottky diodes (~0.3 V) [27] (**Figure 3.14**).

3.4.3. Gas Sensing Measurements

Gas sensing measurements were performed by exposing the dodecanethiol-capped AuNPs Schottky-diode sensing device, placed inside a Teflon test chamber of ~4 cm^3 volume, to acetaldehyde as target VOC (selected as representative breath biomarker identified for lung cancer in previous studies [28]), and ethanol and ethylbenzene as interfering species. The device was operated in direct polarization mode, and the current between the electrodes was monitored while the applied voltage was successively swept forward and backward between 0 V and +10 V. The sensing measurements were performed at room temperature (22.5±1 ºC) and comprized successive exposure cycles to synthetic dry air (40 min) and to different concentrations of VOCs (obtained from 100% purity bottles) diluted in synthetic dry air (20 min) at a constant flow rate of 200 mL/min. Humidity effect was investigated by introducing water vapour to the measurement gas flow by means of a glass bubbler, such that to obtain at the output of the sensors chamber two different relative himidity (RH) levels (30 and 70%), covering a high RH range.

The sensor response was extracted from the *I–V* characteristic at each voltage (see in **Figure 3.15**, as representative example, sensor's response to 30 ppm acetaldehyde extracted at 3.33 V on the backward curve), and indicated good repeatability and recovery. Data were taken to assess the response to the gas at several voltages and to monitor the relative current change produced by sensor's exposure to acetaldehyde in comparison with the current in synthetic dry air according to Equation 1.

$$S^{(V)}(\%) = \frac{I_{VOC}^{(V)} - I_{air}^{(V)}}{I_{air}^{(V)}} \quad \text{.....(1)}$$

where $S^{(V)}$ is the sensor's response at the voltage V, $I_{VOC}^{(V)}$ is the current at voltage V in the presence of the VOC, and $I_{air}^{(V)}$ is the current at voltage V in synthetic dry air prior to VOC exposure. The mean value over three successive exposures to the VOC were used.

Figure 3.16 shows the response curve obtained from sensor's exposure to 30 ppm of acetaldehyde. The diode sensing device was operated in the positive polarization mode, with the metal (i.e., the AuNPs) at a higher potential than the organic material. By increasing the voltage, the potential barrier is decreased.

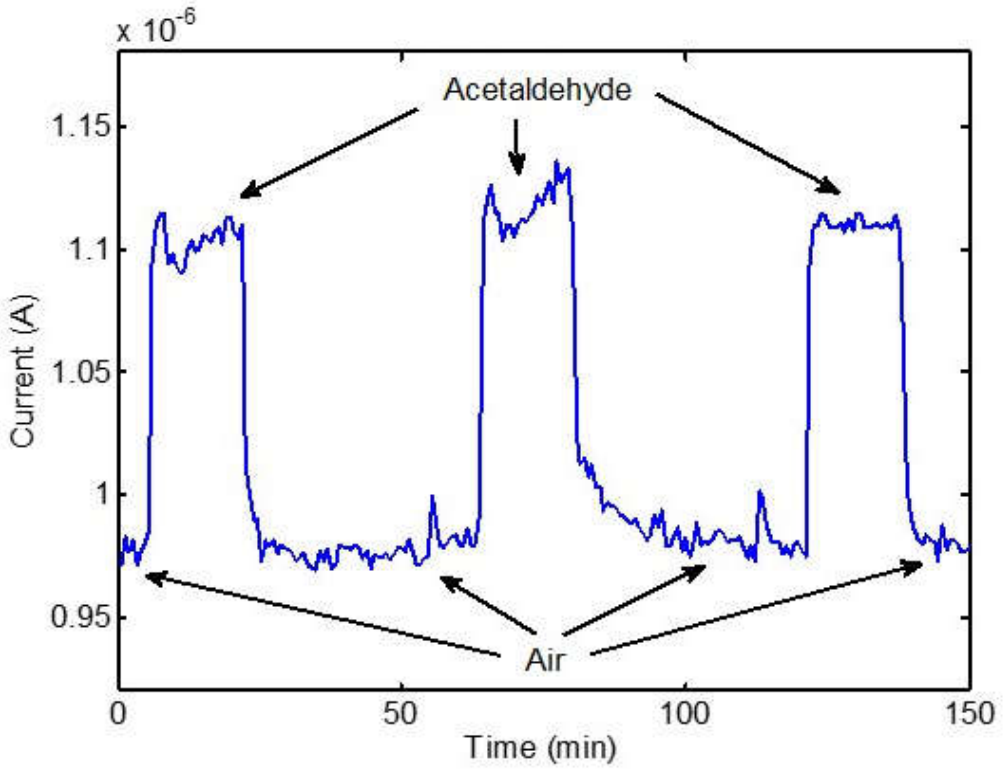

Figure 3.15: Sensor's response extracted from the *I-V* characteristic at 3.33 V on the backward curve.

As the voltage exceeds the conduction threshold voltage (0.4 V; see **Figure 3.14**), electrons from the organic material cross over to the AuNPs. When the dodecanethiol-capped AuNPs sensing material is exposed to acetaldehyde, there is charge exchange between the sensing material and acetaldehyde via steric interaction between the sensing film and the sensed analyte (i.e., film swelling due to analyte adsorption), which alters the charge carrier transport [29]. However, the passing over of the conduction threshold voltage does not produce an increase in the number of electrons that cross the potential barrier upon absorption of the VOC until the applied voltage reaches a sufficient value (3.33 V; see **Figure 3.16**). Favoured by the accumulation of electrons generated by the VOC adsorbed by the sensing film, there is a sudden enhancement of the electrons' carrier transport and the sensor's response reaches its maximum value. The response is then decreasing as the capacity of the adsorbed VOC to generate new electrons is limited by the total VOC concentration. When the voltage is swept backward, the observed phenomena are opposite, with the remark that the sensor's response reaches its maximum value at a lower voltage compared with the forward characteristic (2.5 V; see **Figure 3.16**), which is attributed to the hysteretic behaviour of the Schottky barrier height variation arising from the material's polarization reversal [30]. By further lowering the value of the voltage applied, the potential barrier height increases over the value at which the electrons from the organic material could cross over to the AuNPs, which produces the inhibition of electrons' carrier transport through the Schottky diode device and sensor's response becomes zero.

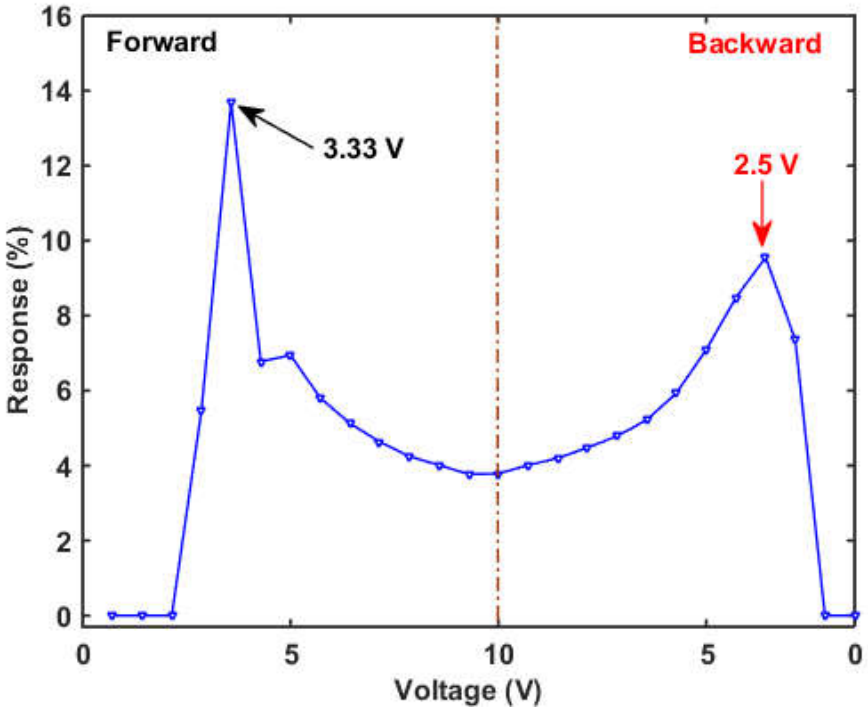

Figure 3.16: Response curve obtained from the dodecanethiol-capped AuNPs sensor exposed to 30 ppm of acetaldehyde.

These results allowed determining the voltage at which the maximum response point could be obtained (3.33 V on the forward curve), which was then used to asses sensor's behavior at a constant bias. Sensor's response to 30 ppm of acetaldehyde at a constant operation voltage of 3.33 V is shown in **Figure 3.17**. The response achieved in this case (13.3%) was quite similar with the response extracted at the same voltage on the forward curve when the sensor was operated as a Schottky diode (13.7%).

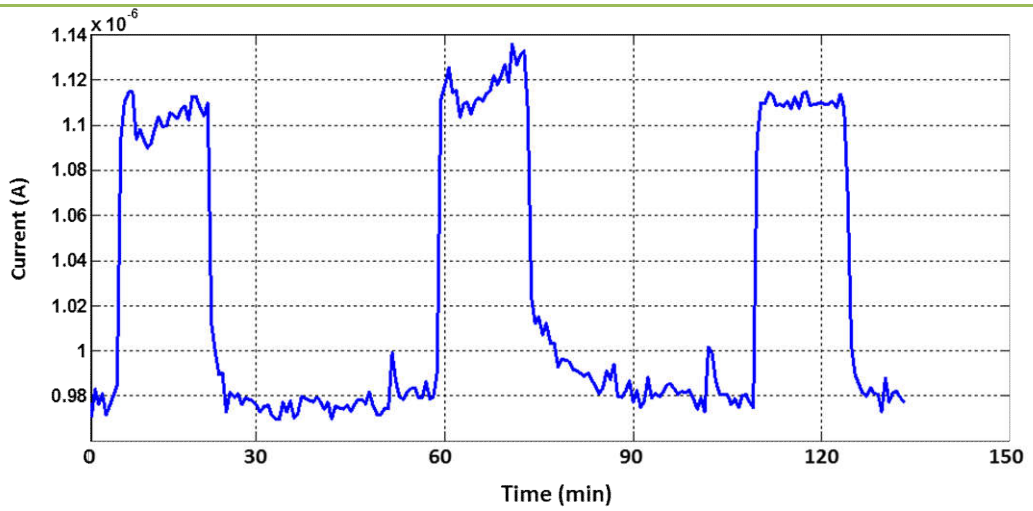

Figure 3.17: Sensor's response to 30 ppm of acetaldehyde at a constant operation voltage of 3.33

For calculating the limit of detection (LOD) for acetaldehyde exposure, the sensor was exposed to different concentrations of acetaldehyde in the concentrations range from 5 to 30 ppm. The calibration curve was plotted with the response values extracted at 3.33 V on the forward curve (see **Figure 3.18**). The LOD was calculated with the formula from equation (2), giving a value of LOD ≈ 2.5 ppm.

$$LOD = 3 \, x \, Sa/b \qquad (2),$$

where *Sa* is the standard deviation of the y-residuals and *b* the slope of the regression line of the calibration curve provided in **Figure 3.18**.

When the sensor was exposed to acetaldehyde under different humidified backgrounds, it was observed a decrease in its response under the low humidity level (30% RH), while under the high humidity level (70%) sensor's response dramatically increased (see **Figure 3.19**). This is similar to other findings, which reported that the response of sensors based on gold-thiolate monolayer-protected nanoparticles decreases with humidity increase in the low humidity range, when the film swelling governs sensor's

responses, while at high humidity the change in the dielectric properties governs the responses, which begin to reverse [31,32].

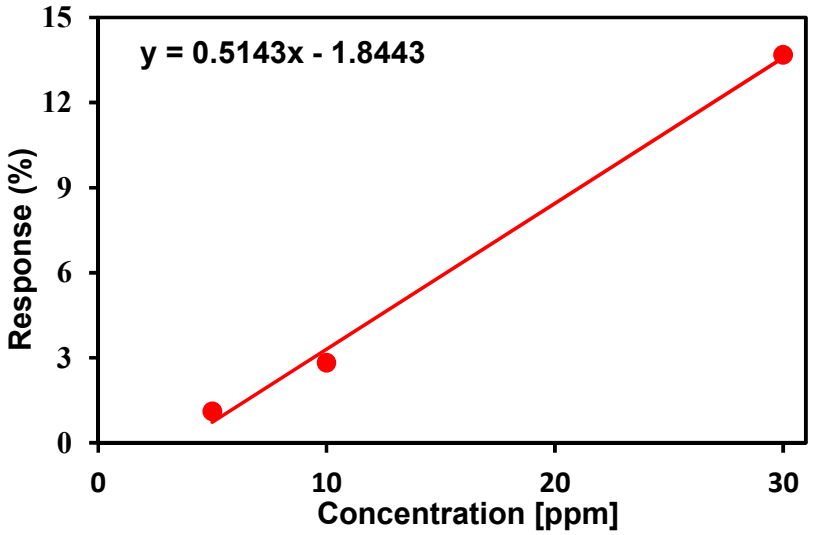

Figure 3.18: Calibration curve for acetaldehyde detection

Sensor's responses to two interfering species (ethanol and ethylbenzene) showed significantly different response patterns (see **Figure 3.19**), which indicates that the measurement technique and the novel method introduced in this study to analyze the response of a Schottky-diode chemical gas sensor offers novel features for fingerprinting VOCs detection.

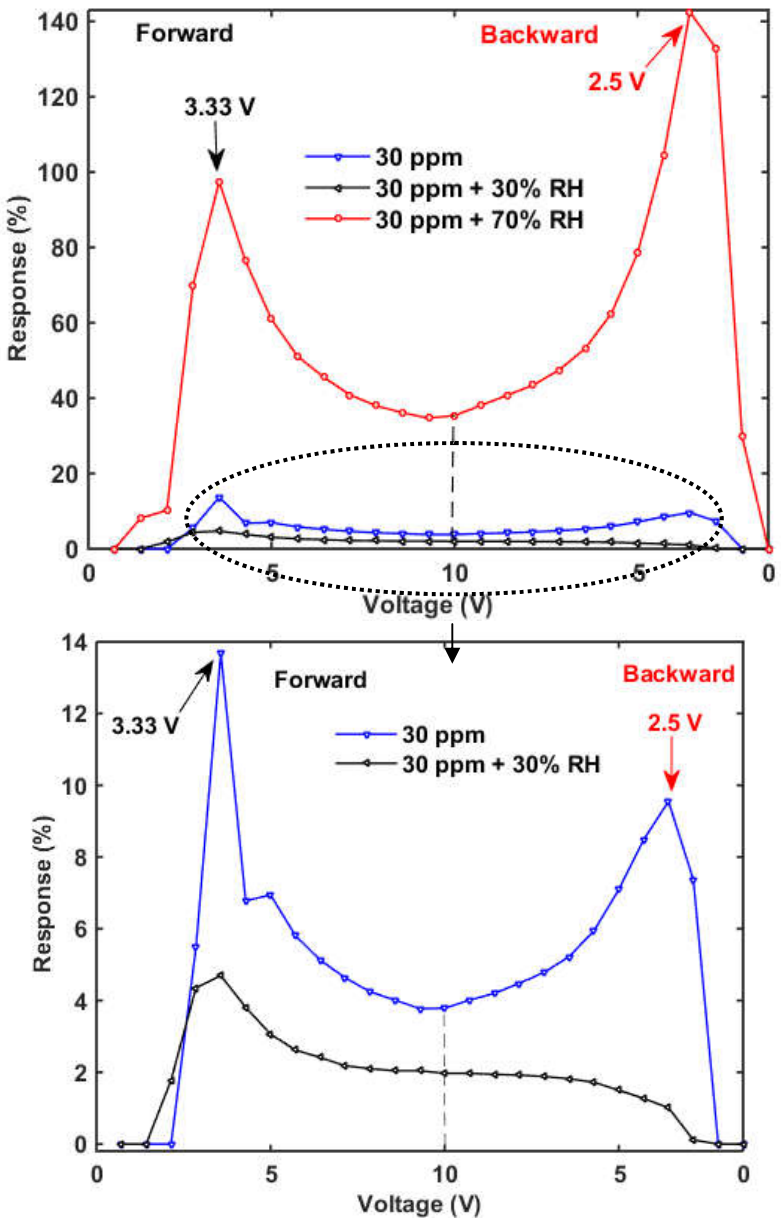

Figure 3.19: (up) Response curves to 30 ppm of acetaldehyde obtained under different RH levels; (down) Inset

Importantly, the sensor was studied over a three years period, keeping intact its operation capabilities throughout all this period, which suggests a good robustness and a long lifetime period.

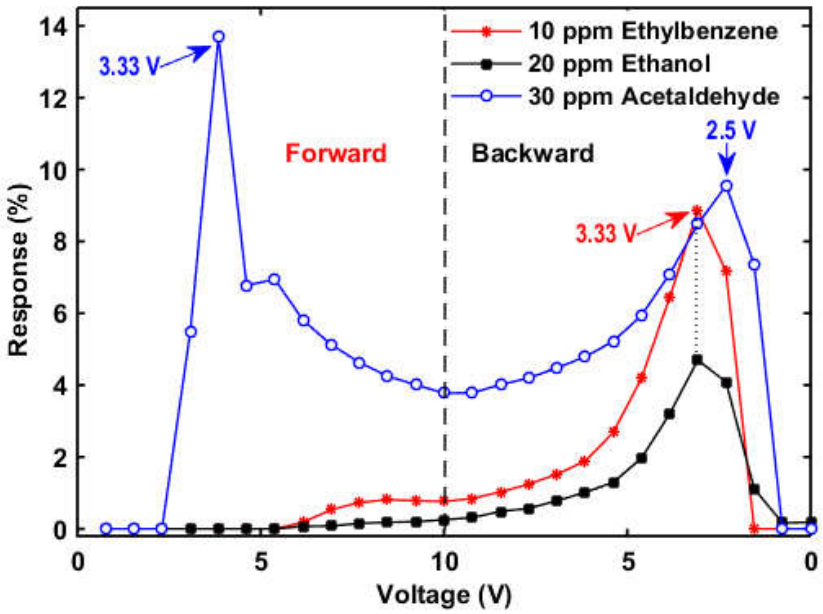

Figure 3.20: Response curve obtained from sensor's exposure to different VOCs.

3.5. Conclusion

Ultrapure monodispersed metal nanoparticles of various metals (Au, Pt and Cu) were fabricated in a single step process from their pure metal precursors by the Advanced Gas Deposition technique. By employing this method, the major problem associated with nanoparticles tendency to aggregate that occurs in the case of other physical deposition techniques was avoided by the direct evaporation of the pure metal and nanoparticles growth by condensation under a high purity inert gas. Although the thesis work was focussed on AuNPs, PtNPs and CuNPs synthesis only (mean crystallites sizes: ~ 10.7 nm, 3 nm and 4 nm, respectively), the technique can be easily extended to practically any MNPs synthesis using the proper metal source and adjusting the synthesis parameters.

A broad range of organic ligands with different carbon chains, tail structures and head groups, were then used to functionalize the MNPs by dip-coating the substrates in a

solution formed in high purity reagents, which led to the formation of self-assembled nanoparticles-organic monolayers with a network-like structure. The MNPs-ligand nanoassemblies presented hybrid characteristics, where the nanoparticles served for electrical conduction, while the capping organic molecule promoted electron tunnelling through the MNPs, which produced a measurable resistance in the range of tens of kΩ to tens of MΩ for most of the nanoassemblies.

These high-purity functional nanoassemblies could impart interesting chemical, physical and electrical properties, suitable for varios applications such as VOCs sensing. Importantly, the characteristic properties such as shape, size, and monodispesity of these nanoassemblies can be tuned by properly adjusting the fabrications parameters.

Chemical gas sensing devices based on these functional nanoassemblies showed Schottky-diode and chemiresistive behavior. This was the first observation of Schottky-diodes fabricated from nanomaterials based on metallic nanoparticles. Preliminary gas sensing experiments demonstrated that these devices were suitable for detection of volatile organic compounds.

An array of chemical gas sensing devices based on these nano-assemblies was next employed during my thesis for assessing the potential of tropical diseases diagnosis through exhaled breath analysis.

3.6. Experimental Methods

3.6.1. Materials Characterization

During the MNP fabrication and functionalization, the morphology and surface analysis studies were performed with a Zeiss LEO 1550 High Resolution Scanning Electron Microscope (HR-SEM), using a field emission gun as electron source, an acceleration

voltage of 10 kV and high magnification values (300,000-1,000,000), and 1 nm resolution. The structure and phase orientation of the metal nanoparticles were acquired by X-ray Diffraction (XRD) using a Siemens D5000 equipment operated with CuK_α radiation (λ=1.54 Å). Crystallites size was calculated from the X-ray diffractograms by applying Scherrer's formula:

$$D= K\lambda/\beta cos\theta,$$

where D is the volume-weighted average crystallite size, K is the Scherrer constant and takes into account the morphology of the crystallites (K = 0.94 corresponding to spherical crystallites was used here), λ is the x-ray wavelength, β is the peak width at Full width at Half Maximum (FWHM), and θ is the diffraction angle. The elemental and chemical composition of the nanoassemblies were characterised by X-Ray Photoelectron Spectroscopy (XPS) using a PHI Quantum 2000 equipment with an AlK_α X-ray energy source of 1486 eV having a beam diameter of 200 μm. Survey scans were measured with a pass energy of 58.7 eV and resolution of 1 eV where high resolution scans were measured with a pass energy of 23.50 eV and 0.025 eV resolution. Energy range of the survey scans were 1100-0 eV. To control samples charging, a neutralizer filament was used in all measurements. CasaXPS software (version 2.3.16) was used for the spectral curve fittings, while the binding energies were referenced to the C1s of alkyl chains at 248.8 eV. The peaks were fitted with a Gaussian-Lorentzian function and Shirely type background. Raman Spectroscopic spectra of Cu_2O NPs thin films were performed using Raman FTIR (Leica DM 2500 equipment) with laser energy of 514 nm. Transmission Electron Microscopy (TEM) images were acquired employing a Jeol JEM 1011 equipment (1 nm maximum resolution), operated at 100 kV accelerating voltage under high vacuum.

Glass substrates (76×26×1 mm^3, Gerhard Menzel GmbH, Germany) were used for XRD and FTIR analysis, and single side polished 4-inch Si wafer with 1 μm thickness silicon oxide on top (Silicon Materials, Germany) for SEM and XPS analysis.

3.6.2. Substrates Treatment

Before placing the substrates in the AGD equipment for nanoparticles synthesis, they were cleaned by successive wash in an ultrasonic bath for 5 min in propanol and acetone, followed by rinsing with deionised water and drying with blowing nitrogen flow. When the silicon substrates with the patterned gold electrodes were employed, the substrate was covered with Kapton tape that left uncovered only the gap between the gold electrodes for the deposition of the nanoparticles exclusively in between them.

3.6.3. Electrical Measurements

The electrical resistance of the sensors was measured with a high-precision Keysight power source (B2902A, Keysight Technologies, Hungary), using an internal applied voltage of 1 V. The characteristic *I-V* curves were measured by applying a sweeping voltage between -10V and +10V between the two sensor's gold electrodes, at a sweep rate of 0.1 V/sec, and acquiring the current between the electrodes.

3.6.4. Materials and Reagents

All chemicals employed for nanoparticles functionalization were of analytical grade and used as received. 1-dodecanethiol: $CH_3(CH_2)_{11}SH$ (98% purity); 4-methxoy-α-toluenethiol: $CH_3OC_6H_4CH_2SH$ (90% purity); oleylamine: $C_{18}H_{35}NH_2$ (98% purity), 2-

mercaptobenzoxazole: C_7H_5NOS (99% purity); 11-mercaptoundecanoic acid: $C_{11}H_{22}O_2S$ (98% purity); 1-butanethiol: $CH_3(CH_2)_3SH$ (99% purity); 1-decanethiol: $CH_3(CH_2)_9SH$ (96 % purity); methyl-3-mercaptopropionate: $HSC_4H_5O_2$ (98% purity); 11-mercapto-1-undecanol: $HO(CH_2)_9SH$ (97% purity); ethanol (99.5% purity); chloroform (99% purity); acetone (95% purity) and isopropanol (96%), were purchased from Sigma Aldrich.

3.7. References

1. Turkevich, J.; Stevenson, P.C.; Hillier, J. A study of the nucleation and growth processes in the synthesis of colloidal gold. *Discussions of the Faraday Society* **1951**, *11*, 55-75.
2. Bönnemann, H.; Richards, Ryan M. Nanoscopic metal particles − synthetic methods and potential applications. *European Journal of Inorganic Chemistry* **2001**, *2001*, 2455-2480.
3. Okitsu, K. Sonochemical synthesis of metal nanoparticles. In *Theoretical and experimental sonochemistry involving inorganic systems*, Ashokkumar, M., Ed. Springer Netherlands: Dordrecht, 2011; pp 131-150.
4. Swihart, M.T. Vapor-phase synthesis of nanoparticles. *Current Opinion in Colloid & Interface Science* **2003**, *8*, 127-133.
5. Capek, I. Preparation of metal nanoparticles in water-in-oil (w/o) microemulsions. *Advances in Colloid and Interface Science* **2004**, *110*, 49-74.
6. Zhang, Y.; Erkey, C. Preparation of supported metallic nanoparticles using supercritical fluids: A review. *The Journal of Supercritical Fluids* **2006**, *38*, 252-267.

7. Kim, J.; Kim, D.; Veriansyah, B.; Won Kang, J.; Kim, J.-D. Metal nanoparticle synthesis using supercritical alcohol. *Materials Letters* **2009**, *63*, 1880-1882.
8. Ma, H.; Yin, B.; Wang, S.; Jiao, Y.; Pan, W.; Huang, S.; Chen, S.; Meng, F. Synthesis of silver and gold nanoparticles by a novel electrochemical method. *ChemPhysChem* **2004**, *5*, 68-75.
9. Dhand, C.; Dwivedi, N.; Loh, X.J.; Jie Ying, A.N.; Verma, N.K.; Beuerman, R.W.; Lakshminarayanan, R.; Ramakrishna, S. Methods and strategies for the synthesis of diverse nanoparticles and their applications: A comprehensive overview. *RSC Advances* **2015**, *5*, 105003-105037.
10. Liang, W.; Harris, A.T. Facile size and shape control of templated au nanoparticles under microwave irradiation. *Materials Letters* **2011**, *65*, 2307-2310.
11. Marine, W.; Patrone, L.; Luk'yanchuk, B.; Sentis, M. Strategy of nanocluster and nanostructure synthesis by conventional pulsed laser ablation. *Applied Surface Science* **2000**, *154–155*, 345-352.
12. Misra, N.; Biswal, J.; Gupta, A.; Sainis, J.K.; Sabharwal, S. Gamma radiation induced synthesis of gold nanoparticles in aqueous polyvinyl pyrrolidone solution and its application for hydrogen peroxide estimation. *Radiation Physics and Chemistry* **2012**, *81*, 195-200.
13. Abedini, A.; Daud, A.R.; Abdul Hamid, M.A.; Kamil Othman, N.; Saion, E. A review on radiation-induced nucleation and growth of colloidal metallic nanoparticles. *Nanoscale Research Letters* **2013**, *8*, 474-474.
14. Brust, M.; Walker, M.; Bethell, D.; Schiffrin, D.J.; Whyman, R. Synthesis of thiol-derivatised gold nanoparticles in a two-phase liquid-liquid system. *Journal of the Chemical Society, Chemical Communications* **1994**, 801-802.

15. Calandra, P.; Calogero, G.; Sinopoli, A.; Gucciardi, P.G. Metal nanoparticles and carbon-based nanostructures as advanced materials for cathode application in dye-sensitized solar cells. *International Journal of Photoenergy* **2010**, *2010*, 15.

16. Lansåker, P.C.; Hallén, A.; Niklasson, G.A.; Granqvist, C.G. Characterization of gold nanoparticle films: Rutherford backscattering spectroscopy, scanning electron microscopy with image analysis, and atomic force microscopy. *AIP Advances* **2014**, *4*, 107101.

17. Granqvist, C.; Buhrman, R. Ultrafine metal particles. *Journal of Applied Physics* **1976**, *47*, 2200-2219.

18. Gawande, M.B.; Goswami, A.; Felpin, F.-X.; Asefa, T.; Huang, X.; Silva, R.; Zou, X.; Zboril, R.; Varma, R.S. Cu and cu-based nanoparticles: Synthesis and applications in catalysis. *Chemical Reviews* **2016**, *116*, 3722-3811.

19. Haitao, Z.; Canying, Z.; Yansheng, Y. Novel synthesis of copper nanoparticles: Influence of the synthesis conditions on the particle size. *Nanotechnology* **2005**, *16*, 3079.

20. Soomro, R.A.; Sherazi, S.H.; Memon, N.; Shah, M.; Kalwar, N.; Hallam, K.R.; Shah, A. Synthesis of air stable copper nanoparticles and their use in catalysis. *Advanced Materials Letters* **2014**, *5*, 191-198.

21. Deng, Y.; Handoko, A.D.; Du, Y.; Xi, S.; Yeo, B.S. In situ raman spectroscopy of copper and copper oxide surfaces during electrochemical oxygen evolution reaction: Identification of cuiii oxides as catalytically active species. *ACS Catalysis* **2016**, *6*, 2473-2481.

22. Orna, B.; Nir, P.; R., H.F.; Hossam, H. Sniffing the unique “odor print” of non-small-cell lung cancer with gold nanoparticles. *Small* **2009**, *5*, 2618-2624.

23. Grönbeck, H.; Curioni, A.; Andreoni, W. Thiols and disulfides on the au(111) surface: The headgroup−gold interaction. *Journal of the American Chemical Society* **2000**, *122*, 3839-3842.

24. Wuelfing, W.P.; Green, S.J.; Pietron, J.J.; Cliffel, D.E.; Murray, R.W. Electronic conductivity of solid-state, mixed-valent, monolayer-protected au clusters. *Journal of the American Chemical Society* **2000**, *122*, 11465-11472.

25. Chen, S.; Sommers, J.M. Alkanethiolate-protected copper nanoparticles: Spectroscopy, electrochemistry, and solid-state morphological evolution. *The Journal of Physical Chemistry B* **2001**, *105*, 8816-8820.

26. Joseph, Y.; Guse, B.; Vossmeyer, T.; Yasuda, A. Gold nanoparticle/organic networks as chemiresistor coatings: The effect of film morphology on vapor sensitivity. *The Journal of Physical Chemistry C* **2008**, *112*, 12507-12514.

27. Dokić, B.L.; Blanuša, B. Power electronics. Converters and regulators. *Diodes and Transistors* **2015**, 43-141.

28. Smith, D.; Wang, T.; Sulé-Suso, J.; Španěl, P.; Haj, A.E. Quantification of acetaldehyde released by lung cancer cells in vitro using selected ion flow tube mass spectrometry. *Rapid communications in mass spectrometry* **2003**, *17*, 845-850.

29. Tisch, U.; Haick, H. Nanomaterials for cross-reactive sensor arrays. *MRS Bulletin* **2010**, *35*, 797-803.

30. Miranda, E.; Jiménez, D.; Tsurumaki-Fukuchi, A.; Blasco, J.; Yamada, H.; Suñé, J.; Sawa, A. Modeling of hysteretic schottky diode-like conduction in pt/bifeo 3/srruo3 switches. *Applied Physics Letters* **2014**, *105*.

31. Pang, P.; Guo, J.; Wu, S.; Cai, Q. Humidity effect on the dithiol-linked gold nanoparticles interfaced chemiresistor sensor for vocs analysis. *Sensors and Actuators, B: Chemical* **2006**, *114*, 799-803.

32. Pang, P.; Guo, Z.; Cai, Q. Humidity effect on the monolayer-protected gold nanoparticles coated chemiresistor sensor for vocs analysis. *Talanta* **2005**, *65*, 1343-1348.

4

CHAPTER

4. BREATH SAMPLING AND POPULATION STUDY

This chapter presents the breath sampling procedure adopted in this study, and the study population that provided breath samples for analysis.

4.1. Breath Sampling

4.1.1. Introduction

The reliable measurement of metabolic body conditions through exhaled breath analysis requires the use of a proper breath acquisition method that captures the alveolar part of the breath (which is most likely to contain the metabolites exchanged by the blood with the lungs and exhaled then through breathing [1]) and avoids as much as possible external interferences. Nevertheless, although the International Association for Breath Research (IABR) set up a sampling and standardization task force, breath sampling is not currently a standardized technique. Different breath capture methods were proposed so far, which ranged from directly breathing into an analysis platform, to the relatively simple collection in plastic Tedlar® bags, aluminized Mylar bags, or Bio-VOC™ samplers [2]. Because of important features such as simplicity of the sampling procedure, which can be performed with minimal training and without the need of attendance from medically qualified staff, and the possibility to capture the alveolar part of the breath, the Bio-VOC™ samplers (Markes International, UK) were selected for the collection of the breath samples provided by the volunteers of this study.

4.1.2. Breath Sampling with the Bio-VOC

The different components of the Bio-VOC sampler kit are presented in **Figure 4.1a**. The kit contains a 129 mL container with an open end without return made of an inert

non-emitting plastic material for avoiding sample contamination, a screw-in plunger that is used to steadily transfer the breath sample either into the measuring device or into a sorbent storage container, and a disposable mouthpiece for preventing disease transmission between patients.

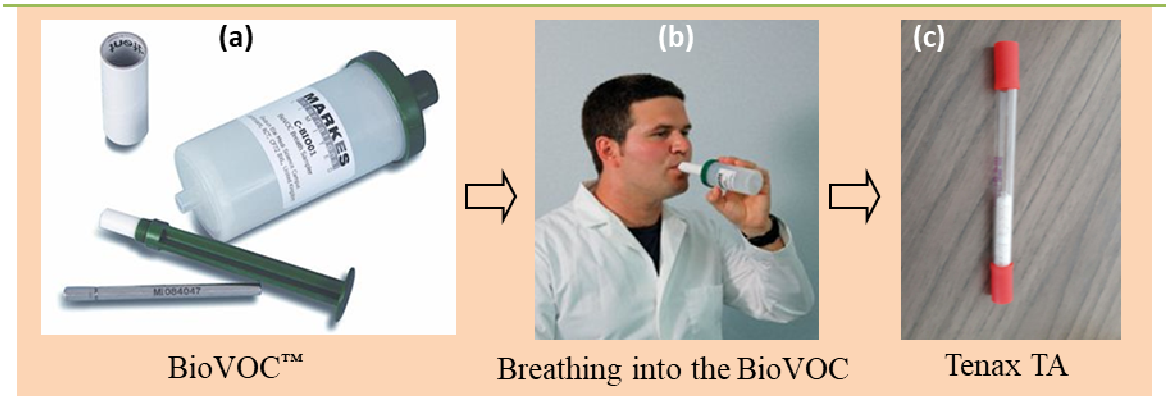

Figure 4.1: (a) Bio-VOC™ breath sampler kit components; (b) Breath sampling procedure with the Bio-VOC™; (c) Breath VOCs storage in Tenax TA absorbent material for offline breath analysis**.**

Before breath samples collection, the volunteers were asked to fast overnight. The breath sampling procedure consisted of volunteers exhaling normally through the disposable mouthpiece into the breath sampler until empting the lungs (**Figure 4.1b**). The first portion of the breath exited through the open end, and the Bio-VOC retained inside only the end-tidal air that corresponds to the alveolar breath. Subsequently, the mouthpiece was replaced with the plunger, which was slowly pushed during 10 seconds within the whole volume of the Bio-VOC™ for transferring the alveolar breath retained inside the breath sampler either into the sensors test chamber (for the direct sensing measurements approach), or into two-bed ORBO 420 Tenax® TA sorption tubes (Sigma-Aldrich, Spain) suitable for breath VOCs preconcentration and storage (for analysis at a later stage employing analytical techniques or the indirect sensing

measurements approach). The sorbent tubes were stored at 4 ºC in a freezer for biomedical samples until analysis. For filling a sorbent tube, the entire process was repeated twice for the same volunteer in order to ensure a higher concentration of the volatiles retained by the sorbent material. Generally, two storage tubes with breath samples were collected per individual, for analysis with the chemical sensors array and with a gas chromatograph coupled with quadruple time of flight (GC/Q-TOF), respectively.

For cleaning purposes, prior to the first use and after each use, the Bio-VOC samplers were disassembled, and all the components were cleaned by introducing them for 15 minutes in a solution of 20 ml concentrated disinfectant (Amukina, Spain) dissolved in 1 L of distilled water. Each component was then rinsed with distilled water and left to naturally dry without wiping to avoid contamination.

4.2. Population Study

Volunteers diagnosed with Dengue, Leishmaniasis and Echinococcosis were recruited in clinics from both endemic regions (Colombia for Dengue, and Tunisia for Leishmaniasis and Echinococcosis), and from a low prevalence region (Poland) for Echinococcosis, where the affected patients are mostly tourists travelling to endemic areas and soldiers fulfilling military missions in endemic regions. Age and gender matched (as much as possible) control volunteers were recruited from the medical staff of the clinics were the patients were attended. All patients and controls provided written informed consent for the collection of their breath samples and subsequent analysis. Only adult volunteers participated in the study. The personal data collected for the purpose of this study were anonymized by applying the aggregation and K-anonymity anonymization techniques for preventing volunteers' identification. Because of this,

three age groups were defined instead of the real patients' age: young (18-29 years), middle-aged (30-49 years), and senior (> 50 years).

The study protocol, consent forms and procedures were reviewed and approved by the Ethics Committee of IPS Unipamplona (Colombia), Research Ethics Committee of ESE Erasmo Meoz Universitary Hospital (Colombia), Institut Pasteur de Tunis Ethical Review Board (Tunisia – valid for all Tunisia), and the Independent Bioethical Commission for Science Research at the Medical University of Gdańsk (Poland).

4.2.1. Dengue

The Dengue study included 46 volunteers: 23 patients diagnosed with Dengue hospitalized at Erasmo Meoz Universitary Hospital and at IPS Unipamplona (both clinics located in Cúcuta, Colombia), and 23 healthy controls. For the diagnosis of Dengue, the normal standard blood and serological tests (IgM) were performed. The patients were at different stages of the disease, and presented between 1 and 8 days of fever. The statistical data of the study groups whose samples were used for each analysis technique employed is presented in **Table 4.1**, while full information about the volunteers included in this study and the number of samples provided by each one of them is presented in **Table 4.2**.

	GC/Q-TOF analysis			Sensors measurements		
	DEN	CON	Total	DEN	CON	Total
Number volunteers	16	17	33	15	13	28
Male/Female	7/9	4/13	11/22	10/5	5/8	15/13
Age:18-29/30-49/≥ 50	7/6/3	8/6/3	15/12/6	7/3/5	7/2/4	14/5/9
Smoking	1	3	4	1	2	3

Table 4.1: Statistical data of the study groups for the Dengue experiment included in each study performed. DEN: Dengue patients; CON: Controls.

Volunteer Label[1]	Age interval	Gender	Smoking	Clinic[2]	Days of fever (Dengue	Other diseases	Medication	No. of samples	
								GC/Q-TOF	Sensors
D01	> 50	Male	No	IPS	4	–	–	–	1
D02	18-29	Female	No	IPS	5	–	Acetaminophen	–	1
D03	> 50	Female	No	IPS	5	–	Aspirin	–	1
D04	18-29	Male	No	IPS	7	–	–	–	1
D05	> 50	Male	No	IPS	6	–	–	–	1
D06	> 50	Male	No	IPS	3	–	–	–	1
D07	18-29	Male	No	IPS	5	–	–	–	1
D08	18-29	Female	No	HUEM	4	–	–	2	-
D09	18-29	Male	No	HUEM	4	–	–	2	1
D10	> 50	Male	No	HUEM	5	Diabetes	–	2	1
D11	30-49	Male	No	IPS	6	Diabetes	–	2	1
D12	18-29	Female	No	HUEM	5	–	–	2	1
D13	18-29	Female	No	HUEM	?	–	–	2	1
D14	18-29	Female	No	HUEM	4	–	–	2	1
D15	30-49	Male	Yes	HUEM	5	–	–	2	1
D16	30-49	Male	No	HUEM	5	Hypo-thyroidism	Levothyroxine	2	1
D17	18-29	Male	No	HUEM	5	–	–	2	-
D18	> 50	Female	No	IPS	2	–	–	2	-
D19	> 50	Female	No	HUEM	1	High blood pressure	Acetaminophen Enalapril	2	-
D20	30-49	Female	No	HUEM	8	–	Acetaminophen	2	-
D21	18-29	Female	No	HUEM	1	–	–	2	-
D22	30-49	Female	No	IPS	1	Ulcer	Acetaminophen Ranitidine	2	-
D23	30-49	Male	No	HUEM	5	–	–	1	-
C01	> 50	Male	No	IPS	–	–	–	–	1
C02	18-29	Female	No	IPS	–	–	–	–	1
C03	> 50	Male	No	IPS	–	Arterial hypertension	Minart	–	1
C04	18-29	Male	No	IPS	–	–	–	–	1
C05	> 50	Male	No	IPS	–	–	–	–	1
C06	> 50	Female	No	IPS	–	–	–	–	1
C07	18-29	Female	No	IPS	–	–	–	1	1
C08	18-29	Female	No	IPS	–	–	–	2	-
C09	18-29	Female	No	HUEM	–	–	–	2	1
C10	> 50	Female	No	IPS	–	Diabetes	Glucovance	2	1
C11	30-49	Female	No	IPS	–	–	–	2	1
C12	18-29	Female	Yes	IPS	–	–	–	2	1
C13	18-29	Male	No	IPS	–	–	–	2	-
C14	18-29	Female	No	IPS	–	Pneumonia	Ciprofloxacin	2	1

C15	30-49	Female	No	IPS	–	–	–	2	-
C16	30-49	Male	Yes	IPS	–	–	–	2	1
C17	18-29	Male	No	IPS	–	–	–	2	-
C18	> 50	Female	Yes	IPS	–	–	–	2	-
C19	> 50	Male	No	IPS	–	High blood pressure	Losartan	2	-
C20	30-49	Female	No	IPS	–	–	–	2	-
C21	18-29	Female	No	IPS	–	–	–	2	-
C22	30-49	Female	No	IPS	–	–	–	2	-
C23	30-49	Female	No	IPS	–	–	–	2	-

[1]D: Dengue, C: Control; [2]IPS: IPS Unipamplona; HUEM: Erasmo Meoz Universitary Hospital

Table 4.2: Information about the volunteers from the Dengue study

4.2.2. Leishmaniasis

Volunteers diagnosed with human cutaneous leishmaniasis (HCL; n = 28) and healthy controls (CCL; n = 32) were recruited at Tunis Charles Nicolle University Hospital (North East Tunisia), Ben Arous Regional Hospital (North East Tunisia), Abderrahman Mami University Hospital (Ariana, North East Tunisia) and Gafsa Houssine Bouzaiene Regional Hospital (South East Tunisia). Patients' diagnosis was based on microscopic tests (examination of skin-scraping smear samples) and clinical aspects of the lesions. The study population is presented in **Table 4.3**, while the statistical data of the study groups included in each study is presented in **Table 4.4**.

Volunteer Label[1]	Age	Gender	Smoking[2]	Hospital[3]	No. of samples		Country
					GC/Q-TOF	Sensors	
L01	18-29	Male	No	BAH	x	x	Tunisia
L02	18-29	Male	No	GH	x	x	Tunisia
L03	30-49	Female	No	CNH	x	x	Tunisia
L04	30-49	Female	No	GH	x	x	Tunisia
L05	30-49	Female	No	GH	x	x	Tunisia
L06	30-49	Male	No	BAH	x	x	Tunisia
L07	30-49	Male	No	GH	x	x	Tunisia
L08	30-49	Female	N/A	GH	x	x	Tunisia
L09	30-49	Female	No	GH	x	x	Tunisia
L10	30-49	Female	No	GH	x	x	Tunisia

L11	30-49	Female	No	GH	x	x	Tunisia
L12	30-49	Male	Yes	GH	x	x	Tunisia
L13	>50	Female	No	GH	x	x	Tunisia
L14	>50	Female	No	GH	x	x	Tunisia
L15	>50	Female	No	GH	x	x	Tunisia
L16	>50	Female	No	GH	x	x	Tunisia
L17	>50	Female	No	GH	x	x	Tunisia
L18	>50	Female	No	CNH	x	x	Tunisia
L19	>50	Female	No	GH	x	x	Tunisia
L20	>50	Female	No	GH	x	x	Tunisia
L21	>50	Female	No	GH	x	x	Tunisia
L22	>50	Female	No	GH	x	x	Tunisia
L23	>50	Female	No	GH	x	x	Tunisia
L24	>50	Male	No	BAH	x	x	Tunisia
L25	>50	Male	No	GH	x	x	Tunisia
L26	>50	Male	No	GH	x	x	Tunisia
L27	>50	Male	No	GH	x	x	Tunisia
L28	>50	Male	Yes	CNH	x	x	Tunisia
C01	18-29	Female	No	CNH	x	x	Tunisia
C02	18-29	Female	No	CNH	x	x	Tunisia
C03	18-29	Female	No	CNH	x	x	Tunisia
C04	18-29	Female	No	CNH	x	x	Tunisia
C05	18-29	Female	No	CNH	x	x	Tunisia
C06	18-29	Female	No	CNH	x	x	Tunisia
C07	18-29	Female	No	CNH	x	x	Tunisia
C08	18-29	Female	No	CNH	x	x	Tunisia
C09	18-29	Female	No	CNH	x	x	Tunisia
C10	18-29	Female	No	CNH	x	x	Tunisia
C11	18-29	Female	No	CNH	x	x	Tunisia
C12	18-29	Female	No	AH	x	x	Tunisia
C13	18-29	Female	No	AH	x	x	Tunisia
C14	18-29	Female	No	AH	x	x	Tunisia
C15	18-29	Female	No	AH	x	x	Tunisia
C16	18-29	Male	No	CNH	x	x	Tunisia
C17	18-29	Male	No	CNH	x	x	Tunisia
C18	18-29	Male	No	AH	x	x	Tunisia
C19	18-29	Male	Yes	AH	x	-	Tunisia
C20	30-49	Female	No	CNH	x	x	Tunisia
C21	30-49	Female	No	CNH	x	x	Tunisia
C22	30-49	Female	No	CNH	x	x	Tunisia
C23	30-49	Female	No	CNH	x	-	Tunisia
C24	30-49	Female	No	CNH	x	x	Tunisia
C25	30-49	Female	No	AH	x	x	Tunisia
C26	30-49	Female	No	AH	x	x	Tunisia
C27	30-49	Male	No	CNH	x	-	Tunisia
C28	30-49	Male	No	AH	x	x	Tunisia

C29	30-49	Male	Yes	CNH	x	x	Tunisia
C30	30-49	Male	N/A	AH	x	x	Tunisia
C31	30-49	Female	No	AH	x	x	Tunisia
C32	>50	Female	No	GH	x	-	Tunisia

[1] L: Volunteer with human cutaneous leishmaniasis; C: healthy control
[2] N/A: Information not available
[2] CNH: Charles Nicolle Hospital; BAH: Ben Arous Hospital; GH: Gafsa Hospital; AH: Ariana Hospital

Table 4.3: Information about the volunteers from the Leishmaniasis study

	GC/Q-TOF analysis			Sensors measurements		
	HCL	CCL	Total	HCL	CCL	Total
Number of volunteers	28	32	60	28	28	56
Male/Female	10/18	8/24	18/42	10/18	6/22	16/40
Age: 18-29/30-49/≥ 50	2/10/16	19/12/1	21/22/7	2/10/16	16/12/0	18/22/16
Smoking	2	2	4	2	1	3

Table 4.4: Statistical data of the study groups for Leishmaniasis included in each analysis performed. HCL: Leishmaniasis patients; CCL: Controls.

4.2.3. Echinococcosis

32 patients diagnosed with Cystic Echinococcosis (CE) were recruited at two medical centers from Tunisia (Charles Nicolle Hospital from Tunis Government and Abderrahman Mami Hospital from Ariana Government). After anamnestic, clinical, radiological and ichnographical suspicion of CE, an ELISA serological investigation using commercial kit (Ridascreen® Echinococcus IgG) was performed for CE diagnosis. Some cases were further confirmed after surgery. 43 CE controls (here denominated CCE) were selected from healthy medical personnel working in these clinics who did not have contact with the etiological agent of CE.

16 patients diagnosed with Alveolar Echinococcosis (AE) were recruited from adult patients without pulmonary disorders hospitalized at the Clinic of Tropical and Parasitic Diseases from Gdynia, Poland. Several tests were performed for AE diagnosis: serological tests (ELISA, Western blot), analysis of DNA samples by Polymerase Chain Reaction (PCR), real-time PCR, and microscopic detection of parasites. Eight AE controls (here denominated CAE) were selected from volunteered personnel of the Clinic of Tropical and Parasitic Diseases from Gdynia. Although they were age and sex matched with the AE patients as much as possible, age matching was not accurately achieved, because most of the personnel of the clinic were younger (below 40, with only one exception) as compared with AE patients (over 40, with only one exception).

Information regarding the volunteers included in each analysis performed is presented in **Tables 4.5, 4.7, 4.9 and 4.11**, while the statistical data of the study population included in each analysis is presented in **Tables 4.6, 4.8, 4.10 and 4.12**.

Volunteer Label	Age	Gender	Smoking	Hospital[1]	No. of samples		Country
					GC/Q-TOF	Sensors	
CE 1	18-29	Male	No	HCN	x	x	Tunisia
CE 2	>50	Female	No	HCN	x	x	Tunisia
CE 3	>50	Female	No	HCN	x	x	Tunisia
CE 4	30-49	Female	No	HCN	x	x	Tunisia
CE 5	30-49	Male	No	HCN	x	x	Tunisia
CE 6	30-49	Female	No	HCN	x	x	Tunisia
CE 7	18-29	Female	No	HCN	x	x	Tunisia
CE 8	>50	Male	No	HCN	x	x	Tunisia
CE 9	>50	Female	No	HCN	x	x	Tunisia
CE 10	30-49	Female	No	HCN	x	x	Tunisia
CE 11	30-49	Female	No	HCN	x	x	Tunisia
CE 12	>50	Female	No	HCN	x	x	Tunisia
CE 13	>50	Female	No	HA	x	x	Tunisia
CE 14	30-49	Female	No	HA	x	x	Tunisia
CE 15	>50	Male	Yes	HA	x	x	Tunisia
CE 16	30-49	Female	No	HCN	x	x	Tunisia
CE 17	18-29	Female	No	HCN	x	x	Tunisia
CE 18	18-29	Male	No	HCN	x	x	Tunisia

CE 19	30-49	Female	No	HCN	x	x	Tunisia
CE 20	30-49	Female	No	HCN	x	x	Tunisia
CE 21	30-49	Female	No	HCN	x	x	Tunisia
CE 22	30-49	Female	No	HCN	x	x	Tunisia
CE 23	30-49	Female	No	HA	x	x	Tunisia
CE 24	30-49	Female	No	HA	–	x	Tunisia
CCE 1	30-49	Female	No	HCN	x	x	Tunisia
CCE 2	30-49	Female	No	HCN	x	x	Tunisia
CCE 3	30-49	Female	No	HCN	x	x	Tunisia
CCE 4	18-29	Male	No	HCN	x	x	Tunisia
CCE 5	30-49	Female	No	HCN	x	x	Tunisia
CCE 6	18-29	Female	No	HCN	x	x	Tunisia
CCE 7	18-29	Female	No	HCN	x	x	Tunisia
CCE 8	30-49	Male	No	HCN	x	x	Tunisia
CCE 9	30-49	Female	No	HCN	x	x	Tunisia
CCE 10	30-49	Female	No	HCN	-	x	Tunisia
CCE 11	18-29	Female	No	HCN	x	x	Tunisia
CCE 12	18-29	Female	No	HCN	x	x	Tunisia
CCE 13	30-49	Male	Yes	HCN	x	x	Tunisia
CCE 14	18-29	Female	No	HCN	x	x	Tunisia
CCE 15	18-29	Female	No	HCN	x	x	Tunisia
CCE 16	18-29	Female	No	HCN	x	x	Tunisia
CCE 17	18-29	Male	No	HCN	x	x	Tunisia
CCE 18	18-29	Female	No	HCN	x	x	Tunisia
CCE 19	18-29	Female	No	HCN	x	x	Tunisia
CCE 20	18-29	Female	No	HCN	x	x	Tunisia
CCE 21	18-29	Female	No	HCN	x	-	Tunisia
CCE 22	30-49	Male	-	HA	x	x	Tunisia
CCE 23	18-29	Female	No	HA	x	x	Tunisia
CCE 24	18-29	Female	No	HA	x	x	Tunisia
CCE 25	30-49	Female	No	HA	x	x	Tunisia
CCE 26	18-29	Female	No	HA	x	x	Tunisia
CCE 27	30-49	Female	No	HA	x	x	Tunisia
CCE 28	30-49	Male	No	HA	x	x	Tunisia
CCE 29	18-29	Female	No	HA	x	-	Tunisia
CCE 30	18-29	Male	No	HA	x	-	Tunisia
CCE 31	18-29	Male	Yes	HA	x	-	Tunisia
CCE 32	>50	Female	No	HG	x	-	Tunisia

[1] HCN: Charles Nicolle Hospital; HA: Ariana Hospital; HG: Gafsa Hospital

Table 4.5: Study population included in the indirect cystic echinococcosis study. CE: cystic echinococcosis; CCE: controls for cystic echinococcosis.

	GC/Q-TOF analysis			**Sensors measurements**		
	CE	CCE	Total	CE	CCE	Total
Number of volunteers	23	32	55	24	28	52
Male/Female	5/18	8/24	13/42	5/19	6/22	11/41
Age: 18-29/30-49/≥ 50	4/13/6	19/12/1	23/25/7	4/14/6	16/12/0	20/26/6
Smoking	1	2	3	1	1	2

Table 4.6: Statistical data of the study groups included in the indirect cystic echinococcosis study. CE: cystic echinococcosis; CCE: controls for cystic echinococcosis.

Volunteer Label	Age	Gender	Smoking	Hospital[1]	Sensor analysis	Country
CE 1	30-49	Female	No	HCN	x	Tunisia
CE 2	>50	Male	Yes	HCN	x	Tunisia
CE 3	18-29	Female	No	HCN	x	Tunisia
CE 4	30-49	Female	No	HCN	x	Tunisia
CE 5	30-49	Female	No	HCN	x	Tunisia
CE 6	>50	Male	No	HCN	x	Tunisia
CE 7	30-49	Female	No	HCN	x	Tunisia
CE 8	18-29	Female	No	HCN	x	Tunisia
CCE 1	>50	Male	Yes	HCN	x	Tunisia
CCE 2	30-49	Female	No	HCN	x	Tunisia
CCE 3	30-49	Female	No	HCN	x	Tunisia
CCE 4	30-49	Male	No	HCN	x	Tunisia
CCE 5	30-49	Female	No	HCN	x	Tunisia
CCE 6	30-49	Male	Yes	HCN	x	Tunisia
CCE 7	30-49	Female	No	HCN	x	Tunisia
CCE 8	>50	Female	No	HCN	x	Tunisia
CCE 9	>50	Female	Yes	HCN	x	Tunisia
CCE 10	18-29	Male	No	HCN	x	Tunisia
CCE 11	18-29	Female	No	HCN	x	Tunisia
CCE 12	18-29	Female	No	HCN	x	Tunisia
CCE 13	18-29	Female	No	HCN	x	Tunisia
CCE 14	18-29	Female	No	HCN	x	Tunisia
CCE 15	>50	Male	No	HCN	x	Tunisia

[1] HCN: Charles Nicolle Hospital

Table 4.7: Study population included in the direct cystic echinococcosis study. CE: cystic echinococcosis; CCE: controls for cystic echinococcosis

	Sensors measurements		
	CE	CCE	Total
Number of volunteers	8	15	23
Male/Female	2/6	6/9	8/15
Age: 18-29/30-49/≥ 50	2/4/2	5/6/4	7/10/8
Smoking	1	3	4

Table 4.8: Statistical data of the study groups included in the direct cystic echinococcosis study. CE: cystic echinococcosis; CCE: controls for cystic echinococcosis.

Volunteer Label	Age	Gender	Smoking	Hospital[1]	No. of samples		Country
					GC/Q-TOF	Sensor	
AE 1	>50	Male	No	TPD	x	x	Poland
AE 2	>50	Male	No	TPD	x	x	Poland
AE 3	>50	Male	No	TPD	x	x	Poland
AE 4	30-49	Female	No	TPD	x	x	Poland
AE 5	>50	Male	Yes	TPD	x	x	Poland
AE 6	30-49	Male	No	TPD	x	x	Poland
AE 7	30-49	Female	No	TPD	x	x	Poland
AE 8	>50	Male	Yes	TPD	x	x	Poland
AE 9	>50	Female	No	TPD	x	x	Poland
AE 10	30-49	Female	No	TPD	x	x	Poland
AE 11	>50	Male	No	TPD	x	x	Poland
AE 12	>50	Female	No	TPD	x	x	Poland
AE 13	>50	Female	No	TPD	x	x	Poland
AE 14	>50	Female	No	TPD	-	x	Poland
CAE 1	18-29	Female	No	TPD	x	x	Poland
CAE 2	18-29	Female	No	TPD	x	x	Poland
CAE 3	30-49	Male	No	TPD	x	x	Poland
CAE 4	30-49	Female	No	TPD	x	x	Poland
CAE 5	30-49	Female	No	TPD	x	x	Poland
CAE 6	18-29	Female	No	TPD	x	x	Poland
CAE 7	30-49	Male	No	TPD	x	X	Poland
CAE 8	30-49	Male	No	TPD	x	X	Poland

[1] TPD: Clinic of Tropical and Parasitic Diseases, Gdynia

Table 4.9: Study population included in the alveolar echinococcosis study. AE: alveolar echinococcosis; CAE: controls for cystic echinococcosis

	GC/Q-TOF analysis			Sensors measurements		
	AE	CAE	Total	AE	CAE	Total
Number of volunteers	13	8	21	14	8	22
Male/Female	7/6	3/5	10/11	7/7	3/5	10/12
Age: 18-29/30-49/≥ 50	0/4/9	3/5/0	3/9/9	0/4/10	3/5/0	3/9/10
Smoking	2	0	2	2	0	2

Table 4.10: Statistical data of the study groups included in the alveolar echinococcosis study. AE: alveolar echinococcosis; CAE: controls for cystic echinococcosis.

Volunteer Label	Age	Gender	Smoking	Hospital[1]	No. of samples	
					Sensors	Country
CE 1	18-29	Male	No	HCN	x	Tunisia
CE 2	>50	Female	No	HCN	x	Tunisia
CE 3	>50	Female	No	HCN	x	Tunisia
CE 4	30-49	Female	No	HCN	x	Tunisia
CE 5	30-39	Male	No	HCN	x	Tunisia
CE 6	30-49	Female	No	HCN	x	Tunisia
CE 7	18-29	Female	No	HCN	x	Tunisia

CE 8	>50	Male	No	HCN	x	Tunisia
CE 9	>50	Female	No	HCN	x	Tunisia
CE 10	30-49	Female	No	HCN	x	Tunisia
CE 11	30-49	Female	No	HCN	x	Tunisia
CE 12	30-59	Female	No	HCN	x	Tunisia
CE 13	>50	Female	No	HA	x	Tunisia
CE 14	30-49	Female	No	HA	x	Tunisia
CE 15	>50	Male	Yes	HA	x	Tunisia
CE 16	30-49	Female	No	HCN	x	Tunisia
CE 17	18-29	Female	No	HCN	x	Tunisia
CE 18	18-29	Male	No	HCN	x	Tunisia
CE 19	30-49	Female	No	HCN	x	Tunisia
CE 20	30-39	Female	No	HCN	x	Tunisia
CE 21	30-49	Female	No	HCN	x	Tunisia
CE 22	30-49	Female	No	HCN	x	Tunisia
CE 23	30-49	Female	No	HA	x	Tunisia
CE 24	30-49	Female	No	HA	x	Tunisia
AE 1	>50	Male	No	TPD	x	Poland
AE 2	>50	Male	No	TPD	x	Poland
AE 3	>50	Male	No	TPD	x	Poland
AE 4	30-49	Female	No	TPD	x	Poland
AE 5	>50	Male	Yes	TPD	x	Poland
AE 6	30-49	Male	No	TPD	x	Poland
AE 7	30-49	Female	No	TPD	x	Poland
AE 8	>50	Male	Yes	TPD	x	Poland
AE 9	>50	Female	No	TPD	x	Poland
AE 10	30-49	Female	No	TPD	x	Poland
AE 11	>50	Male	No	TPD	x	Poland
AE 12	>50	Female	No	TPD	x	Poland
AE 13	>50	Female	No	TPD	x	Poland
AE 14	>50	Female	No	TPD	x	Poland

[1] HCN: Charles Nicolle Hospital; HA: Ariana Hospital; HG: Gafsa Hospital; TPD: Clinic of Tropical and Parasitic Diseases, Gdynia.

Table **4.11:** Study population included in the comparative study between cystic echinococcosis (CE) and alveolar echinococcosis, AE.

	Sensors measurements		
	CE	AE	Total
Number of volunteers	24	14	38
Male/Female	5/19	7/7	12/26
Age: 18-29/30-49/≥ 50	4/14/6	0/4/10	4/18/16
Smoking	1	2	3

Table 4.12: Statistical data of the study groups included in the comparative study between cystic echinococcosis (CE) and alveolar echinococcosis (AE).

4.3. Conclusion

The Bio-VOC^{TM} samplers (Markes International, UK) were selected for the collection of the breath samples provided by the volunteers of this study because of important features such as simplicity of the sampling procedure that can be performed with minimal training and without the need of attendance from medically qualified staff, and the possibility to capture the alveolar part of the breath, which is most likely to contain the breath VOCs characteristic to the state of the body.

After setting up the breath sampling protocol to be followed at all breath samples collection sites in order to avoid artefacts introduced by differences in the sampling procedure, breath samples were collected from patients diagnosed with Dengue (Colombia), Leishmaniasis (Tunisia) and Echinococcosis (Tunisia as endemic region and Poland as low prevalence region), as well as from a group of control volunteers recruited among the medical staff of the clinics where the patients were attended, which were age and gender matched with the patients as much as possible.

The results of the breath samples analysis with analytical equipment and chemical gas sensors will be presented in the following chapters.

4.4. References

1. Miekisch, W.; Schubert, J.K.; Noeldge-Schomburg, G.F. Diagnostic potential of breath analysis--focus on volatile organic compounds. *Clinica chimica acta; international journal of clinical chemistry* **2004**, *347*, 25-39.

2. Rattray, N.J.; Hamrang, Z.; Trivedi, D.K.; Goodacre, R.; Fowler, S.J. Taking your breath away: Metabolomics breathes life in to personalized medicine. *Trends in biotechnology* **2014**, *32*, 538-548.

5

CHAPTER

5. BREATH BIOMARKERS IDENTIFICATION

This chapter presents the results of exhaled breath samples analysis with standard GC-Q/TOF analytical equipment. The putative breath biomarkers for each infectious tropical disease studied (Dengue, Leishmaniasis and Echinococcosis) were identified, and their possible origin during body infection was discussed. Discrimination models built with the identified biomarkers were moreover assessed.

5.1. Analytical Studies and Biomarkers Identification

Analytical studies of the breath sample were performed employing a 7890A gas chromatograph (GC) coupled to a 7200 quadruple time of flight (Q-TOF) mass spectrometer (Agilent Technologies, Santa Clara, CA, USA).

For analyzing the breath samples stored in the sorbent tubes, the Tenax TA material storing the breath volatiles was transferred into a 20 mL glass vial that was sealed with a septum and introduced for 20 min in an oil bath placed on a temperature-controlled hotplate heated at a suitable temperature (200 ºC were used in the case of the samples from the Dengue experiment, while 100 ºC were used in the case of the samples from the Leishmaniasis and Echinococcosis experiments). This procedure caused desorption of the VOCs trapped by the sorbent material, which formed a headspace above the Tenax material inside the sealed vial. Solid Phase Micro-Extraction (SPME) with Divinilbenzene/Carboxene/Polydimethylsiloxane (DVB/CAR/PDMS) fiber, introduced for 30 min in the headspace formed by the released breath volatiles inside the vial, was used to capture and concentrate the desorbed VOCs and to inject them into the GC/Q-TOF splitless port for analysis. The oven conditions of the chromatograph were:

desorption time: 1 min, desorption temperature: 250 ºC. The oven program was set as follows: initial temperature: 50 ºC, 10 ºC/min ramp until 155 ºC, 20 ºC/min ramp until 270 ºC, 10 min at 270 °C. Mass spectrometry measurements were performed by electron impact ionization, with 70 eV electron energy and the temperature source held at 230 ºC. Mass-to-charge ratios between 35 and 400 m/z were acquired at 5 spectra/s rate. Chromatograms deconvolution was processed employing the Unknown Analysis software (Qualitative and Quantitative Analysis B.07.00, Unknown Analysis, Agilent Technologies, Santa Clara, USA) operated in the automatic mode, with a match factor set to 70. Compounds identification was achieved using the NIST 14 mass spectral library.

The experimental flow cycle employed for the analysis of the breath samples stored in the Tenax sorbent tubes with the GC/Q-TOF equipment is shown in **Figure 5.1**.

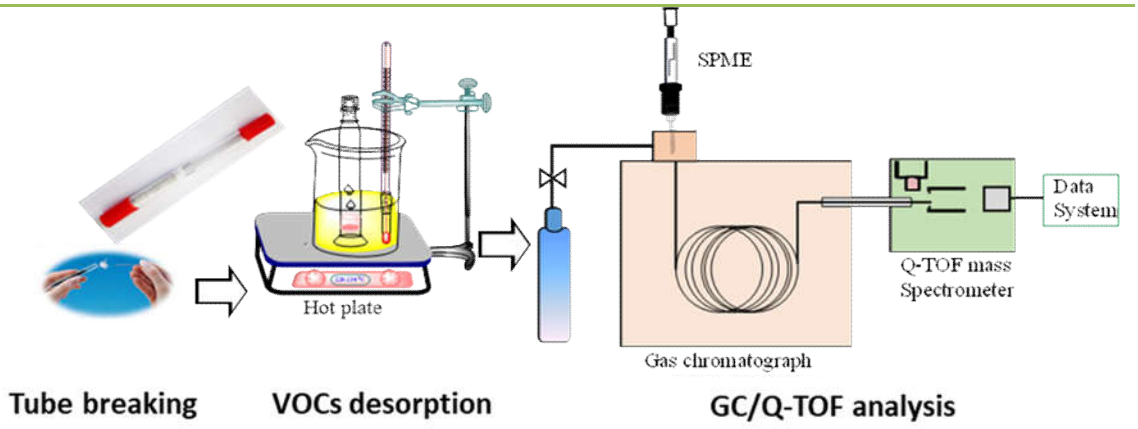

Figure 5.1: Experimental flow cycle employed for breath samples analysis with the analytical equipment

As a typical example, chromatogram obtained from the analysis of different breath samples is shown in **Figure 5.2**. On the other hand, several breath samples provided by the same volunteer that were analyzed at established time intervals (every six month)

over a prolonged period of time (two years) in order to determine the maximum storage time of the samples in the Tenax tubes without significant losses, revealed a suitable storing period of at least 1.5 years.

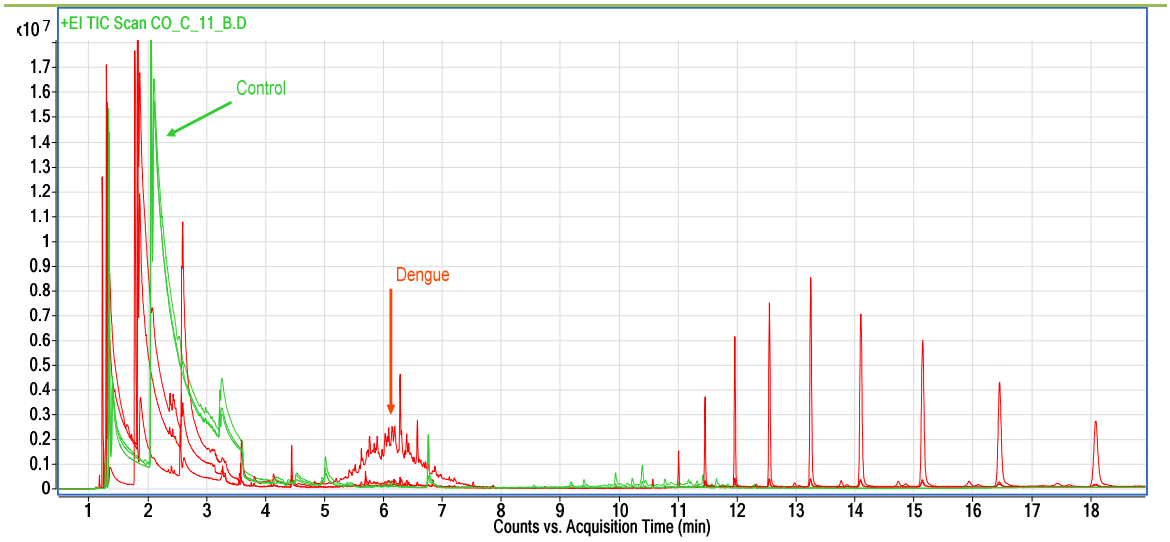

Figure 5.2: Typical chromatograms acquired by GC-Q/TOF. The red chromatogram was acquired from the analysis of the breath composition of a Dengue patient, and the green chromatogram from the analysis of the breath composition of a control volunteer.

It is noted that the chromatograms resulted from the breath samples of patient (Dengue-green), and control (red) revealed significant differences between the breath compositions of the two subjects.

The putative breath biomarkers of the studied diseases were identified applying the two-tailed t-test for normally distributed data (the normal data distribution is shown in **Figure 5.3**). A standard cut-off value $\alpha = 0.05$ was used for finding statistical significant differences between the patients and the control groups of each disease. The confounding factors assessed in this study for disregarding from the initial list of compounds those affected by external conditions were volunteers' gender (for all studies) and age (with the exception of the AE study, because as explained in Chapter 4, the AE and CAE groups could not be age-matched). The three defined age groups were:

young (18-29 years), middle-aged (30-49 years), and senior (> 50 years). Smoking habit was not assessed as a confounding factor because of the low number of smoking volunteers that participated in this study.

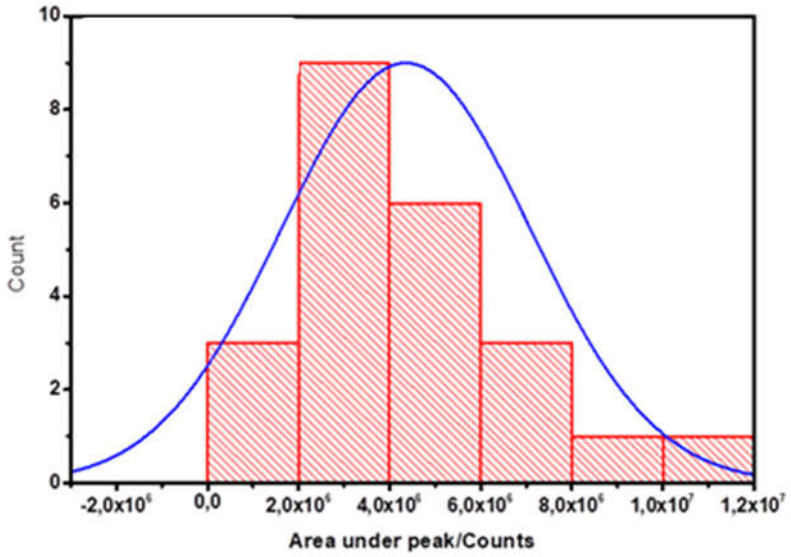

Figure 5.3: Representative example of one of the compounds (1-tridecene) identified as breath biomarker for CE, showing the normal distribution of the data.

5.2. Dengue Breath Biomarkers

The chemical analysis of the breath samples of 16 Dengue patients and 17 healthy controls identified 104 compounds in the majority of the breath samples. Among them, six compounds were found to have statistically significant different concentrations between the Dengue and Control groups. These compounds, presented in **Table 5.1**, were identified in the breath of at least 80% of the volunteers from each study group, and could represent putative breath biomarkers of Dengue disease. Four of them (styrene, toluene, 1-acetyl-1H-benzotriazole and 2-ethylsulfonyl ethanol) increased their concentration in the exhaled breath as a consequence of the disease, while the other two (n-propyl acrylate and 1-undecyne) were exhaled in lower concentrations as compared

with the normal state (**Figure 5.4**). The box plots drawn with their abundance in the breath of each patient are shown in **Figure 5.5**.

VOC	Compound	CAS No.	m/z	R.T	p-value
VOC01	Toluene	629-20-9	104.0631	3.253	0.0002
VOC02	n-propyl acrylate	100-42-5	73.0464	3.276	0.019
VOC03	Styrene	108-88-3	91.0558	4.037	0.014
VOC04	1-undecyne	2243-98-3	67.0539	6.107	0.015
VOC05	1-acetyl-1H-benzotriazole	1135-66-6	161.1329	10.134	0.004
VOC06	2-ethylsulfonyl ethanol	513-12-2	161.1321	10.309	0.011

Table 5.1: Putative Dengue breath biomarkers

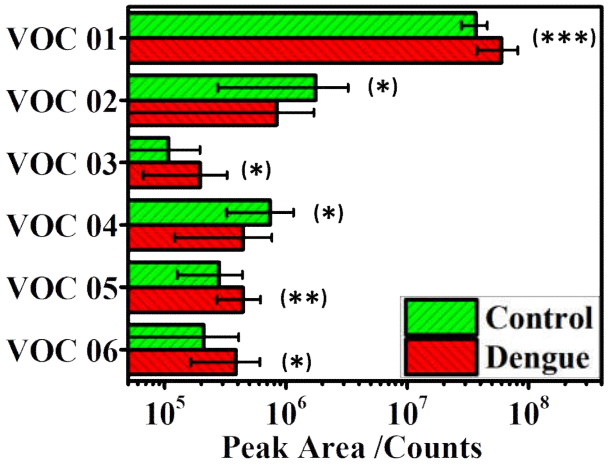

Figure 5.4: Mean values of the abundance (chromatographic peak areas) and error bars of the putative breath biomarkers for Dengue disease identified by GC/Q-TOF analyses. (*) p-value < 0.05; (**) p-value < 0.01; (***) p-value < 0.001.

The diagnosis potential of Dengue disease based on the putative breath biomarkers identified by the GC/Q-TOF studies was assessed by building a discrimination model employing the Discriminant Function Analysis (DFA) pattern recognition algorithm. The DFA model, built with the GC/Q-TOF peak areas of the breath biomarkers, showed very good discrimination of the Control volunteers (only one misclassified sample), whereas several Dengue patients were misclassified by the model (**Figure 5.6a**).

Volunteers' classification, calculated using leave-one-out cross-validation, achieved 84.4% accuracy, 94.1% specificity and 75% sensitivity.

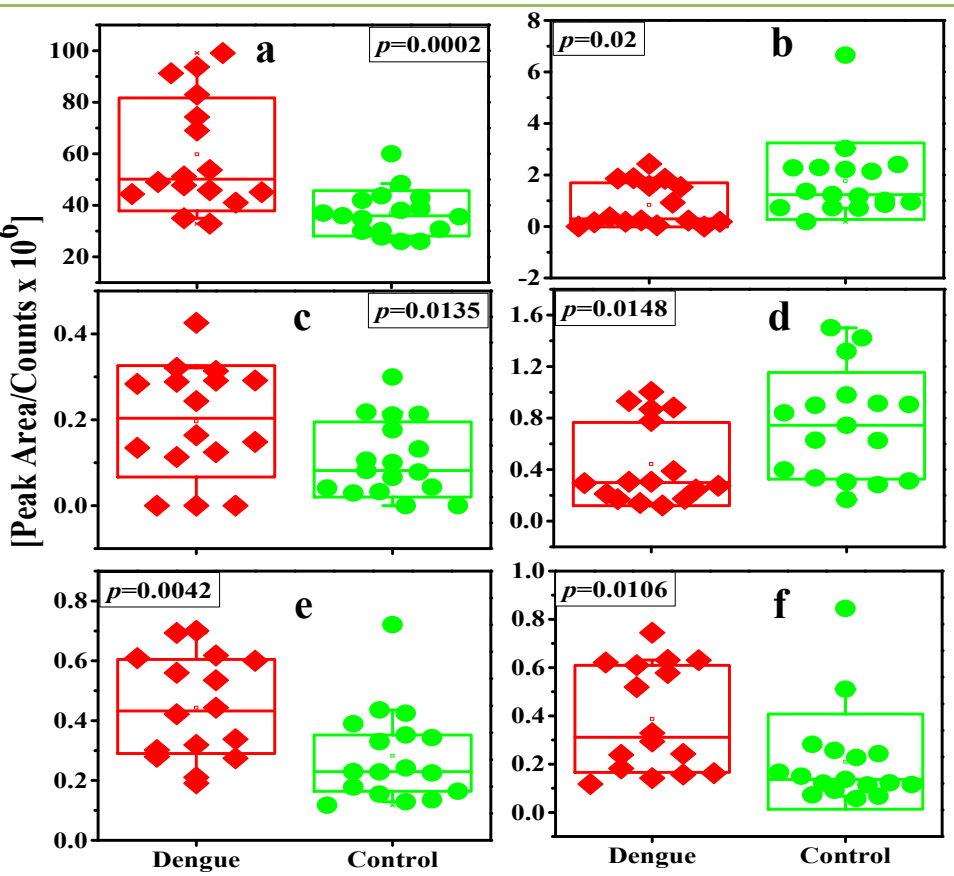

Figure 5.5: Box plots obtained with the abundances of the Dengue biomarkers: (a) VOC01; (b) VOC02; (c) VOC03; (d) VOC04; (e) VOC05; (f) VOC06. Each patient is represented by one point in the box plots.

The area under curve (AUC) of the receiver operating characteristic (ROC) curve constructed with the values of the first canonical variable (CV1) of the DFA model was 90.8% (**Figure 5.6b**), confirming the very good classification between Dengue and Control volunteers. Volunteers' classification based on confounding factors such as gender and age achieved 54.5% and 33.3% accuracy, respectively, indicating that the breath biomarkers identified for Dengue disease in this study are not influenced by confounding factors.

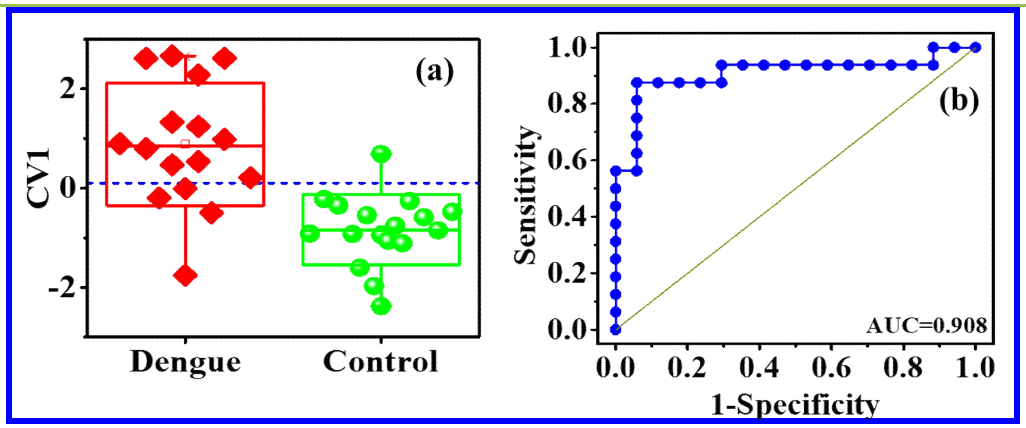

Figure 5.6. Classification between Dengue and Control volunteers using the breath biomarkers: (a) Box plot of the first canonical variable (CV1) of the DFA model calculated with the peak areas of the biomarkers identified by GC/Q-TOF studies; each patient is represented by one point in the box plot; the dashed line represents the classification border between the two groups, Dengue being estimated above the dashed line and Control below the dashed line; (b) ROC curve constructed with the CV1 of the DFA model, yielding AUC = 90.8%.

A rationale for the putative Dengue breath biomarkers identified in this study is next presented.

Previous studies claimed that oxidative stress has a prime importance in the pathogenesis of Dengue infection [1,2]. In this regards, two of the identified biomarkers, *styrene* and *toluene*, are among the most significant compounds associated with oxidative stress [3,4]. Changes in the concentration of styrene and toluene invoke upregulation of various enzymes in the prostaglandin pathway that plays a critical role in the generation of inflammatory response as a consequence of disease onset, expressed by the generation of VOCs-induced oxidative stress markers [1,4]. Such oxidative stress can lead to lipid peroxidation that, mediated by hydroxyl radicals (OH*), possesses potential endothelial cell injury during Dengue pathogenesis [1,5].

Being a viral disease, Dengue infection causes an early immunological reaction in humans. In response to the acute inflammation produced by Dengue virus, the

phospholipase enzymes regulate the formation of different anti-inflammatory molecules such as ω-3 polyunsaturated fatty acids (PUFA), which are released from cell membrane phospholipids by phospholipid hydrolysis [6]. The PUFAs fragment into various metabolites such as saturated and unsaturated hydrocarbons, some of them being released through the alveolar breath, and less volatile molecules excreted through other body fluids. Although fatty acid production is a normal process in the human body, the production of some PUFA could be either inhibited or overexpressed during inflammation. This might explain the decrease of *1-undecyne* level (one of the products of PUFA fragmentation) in the exhaled air of Dengue patients.

Moreover, as the pathogenesis of Dengue is host mediated, the infection with Dengue virus induces an elevated cytokine production in T-cells and macrophages in responses to the infection [7-10]. As a result of the unbalance between pro-inflammatory and anti-inflammatory cytokines, endothelial cell lines might be damaged and the energy metabolism and proteins metabolism perturbed, leading to changes in the production of various secondary metabolites such as *n-propyl acrylate* and *1-acetyl-1H-benzotriazole*. N-propyl acrylate can be produced through the decarboxylation of excess acetyl coenzyme A via Krebs cycle in peripheral tissue, and as a secondary metabolite in lipid peroxidation [11]; its decreased level in Dengue patients could be related to the rate of formation and excretion through the alveolar breath. The increased level of the heteroatom 1-acetyl-1H-benzotriazole in Dengue patients is not completely clear, however it might be associated with the RNA genome translation to polyproteins caused by the dengue virus as a consequence of its viral replication in the endoplasmic reticulum of the infected cells [12].

The last biomarker, *2-ethylsulfonyl ethanol*, which showed an increased level in Dengue patients, might be associated with the incomplete metabolism of methionine in the

transmission pathway and with its oxidation in the liver mitochondria coupled with the Krebs cycle [11,13].

5.3. Leishmaniasis Breath Biomarkers

The chemical analysis of the breath samples of 28 Human Cutaneous Leishmaniasis (HCL) patients, simply Leishmaniasis, and 32 healthy controls (CCL) identified approximately 120 chemical compounds in each breath samples. Among them, nine compounds were found in statistically different concentrations between HCL and CCL groups. They are indicated in **Table 5.2** as putative breath biomarkers for HCL. All of them were present in at least 80% of the breath samples from each study group. Importantly, the abundance (area under the chromatographic peak) of all these compounds was higher in the breath of HCL patients as compared with the healthy controls (**Figure 5.7a**). Moreover, the mean variance of these compounds within the HCL group was much smaller than in the case of CCL group, indicating the homogeneity of the abundance of the HCL breath biomarkers in the breath of all patients. Although presenting lower abundance in the CCL group, the higher spread of these compounds in the controls group is due to the higher variability of the normal state. The diagnostic potential of the breath biomarkers to discriminate between HCL and CCL was assessed by building classification models based on the DFA algorithm using as input different biomarkers combinations.

VOCs	Compounds	CAS No	m/z	R.T	*p*-value
VOC 01	2,2,4-trimethyl pentane	540-84-1	57.05	4.35	0.028
VOC 02	4-methyl-2-ethyl-1-pentanol	106-67-2	67.05	4.9	0.042
VOC 03	Methylvinyl ketone	78-94-4	43.05	5.28	0.015
VOC 04	Nonane	1184-2	43.05	5.99	0.02
VOC 05	2,3,5-trimethyl hexane	1069-53-0	85.01	6.53	0.012
VOC 06	Hydroxy-2,4,6-trimethyl-5-(3-methyl-2 butenyl) cyclohexyl) methylacetate	1139-17-9	81.06	9.50	0.001
VOC 07	Octane	111-65-9	57.05	9.75	0.008
VOC 08	3-ethyl-3-methylheptane	17302-01-1	71.06	10.08	0.01
VOC 09	2-methyl-6-methylene-octa-1,7-dien-3-ol	22459-10-5	67.05	10.86	0.03

Table 5.2: Putative breath biomarkers for human cutaneous leishmaniasis (HCL) identified in the present study.

The DFA classification model built with the abundances of only two biomarkers (VOC03 and VOC06) yielded 80% accuracy, 71.4% sensitivity and 87.5% specificity, while the DFA classification model built with the abundances of three biomarkers (VOC01, VOC06 and VOC07) yielded 80% accuracy, 75% sensitivity and 84.5% specificity (**Figure 5.7b**), revealing the remarkable discrimination capability of the breath biomarkers between the study groups.

However, not all VOC biomarkers are equally significant for distinguishing between the diseased and healthy states. This is evidenced by the correlation matrix of biomarkers abundances (**Figure 5.7c**), which indicates that several biomarkers are highly correlated with each other (VOC03, VOC04 and VOC05), while others (VOC02 and VOC06) showed a negative correlation with the first ones. On the other hand, one biomarker (VOC07) showed a general correlation with almost all VOCs (with the exception of

VOC02 and VOC06), while VOC08 and VOC09 exhibited positive correlation with all the other biomarkers.

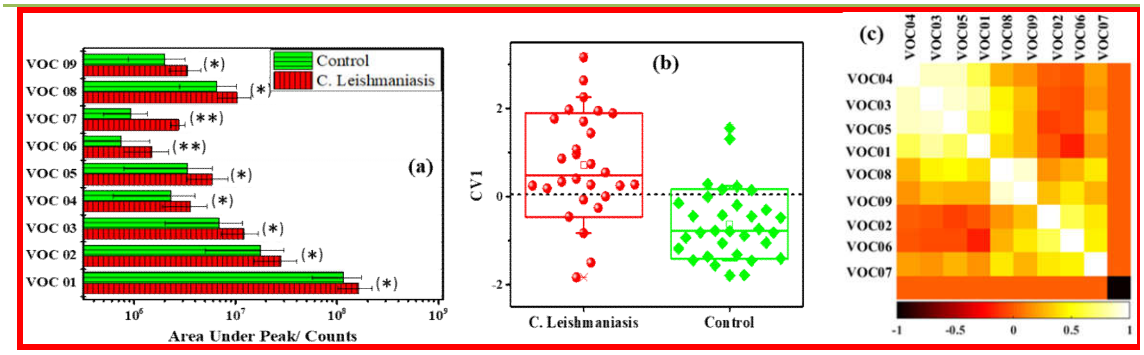

Figure 5.7: (a) Abundance of the HCL breath biomarkers. (*) $p < 0.05$; (**); $p < 0.01$; (b) Box plot of the first canonical variable (CV1) of the DFA model built with the abundances of three biomarkers (VOC01, VOC06 and VOC07 in **Table 5.2**); each volunteer is represented by one point in the box plot; the dashed line represents the threshold classification line between the two groups, HCL patients being estimated above the dashed line and healthy controls below the dashed line; (c) Biomarkers correlation map; (+1), (-1) and (0) indicate maximum positive, maximum negative, and no correlation, respectively.

This explains why the DFA model built with the abundances of all biomarkers presented a lower classification potential (66.7% accuracy) than the models built with a limited number of selected biomarkers.

An attempt to elucidate the biochemical processes that originated the biomarkers identified in the present study is presented below.

First signs of lesions due to HCL, a widely distributed vector-borne disease that is never fatal, even if non-treated, are characterized by the appearance of a small erythema at the site of a sandfly bite. This erythema develops into a papule and nodule and the lesion becomes ulcerated. Both innate and adaptive immune systems form together the driving forces, which shape the disease outcome. The initial interaction with the innate immune

cells shapes the subsequent effector response. Effector function of activated CD4+ T helper cells is an integral component in determining the course of the disease. A Th1-like response activates macrophages to clear the parasite. The cascade induced by interferon gamma (IFN-γ) in infected macrophages results in the production of Reactive Oxygen Species (ROS) that have the ability to kill intracellular *Leishmania*. In addition to ROS, IFN-γ and tumor necrosis factor (TNF) synergistically induce Nitric Oxide Synthase (iNOS) in macrophages, and Nitric Oxide (NO) production further promotes effective parasite killing. The increased IFN-γ production to elevate ROS level for controlling parasite invasion is associated with increased inflammatory reaction and development of cutaneous ulcers in the skin [14]. The imbalance of the general equilibrium between the formation and deactivation of ROS and free radicals can boost oxidative stress in the body. Thus, ROS can damage cellular and subcellular structures such as lipids, and induce upregulation of cytochrome p-450 enzymes to catalyze the oxidation of organic chemicals in the human tissues [15]. More specifically, lipid peroxidation occurs as a result of oxidative degradation of lipids, when free radicals attach themselves to electrons in cell membranes and thereby damage components of the cell membrane [16]. Due to the presence of reactive hydrogen of the methylene groups between the multiple double bonds, polyunsaturated fatty acids are commonly affecting the cell components [17-19]. For example, aldehyde, ethane, pentane, malondialdehyde, acrolein, hydroxynonenal and crotonaldehyde are well known PUFA products in the lipid peroxidation process [18].

Nevertheless, the origin of the exhaled breath VOCs that were putatively identified in the breath of HCL patients is not completely elucidated. Although several biochemical pathways are possible, the peroxidation of PUFAs during the pathophysiology of HCL

might be considered as the main source of aliphatic hydrocarbons in the exhaled breath, such as *nonane* and *octane*.

Earlier reports showed that enhanced levels of ethane and pentane can be associated to lipid peroxidation during oxidative stress in critical body conditions [20,21]. The generation of branched alkanes such as *2,2,4-trimethylpentane*, *2,3,5-trimethylhexane* and *3-ethyl-3-methylpentane* might be also related to the byproducts of PUFA peroxidation. Nevertheless, it is argued that oxidative stress mechanism in mammals cannot produce straight chained or branched alkanes, and hence such branching alkanes occur during the isoprenoid synthesis [22]. On the other hand, alkanes are also present in the environment and are inhaled on a daily basis, being broken in the liver by the cytochrome p-450 enzymes, therefore the exogenous origin of these biomarkers cannot be discarded.

Alcohols such as *4-methyl-2-ethyl-1-pentanol* and *2-methyl-6-methylene-octa-1,7-dien-3-ol* might originate from the hydrocarbon metabolism. This could be either due to the alcohol metabolism catalyzed by cytochrome p-450 enzymes in the liver, or due to the oxidation of several different alcohols by alcohol dehydrogenase in the body [23]. Moreover, byproducts of lipid peroxidation might underway oxidation when they are catalyzed by the peripheral cell enzymes, being then exhaled through breath.

Ketones such as *methylvinyl ketone* are related to excessive fatty acid oxidation due to metabolic changes produced by HLC disease onset, when the body uses fat instead of glucose for energy. For instance, acetone is produced in the liver by decarboxylation of acetoacetate during lipolysis as a secondary source of energy for the body [18]. Thus, methylvinyl ketone might be produced as a result of secondary metabolites in lipid peroxidation. *Hydroxy-2, 4, 6-trimethyl-5-(3-methyl-2-buytenyl)cyclohexylmethylacetate*

belongs to the branched ketone group and might be also related to excessive oxidation of fatty acids.

Although deeper investigations are required to fully understand the origin of the HCL breath biomarkers identified in this study, based on the above analysis they are associated with biochemical changes linked to molecular processes such as oxidative stress, lipid metabolism, cytochrome p-450 enzymes, and carbohydrate metabolisms, produced in the body during pathogen infections with leishmania parasite.

5.4. Echinococcosis Breath Biomarkers

Exhaled breath samples collected from Cystic Echinococcosis (CE), Alveolar Echinococcosis (AE), and healthy controls for each group (here denominated CCE and CAE, respectively), were subjected to two independent analyses. Breath samples of 55 volunteers (23 patients with CE and 32 CCE controls) were measured for the identification of CE biomarkers, whereas breath samples of 21 volunteers (13 patients with AE and 8 CAE controls) were measured for the identification of AE biomarkers. The chemical analyses revealed approximately 120 compounds in each breath sample. When comparing the CE and AE groups versus their corresponding control groups, it was found that two VOCs in the exhaled breath were present in statistically different concentrations between CE and CCE groups, while seven VOCs were found to be different between the AE and CAE groups. These compounds, presented in **Table 5.3**, represent putative breath biomarkers for CE and AE, respectively. The abundance of these compounds in the breath samples of all volunteers from each study group is shown in **Figure 5.8**.

Disease	VOCs	Chemical Name	Family	*p*-value
Cystic Echinococcosis	VOC 01	1-Tridecene	Alkene	0.027
	VOC 02	(E)-13-Docosenoic acid	Unsaturated carboxylic acid	0.045
Alveolar Echinococcosis	VOC 03	Hexadecane	Unbranched alkane	0.032
	VOC 04	Heptadecane	Unbranched alkane	0.029
	VOC 05	Eicosane	Unbranched alkane	0.027
	VOC 06	11-(pentan-3-yl)henicosane	Branched alkane	0.033
	VOC 07	Tetratriacontane	Unbranched alkane	0.046
	VOC 08	2-methyloctacosane	Branched alkane	0.049
	VOC 09	Hentriacontane	Unbranched alkane	0.044

Table 5.3: Putative breath VOC biomarkers found for Cystic Echinococcosis and Alveolar Echinococcosis.

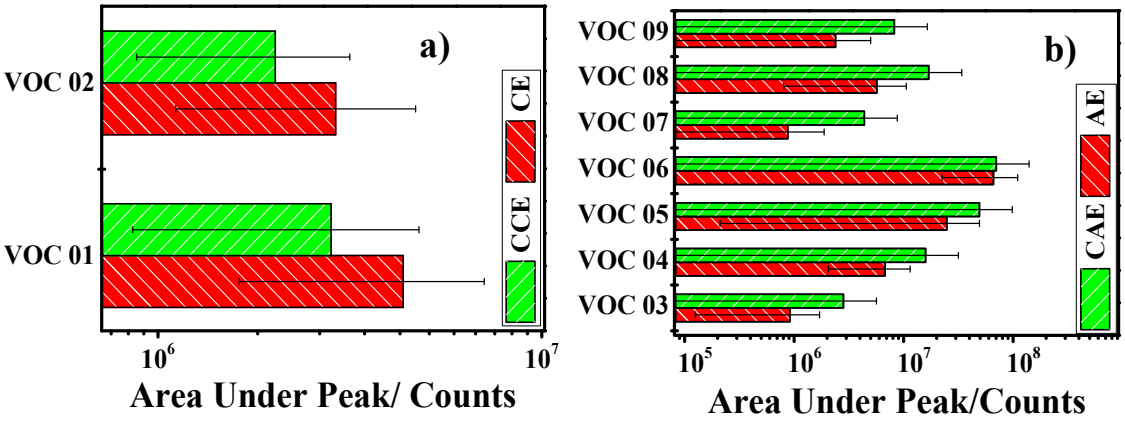

Figure 5.8: Mean values of the abundance of the breath biomarkers found in this study for: a) Cystic Echinococcosis; b) Alveolar Echinococcosis. The error bars represent the standard error of the mean.

The diagnostic potential of the identified breath biomarkers was assessed by building classifications model based on Discriminant Function Analysis. The DFA model built with the abundances of the two breath biomarkers of CE showed a fair discrimination between the CE and CCE volunteers (60.9% sensitivity, 68.8% specificity and 65.5% accuracy), while the DFA model built with two AE biomarkers (VOC03 and VOC05 in

Table 5.3) showed a good discrimination between the AE and CAE volunteers (92.3% sensitivity, 62.5% specificity and 80.9% accuracy). The box plot of the DFA classification model built with these two AE biomarkers, as well as ROC curve analysis that provided a maximum diagnostic accuracy of 77.9%, are presented in **Figure 5.9**.

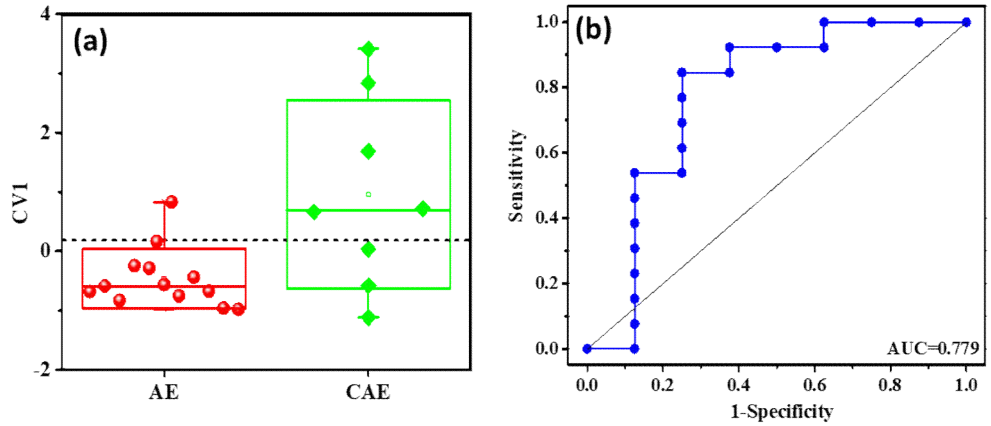

Figure 5.9: Classification between AE and CAE volunteers using two AE breath biomarkers (VOC03 and VOC05 in **Table 5.3**): (a) Box plot of the first canonical variable (CV1) of the DFA model calculated with the peak areas of the two biomarkers; each patient is represented by one point in the box plot; (b) ROC curve constructed with the CV1 of the DFA model, yielding AUC = 77.9%.

An important remark from the closer examination of **Figure 5.8** is that the concentration of all CE biomarkers increased in the CE group as compared with their corresponding controls (CCE), whereas the concentration of all AE biomarkers decreased in the AE group as compared with their corresponding controls (CAE). It is also remarkable that the putative biomarkers found for CE and AE are totally different for these two forms of the disease. Thus, even though these diseases are from the same family of *Echinococcus*, the pathogenesis of CE and AE infectious and the changes that they produce in the body chemistry appear to be completely different [24,25]. The identified biomarkers belong to the family of aliphatic hydrocarbons, except (E)-13-docosenoic acid that is a monounsaturated fatty acid. A discussion about the possible

origin of the breath biomarkers for each type of the Echinococcosis disease is presented below.

Cystic Echinococcosis

Echinococcus granulosus infection is always asymptomatic and persists without noticeable pathologic events for a long period of time while a hydatid cyst is developed for avoiding host immune response. As a result, the parasite modulates host immune reaction to reduce the host response to pathogen invasion [26]. More specifically, the Antigen B from the hydatid cyst fluid guarantees parasite survival by suppressing human neutrophil chemotaxis, inhibiting lipid detoxification and affecting the metabolism by fatty acid binding, as well as by increasing cytokine dysfunctions [27]. Therefore, the infection induces an immune imbalance in the hepatic tissue leading to sever destruction of its architecture due to intensive inflammatory infiltrations in various sites of the body [28]. The pro-oxidant species tend to enhance the formation of reactive superoxide species in order to destroy the pathogen that in some cases introduces physiological disturbance in the cells that produce oxidative stress. Important metabolic processes such as the central carbon catabolism, protein synthesis and different cellular processes are therefore perturbed. As a result, alkene derivatives are thought to be generated from chain cleavage and recurrent oxidation products in the process of lipid peroxidation [29].

The long chain hydrocarbon, *1-tridecene*, might originate as an intermediary specie from the carbon catabolism in the process of acetyl coenzyme A decarboxylation, and its presence in CE pathogenesis might be related to enhanced production of inflammatory molecules during chronic echinococcal infection at different parts of the body, mainly in the liver [28,30].

(E)-13-Docosenoic acid belongs to the family of monounsaturated hydrocarbons with polar carboxylic functional group, and is related to lipid peroxidation of polyunsaturated fatty acids during and after monocyte adhesion to endothelial cells to enable parasite survival in a pro-oxidant environment. Its presence in the exhaled breath might be associated with the long chain ω-9 polyunsaturated fatty acids generation as a result of parasite induced cytokine inflammatory activation and the oxidative damage of the cell membrane lipids [31].

Alveolar Echinococcosis

In the case of Alveolar Echinococcosis infection, *hexadecane*, *heptadecane* and *eicosane* might be a result of oxidative degradation of polyunsaturated fatty acids inflicted by oxidative stress during Echinococcal chronic inflammatory infection [21,32]. They are all straight chain alkanes and their presence in the exhaled breath can be associated with the peroxidation of various PUFA such as linoleic and linolenic acids, which are cell membrane components [33].

The long chain alkanes *11-(pentan-3-yl)henicosane*, *tetratriacontane*, *2-methyloctacosane* and *hentriacontane* can also be produced from the lipid peroxidation of long chain PUFAs. These VOCs are generated as a result of excess reactive oxygen species due to either overproduction of pro-oxidants, or insufficient activity of antioxidants in the body. During the process of PUFA peroxidation, there is a scission of alkane fragments extending from the methyl end of the fatty acid to the double bond. Depending on the nature of the initial fatty acid, alkane molecules such as ethane and pentane are released by the oxidative damage of ω-3 polyunsaturated fatty acid and ω-6-polyunsaturated fatty acid, respectively [34,35]. These molecules are partly metabolized in the liver by the microsomal oxidizing enzyme associated with the cytochrome P-450

and/or released in the breath, indicating the extent of lipid peroxidation in the body during inflammation [11,34]. Hence, the branched alkanes 11-(pentane-3-yl)henicosane and 2-methyloctacosane might undergo the Cytochrome P-450 metabolic process once they are released as intermediate products of lipid peroxidation of long chain PUFAs.

5.5. Conclusion

The chemical analysis at different time intervals of the composition of several breath samples provided by the same volunteer revealed that the breath volatiles can be stored without significant losses in the Tenax TA sorbent tubes for at least 1.5 years.

The comparison of the breath composition of the volunteers diagnosed with each one of the studied diseases and their corresponding control groups permitted the identification of putative breath biomarkers of these diseases. Six biomarkers were identified for Dengue (toluene, n-propyl acrylate, styrene, 1-undecyne, 1-acetyl-1H-benzotriazole, and 2-ethylsulfonyl ethanol), nine biomarkers were identified for Cutaneous Leishmaniasis (2,2,4-trimethyl pentane, 4-methyl-2-ethyl-1-pentanol, methylvinyl ketone, nonane, 2,3,5-trimethyl hexane, hydroxy-2,4,6-trimethyl-5-(3-methyl-2 butenyl) cyclohexyl) methylacetate, octane, 3-ethyl-3-methylheptane, and 2-methyl-6-methylene-octa-1,7-dien-3-ol), two biomarkers were identified for Cystic Echinococcosis (1-tridecene, and (E)-13-docosenoic acid) and seven biomarkers were identified for Alveolar Echinoccocosis (hexadecane, heptadecane, eicosane, 11-(pentan-3-yl)henicosane, tetratriacontane, 2-methyloctacosane, and hentriacontane). By comparing them, it was observed that *aromatic compounds* were identified as biomarkers only for Dengue disease, *esters* for Dengue and Cutaneous Leishmaniasis,

alcohols and one *ketone* for Cutaneous Leishmaniasis, *alkanes* for Cutaneous Leishmaniasis and Alveolar Echinococcosis, one *alkene* for Dengue and a different one for Cystic Echinococcosis, and one *acid* for Cystic Echinococcosis. It is important to note also that, although Cystic Echinococcosis and Alveolar Echinococcosis are from the same family of *Echinococcus*, the putative biomarkers found for CE and AE were totally different for these two forms of the disease, indicating that the pathogenesis of CE and AE infectious and the changes that they produce in the body chemistry appear to be completely different.

Classification models based on the DFA algorithm built with the putative biomarkers identified in this study yielded fair to good discrimination accuracies: 84.4% for Dengue diagnosis, 80% for Cutaneous Leishmaniasis diagnosis, 65.5% for Cystic Echinococcosis diagnosis, and 80.9% for Alveolar Echinococcosis diagnosis (all these statistical values were calculated through leave-one-out cross-validation).

The possible origin of the biomarkers was discussed in light of previous reports related with infectious diseases and metabolic studies. Further investigation of their origin could provide new insight in the metabolism, biochemical pathway and disease pathogenesis, which presumably could lead to the development of improved therapeutic strategies. The biomarkers identified by the analytical studies formed the basis for a rational selection of the MNPs-ligands nanoassemblies that possess high affinity to them, which were employed as sensing materials for the chemical gas sensors arrays that were assessed in the next chapter of my thesis for the diagnosis of the studied tropical diseases from exhaled breath analysis.

5.6. Pattern Recognition Applied in this Chapter

The Discriminant Function Analysis was used for building the classification models for diseases diagnosis. DFA is a supervised linear pattern recognition algorithm that calculates new, orthogonal variables (called Canonical Variables or CVs) as a linear combination of the input variables, under the constrain of minimizing the distances between the data points of the same class, while maximizing the distances between the data points of different classes. Linear discriminant analysis (LDA) finds a linear discriminant function (LDF) which is a linear combination of the original variables, such that the ratio of the between –class scatter and within-class scatter is maximized. Thus, the most discriminative DFA variable is the first canonical variable (CV1), for two-group classification cases (e.g., classification between the groups of patients diagnosed with one of the studied diseases and their corresponding controls, and between male and female groups) the mean values on the CV1 axis of all the samples from each group were calculated, and the separation between the two groups was given by the orthogonal line drawn on the CV1 axis that passed through the median point between the mean values of the two groups. For the separation between three groups (i.e., when volunteers age was considered as confounding factor), the classification of any sample was provided by the minimum distance from that sample to the centers of each group on the (CV1, CV2) axis, as the second canonical variable (CV2) represents an additional dimension of differentiation when three groups are to be distinguished [36].

The DFA models were built with the abundances (peak areas) of the breath biomarkers. As DFA is a supervised algorithm, the accuracy of the models was calculated applying leave-one-out cross-validation to avoid model overtraining while reducing its

generalization potential for the identification of new samples. Thus, while one sample was taken out from the available data set, the DFA classification model was built with the rest of the samples from the data set, and the sample taken out was then blindly projected onto the DFA model, which predicted its class. Applying this procedure for all the samples from the data set, allowed to calculate the classification accuracy, sensitivity and specificity from the true positives (TP), true negatives (TN), false positives (FP) and false negatives (FN) values, as follows: accuracy = (TP+TN)/(TP+TN+FP+FN); sensitivity = TP/(TP+FN); specificity = TN/(TN+FP) [37]. The area under curve (AUC) of the receiver operating characteristic (ROC) curve was constructed with the values of the first canonical variable (CV1) of the DFA models. The ROC curve is plotted as a function of true positive rate (sensitivity) versus false positive rate (1-specificity) for different cut-off points, whereas the area under the curve, defined as the area of the ROC curve minus the random result, measures how well the diagnostic test (accuracy) distinguished the diseased from the normal healthy state.

5.7. References

1. Seet, R.C.; Lee, C.-Y.J.; Lim, E.C.; Quek, A.M.; Yeo, L.L.; Huang, S.-H.; Halliwell, B. Oxidative damage in dengue fever. *Free Radical Biology and Medicine* **2009**, *47*, 375-380.
2. Olagnier, D.; Amatore, D.; Castiello, L.; Ferrari, M.; Palermo, E.; Diamond, M.S.; Palamara, A.T.; Hiscott, J. Dengue virus immunopathogenesis: Lessons applicable to the emergence of zika virus. *Journal of Molecular Biology* **2016**, *428*, 3429-3448.

3. Sati, P.C.; Khaliq, F.; Vaney, N.; Ahmed, T.; Tripathi, A.K.; Banerjee, B.D. Pulmonary function and oxidative stress in workers exposed to styrene in plastic factory: Occupational hazards in styrene-exposed plastic factory workers. *Human & experimental toxicology* **2011**, *30*, 1743-1750.
4. Mögel, I.; Baumann, S.; Böhme, A.; Kohajda, T.; von Bergen, M.; Simon, J.-C.; Lehmann, I. The aromatic volatile organic compounds toluene, benzene and styrene induce cox-2 and prostaglandins in human lung epithelial cells via oxidative stress and p38 mapk activation. *Toxicology* **2011**, *289*, 28-37.
5. Silverman, D.J.; Santucci, L.A. Potential for free radical-induced lipid peroxidation as a cause of endothelial cell injury in rocky mountain spotted fever. *Infection and immunity* **1988**, *56*, 3110-3115.
6. Mathew, A.; Rothman, A.L. Understanding the contribution of cellular immunity to dengue disease pathogenesis. *Immunological Reviews* **2008**, *225*, 300-313.
7. Alayli, F.; Scholle, F. Dengue virus ns1 enhances viral replication and pro-inflammatory cytokine production in human dendritic cells. *Virology* **2016**, *496*, 227-236.
8. John, D.V.; Lin, Y.-S.; Perng, G.C. Biomarkers of severe dengue disease – a review. *Journal of Biomedical Science* **2015**, *22*, 83.
9. Green, S.; Rothman, A. Immunopathological mechanisms in dengue and dengue hemorrhagic fever. *Curr Opin Infect Dis* **2006**, *19*.
10. Bethell, D.B.; Flobbe, K.; Cao, X.T.; Day, N.P.; Pham, T.P.; Buurman, W.A. Pathophysiologic and prognostic role of cytokines in dengue hemorrhagic fever. *J Infect Dis* **1998**, *177*.

11. Miekisch, W.; Schubert, J.K.; Noeldge-Schomburg, G.F.E. Diagnostic potential of breath analysis—focus on volatile organic compounds. *Clinica Chimica Acta* **2004**, *347*, 25-39.

12. Tai, C.-L.; Pan, W.-C.; Liaw, S.-H.; Yang, U.-C.; Hwang, L.-H.; Chen, D.-S. Structure-based mutational analysis of the hepatitis c virus ns3 helicase. *Journal of Virology* **2001**, *75*, 8289-8297.

13. Chen, S.; Zieve, L.; Mahadevan, V. Mercaptans and dimethyl sulfide in the breath of patients with cirrhosis of the liver. *The Journal of Laboratory and Clinical Medicine 75*, 628-635.

14. Oliveira, W.N.; Ribeiro, L.E.; Schrieffer, A.; Machado, P.; Carvalho, E.M.; Bacellar, O. The role of inflammatory and anti-inflammatory cytokines in the pathogenesis of human tegumentary leishmaniasis. *Cytokine* **2014**, *66*, 127-132.

15. Murray, G.I. The role of cytochrome p450 in tumour development and progression and its potential in therapy. *The Journal of pathology* **2000**, *192*, 419-426.

16. Buszewski, B.; Kęsy, M.; Ligor, T.; Amann, A. Human exhaled air analytics: Biomarkers of diseases. *Biomedical Chromatography* **2007**, *21*, 553-566.

17. Broza, Y.Y.; Mochalski, P.; Ruzsanyi, V.; Amann, A.; Haick, H. Hybrid volatolomics and disease detection. *Angewandte Chemie - International Edition* **2015**, *54*, 11036-11048.

18. Miekisch, W.; Schubert, J.K.; Noeldge-Schomburg, G.F. Diagnostic potential of breath analysis--focus on volatile organic compounds. *Clinica chimica acta; international journal of clinical chemistry* **2004**, *347*, 25-39.

19. Amal, H.; Shi, D.Y.; Ionescu, R.; Zhang, W.; Hua, Q.L.; Pan, Y.Y.; Tao, L.; Liu, H.; Haick, H. Assessment of ovarian cancer conditions from exhaled breath. *International Journal of Cancer* **2015**, *136*, E614-E622.

20. Kneepkens, C.M.; Lepage, G.; Roy, C.C. The potential of the hydrocarbon breath test as a measure of lipid peroxidation. *Free radical biology & medicine* **1994**, *17*, 127-160.

21. Aghdassi, E.; Allard, J.P. Breath alkanes as a marker of oxidative stress in different clinical conditions. *Free Radical Biology and Medicine* **2000**, *28*, 880-886.

22. Kwak, J.; Preti, G. Volatile disease biomarkers in breath: A critique. *Current pharmaceutical biotechnology* **2011**, *12*, 1067-1074.

23. Hakim, M.; Broza, Y.Y.; Barash, O.; Peled, N.; Phillips, M.; Amann, A.; Haick, H. Volatile organic compounds of lung cancer and possible biochemical pathways. *Chemical Reviews* **2012**, *112*, 5949-5966.

24. Nakhleh, M.K.; Amal, H.; Jeries, R.; Broza, Y.Y.; Aboud, M.; Gharra, A.; Ivgi, H.; Khatib, S.; Badarneh, S.; Har-Shai, L.*, et al.* Diagnosis and classification of 17 diseases from 1404 subjects via pattern analysis of exhaled molecules. *ACS Nano* **2017**, *11*, 112-125.

25. Peng, G.; Hakim, M.; Broza, Y.Y.; Billan, S.; Abdah-Bortnyak, R.; Kuten, A.; Tisch, U.; Haick, H. Detection of lung, breast, colorectal, and prostate cancers from exhaled breath using a single array of nanosensors. *British Journal Of Cancer* **2010**, *103*, 542.

26. Wang, H.; Li, J.; Pu, H.; Hasan, B.; Ma, J.; Jones, M.K.; Zheng, K.; Zhang, X.; Ma, H.; McManus, D.P.*, et al.* Echinococcus granulosus infection reduces

airway inflammation of mice likely through enhancing il-10 and down-regulation of il-5 and il-17a. *Parasites & Vectors* **2014**, *7*, 522.

27. Grubor, N.M.; Jovanova-Nesic, K.D.; Shoenfeld, Y. Liver cystic echinococcosis and human host immune and autoimmune follow-up: A review. *World journal of hepatology* **2017**, *9*, 1176.
28. Vatankhah, A.; Halász, J.; Piurkó, V.; Barbai, T.; Rásó, E.; Tímár, J. Characterization of the inflammatory cell infiltrate and expression of costimulatory molecules in chronic echinococcus granulosus infection of the human liver. *BMC Infectious Diseases* **2015**, *15*, 530.
29. Sies, H. Biochemistry of oxidative stress. *Angewandte Chemie International Edition in English* **1986**, *25*, 1058-1071.
30. Siracusano, A.; Riganò, R.; Ortona, E.; Profumo, E.; Margutti, P.; Buttari, B.; Delunardo, F.; Teggi, A. Immunomodulatory mechanisms during echinococcus granulosus infection. *Experimental Parasitology* **2008**, *119*, 483-489.
31. Fruhwirth, G.O.; Loidl, A.; Hermetter, A. Oxidized phospholipids: From molecular properties to disease. *Biochim Biophys Acta* **2007**, *1772*, 718-736.
32. Frank Kneepkens, C.M.; Lepage, G.; Roy, C.C. The potential of the hydrocarbon breath test as a measure of lipid peroxidation. *Free Radical Biology and Medicine* **1994**, *17*, 127-160.
33. Van Gossum, A.; Decuyper, J. Breath alkanes as an index of lipid peroxidation. *The European respiratory journal* **1989**, *2*, 787-791.
34. Jeejeebhoy, K.N. In vivo breath alkane as an index of lipid peroxidation. *Free radical biology & medicine* **1991**, *10*, 191-193.

35. Wade, C.R.; van Rij, A.M. In vivo lipid peroxidation in man as measured by the respiratory excretion of ethane, pentane, and other low-molecular-weight hydrocarbons. *Analytical biochemistry* **1985**, *150*, 1-7.

36. Tisch, U.; Schlesinger, I.; Ionescu, R.; Nassar, M.; Axelrod, N.; Robertman, D.; Tessler, Y.; Azar, F.; Marmur, A.; Aharon-Peretz, J. Detection of alzheimer's and parkinson's disease from exhaled breath using nanomaterial-based sensors. *Nanomedicine* **2013**, *8*, 43-56.

37. Peled, N.; Barash, O.; Tisch, U.; Ionescu, R.; Broza, Y.Y.; Ilouze, M.; Mattei, J.; Bunn, P.A.; Hirsch, F.R.; Haick, H. Volatile fingerprints of cancer specific genetic mutations. *Nanomedicine: Nanotechnology, Biology and Medicine* **2013**, *9*, 758-766.

CHAPTER 6

6. EXHALED BREATH ANALYSIS WITH THE CHEMICAL GAS SENSORS

This chapter presents the diagnosis potential of infectious tropical diseases (Dengue, Cutaneous Leishmaniasis and Human Echinococcosis) through the analysis of exhaled breath samples with chemical gas sensor arrays. Both the direct breath measurement approach (which can be employed for on-site measurements) and the indirect breath measurement approach (which is necessary when the collection and measurement sites of the breath samples are different) were evaluated during this study.

6.1. Breath Samples Measurement Setup

Two different approaches were followed to measure the breath samples aiming both direct and indirect breath measurement, for which different setups were designed and fabricated. These setups are next presented.

6.1.1. Direct Breath Measurement Approach

In this approach, the breath samples are directly transferred after collection from the Bio-VOC sampler into the sensors test chamber.

A Teflon test chamber (120×26×10 mm^3 volume) provided with two openings for sample inlet and sample outlet, respectively, was designed and fabricated for the direct breath measurement approach. An electronics circuit board with pin sockets able to accommodate up to 10 chemical gas sensors was introduced inside the test chamber. For performing the breath measurements, the breath sample was directly injected from the Bio-VOC sampler into the sensors test chamber by steadily pushing the plunger during

10 seconds. The output opening of the test chamber was closed immediately after the whole volume of the breath sample was transferred from the Bio-VOC into the test chamber. Each sensing measurement comprised the following cycles: (i) 5 min under continuous synthetic dry air flow (0.5 L/min flow rate) for measuring sensors baseline; (ii) 5 min exposure to the breath sample under stationary conditions; (iii) 30 min under continuous synthetic dry air flow (0.5 L/min flow rate) for cleaning sensors surface and the measurement chamber.

The direct breath measurement setup is shown in **Figure 6.1**.

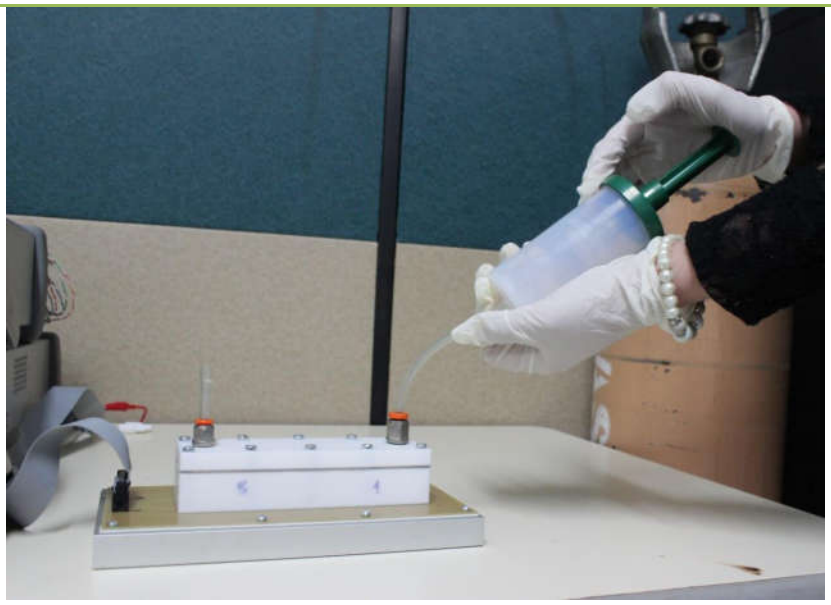

Figure 6.1: Direct breath measurement approach

6.1.2. Indirect Breath Measurement Approach

In this approach it is employed an intermediary step when the exhaled breath sample collected with the Bio-VOC sampler is stored in a sorbent tube before analysis. This

approach was necessary when the samples were measured at a different site than their collection place.

A stainless steel test chamber (70×35×30 mm^3 volume) provided with two openings, one used for sample inlet and for realizing the vacuum inside the test chamber, and the other one for sample outlet, respectively, was designed and fabricated for the indirect breath measurement approach. An electronics circuit board with pin sockets able to accommodate up to 8 chemical gas sensors was introduced inside the test chamber.

In order to analyze the breath sample, the storage tube was cut and the sorbent material was introduced in a 20 ml glass vial that was hermetically sealed. To desorb the breath volatiles trapped by the sorbent material, the vial was heated for 10 min at 270 ºC in a conventional oven (UNE 300, Memmert GmbH, Germany). 10 mL of the headspace formed by the desorbed VOCs inside the sealed vial were extracted with a gas tight sampling syringe (VWR International EuroLab, Spain) and transferred into the test chamber for measurement.

For sample measurement with the chemical gas sensors, at first it was evaluated the injection into a carrier gas of the breath volatiles captured by the gas syringe. Both N_2 and synthetic dry air were assessed as carrier gases, using different flow rates, starting with 100 ml/min. However, sensors response in this continuous flow approach, where the gaseous flow enters the measurement chamber through the inlet opening and immediately exits through the outlet opening, was much smaller than in the case of the stationary measurement approach that was next assessed. In this later approach, low vacuum (~ 600 mbar) condition was created for 5 min inside the sensor test chamber by means of an external electrical pump (Model C5, Electro A.D., Spain) prior to sample

measurement, and the breath volatiles captured by the gas syringe were directly injected into the sensors test chamber in vacuum and measured under stationary conditions for the desired period of time. Thus, by setting sensors exposure time to the breath sample to 320 seconds, which is considerable higher than their exposure time in the continuous flow approach (< 1 min even at the lowest carrier gas flow set), their responses were considerably higher.

Therefore, the stationary approach was further adopted for measuring the breath samples in the indirect measurement approach, which led to the design of the measurement setup shown in **Figure 6.2**. Each breath sample measurement comprised the following cycles: (i) 320 sec under low vacuum conditions (~ 600 mbar); (ii) 320 sec exposure to the breath VOCs under stationary conditions (pressure inside sensors chamber: ~ 875 mbar ± 3%); (iii) 30 min flushing with synthetic dry air (2 L/min flow rate) for sample evacuation and cleaning sensors surface and the measurement chamber.

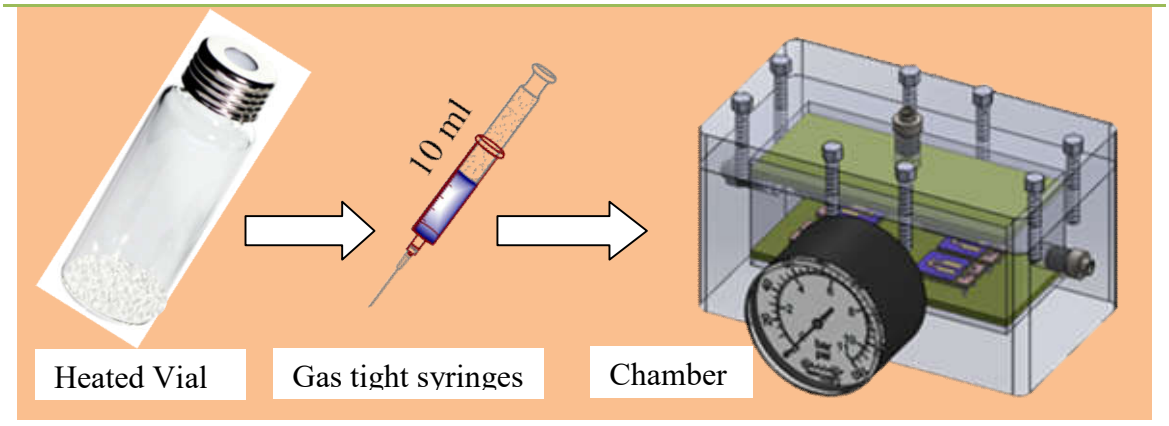

Figure 6.2: Indirect breath measurement approach.

6.2. Sensors Operation

In this study, the sensors were operated in the dynamic mode by switching them successively for short periods of time between the ON (application of DC voltage) and OFF (no DC voltage) states without reaching steady state conditions, in order to assess

their transient responses to the breath VOCs mixture, which contain more information than the static measurements [1].

In the direct breath measurement approach, the sensors were sequentially operated at 5 V for 10 sec in a switching mode, followed by 70 sec of inactivity. During the inactivity of one of the sensors, all the other sensors were operated each one for 10 sec in the mentioned switching mode.

In the indirect breath measurement approach, both during the vacuum stage and breath sample exposure, the sensors were sequentially operated at 8 V for 10 sec in switching mode, followed by 70 sec of inactivity. During the inactivity of one of the sensors, all the other sensors were operated each one for 10 sec in the aforementioned switching mode. For speeding up the cleaning process after sample measurement, the sensors were operated at 10 V for 10 sec followed by 70 sec of inactivity in the same switching mode.

Although a higher voltage span can favor the kinetic reactions that occur between the sensing nanomaterial and the breath volatiles, a lower voltage was applied in the case of the direct breath measurement approach to reduce sensors response due to local condensation of water from the humidified breath sample, which adds a competing conduction mechanism by ionic conduction in addition to the electrons tunnelling mechanism throughout the sensing film, and thus introduces additional noise in the data [2].

Each breath sample measurement comprised four consecutive acquisition cycles, lasting totally for 320 sec. During the whole measurement process, the DC current through the sensors was acquired at a sampling rate of 9 samples/sec for further analysis, so during one measurement cycle 90 data points were acquired for each sensor. For all sensing measurements, a high precision power source (B2902A, Keysight Technologies,

Hungary) was used to apply the desired DC operation voltage to the sensors, and a high-resolution data acquisition system (34972A, Keysight Technologies, Hungary) for acquiring the DC current through the sensors.

The results of a preliminary study performed with one of the sensors based on AuNP capped with decanethiol for assessing sensor's detection potential in the direct and indirect breath measurement approaches is shown in **Figure 6.3**. Both breath samples were measured in the stationary mode during 10 min, while the sensor was successively operated at 8 V during 10 sec, followed by 0.16 sec of inactivity. The observed current changes through the sensor during one operation cycle were due to the dynamic modulation between the OFF and ON states of the switching sensor's operation methodology proposed in this study.

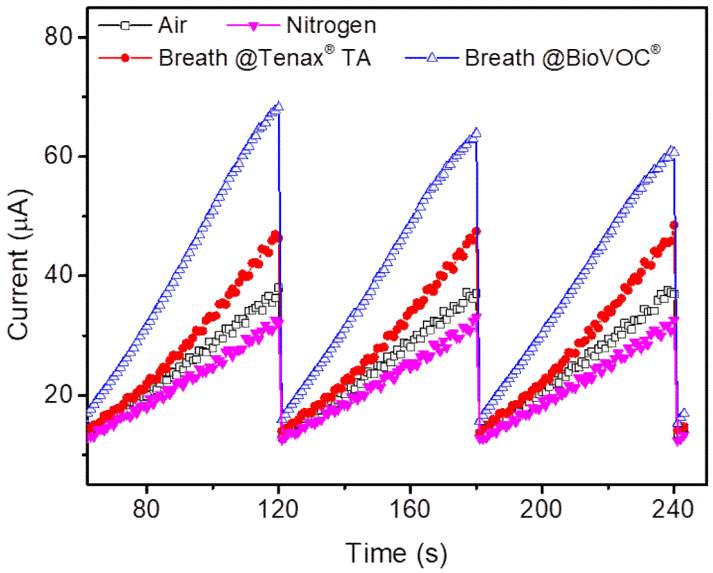

Figure 6.3: Sensor's response to: Synthetic dry air flow (black); N_2 flow (pink); Breath volatiles measured under stationary conditions in the indirect measurement mode (red); Breath sample measured under stationary conditions in the direct measurement mode (blue).

The higher sensor response in the case of the direct breath sample measurement is assumed to be due to the fact that, by avoiding the intermediate step of breath VOCs

storage and their posterior desorption, all the volatiles were transferred with no loss from the Bio-VOC sampler into the sensors test chamber

, as well as due to the humidity content present in the exhaled breath (Tenax TA is a hydrophobic material that does not retain the humidity from breath). On the other hand, as expected, sensor response to continuous flows of synthetic dry air and N_2 (200ml/min) was much lower.

6.3. Tropical Diseases Diagnosis through Exhaled Breath Analysis

6.3.1. Dengue Diagnosis

The chemical gas sensors selected for assessing the diagnosis of Dengue from exhaled breath analysis are presented in **Table 6.1**. The organic functionalities of the sensors were selected based on their affinity to the breath biomarkers of Dengue identified by the analytical studies. In this regard, dodecanethiol and oleylamine, organic functionalities with saturated hydrocarbon in the tail, have good affinity to non-polar hydrocarbons such as 1-undecyne; 4-methoxy-α-toluenethiol and 2-mercaptobenzoxazole, which possess an aromatic functionality, have high affinity to styrene and toluene; 11-mercaptoundecanol and 11-mercaptoundecanoic acid, with polar tail, have high affinity to n-propyl acrylate and 2-ethylsulfonyl through short range hydrogen interactions [3], while the benzoxazole group of 2-mercaptobenzoxazole allows for good diffusion of 1-acetyl-1H-benzotriazole. It is important to note that the sensors having the same sensing material were not identical; they were fabricated in different batches and presented slightly different morphologies

and different reference values of their baseline resistance, thus suggesting slightly different behavior to the volatiles from the exhaled breath.

Nº	Sensor	Metal nanoparticles	Organic functionality	R (MΩ)
1	S1	AuNPs	1-decanethiol	2.2
2	S2	CuNPs	Oleylamine	41
3	S3	CuNPs	11-mercaptoundecanol	4.3
4	S4	PtNPs	4-methoxy-α-toluenethiol	0.5
5	S5	CuNPs	11-mercaptoundecanoic acid	6.2
6	S6	CuNPs	Oleylamine	7.8
7	S7	CuNPs	11-mercaptoundecanol	7.1
8	S8	CuNPs	2-mercaptobenzoxazole	11.5

Table 6.1: List of the chemical gas sensors used in the Dengue study

This sensors array was used to measure the breath samples provided by 15 Dengue patients and 13 Control volunteers employing the indirect breath measurement approach. All sensors responded to the breath volatiles, exhibiting significant differences when exposed to breath samples of Dengue and Control volunteers (**Figure 6.4**). When the sensors were exposed to the breath VOCs, Van der Waals interactions between the VOCs and the ligands are expected to be dominant [4], which is consistent with the observed rapid and reversible sensor responses from **Figure 6.4**. Moreover, sensors responses were similar during the four operation cycles, therefore for performing the data analysis it was selected the first operation cycle only, in order to reduce the computational costs. The current extracted at different time intervals after sensors exposure to the breath samples (during the first operation cycle) was used to build DFA discrimination models for Dengue. The exposure times selected for each sensor are given in **Table 6.2**. Volunteer classification achieved by the individual sensors, calculated employing leave-one-out cross-validation, is summarized in **Table 6.3**.

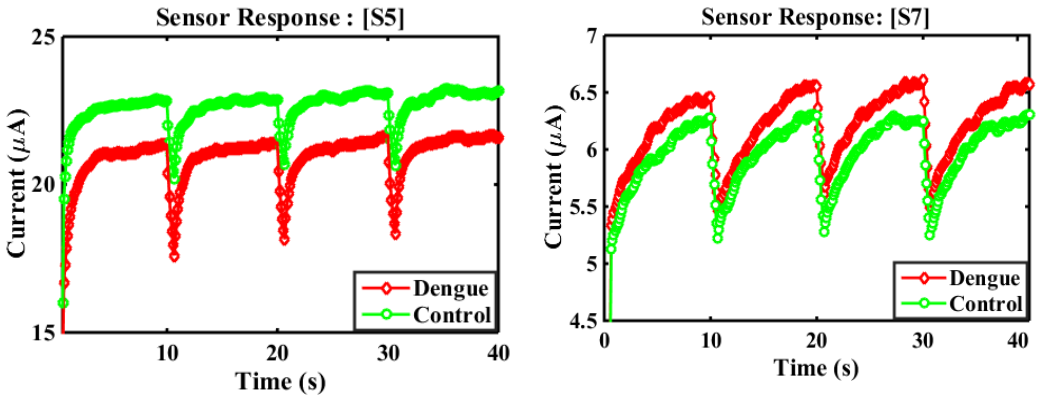

Figure 6.4. Representative sensor responses to the exhaled breath of Dengue and Control volunteers: (left) Response produced by sensor S5 based on CuNPs functionalized with 11-mercaptoundecanoic acid; (right): Response produced by sensor S7 based on CuNPs functionalized with 11-mercaptoundecanol.

All sensors showed very high discrimination potential, with classification accuracy ranging between 82.1% and 96.4% – the highest achieved by S7, based on CuNPs capped with 11-mercaptoundecanol. The DFA models built with sensors responses and ROC curves are shown in **Figure 6.5**.

Sensor	Time intervals selected for each sensor (s)							
S1	6.9	7.7	8.0	8.3	8.8	8.9	9.7	9.8
S2	6.9	7.3	7.4	7.8	8.0	8.4	8.7	9.1
S3	6.9	7.3	7.6	7.9	8.0	8.1	8.3	8.5
S4	7.1	7.5	8.3	8.4	8.7	8.9	9.1	9.2
S5	6.9	7.3	7.6	7.9	8.1	8.3	9.3	9.6
S6	7.2	7.3	8.4	8.9	9.2	9.7	9.8	9.9
S7	7.7	7.8	8.0	9.1	9.3	9.4	9.7	9.9
S8	6.9	7.2	7.4	7.7	8.3	8.4	8.7	9.2

Table 6.2: Exposure times for each sensor at which were extracted the values of the current used to build the DFA models for Dengue discrimination. S1 to S8 indicate each one of the different sensors employed in this study.

Sensor	S1	S2	S3	S4	S5	S6	S7	S8
TP	14	14	14	13	14	12	14	14
TN	12	12	11	11	12	11	13	12
FP	1	1	2	2	1	2	0	1
FN	1	1	1	2	1	3	1	1
Accuracy (%)	92.9	92.9	89.3	85.7	92.9	82.1	96.4	92.9
Specificity (%)	92.3	92.3	84.6	84.6	92.3	84.6	100	92.3
Sensitivity (%)	93.3	93.3	93.3	86.7	93.3	80	93.3	93.3

Table 6.3: Classification between Dengue and Control volunteers, calculated employing leave-

one-out cross-validation, using DFA models built with the current extracted at different exposure time intervals of the individual sensors to the breath samples. S1 to S8 indicate each one of the different sensors employed in this study.

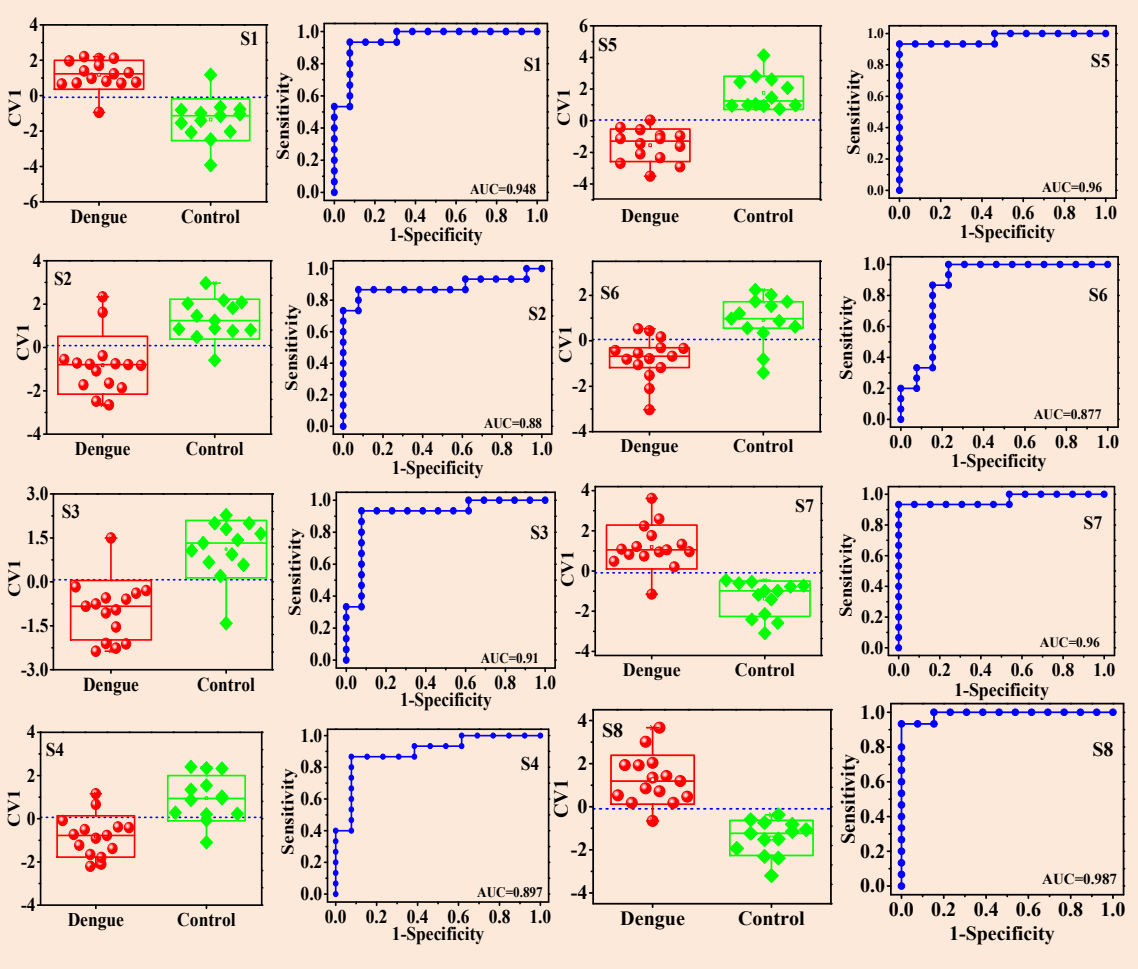

Figure 6.5: Classification between Dengue and Control volunteers using sensors responses to exhaled breath: (left) Box plots of the first canonical variable (CV1) of the DFA models calculated with the current extracted at different time intervals from each sensor response; each patient is represented by one point in the box plots; the dashed lines represent the classification border between the two groups; (right) ROC curves constructed with the CV1 of the DFA models; the resulting AUCs are indicated in each figure. S1 to S8 indicate each one of the different sensors employed in this study.

In order to analyze the influence of volunteers' gender and age on the models built with sensors responses, the classification based on these confounding factors was assessed using the DFA models built with the same currents as those selected for Dengue

classification. The low classification accuracy of these analyses proved the insensitivity of the sensors breath test to these possible confounding factors (**Table 6.4**).

Accuracy (%)	**S1**	**S2**	**S3**	**S4**	**S5**	**S6**	**S7**	**S8**
Gender	46.4	42.9	39.3	17.9	42.9	42.9	46.4	39.3
Age	25	28.6	21.4	53.6	42.9	64.3	42.9	25

Table 6.4: Classification accuracy based on the confounding factors gender and age obtained from the DFA models built with sensors' responses. S1 to S8 indicate each one of the different sensors employed in this study.

The overall classification of each sample obtained by the predominant prediction of the majority of the chemical gas sensors is presented in **Table 6.5**. Based on this classification, the combined sensor system comprising 8 different sensors was able to obtain 100% accuracy in Dengue diagnosis, while samples classification based on confounding factors such as volunteers gender and age, reached 21.4% and 32.1% accuracy, respectively.

Volunteer	No. of sensors that classified as Dengue	No. of sensors that classified as Control	Disease prediction	Gender prediction (M/F)	Age prediction (Young/Middle-Aged/Senior)
D01	8	-	Dengue	*F*	Senior
D02	7	1	Dengue	*Unclassified*	*Unclassified*
D03	8	-	Dengue	*M*	*Unclassified*
D04	7	1	Dengue	M	Young
D05	7	1	Dengue	M	*Middle-Aged*
D06	8	-	Dengue	M	*Middle-Aged*
D07	6	2	Dengue	*Unclassified*	*Unclassified*
D09	7	1	Dengue	*Unclassified*	Young
D10	8	-	Dengue	*F*	*Young*
D11	8	-	Dengue	*Unclassified*	Middle-Aged
D12	8	-	Dengue	F	Young
D13	7	1	Dengue	*M*	Young
D14	7	1	Dengue	*M*	Young
D15	7	1	Dengue	M	*Young*
D16	7	1	Dengue	*Unclassified*	Middle-Aged
C01	-	8	Control	*F*	*Unclassified*
C02	-	8	Control	*M*	*Unclassified*
C03	-	8	Control	*F*	*Unclassified*
C04	2	6	Control	*F*	*Senior*
C05	1	7	Control	*F*	*Unclassified*
C06	1	7	Control	*F*	*Middle-Aged*

C07	1	7	Control	*M*	Young
C08	1	7	Control	*M*	*Unclassified*
C10	-	8	Control	*M*	*Middle-Aged*
C11	2	6	Control	F	*Young*
C12	1	7	Control	*M*	*Middle-Aged*
C14	-	8	Control	*M*	*Unclassified*
C16	1	7	Control	*F*	*Unclassified*

Table 6.5: Samples classification achieved by the majority of the chemical gas sensors from the array. Correct predictions are indicated in bold; wrong predictions are indicated in italic. Unclassified samples refer to the cases when two classes obtained the same prediction score.

The fact that each individual sensor was able to provide high classification accuracy greatly enhances the application potential of the breath test proposed in this study, as the misclassification produced by one or very few sensors is readily compensated by the accurate classification of the other sensors in the array. Therefore, the false response from one sensor will not compromise the overall functionality of the whole sensing system. Moreover, additional sensors could be trained in a similar way for the detection of the Dengue breath volatiles pattern and replace damaged sensors from the array, if needed.

6.3.2. Leishmaniasis Diagnosis

The chemical gas sensors selected for assessing the diagnosis of Leishmaniasis from exhaled breath analysis are presented in **Table 6.6**. The organic functionalities of the sensors were selected based on their affinity to the breath biomarkers of Leishmaniasis identified by the analytical studies. The molecular ligands of sensors S1, S2, S3, and S6, with polar and aromatic functional groups in the tail, are likely to have good affinity to breath VOCs with similar functional characteristics, such as methylvinyl ketone, 4-methyl-2-ethyl-1-pentanol, hydroxyl-2,4,6-trimethyl-5-(3-methyl-2-butenyl)cyclohexyl methylacetate and 2-methyl-6-methylene-octa1,7-dien-3-ol. On the other hand, the non-polar tail of the ligand of sensors S4 and S5 interacts more preferably with non-polar

VOCs such as 2,2,4-trimethylpentane, nonane, octane, 2,3,5-trimethylhexane, and 3-ethyl-3-methylpentane.

Sensor	MNP	Molecular organic ligand	Resistance (MΩ)
S1	CuNPs	2-mercaptobenzoxazole	0.6
S2	CuNPs	11-mercaptoundecanol	2.3
S3	AuNPs	2-mercaptobenzoxazole	5.8
S4	PtNPs	1-dodecanethiol	7.8
S5	AuNPs	1-dodecanethiol	0.7
S6	CuNPs	11-mercaptoundecanoic acid	4.5

Table 6.6: List of the chemical gas sensors used in the Leishmaniasis study.

This sensors array was used to measure breath samples collected from 56 volunteers (28 HCL patients and 28 CCL controls) employing the indirect breath measurement approach. **Figure 6.6a** shows the response of sensor S1 under vacuum conditions, and to the breath samples of HCL and CCL volunteers, during four operation cycles, illustrating the rapid and reproducible response of the sensor towards the different samples analyzed.

The MNPs are electrically insulated as deposited, but upon ligand functionalization they become conductive, albeit with an intrinsic high resistance (**Table 6.6**). The organic ligand provides sorption sites for the breath VOCs, and the conductance of the sensing layer is modified upon VOCs adsorption on the ligands [3,5-8] .The decrease in the electrical DC current through the sensor upon exposure to the breath samples can be explained by VOCs sorption onto the MNPs-ligand matrix favoring film swelling, and hence increasing the distance between the MNPs cores, which thereby reduces the electron transfer between the MNPs [3,5,9]. The swelling effect is reversible when the sample is evacuated from the sensors test chamber [5,10,11], leading to the observed recovery of sensor's baseline conditions.

On the other hand, it is noted that the sensor response presents different profiles to the breath VOCs of HCL and CCL volunteers, suggesting that it is possible to discriminate breath volatiles patterns of the HCL and CCL groups. To assess the sensor's capability to discriminate the two study groups (HCL and CCL), an unsupervised PCA pattern recognition algorithm was computed with three features extracted from sensor's response to the breath samples of all volunteers from this study (see Annex II):

- F1: Mean DC current acquired during 1.22 seconds (11 sampling points) at the middle of sensor exposure to the breath sample;

- F2: Mean DC current acquired during the last 1.22 seconds (last 11 sampling points) of sensor exposure to the breath sample;

- F3: Area under the response curve during the last 1.78 seconds (last 16 sampling points) of sensor exposure to the breath sample.

Figure 6.6b presents the patients classification achieved by the PCA plot. The first principal component (PC1) of the PCA model, which accounted for 99.8% of the variance in the data (**Figure 6.6c)**, provided 80.3% accuracy, 78.6% sensitivity and 82.1% specificity for HCL discrimination, while the AUC of the ROC curve (**Figure 6.6d**), indicated 87.6% accuracy. Given these promising results, the supervised DFA pattern recognition algorithm was also investigated for training the discrimination model between the HCL and CCL groups. **Figure 6.6e** shows the classification obtained by the first canonical variable (CV1) of the DFA model, where all volunteers were correctly classified in function of their health state. The HCL classification accuracy, sensitivity and specificity calculated through leave-one-out cross-validation were all 100%.

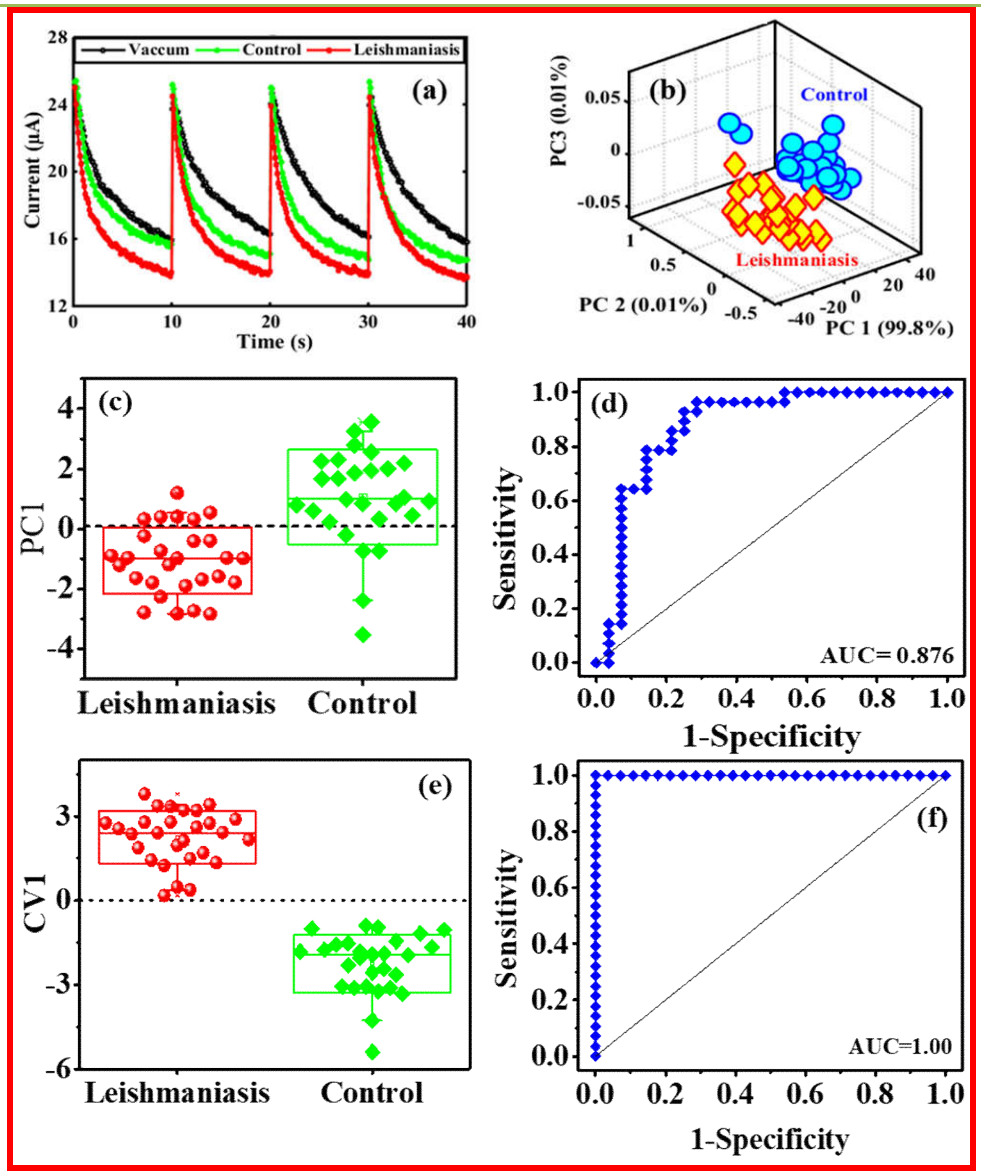

Figure 6.6: (a) Typical response of one of the sensors (sensor S1, based on CuNPs functionalized with 2-mercaptobenzoxazole) towards exposures to vacuum and breath samples of HCL and CCL volunteers; (b) PCA plot computed with the features extracted from the response of sensor S1 to the breath samples of all volunteers; each volunteer is represented by one point in the plot; (c) Boxplot of the first principal component (PC1) of the of the PCA model computed with the features extracted from the response of sensor S1 to the breath samples of all volunteers; each volunteer is represented by one point in the plot; the standard deviation of the PC1 values is represented by the error bars, while the boxes represent the 95% confidence interval; the dashed line represents the threshold classification line between the two groups, HCL patients being estimated below the dashed line and healthy controls above the dashed line; (d) ROC curve analysis of the PC1 values of the PCA model; (e) Boxplot of the most discriminative canonical variable (CV1) of the DFA model computed with the features extracted from the responses of sensor S1 to the breath samples of all volunteers; each volunteer is represented by one point in the plot; the standard deviation of the CV1 values is represented by the error bars, while the boxes represent the 95% confidence interval; the dashed line represents the threshold classification line between the two groups, HCL patients being estimated above the dashed line and healthy controls below the dashed line; (f) ROC curve analysis of the CV1 values of the DFA model.

The diagnostic model, further validated employing the ROC curve analysis (**Figure 6.6f**), gave AUC equal to 1.00, corresponding to 100% accuracy. Pursuing the same analysis for the other chemical sensors (S2-S6), the results presented in **Table 6.7** were obtained. The different sensors comprise different MNPs-ligand nanoassemblies, which differ in MNPs core size, molecular ligand structure, nanoassembly morphology and surface coverage [12]. It is clear from the results collected in **Table 6.7** that sensors based on CuNPs (i.e., S1, S2, and S6), provided the highest classification accuracy. While AuNPs have been the most extensively used in MNPs-ligand sensing films for breath VOCs sensing [13-16], these results demonstrate that chemical sensors based on ligand-capped CuNPs hold great potential for breath VOC detection.

The sensing properties of MNPs-ligand nanoassemblies depend on a number of factors, among which the MNPs core size has been assumed to be of paramount importance, and determines the effectiveness of film swelling and dielectric changes upon VOCs sorption [17]. It has further been reported that the electronic conduction of the nanoassembly, and hence its sensitivity to VOCs, depends on the morphology and size of the MNPs cores as well as on how the ligand is attached to the metal cores [11,17,18].Thus, the high sensing capability achieved in the present study by the CuNPs-ligand nanoassemblies might be attributed to the small CuNPs core size (~ 4 nm), ligand attachment and film morphology, which exhibited a well-ordered structure in the case of the CuNPs capped with 2-mercaptobenzoxazole [12]. As a result, the swelling efficiency of the film might be predominantly governed by the formation of percolation pathways upon VOCs adsorption [11,19], maximizing electrons transfer.

The overall classification ability of the chemical sensors array was next considered for assessing the synergic effect of an array of non-specific cross-reactive sensors to

respond to a variety of VOCs in the exhaled breath, enabling the identification of specific breath print patterns in multicomponent VOCs mixtures [15,20]. Employing this approach, the DFA model built with the three features F1, F2 and F3 extracted from the responses of all six sensors from the array to the breath samples analyzed yielded 98.2% accuracy, 96.4% sensitivity and 100% specificity in the classification of HCL patients (last column in **Table 6.7**). Thus, the sensor array achieved excellent discrimination capability between the study groups, suggesting that the cross reactive sensors array can be devised to achieve distinct and robust sensing features for multicomponent VOCs pattern analysis. This is because the combination of different sensors, with different MNPs and functional organic ligands, provide the desired panels of MNPs-ligands for combined sensitivity and selectivity towards the disease specific breath VOCs pattern.

	S1	S2	S3	S4	S5	S6	Sensors array
Accuracy	100	80.4	73.2	73.2	78.6	85.7	98.2
Sensitivity	100	78.6	75	57.1	75	89.3	96.4
Specificity	100	82.1	71.4	89.3	82.1	82.1	100
TP/TN	28/28	22/23	21/20	16/25	21/23	25/23	27/28
FP/FN	0/0	5/6	8/7	3/12	5/7	5/3	0/1

Table 6.7: HCL classification results obtained by the DFA models built with the responses of each individual sensor, as well as with the overall responses of all sensors from the array

The role of confounding factors (gender and age in the case of this study), which could influence sensors performance, was finally assessed for all the discriminative models built in this study. The results of these analyses confirmed that the obtained HCL classification results were not affected by patients' age, but could be slightly affected by patients gender (the accuracy of age classification ranged between 26.8% and 55.4% for

the different models, while the accuracy of gender classification ranged between 37.5% and 60.7%).

6.3.3. Echinococcosis Diagnosis

The chemical gas sensors selected for assessing the diagnosis of Echinococcosis from exhaled breath analysis are presented in **Table 6.8**. The organic functionalities of the sensors were selected based on their affinity to the breath biomarkers of Echinococcosis identified by the analytical studies. Thus, sensors S3 to S6 and S8 have a polar functional organic ligand in their tail with affinity to the CE biomarkers, while sensors S1, S2 and S7, with long chain hydrocarbons ligands with non-polar functional groups in their tail, exhibit relatively high affinity to the AE biomarkers with long non-polar hydrocarbon chains.

Sensor	Metal nanoparticle	Molecular organic ligand	Resistance (MΩ)
S1	AuNPs	1-dodecanethiol	0.7
S2	AuNPs	1-dodecanethiol	4.1
S3	CuNPs	11-mercapto-1-undecanol	2.3
S4	PtNPs	4-methoxy-α-toluenethiol	0.4
S5	CuNPs	2-mercaptobenzoxazole	0.6
S6	AuNPs	2-mercaptobenzoxazole	5.8
S7	PtNPs	1-dodecanethiol	7.8
S8	CuNPs	11-mercaptoundecanoic acid	4.5

Table 6.8: List of the chemical gas sensors used in the Echinococcosis study

When exposed to the breath samples, each sensor was characterized by rapid and reproducible response signals as well as good reversibility after finishing sample exposure. A typical response of one sensor to the breath samples provided by two volunteers is presented in **Figure 6.7**, which shows successive responses of the sensor to the breath samples during the four transient ON-OFF measurement cycles using the

indirect breath measurement approach. This was further confirmed by calculating the average current through all sensors during breath sample measurement in all measurement cycles, which was very similar for each measurement cycle (**Figure 6.8**). The sensors exhibited on one hand completely different sensitivities when exposed to the same breath sample, while on the other hand they presented different overall response patterns for different health states, suggesting a broad cross reactive sensors array that react differently with the breath VOCs mixture and thus could a priori be employed to differentiate different breath patterns [19,21].

The differences of the sensors response to different breath volatiles patterns were initially assessed for discrimination between the breath samples of CE and CCE volunteers by analyzing the responses of the sensors array to the breath samples of 52 volunteers (24 patients with CE patients and 28 CCE controls) measured employing the indirect measurement approach. Because of the reproducibility of the sensor responses during the different measurement cycles (as evidenced by **Figure 6.8**), only the first cycle was investigated in this analysis.

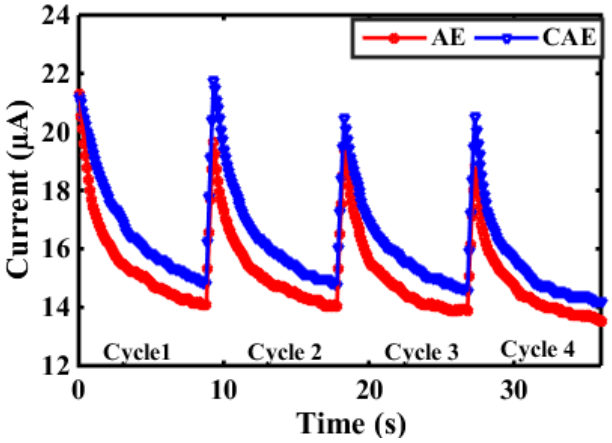

Figure 6.7: Representative response obtained by sensor S5 based on CuNPs functionalized with 2-mercaptobenzoxazole to the exhaled breath of two volunteers from the AE and CAE group, measured employing the indirect approach.

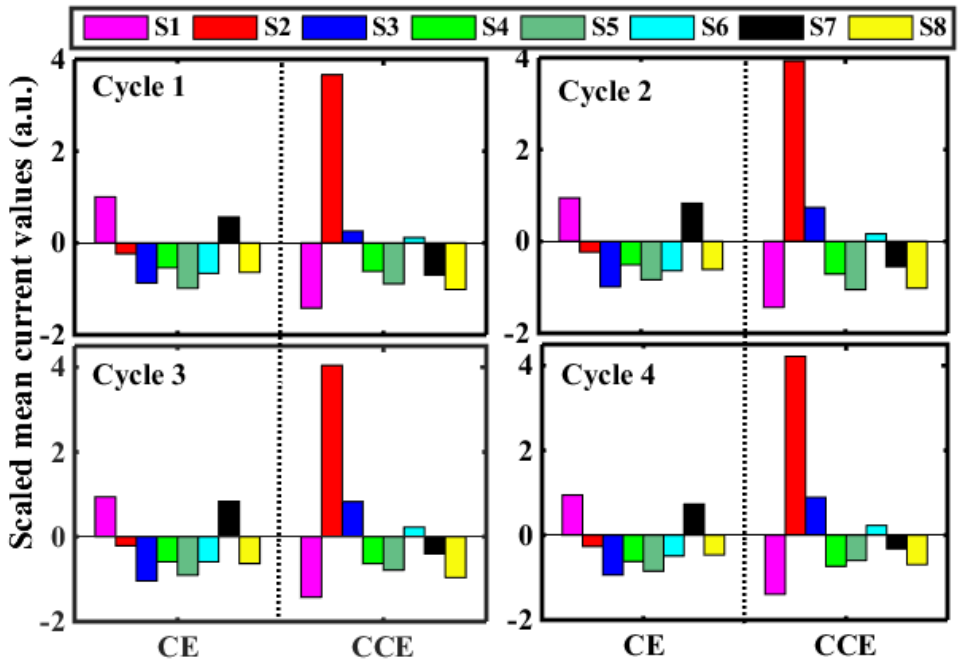

Figure 6.8: Mean current through the different sensors during breath samples measurement calculated for four measurement cycles, scaled to zero-mean and unitary variance for each sample measured and each measurement cycle. Samples measurements were performed employing indirect measurement approach.

The three features F1, F2 and F3 (calculated in the same way as in the case of the Leishmaniasis study), which were extracted from the first measurement cycle, were not able to distinguish between the breath prints of the volunteers from the CE and CCE groups, as illustrated by the heat map shown in **Figure 6.9**.

To improve data classification, different combinations of features were tested in order to develop a classification model for the CE and CCE groups employing Discriminant Function Analysis (DFA) pattern recognition algorithm. The features calculated for all sensors were scaled to zero-mean and unitary variance for each sample measured. **Table 6.9** shows all sensor and feature combinations used in the present study. The DFA model built with eight features extracted from 7 different sensors provided 100% accuracy, 100% sensitivity and 100 % specificity (values estimated through leave-one-

out cross-validation) for CE classification, indicating an excellent potential of the sensors system to diagnose Cystic Echinococcosis from breath analysis.

Given these very promising results, the capability of the sensors array to diagnose Cystic Echinococcosis on-site (directly in the hospital) was also assessed by using the direct measurement approach, whereby the sampled exhaled breath was directly exposed to the sensors without pre-concentration and headspace extraction.

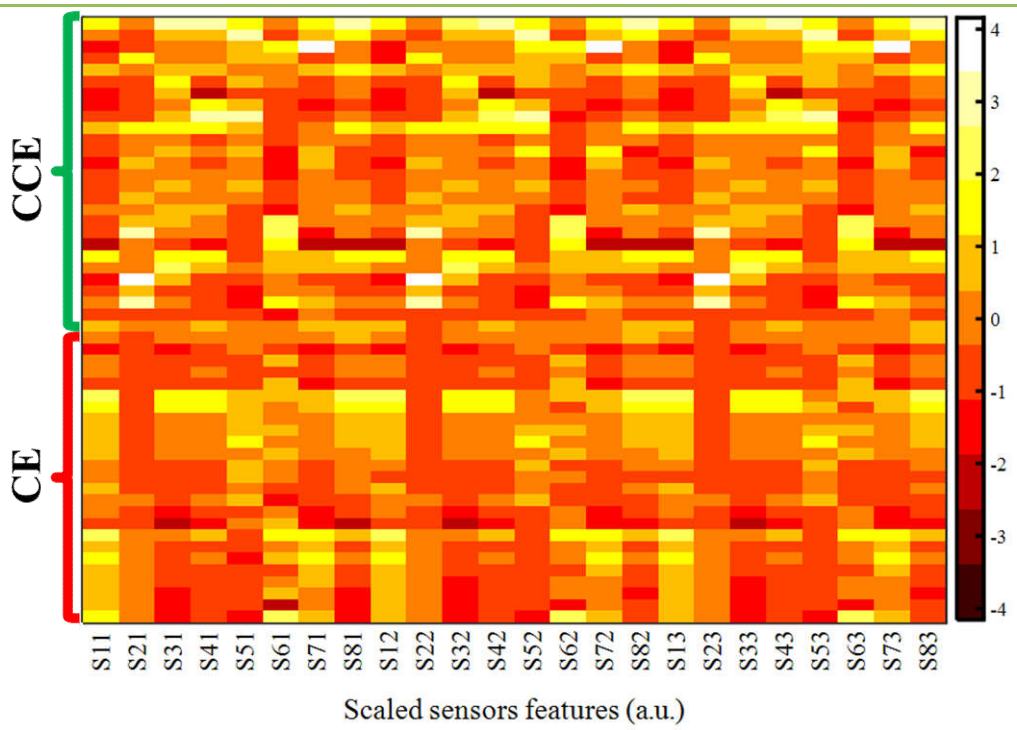

Figure 6.9: Heat map of the sensing features extracted from the sensors employed in this study, scaled to zero-mean and unitary variance for each sample measured. The first number after letter S denotes sensor's number, while the second number denotes feature number.

In this study, breath samples provided by 23 volunteers (8 CE patients and 15 CCE controls) were analyzed However, the classification results were inferior in this case (82.6% accuracy, 75% sensitivity and 86.7% specificity), which is attributed to the high relative humidity from the breath, which is not overcome in the direct measurements approach as happens in the indirect measurements approach when a suitable VOCs

hydrophobic storage material (Tenax TA) that does not retain the water vapor is used. This result was produced even though the sensors were operated at a lower voltage in the direct approach than in the indirect approach (5 V instead of 8 V) for reducing the sensors response due to local condensation of water from the humidified breath samples that adds a competing conduction mechanism by ionic conduction in addition to the electrons tunneling mechanism throughout the sensing film [2].

Based on this result, the indirect method was employed for assessing the potential of the sensors system to diagnose the AE form of the disease. In this study were analyzed breath samples provided by 22 volunteers (14 patients with AE and 8 CAE controls). The discrimination accuracy between the breath prints of AE and CAE volunteers achieved by the DFA model built with 8 features extracted from 6 different sensors was 92.9%, while the sensitivity and specificity were 92.9% and 88.9 %, respectively, demonstrating the high capability of the sensors system developed in this study to accurately diagnose also the Alveolar Echinococcosis type of the Echinococcosis disease.

Finally, since the analytical studies revealed different breath biomarkers for CE and AE, the capability of the sensors array was evaluated to discriminate between the CE and AE patients from exhaled breath analysis. This analysis was performed with the breath samples provided by 38 patients (24 patients with CE and 14 patients with AE), and the DFA discriminative model built for this analysis with 8 features extracted from 5 different sensors achieved 92.1% accuracy, 91.7% sensitivity and 92.7% specificity.

Table 6.10 summarizes the classification results obtained in this study, and **Figure 6.10** presents the corresponding graphical representation of the results.

Sensors	CE vs CCE[a]			CE vs CCE[b]			AE vs CAE[a]			CE vs AE[a]		
	F1	F2	F3	F1	F2	F3	F1	F2	F3	F1	F2	F3
S1	x									x	x	x
S2		x		x					x			
S3	x							x				
S4	x			x	x		x	x		x	x	
S5	x	x			x							x
S6			x	x		x		x				
S7	x					x	x		x			x
S8					x			x		x		

Table 6.9: Sensors and feature used in the discrimination models built for the different analysis realized in this study. *(a)* denotes indirect breath measurements, and *(b)* denotes direct breath measurements.

DFA analysis	CE vs CCE[a]	CE vs CCE[b]	AE vs CAE[a]	CE vs AE[a]
Sensitivity (%)	100	75.0	92.9	91.7
Specificity (%)	100	86.7	88.9	92.7
Accuracy (%)	100	82.6	92.9	92.1
ROC- AUC (%)	100	95.0	98.2	99.4

Table 6.10: Summary of the classification results obtained by the DFA models built with sensors responses and the area under the curve (AUC) of the receiver operating characteristic curve (ROC) built with the first canonical variable (CV1) of the DFA models. *(a)* denotes indirect breath measurements, and *(b)* denotes direct breath measurements.

The collected results show remarkable accuracy for the diagnosis and detection of different types of Human Echinococcosis disease (Cystic Echinococcosis and Alveolar Echinococcosis) considering the simplicity of data collection and associated straightforward DFA analysis of exhaled breath samples employing a chemiresistive sensors array. Such excellent classification capability of the sensors array might be attributed to the broad range of MNPs – ligand nanoassemblies used as sensing layer, which provided different network structures that contributed to the development of a highly cross reactive sensors array, where each sensor reacts differently with the VOCs mixtures exhaled through breathing.

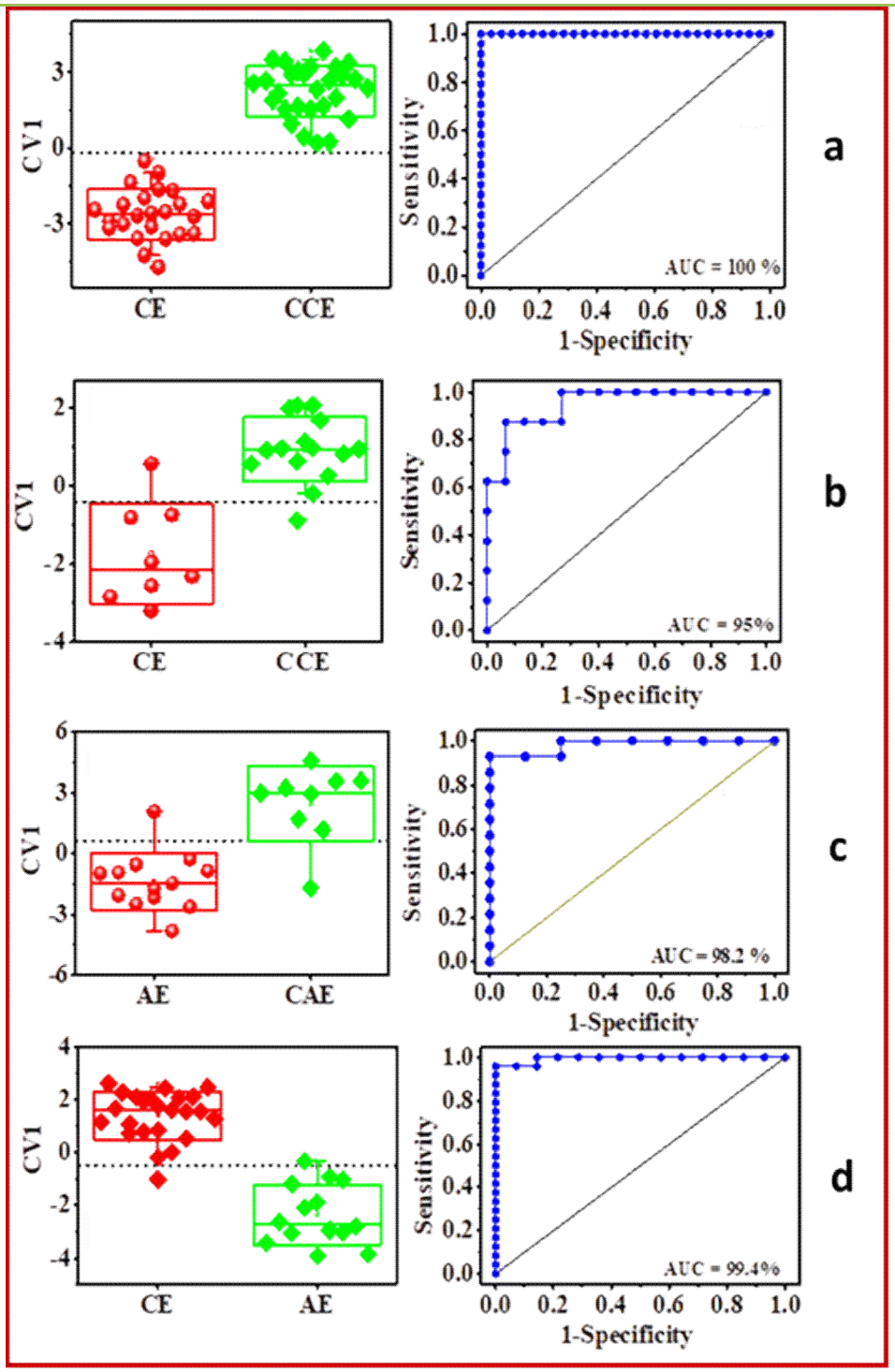

Figure 6.10: Classification between: (a) CE and CCE (indirect breath measurement method); (b) CE and CCE (direct breath measurement method); (c) AE and CAE (indirect breath measurement method); (d) CE and AE (indirect breath measurement method). (Left panels): Box plot of the first canonical variable (CV1) of the DFA models built with the sensors features presented in **Table 6.9**; each volunteer is represented by one point in the box plot; the horizontal dashed lines represent the classification border between the groups. (Right panels): ROC curves constructed with the CV1 of the DFA models. The areas under curve (AUC) values are indicated in the lower right parts of the diagrams.

This can be supported by the fact that different sensors/features were suitable for the diagnosis and discrimination of the two types of the Echinococcosis disease analyzed in this study, which is in accordance with the differences between CE and AE found by the analytical GC/Q-TOF studies. Therefore, the combinations of individual sensor/feature responses obtained with the highest sensitivity to the individual breath VOC patterns revealed the desired selectivity and provided distinguishable breath VOC patterns between CE and AE. One reason for differentiation of CE and AE may be associated with the volatile biomarkers chemical properties. The breath VOCs biomarkers identified for AE are longer chained alkane hydrocarbons compared with those for CE, which can result in reduced ability for adsorption and diffusion into the nanoassembly network, and a concomitant reduced swelling of the nanoassembly films [22].

6.4. Conclusion

Specific chemical gas sensors arrays were developed for assessing the diagnosis potential through exhaled breath analysis of the neglected tropical diseases investigated in this study. The sensing materials of the sensors arrays were judiciously selected such that to possess high affinity to the breath biomarkers identified by the analytical studies for each disease.

Two breath analysis setups were designed and developed, aiming both the direct breath samples measurement (for on-site analysis) and the indirect breath samples measurement (when the samples were measured at a different site than their collection site) with the chemical gas sensors systems.

Indirect breath samples measurements were performed for all studied diseases, revealing a remarkable diagnostic performance in distinguished diseased subjects from healthy volunteers. DFA models built with selected features extracted from sensors

responses yielded diagnostic accuracies that ranged from 100% for Dengue and Cystic Echinococcosis, to 98.2% for Cutaneous Leishmaniasis and 92.9% for Alveolar Echinococcosis. Moreover, the two dominant forms of Human Echinococcal infections, Cystic Echinococcosis and Alveolar Echinococcosis, were discriminated with 92.1% accuracy.

On the other hand, the indirect breath samples measurement approach outperformed the results obtained in the direct measurement approach, presumably due to the high humidity level from the breath in the case of the later one (the diagnosis accuracy for Cystic Echinococcosis was 82.6% employing the direct breath measurement approach, compared with 100% in the indirect breath measurement approach).

Importantly, the diagnostic models built with sensors responses were not affected by confounding factors such as volunteers' gender or age. Smoking habit was not considered as a confounding factor in this study because of the low number of smoking volunteers that participated in the study.

The combination of different sensors, with different MNPs and functional organic ligands, provided the desired panels of MNPs-ligands for combined sensitivity and selectivity towards the disease specific breath VOCs patterns, which led to the excellent results obtained. The results were furthermore favored by the sensor operation methodology proposed in this study, where the sensors were operated for 10 sec in a switching sequence, which provided a dynamic modulation between the OFF and ON states. This allowed to extract multivariate information from the kinetic reactions that occurred between the sensing material and the breath volatiles. This multivariate information enabled the selection, from the transient response of each sensor, of a set of significant features that gave very accurate classification results.

An important finding is that CuNPs-based nanoassemblies yielded higher diagnostic accuracy than AuNPs sensors, which up to date by far have been the most used biosensor MNPs material in breath detection. While sensors based on organically-functionalized AuNPs have been previously studied for the diagnosis of a number of diseases [16], the sensors based on CuNPs organic nanoassemblies used in this study have very different morphologies. They have higher exposure ratio of the organic functionality to the breath volatiles because of the much smaller particles size of CuNPs (~4 nm) as compared with AuNP (~10 nm), which is of utmost importance for chemiresistive gas sensors.

The results of the present study paves the way for the development of reliable, fast and easy-to-use tests for rapid diagnosis of neglected tropical diseases, which would counteract the present lack of reliable diagnosis tests for NTDs. The measurement of exhaled breath samples with a simple and easy to use chemical sensors array could represent a strategic tackling for the diagnosis and control of the most prevalent neglected tropical diseases caused by viral, helminthic and protozoan infections in remote areas that lack the necessary socioeconomic and medical facilities for combating these infectious diseases.

The test proposed in this study presents outstanding features, such as: **(i)** it is easy to perform and interpret in both specialist (e.g., medical doctors) and non-specialist (e.g., disease-suspected individuals) settings; **(ii)** the biological samples analyzed (e.g., exhaled breath) are collected non-invasively; **(iii)** the results are obtained in a few minutes; and **(iv)** the disease could be diagnosed in an early-stage. Therefore, it holds excellent potential for fighting against the spread of neglected tropical diseases by providing early diagnosis and adequate hospitalization and specialized medical care to the patients positively diagnoses by the breath test.

6.5. Pattern Recognition Applied in this Chapter

Besides of the supervised Discriminant Function Analysis (DFA) algorithm that was explained in the previous chapter, in this chapter was also employed the unsupervised Principal Component Analysis (PCA) algorithm.

PCA is a linear and unsupervised technique that reduces multidimensional data by calculating new orthogonal variables, called principal components (PC), as a linear combination of the input variables, which capture the maximum variance in the data, for projecting them into a low dimensional space [23]. The classification success rate of the PCA models was estimated based on samples grouping [24].

6.6. References

1. Lee, A.P.; Reedy, B.J. Temperature modulation in semiconductor gas sensing. *Sensors and Actuators B: Chemical* **1999**, *60*, 35-42.
2. Segev-Bar, M.; Shuster, G.; Haick, H. Effect of perforation on the sensing properties of monolayer-capped metallic nanoparticle films. *The Journal of Physical Chemistry C* **2012**, *116*, 15361-15368.
3. Hossam, H. Chemical sensors based on molecularly modified metallic nanoparticles. *Journal of Physics D: Applied Physics* **2007**, *40*, 7173.
4. Wang, B.; Haick, H. Effect of functional groups on the sensing properties of silicon nanowires toward volatile compounds. *ACS Applied Materials & Interfaces* **2013**, *5*, 2289-2299.
5. Zhang, H.L.; Evans, S.D.; Henderson, J.R.; Miles, R.E.; Shen, T.H. Vapour sensing using surface functionalized gold nanoparticles. *Nanotechnology* **2002**, *13*, 439.

6. Ionescu, R.; Cindemir, U.; Welearegay, T.G.; Calavia, R.; Haddi, Z.; Topalian, Z.; Granqvist, C.-G.; Llobet, E. Fabrication of ultra-pure gold nanoparticles capped with dodecanethiol for schottky-diode chemical gas sensing devices. *Sensors and Actuators B: Chemical* **2017**, *239*, 455-461.
7. Potyrailo, R.A. Toward high value sensing: Monolayer-protected metal nanoparticles in multivariable gas and vapor sensors. *Chemical Society Reviews* **2017**, *46*, 5311-5346.
8. Broza, Y.Y.; Haick, H. Nanomaterial-based sensors for detection of disease by volatile organic compounds. *Nanomedicine* **2013**, *8*, 785-806.
9. Steinecker, W.H.; Rowe, M.P.; Zellers, E.T. Model of vapor-induced resistivity changes in gold−thiolate monolayer-protected nanoparticle sensor films. *Analytical Chemistry* **2007**, *79*, 4977-4986.
10. Bashouti, M.Y.; de la Zerda, A.-S.; Geva, D.; Haick, H. Designing thin film-capped metallic nanoparticles configurations for sensing applications. *The Journal of Physical Chemistry C* **2014**, *118*, 1903-1909.
11. Joseph, Y.; Guse, B.; Vossmeyer, T.; Yasuda, A. Gold nanoparticle/organic networks as chemiresistor coatings: The effect of film morphology on vapor sensitivity. *The Journal of Physical Chemistry C* **2008**, *112*, 12507-12514.
12. Welearegay, T.G.; Cindemir, U.; Österlund, L.; Ionescu, R. Fabrication and characterisation of ligand-functionalised ultrapure monodispersed metal nanoparticle nanoassemblies employing advanced gas deposition technique. *Nanotechnology* **2018**, *29*, 065603.
13. Marom, O.; Nakhoul, F.; Tisch, U.; Shiban, A.; Abassi, Z.; Haick, H. Gold nanoparticle sensors for detecting chronic kidney disease and disease progression. *Nanomedicine* **2012**, *7*, 639-650.

14. Nakhleh, M.K.; Broza, Y.Y.; Haick, H. Monolayer-capped gold nanoparticles for disease detection from breath. *Nanomedicine* **2014**, *9*, 1991-2002.

15. Peng, G.; Tisch, U.; Adams, O.; Hakim, M.; Shehada, N.; Broza, Y.Y.; Billan, S.; Abdah-Bortnyak, R.; Kuten, A.; Haick, H. Diagnosing lung cancer in exhaled breath using gold nanoparticles. *Nature Nanotechnology* **2009**, *4*, 669.

16. Nakhleh, M.K.; Amal, H.; Jeries, R.; Broza, Y.Y.; Aboud, M.; Gharra, A.; Ivgi, H.; Khatib, S.; Badarneh, S.; Har-Shai, L. Diagnosis and classification of 17 diseases from 1404 subjects via pattern analysis of exhaled molecules. *ACS Nano* **2017**, *11*, 112-125.

17. Han, L.; Daniel, D.R.; Maye, M.M.; Zhong, C.-J. Core−shell nanostructured nanoparticle films as chemically sensitive interfaces. *Analytical Chemistry* **2001**, *73*, 4441-4449.

18. Dovgolevsky, E.; Tisch, U.; Haick, H. Chemically sensitive resistors based on monolayer-capped cubic nanoparticles: Towards configurable nanoporous sensors. *Small* **2009**, *5*, 1158-1161.

19. Tisch, U.; Haick, H. Arrays of chemisensitive monolayer-capped metallic nanoparticles for diagnostic breath testing. In *Reviews in Chemical Engineering*, 2010; Vol. 26, p 171.

20. Shehada, N.; Cancilla, J.C.; Torrecilla, J.S.; Pariente, E.S.; Brönstrup, G.; Christiansen, S.; Johnson, D.W.; Leja, M.; Davies, M.P.A.; Liran, O.*, et al.* Silicon nanowire sensors enable diagnosis of patients via exhaled breath. *ACS Nano* **2016**, *10*, 7047-7057.

21. Peng, G.; Hakim, M.; Broza, Y.Y.; Billan, S.; Abdah-Bortnyak, R.; Kuten, A.; Tisch, U.; Haick, H. Detection of lung, breast, colorectal, and prostate cancers

from exhaled breath using a single array of nanosensors. *British Journal Of Cancer* **2010**, *103*, 542.

22. Dovgolevsky, E.; Konvalina, G.; Tisch, U.; Haick, H. Monolayer-capped cubic platinum nanoparticles for sensing nonpolar analytes in highly humid atmospheres. *The Journal of Physical Chemistry C* **2010**, *114*, 14042-14049.
23. Scott, S.M.; James, D.; Ali, Z. Data analysis for electronic nose systems. *Microchimica Acta* **2006**, *156*, 183-207.
24. Durán-Acevedo, C.M.; Aylen Lisset, J.-M.; Gualdrón-Guerrero, O.E.; Welearegay, T.G.; Martinez-Marín, J.D.; Caceres-Tarazona, J.M.; Acevedo, Z.C.S.; Beleño-Saenz, K.d.J.; Cindemir, U.; and, L.Ö.*, et al.* Exhaled breath analysis for gastric cancer diagnosis in colombian patients. *Oncotarget* **2018**, *9*, 28805-28817.

CHAPTER 7

7. GENERAL CONCLUSIONS AND FUTURE PERSPECTIVES

This chapter presents the general conclusions of the thesis work and the future perspectives.

7.1. General Conclusions

The aim of the PhD thesis was twofold: on one hand, a novel technique for the fabrication of ultrapure metal nanoparticles was introduced, while on the other hand it revealed the diagnostic potential of chemical gas sensors based on ultrapure ligand-capped metal nanoparticles for the diagnosis of three different neglected tropical diseases (Dengue, Leishmaniasis and Echinococcosis), whose sensing films were selected based on their affinity to the breath biomarkers of these diseases that were identified through analytical studies.

The first goal of the thesis was to design, fabricate and characterize chemical gas sensors based on ultrapure ligand-capped metal nanoparticles. For this end, it has shown that the Advanced Gas Deposition technique employed in this thesis work provided the synthesis of ultrapure monodispersed metal nanoparticles (MNPs) from the evaporation of a pure metal precursor in vacuum. I focused on the synthesis of three metal nanoparticles (AuNPs, PtNPs and CuNPs), however the novel technique that I introduced in my thesis can be easily extended to practically any MNPs synthesis using the proper metal source and adjusting the synthesis parameters. MNPs capping with organic ligands was achieved by dip-coating the substrates in a solution formed in high purity reagents, which led to the formation of self-assembled nanoparticles-organic monolayers with a network-like structure. The MNPs-ligand nanoassemblies presented hybrid characteristics, where the nanoparticles served for electrical conduction, while

the capping organic molecules promoted electron tunneling through the MNPs. The electrical characterization of the AuNPs and PtNPs nanoassemblies led to the first ever observation of Schottky diodes fabricated from nanomaterials based on metal nanoparticles. Preliminary sensing measurements showed the good potential of the novel chemical gas sensors that I produced for breath VOCs detection.

The second goal of the thesis was to develop a non-invasive, easy-to-use and patient-friendly methodology for rapid diagnosis of neglected tropical diseases. For this end, I investigated disease diagnosis via exhaled breath samples analyses, which are easy to obtain and present no discomfort or risk for patients' health. In my thesis I focused on three different types of neglected tropical diseases (Dengue, Leishmaniasis and Echinococcosis) caused by three different pathogens (viral, helminthic and protozoan infections, respectively). Breath samples were collected from patients and controls in Colombia (Dengue), Tunisia (Cutaneous Leishmaniasis and Cystic Echinococcosis) and Poland (Alveolar Echinococcosis) with a simple to use Bio-VOC^{TM} breath sampler, and stored in Tenax TA sorbent tubes before analysis.

Analytical studies performed with a GC/Q-TOF equipment (state-of-the-art in analytical chemistry, which was employed for the first time for breath samples analysis in my thesis) identified six putative biomarkers for Dengue (three aromatic compounds, two esters and one alkene), nine putative biomarkers for Cutaneous Leishmaniasis (one ester, two alcohols, one ketone and five alkanes), two putative biomarkers for Cystic Echinococcosis (one alkene and one acid), and seven putative biomarkers for Alveolar Echinococcosis (all alkanes). Importantly, although Cystic Echinococcosis and Alveolar Echinococcosis are from the same family of Echinococcus, the putative biomarkers found for CE and AE were totally different, indicating that the pathogenesis of CE and

AE infections and the changes that they produce in the body chemistry appear to be completely different. Classification models built with the identified biomarkers yielded fair to good discrimination accuracies: 84.4% for Dengue diagnosis, 80% for Cutaneous Leishmaniasis diagnosis, 65.5% for Cystic Echinococcosis diagnosis, and 80.9% for Alveolar Echinococcosis diagnosis.

Based on these biomarkers, I selected several chemiresistive gas sensors based on the ultrapure ligand-capped metal nanoparticles that I produced in the first part of my thesis, targeting to detect the breath volatiles patterns of the studied neglected tropical diseases. Although the sensors are not sensitive to a specific volatile, but they respond to the collective exhaled VOCs pattern that comprises a range of compounds with concentrations under the limit of detection of the GC/Q-TOF equipment (and therefore not detected in the analytical studies), the putative biomarkers that I identified did however form a sufficient basis for a rational design of the sensors arrays for each disease. Classification models built with selected features extracted from sensors responses to the exhaled breath samples of the patients and controls yielded diagnostic accuracies that ranged from 100% for Dengue and Cystic Echinococcosis, to 98.2% for Cutaneous Leishmaniasis and 92.9% for Alveolar Echinococcosis, while the two dominant forms of Human Echinococcal infection (Cystic Echinococcosis and Alveolar Echinococcosis) were discriminated with 92.1% accuracy.

Remarkably, CuNPs-based nanoassemblies yielded higher diagnostic accuracy than AuNPs sensors, which up to date have been by far the most used sensing MNPs materials in breath detection. The CuNPs sensors have higher exposure ratio of the organic functionality to the breath volatiles because of their much smaller particles size (~4 nm) as compared with AuNPs (~10 nm), which is of utmost importance for

chemiresistive sensors. Moreover, in comparison with the metal nanoparticles sensors used in previous studies, which employ chemical precursors that often leave traces of residual compounds, the active materials of the sensors used in my thesis were synthesized from a pure metal evaporated in vacuum. With this technique, ultrapure nanoparticles are produced, which ensures reproducible sensors responses with no influence of confounding reactions with synthesis residuals, which is crucial in chemical sensor technology.

Finally, it is worth mentioning that the sensing methodology that I introduced in my thesis for neglected tropical diseases diagnosis is simple to use and interpret, and is amenable for use in both specialist and non-specialist settings. Therefore, it could provide a powerful tool for the facile, rapid and non-invasive diagnosis of NTDs even at an early stage when metabolic changes are already produced, and would be especially important in regions lacking specialized healthcare diagnostic facilities.

7.2. Future Perspectives

I performed my PhD studies in the framework of the H2020-MSCA-RISE-2014 TROPSENSE project “Development of a non-invasive breath test for early diagnosis of tropical diseases” (ref. 645758). Based on my results, a portable prototype has been developed and is currently employed for on-site validation tests.

On the other hand, further studies are necessary to elucidate the similarities and differences between the breath volatiles patterns of other diseases with similar clinical profile or characteristics (e.g., arboviral infections such as Zika and Chikungunya for

Dengue, other diseases that produce cutaneous lessions for Cutaneous Leishmaniasis and lung cancer or other diseases produced by helminthes for Echinococcosis).

Finally, the novel ultrapure ligand-capped metal nanoparticles nanoassemblies that I produced in my study are of high technological importance for different applications, and allows to considerably widen the variety of MNPs-organic ligands combinations that can be used as (bio)chemical sensors, SERS surfaces and molecular electronic rectifiers.

ANNEX

ANNEX I

XPS Analysis of the Ligand-Nanoparticle Nanoassemblies

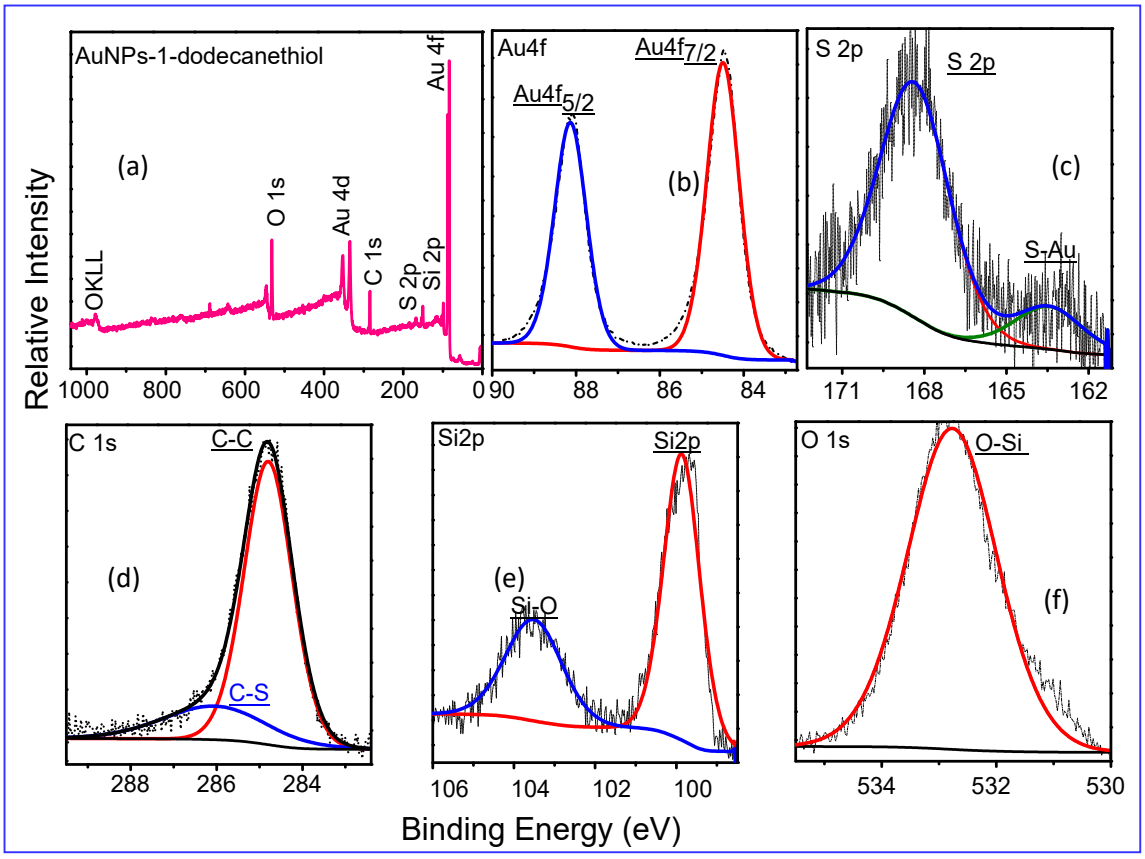

Figure AI-1: (a) High resolution XPS spectra for the AuNPs-1-DDT nanoassembly; Corresponding elemental spectra for: (b) Au4f, (c) S2p, (d) C1s, (e) Si2p, (f) O1s.

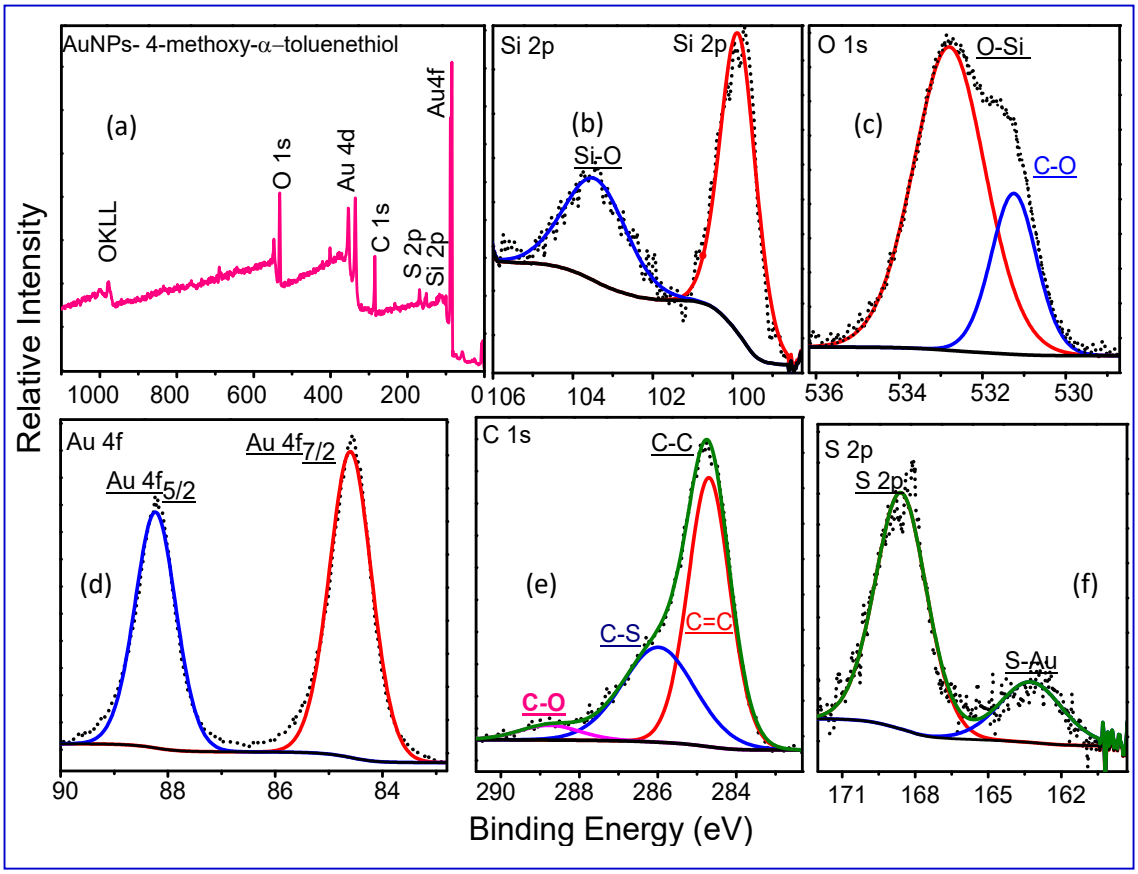

Figure AI-2: (a) High resolution XPS spectra for the AuNPs-4-MTT nanoassembly; Corresponding elemental spectra for: (b) Si2p, (c) O1s, (d) Au4f, (e) C1s, (f) S2p.

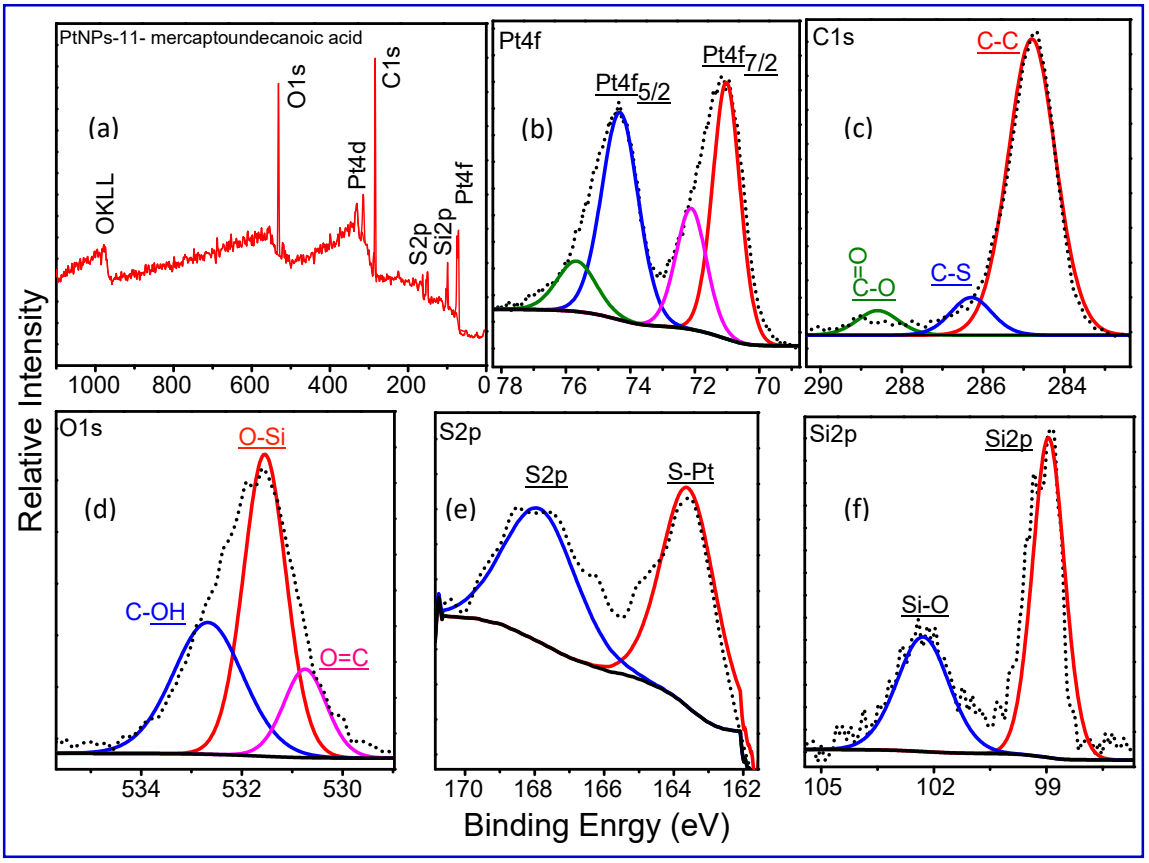

Figure AI-3: (a) High resolution XPS spectra for the PtNPs-11-MUDA nanoassembly; Corresponding elemental scans for: (b) Pt4f, (c) C1s, (d) O1s, (e) S2p, (f) Si2p.

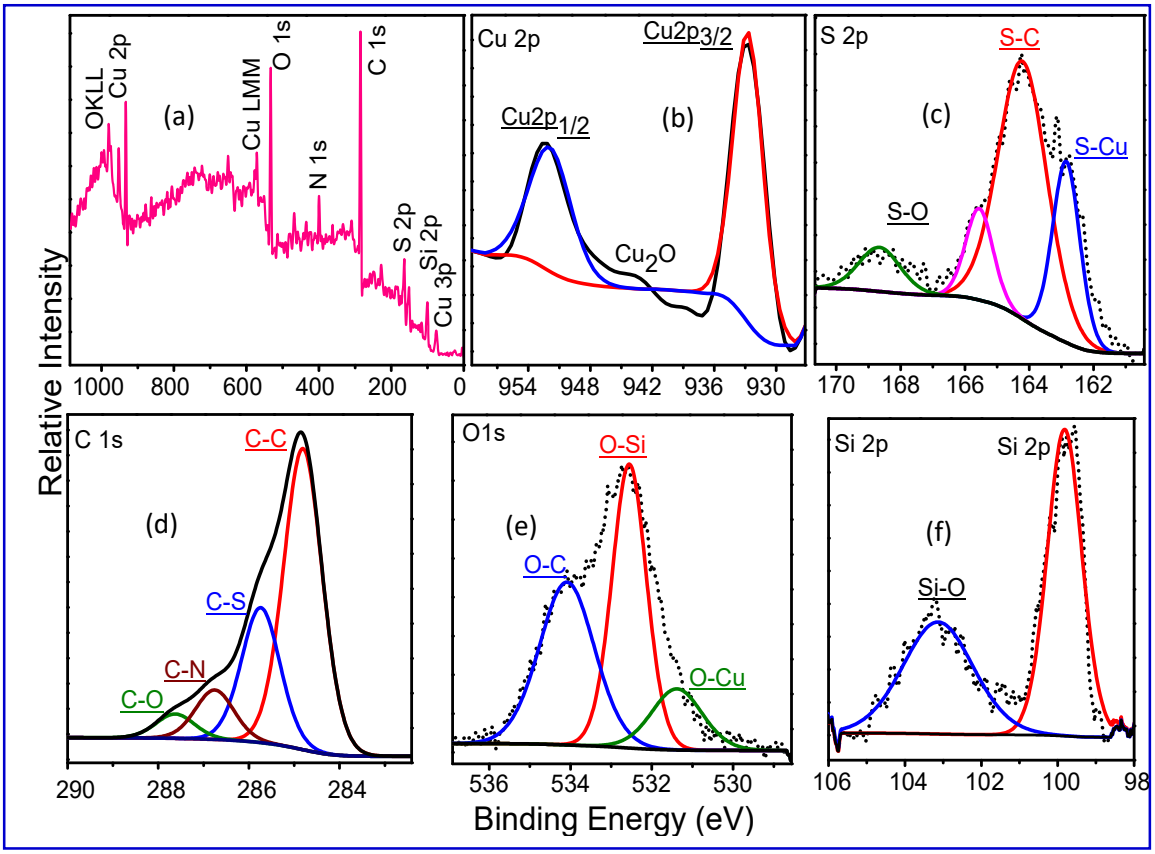

Figure AI-4: (a) High resolution XPS spectra for the CuNPs-2-MBZO nanoassembly; Corresponding elemental scans for: (b) Cu2p, (c) S2p, (d) C1s, (e) O1s, (f) Si2p.

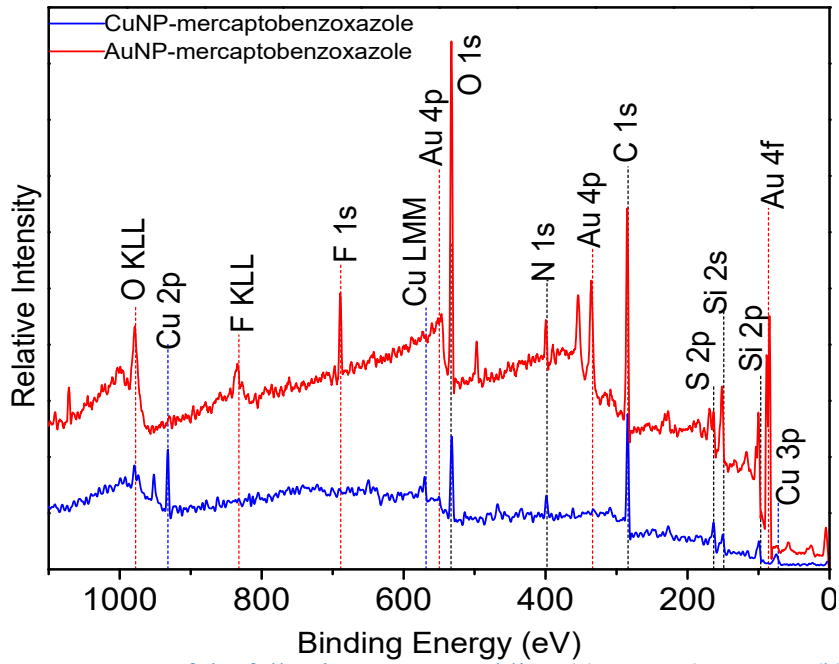

Figure AI-5: XPS spectra of the following nanoassemblies: (a) AuNP-2-MBZO, (b) CuNPs-2-MBZO.

ANNEX II

Schematic representation of the sensors features extracted

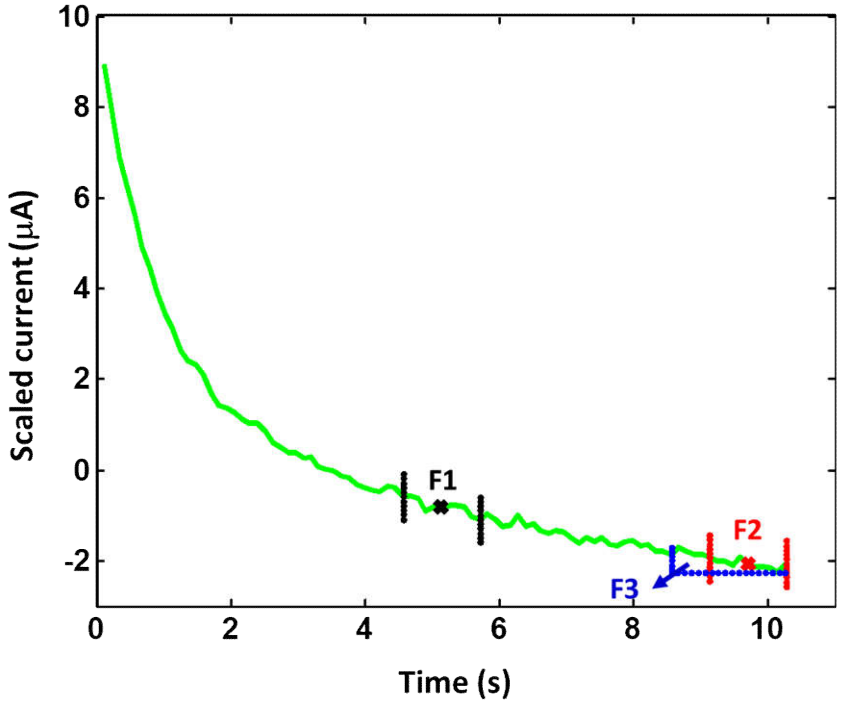

ANNEX III

Thesis Publications

1. **Tesfalem Geremariam Welearegay**, Mohammed Fethi Diouani, Florina Ionescu, Dhafer Laouini, Samira Khaled, Lars Österlund , and Radu Ionescu, *Ligand-capped Ultrapure Metal Nanoparticle Sensors for the Detection of Cutaneous Leishmaniasis Disease in Exhaled Breath*, ***ACS Sensors***, 2018, xx,xx, DOI:10.1021/acssensors.8b00759, Impact Factor: 5.711

2. **Tesfalem Geremariam Welearegay**, Mohamed Fethi Diouani, Lars Österlund, Sebastian Borys, Florina Ionescu, Dhafer Laouini, Samira Khaled, Umut Cindemir, Radu Ionescu, Diagnosis *of Human Echinococcosis via Exhaled Breath Analysis: A Promise for Rapid Diagnosis of Infectious Diseases Caused by Helminths* , ***Journal of Infectious Diseases***, 2018, 40, 1-9, DOI:10.1093/infdis/jiy449, Impact Factor: 5.186

3. **Tesfalem Geremariam Welearegay**, Umut Cindemir, Lars Österlund and Radu Ionescu, *Fabrication and Characterization of Ligand-Functionalised Ultrapure Monodispersed Metal Nanoparticles Nanoassemblies Employing Advanced Gas Deposition Technique*, ***Nanotechnology*** 2018 (29), 065603, DOI:10.1088/1361-6528/aa9f65, Impact Factor: 3.44

4. Radu Ionescu, Umut Cindemir, **Tesfalem Geremariam Welearegay**, Raul Calavia, Zouhair Haddia, Zareh Topalian, Claes-Göran Granqvist, Eduard Llobet, *Fabrication of ultra-pure gold nanoparticles capped with dodecanethiol for Schottky-diode chemical gas sensing devices*, ***Sensors and Actuators B: Chemical***, 2017, (239), 455-461, DOI:10.1016/j.snb.2016.07.182, Impact Factor: 5.667

5. **Tesfalem Geremariam Welearegay**, Cristhian Manuel Durán-Acevedo, Aylen Lisset Jaimes-Mogollón,Giovanni Pugliese, Florina Ionescu1, Omar Geovanny Perez-Ortiz, Oscar Eduardo Gualdrón-Guerrero, Umut Cindemir, Lars Österlund, Radu Ionescu, *Exhaled Air Analysis as a Potential Fast Method for Early Diagnosis of Dengue Diseases (submitted)*

6. **Tesfalem Geremariam Welearegay**, T arik Saidi,. Alfonso Romero, Benachir Bouchikhi, Radu Ionescu, Metal Nanoparticle –Ligand Nanoassemblies for VOCs Capacitive Sensing (under preparation)

Publications not included in thesis

7. Cristhian Durán Acevedo*, Aylen Lisset Mogollón, Oscar Eduardo Guerrero, **Tesfalem Geremariam Welearegay***, Julián Martínez Marín, Juan Martin Tarazona, Zayda Constanza Acevedo, Kelvin de Jesus Saenz, Umut Cindemir, Lars Österlund, Radu Ionescu, *Exhaled breath analysis for gastric cancer diagnosis in Colombian patients*, ***Oncotarget*** 2018, (9), 28805-28817, **(*equal contribution)**, DOI:10.18632/oncotarget.25331, Impact Factor: 5.168
8. Oriol Gonzalez, **Tesfalem Geremariam Welearegay**, Xavier Vilanova and Eduard Llobet, *Using the transient response of WO3 nanoneedles under pulsed UV light in the detection of NH_3 and NO_2*, *Sensors* **2018**, *18*(5), 1346; DOI:10.3390/s18051346, Impact Factor: 2.475
9. Tarik Saidi, Dariusz Palmowski, Sylwia Babicz-Kiewlicz, **Tesfalem Geremariam Welearegay**, Nezha El Bari, Radu Ionescu, Janusz Smulko, *Exhaled breath gas sensing using pristine and functionalised WO3 nanowire sensors enhanced by UV-light irradiation*, ***Sensors and Actuators B Chemical*** ,2018, 273, 1719-1729,DOI:10.1016/j.snb.2018.07.098, Impact Factor: 5.667
10. **Tesfalem Geremariam Welearegay**, Raul Calavia, Radu Ionescu, Xavier Vilanova and Eduard Llobet, *Gas Sensing with Back-gated FET Sensors Employing Pt/WO_3 Nanowires as Channel* (To be submitted)
11. Tarik Saidi, Mohammed Moufid, Maria Rosa, **Tesfalem Geremariam Welearegay**, Nezha El Bari, Radu Ionescu, Jamal Eddine Bourkadi, Jouda Benamor, Mustapha El Ftouh, Benachir Bouchikhi, *Non-invasive diagnosis of the histological lung cancer using GC/Q-TOF/MS in combination with an electronic nose based on WO3 nanowires sensors under UV-irradiation* (submitted)

Conference attendance and conference Proceedings

1. **Tesfalem Geremariam Welearegay**, Radu Ionescu, *Neglected Tropical Diseases Diagnosis Through Exhaled Breath Analysis of VOCs Analysis with E-Nose System*, ISOCS Short Course Winter 2018, 10-13 January, Kühtai,- Austria. **Invited talk and Course Assistant**

2. **Tesfalem Geremariam Welearegay,** Aylen Lisset Mogollón, Oscar Eduardo Guerrero, Cristhian Durán Acevedo, Radu Ionescu, *Ligand-capped AuNPs Gas Sensor Array for Gastric Cancer Diagnosis in Exhaled Breath*, Graduate Student Meeting on Electronics Engineering 2017, Tarragona, Spain, June 29-30, **Oral presentation**
3. Radu Ionescu, **Tesfalem Geremariam Welearegay**, *Fabrication Of Ultrapure Monolayer Capped Au Nanoparticles Chemical Gas Sensors For Breath Analysis*, BIT 5th Annual Conference of AnalytiX, Fukuoka, Japan, March 22-24, 2017, **Invited Talk**

4. **Tesfalem Geremariam Welearegay** Raul Calavia, Radu Ionescu, Eduard Llobet, *Gas sensing Approaches based on WO3 Nanowire-back Gated Devices*, 31th Eurosensors Conference, Paris, France, Sept. 04-06, 2017, **Oral presentation**

5. **Tesfalem Geremariam Welearegay**, O.E. Gualdrón, A.L. Jaimes, J.M. Cáceres, G. Pugliese, U. Cindemir, C.M. Durán , L. Österlund, R. Ionescu, *Ultrapure Organically Modified Gold Nanoparticles for Breath Analysis*, 30th Eurosensors Conference, Budapest, Hungary, Sept. 04-07, 2016, **Poster presentation**

6. **Tesfalem Geremariam Welearegay**, Radu Ionescu, Giovannie Pugliese, Umut Cindemir, Lars Österlun, *Ultrapure Organically Functionalized Gold Nanoparticles Nanoassemblies for Schottky-diode Gas Sensors*, CIMTEC Congress, Perugia, Italy, June 05-09, 2016, **Invited Talk**

7. **Tesfalem Geremariam Welearegay**, Raul Calavia, Radu Ionescu, and Eduard Llobet, *Fabrication of Back-Gated Field Effect Transistor Based Gas Sensors*, TROPSENSE Symposium, Tarragona, Spain, April 21-22, 2016, **Invited Talk**

8. Radu Ionescu, **Tesfalem Geremariam Welearegay**, *Non-invasive Diseases Diagnosis with Schottky –diode Chemical Gas Sensors based on Ultrapure monolayer capped*

Gold Nanoparticles Nanoassemblies, BIT's 2nd World Congress of Smart Materials WCSM-2016, Singapore, March 04-06, **Invited Talk**

9. Radu Ionescu, **Tesfalem Geremariam Welearegay,** *Ultrapure Monolayer capped Gold Nanoparticles Chemical Gas Sensors for Biomedical Application*, 5th Conference on Nanomaterials (CN2016) Bangkok, Thailand, January 14-16, **Invited Talk**

10. Radu Ionescu, **Tesfalem Geremariam Welearegay**, *Schottky-diode Gas Sensors based on Ultrapure Gold Nanoparticles*, 39th International Microelectronics and Packaging IMAPS, Conference, Gdansk, Poland, Sept 20-23, 2015, **Invited Talk**

Patents

1. S.R. Ionescu, **T.G. Welearegay**, "Method for the diagnosis of cutaneous leishmaniasis" / *"Método para el diagnóstico de la leishmaniasis cutánea"*. Patent request P2018/105363 (Spain). Priority date: 18/04/2018. Spanish patent.

2. S.R. Ionescu, **T.G. Welearegay**, "Method for the diagnosis of diseases caused by helminths" / *"Método para el diagnóstico de enfermedades causadas por helmintos".* Patent request P2018/105283 (Spain). Priority date: 18/04/2018. Spanish patent.

3. C.M. Durán-Acevedo, O.E. Gualdrón-Guerrero, S.R. Ionescu, **T.G. Welearegay**, "Method for the diagnosis of Dengue" / *"Método para el diagnóstico del Dengue"*. Patent request NC2018/0004119 (Colombia). Priority date: 26/10/2017. Colombian patent.


2018!

UNIVERSITAT
ROVIRA i VIRGILI